Towards advanced operation modes of magnetic and electrostatic confined fusion machines

Towards Advanced Operation Modes of Magnetic and Electrostatic Confined Fusion Machines

PROEFSCHRIFT

ter verkrijging van de graad van doctor aan de Technische Universiteit Eindhoven, op gezag van de rector magnificus prof.dr.ir. F. P. T. Baaijens, voor een commissie aangewezen door het College voor Promoties, in het openbaar te verdedigen op maandag 1 juli 2019 om 11:00 uur

door

Maximilian Claus Constantin Messmer

geboren te Würzburg, Germany

Dit proefschrift is goedgekeurd door de promotoren en de samenstelling van de promotiecommissie is als volgt:

voorzitter:	prof.dr.ir. E.J.E. Cottaar
1e promotor:	prof.dr. R.J.E. Jaspers
2e promotor:	prof.dr. N.J. Lopes Cardozo
co-promotor:	dr.ir. F.A.A. Felici (École polytechnique fédérale de Lausanne)
leden:	prof.dr.ir. O.J. Luiten
	prof.dr. T. Fülöp (Chalmers University of Technology)
	dr. S.B. Korsholm (Technical University of Denmark)

Het onderzoek of ontwerp dat in dit proefschrift wordt beschreven is uitgevoerd in overeenstemming met de TU/e Gedragscode Wetenschapsbeoefening.

Towards Advanced Operation Modes of Magnetic and Electrostatic Confined Fusion Machines

Maximilian Claus Constantin Messmer

This work has been carried out within the framework of the EUROfusion Consortium and has received funding from the Euratom research and training programme 2014-2018 and 2019-2020 under grant agreement No 633053. The views and opinions expressed herein do not necessarily reflect those of the European Commission.

A catalogue record is available from the Eindhoven University of Technology Library
ISBN: 978-90-386-4812-5
NUR: 924
Printed by: Gildeprint - The Netherlands

Summary

Nuclear fusion is the process where two light nuclei collide to form one heavier nucleus. The process is accompanied by the release of energy, which scientists have tried to harness in a controlled way since the 1950s. In a fusion machine the fuel is heated to millions of degrees Celsius, at which it is in the plasma state. In the most advanced fusion reactor design, the tokamak, the plasma is confined in a torus by a magnetic field which is created by external coils and a current induced in the plasma. The configuration of the magnetic field has a direct influence on the performance of the reactor, measured by how long the energy can be confined by the system. The magnetic field is, however, not accurately known, because the current density profile, resulting from self-organisation of the plasma, is not known to high accuracy. To understand and control the performance-enhancing effects of the magnetic field on the energy confinement, it must first be determined experimentally, either by a direct measurement, or by an indirect reconstruction of the plasma equilibrium.
The research in the first part of this thesis is focussed on the reconstruction of the magnetic field using the motional Stark effect (MSE) diagnostic. The MSE diagnostic measures the emission of fast neutral particles injected into the plasma. The particles experience a Lorentz electric field $\boldsymbol{E_L} = \boldsymbol{v} \times \boldsymbol{B}$, depending on their velocity $\boldsymbol{v}$ and magnetic field $\boldsymbol{B}$, resulting in a Stark splitting of the emission lines. The degenerate emission is polarised with respect to $\boldsymbol{E_L}$, from which information about the pitch of the magnetic field can be inferred. The magnetic field is reconstructed from measurements of the polarisation angle in combination with a physical model of the system. Research has been done on MSE systems at two different tokamaks: KSTAR in Daejeon, South Korea and
ASDEX Upgrade in Garching, Germany.

Measuring the polarised emission with an accuracy of only a few tenths of degrees, required for a physical evaluation, is challenging due to the many error sources and because the polarisation angle itself is a small quantity. At KSTAR, a multi-step calibration routine has been developed for the commissioning of a newly installed MSE system. The calibration involves an in-vessel calibration to correct changes in the measured polarisation angle induced by optical components, elimination of Faraday rotation caused by changes in the retardance of optical components exposed to magnetic fields, a calibration of the (hardware) bandpass filters used to select the polarised emission from the background emission, as well as a cross-check of the reconstructed magnetic field against magnetic instabilities recorded by secondary diagnostics, which is required to eliminate systematic uncertainties of currently unknown origin. With the calibration routine the polarisation angle can be reconstructed with an accuracy of 0.2° in 10 ms intervals. The diagnostic was used to measure changes in the magnetic field structure during the sawtooth

instability, a plasma instability which expels the hot plasma core when too much current is driven in the plasma centre. No conclusive theories describing the phenomena have been established since it was first measured in 1974. The developed theories make different predictions of changes of the magnetic topology in the plasma centre, which could not be confirmed experimentally with the required accuracy. In this work so-called monster sawtooth instabilities (sawtooth instabilities with exceptionally long durations) have been analysed and the change in magnetic topology is shown to be in accordance with the Kadomtsev model of magnetic reconnection.
Secondly, at ASDEX Upgrade an "MSE observer" has been implemented to provide accurate estimates of the pitch angle in situations where only noisy measurements are available. A state observer estimates the state of a system based on input and output measurements. The implemented observer uses an extended Kalman filter (EKF) to combine polarisation angle measurements with predicted measurements from the plasma simulator RAPTOR (which solves the poloidal flux diffusion and electron transport equation). It is shown that by combining (noisy) measurements and (inaccurate) model predicted measurements a more accurate estimation of the magnetic topology is possible than by either alone. The implemented design is able to reconstruct the current density profile with high accuracy in situations where the measurement uncertainty is as high as 0.5° and the model is (deliberately) severely perturbed. This is an important first step towards a robust, real-time MSE constrained equilibrium reconstruction, for which both the EKF and RAPTOR code are suitable, owing to their high speed. Furthermore, the measurement predicted by RAPTOR can be used in situations, or at machines, where no MSE diagnostic is available. Then, the EKF will provide the measurement predicted by RAPTOR to the Grad-Shafranov solver as a physics-based constraint to the internal magnetic field. This can improve today's equilibrium reconstruction, where, if no MSE diagnostic is available, information about the magnetic field is only available at the plasma edge and the magnetic topology in the plasma centre is estimated based on predefined profiles matching the boundary condition at the edge.

The tokamak is only one of many fusion concepts. Devices commonly referred to as Fusors confine ions with static electric fields. This confinement principle is called inertial electrostatic confinement (IEC). IEC devices consist of a grounded, typically spherical, vacuum vessel in which a transparent grid is centred. The vessel is filled with the fuel gas at low pressures and a negative potential is applied to the grid. If the potential difference between the grid and vacuum vessel is high enough, plasma breakdown occurs and ions accelerate towards the centre of the device where they can collide with other ions or neutrals and might fuse. Fusors are not under consideration as a fusion power plant due to their low performance, but could serve for industrial applications requiring a cheap neutron source.
In this work the influence of experimental and geometric parameters on the neutron production rate is analysed. A model is developed to determine the ion source-function, describing at which distance from the cathode grid ions are created. The model matches spectroscopic observations, which show that the bulk of

the ions are created in the vicinity of the grid, and thus have little kinetic energy when passing through the cathode. The model shows a weak dependence of the source function on experimental parameters (pressure, grid potential and grid radius), but predicts a decrease in slow ion current (i.e. ions generated inside the cathode and colliding with the grid) at low pressures. Then, more current is available for high energy ions and an increased fusion rate is expected, which is experimentally confirmed. Furthermore, the influence of the high voltage feedthrough (which connects the grid to the power supply) on the ion trajectories is analysed. It is shown that an insulator surrounding the stalk is necessary to restore radial symmetry of the electric field. Without such an insulator, the majority of the ions will collide with the stalk and not oscillate at all.

A fundamental problem with IEC devices are scattering losses caused by collisions between ions and electrons. Fusors were designed with the goal to sustain a non-Maxwellian ion velocity distribution. However, ions quickly thermalise due to the large Coulomb scattering cross section and their reduced energy lowers the fusion cross section and thus the performance. To overcome this principal limitation, a redesign based on the geometry of a fusor is proposed. The conceptual design confines pure ion bunches in a spherical geometry at low pressures in an electron free system. Similar to a classical IEC device, the ion bunches are confined on oscillatory trajectories and collide in the centre of the device. However, additional pulsed grids are used to spatially compress the bunches during each oscillation and to retain them at a non-Maxwellian velocity distribution. This increases the efficiency by reducing energy losses to electrons, mitigates thermalisation caused by ion-ion collisions and maximises the fusion cross section. A spherical geometry is chosen to compress the bunches transversal to the oscillatory direction and to ensure that all ions converge in the centre of the device. The design is simulated with the General Particle Tracer (GPT©), code. The simulations are used to determine the timing and strength of the pulsed electric field to compress and sustain the ion bunches. It is shown that a geometry similar to the TU/e fusor can be used to confine pure ion bunches with densities up to $1 \cdot 10^{14}$ m^{-3} for thousands of oscillations. The concept is limited to confining only ions with equal mass, effectively limiting the available fuel to deuterium. Fuel composed of different species, such as the favoured deuterium-tritium, would result in different oscillation periods and consequent debunching. A workaround for this limitation could be to collide the species at their lowest common oscillation time, e.g. pure deuterium-tritium bunches at a period of $2 \times 3 = 6$ times the hydrogen oscillation time.
In the current design the density is limited by transversal bunch confinement. For the advancement of the concept, for example to an industrial viable neutron source, design modifications are required. Such can be an increased number of bunches, or the addition of high-density targets in the centre of the device. With the later, the largest gains are possible, but the principle challenge of removing the electrons from the target must be overcome to keep the losses low. Now that the feasibility has been shown, an experimental proof of principle and design optimisations are required as the next steps.

Contents

Introduction

I.1 Prelude

I.1.1 The dream of never-ending energy

Figure I.1.1: Cropped view of the most complete picture of the observable universe by P. Budassi [1]. Our local gravitational fusion reactor – *the sun* – is shown centred amidst millions of other fusion devices brightening up our nights.

Since the beginning of time, humans were fascinated by the sun, its importance manifested by an array of solar deities [2]. Kiloyears later, once the old gods were shaken off, and a new god called *science* took over, we strived to understand the sun and its processes. At last, breakthrough came when Eddington [3, 4] and Bethe [5], with the help of a little $E = mc^2$, explained the suns energy production cycle based on nuclear fusion: the process of combining light particles into heavier ones accompanied by a release of energy.

The curiosity of mankind has however not stopped here, but one wonders if we can tame the old gods and ignite the fire of the sun on earth to produce energy for generations to come. After the fast success with fission power plants and achieving the first stellar fire on earth, the hydrogen bomb, in 1952 [6], scientists were optimistic to create a stable, burning fusion reactor soon after.
And thus began a long journey riddled with stepping stones and setback which is still ongoing at the time of writing ...

I.1.2 Harnessing fusion on earth

Creating a machine which can produce net power based on nuclear fusion offers the promise of never-ending energy due to the abundance of hydrogen. There are a variety of approaches pursued today. The technologically most advanced concepts are designed to fuse two heavy hydrogen isotopes, specifically:

$$D + T \longrightarrow {}^4He(3.5\ MeV) + n(14.1\ MeV) \tag{I.1.1}$$

This reaction is favoured because it has the highest fusion cross section (a characterisation for the probability that a fusion reaction will occur) at the lowest particle energy (or temperature).

The reasons why after 60 years of intense research we have not been able to achieve a stable, power generating fusion discharge are manyfold, but the fundamental physics limitation is captured in figure I.1.2.

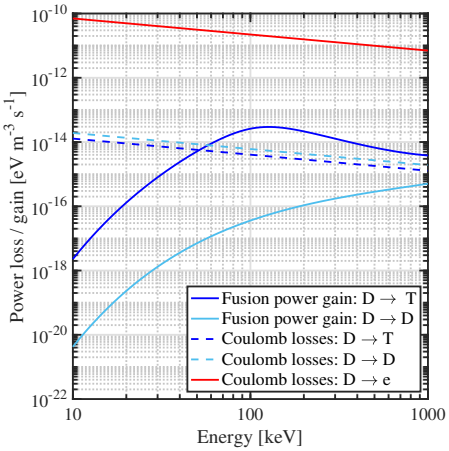

Figure I.1.2: Comparison between fusion power gain and the losses due to Coulomb scattering of a fast deuterium ion transversing through a deuterium or tritium target. In a charge neutral system the losses always outweigh the gains (see red line), leading to fast thermalisation of the fuel and the requirement for confinement of high temperature plasmas.

Figure I.1.2 compares the power lost due to Coulomb collisions against the power gained from fusion reactions of a fast deuterium particle transversing through a stationary deuterium and tritium target. In a charge neutral target, i.e. when electrons are present, the losses always exceed the gains independent of the incidents particle energy. This is a fundamental limitation and direct result of the (unfortunately) small fusion cross sections. Since the fusion reaction between deuterium and tritium has the highest cross section, the situation worsens for other fuels.

However, the sun does shine and achieving energy gain through fusion reactions is possible, but it is not as simple as firing fast particles at each other. Because the particles always thermalise faster as fusion reactions take place, reactors are designed to confine a thermal plasma. Whether the gains outweigh the losses in a thermal plasma depends on the plasma density n, its temperature T, and the energy confinement time τ_E. Fusion reactors are designed to reach "ignition" of the plasma, which is achieved when the plasma temperature is sustained by α-particle heating alone. The requirements on the density, temperature and confinement time to ignite the plasma are [7]:

$$n\tau_E \geq \frac{12}{\langle \sigma v \rangle} \frac{T}{E_f}, \tag{I.1.2}$$

where $\langle \sigma v \rangle$ is the over the temperature averaged cross section and velocity of the ions and E_f the energy released per fusion reaction. For deuterium-tritium, the minimum is expected at temperatures between $10-20$ keV, where equation I.1.2 can be approximated as

$$n\tau_E T > 3 \cdot 10^{21}\,\mathrm{keV\ m^{-3}s}. \tag{I.1.3}$$

This gives a clear requirement on the density, temperature and confinement time when designing a fusion reactor. Numerous different designs have been concepted over the years to overcome the losses and create an energy producing fusion reactor. Two of them, which are subject to this thesis, are the tokamak and IEC devices:

Part A: Tokamaks A tokamak is a type of fusion reactor which confines a thermal plasma with magnetic fields. The performance of a tokamak and stability of the plasma confinement are strongly interlinked with the magnetic topology, which is generated by external coils and a current induced in the plasma. The distribution of the current is however not known, as is the resulting magnetic field. In the first part of the thesis the magnetic field structure in a tokamak is calculated by constraining plasma equilibrium solvers with the motional Stark effect (MSE) diagnostic.

Part B: IEC and EdC devices Due to the high cross section of Coulomb scattering, plasmas quickly thermalise. Inertial electrostatic confinement (IEC) devices confine ions with static electric fields and are believed to be able to uphold a non-Maxwellian ion velocity distribution, although this is a controversial claim. In part B of the thesis, ways to increase the performance of IEC devices are explored, and secondly, a novel design confining ions using electrodynamic confinement (EdC) is proposed. The EdC reactor uses pulsed electric fields to uphold a non-thermal distribution of ions in order to optimise the fusion cross section and minimises other loss mechanisms dominant in IEC devices.

In the next two sections, both parts of the thesis are introduced with their associated research question.

I.2 Part A: Reconstruction of the current density profiles in tokamaks

The technologically most advanced concepts for a net energy generating fusion machine is the tokamak. In a tokamak, magnetic fields are used to confine a deuterium-tritium plasma, which is heated to approximately 150.000.000°C. A schematic of a tokamak is shown in figure I.2.1.
To confine both electrons and ions, a helical magnetic field is required. Using solely a toroidal field would lead to charge separation in the plasma, resulting in a drift of the plasma column into the wall [8]. The toroidal component of the field is generated by toroidal magnetic field coils surrounding the plasma. To generate the poloidal magnetic field, a current is induced in the plasma by the transformer principle: The inner poloidal field coils, also referred to the central solenoid, act as the primary winding of a transformer, the plasma is the secondary winding. The induced current creates the poloidal magnetic field required for plasma confinement.

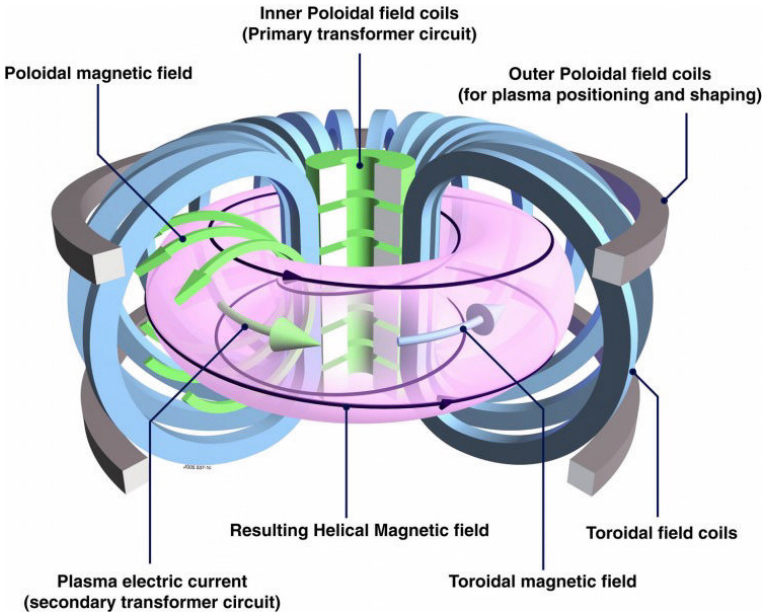

Figure I.2.1: Schematic of a tokamak. The helical magnetic field required for plasma confinement is generated by the toroidal field coils and a current induced in the plasma. The plasma current is induced through the inner poloidal field coils. Additional magnetic coils are required for plasma positioning and shaping. Image reprinted from [9].

Tokamaks have made tremendous progress since their inception. However, their operation is difficult due to numerous instabilities in the plasma and energy break-

even has not been demonstrated, yet. To list all difficulties associated with tokamak operation is out of the scope of this thesis; three problems directly associated with the conducted research are:

Tokamak plasmas are pulsed by design, rather than continuous:
The plasma current required to uphold the poloidal magnetic field is induced via the transformer principle. This requires a constantly changing current in the central solenoid, which is not indefinitely possible. These ohmically driven discharges are limited to ≈ 1000 s for a reactor the size of ITER (the largest tokamak to date, currently being built in Cadarache, France).

The performance of tokamaks strongly depends on plasma configuration:
In an ohmic scenario, the current density profile is peaked in the plasma centre and monotonically decreases towards the plasma edge. Using various actuators it is possible to manipulate the current density profile in such a way, that it is peaked off-axis. It was found that this can improve the energy confinement time, the metric of how well energy is confined in the system, leading to increased core temperatures and ultimately higher fusion output. These so-called advanced scenarios are also investigated as a way to increase the pulse length, or even operate the tokamak continuously.

Plasma instabilities decrease the performance and can cause structural damage:
A number of current driven instabilities exist which degrade plasma confinement and lead to a decrease in performance. The most severe instabilities can lead to disruptions - the sudden loss of confinement. During a disruption the energy stored in the plasma is deposited in the tokamak structure. For the current generation of devices this is still acceptable and a frequently occurring event. However, in the next generation device ITER, the energy stored in the plasma is so large, that a disruption can lead to structural damage of the reactor and must be avoided [10].

To understand and control these problems as well as to optimise the performance of a tokamak, the current distribution in the plasma must be known, and controlled. However, even 60 years after the first tokamak was built, no direct, local measurement of the current density profile is available. Instead, equilibrium solvers, which solve the plasma force balance

$$\nabla \boldsymbol{p} = \boldsymbol{j} \times \boldsymbol{B} \tag{I.2.1}$$

are used to calculate the pressure and current distribution in the plasma. In equation I.2.1, $\boldsymbol{p}$ is the plasma pressure, $\boldsymbol{j}$ the current density and $\boldsymbol{B}$ the magnetic field. To solve the force balance, i.e. reconstruct the equilibrium, the solver must be constrained by internal and external measurements to arrive at meaningful results. The Motional Stark Effect (MSE) diagnostic can be used as a constraint on the current density profile. The MSE diagnostic provides a measure of the magnetic pitch angle, the angle between the poloidal and toroidal magnetic field. It analyses the emission of fast neutral particles injected into the plasma which is

polarised with respect to the magnetic field. The first MSE system was designed and built by Levinton in 1989 [11] and similar diagnostics have been built at a number of different tokamaks [12, 13, 14, 15].

Depending on the investigated physics, the tolerable measurement uncertainty can be as low as 0.1°, a challenging task at hand due to numerous sources of measurement uncertainties. Furthermore, offline reconstruction is merely the first step, towards control of current density profile where real-time measurements are required. Real-time capable MSE diagnostics have been built at ASDEX Upgrade [16] and JT-60 [17] and DIII-D [18]. Unfortunately, the MSE system at ASDEX Upgrade can only be used in a limited number of discharges because polarised background light distorts the measurement. With this in mind, the author investigates:

Research questions and approach

> **Q1:** ***Can the polarisation angle be measured with an uncertainty of*** $\Delta\gamma \leq 0.2^\circ$ ***on a newly installed MSE system at the KSTAR tokamak*****?**
>
> **Q2:** ***Is it possible to use model-based prediction to reduce the high uncertainties at the MSE diagnostic at ASDEX-Upgrade tokamak*****?**

These questions are investigated in Part A of the thesis. A brief summary of the research on the two tokamaks is:

KSTAR (Q1): An MSE system was designed and built in collaboration with Eindhoven University at the KSTAR tokamak. For the commissioning of the diagnostic a device independent calibration routine was developed. The calibration accounts for systematic uncertainties arising from the diagnostic assembly, measurement deviations due to the strong magnetic fields of the tokamak as well as systematic uncertainties of unknown origin. With this, it was possible reduce $\Delta\gamma$ below 0.2° for measurements averaged over 10 ms and accurately reconstruct the current density profile.
The diagnostic is used to investigate the sawtooth instability, a current driven instability which expels the hot plasma core if too much current is driven in the plasma centre. For this event, theoretical models have different predictions of the response of the current density profile. The results of the analysis point towards the Kadomtsev model of magnetic reconnection.

ASDEX Upgrade (Q2): The ASDEX Upgrade tokamak has a real-time capable MSE system. However, since the wall surrounding the plasma has been equipped with metallic tiles, measurements of the MSE system are perturbed

due to polarised reflections originating from the wall opposite of the MSE diagnostic window. To obtain accurate estimates of the polarisation angle, a model-based observer is implemented. It combines error-prone measurements with predicted measurements from a model describing the system to obtain accurate estimates of the system. As a model the plasma simulator RAPTOR is used to estimate the current density profile and by using an extended Kalman filter, the predicted measurement and real measurement are combined to improve the accuracy of the MSE diagnostic. With this approach an accurate estimation of the current density profile is demonstrated in situations where the model was deliberately perturbed and the uncertainty $\Delta\gamma$ is as high as $\Delta\gamma = 0.5°$.

These topics are discussed in detail in the first half of the thesis: After a more in depth introduction to tokamaks in section A.1, the MSE diagnostic and the setup at the KSTAR tokamak are explained in section A.2. Challenges and recent developments of MSE systems are reviewed in section A.3 before the reconstruction algorithm, used to calculate the polarisation angle from the raw data, is explained in section A.4. The work at the KSTAR tokamak (research question Q1) is presented in section A.6, followed by the implementation of the observer at the ASDEX Upgrade tokamak in section A.6 (research question Q2). Part A is concluded in A.7.

I.3 Part B: Design of a non-thermalising fusion reactor based on the concept of inertial electrostatic confinement

The previously introduced tokamak reactor is only one of a whole zoo of fusion concepts; an overview of various concepts grouped by confinement principle is shown in figure I.3.1. Two of the confinement principles are magnetically confined (MFE) or inertial confined (IFE) devices. The tokamak is a type of closed, magnetically confined machine: the plasma is closed upon itself in a torus and confined by magnetic fields. In inertial confinement reactors, the fuel, usually provided in the form of a solid pellet, is heated in a very short time by an external energy source, for example a laser. The pellet implodes upon itself and for a very short time fusion relevant conditions are reached. During this time the plasma is confined by the inertia of the particles. Thus the name, inertial confinement fusion.

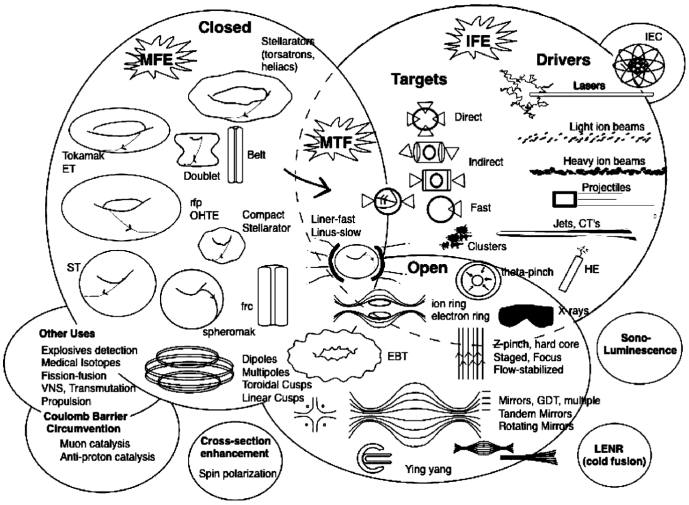

Figure I.3.1: Taxonomy of various fusion machines, reprinted from [19]. The different concepts are grouped into closed and open systems, inertial fusion experiments and smaller subcategories. As depicted, in comparison to open systems, closed systems do not have open ends to reduce the losses. In closed and open systems the fuel is confined by electric or magnetic field. In inertial fusion experiments the fuel is rapidly heated and fusion conditions are achieved for only a short time, in which the ions are confined by their own inertia.

A subset of the described inertially confined fusion machines are inertial electrostatic confinement (IEC) devices, often referenced as fusors (top right in figure I.3.1). The concept stems from designs by Farnsworth and Hirsch [20, 21] from the 1960s. In a fusor, a highly transparent grid at negative potential is placed in a grounded vacuum chamber. The chamber is filled with the fusion fuel. If the right experimental settings are chosen for the pressure, the distance between electrodes and a high enough potential difference is applied between the grid and the vacuum chamber, plasma breakdown occurs. The ions are attracted towards the centre, electrons accelerate towards the vacuum vessel. Ions missing the grid will pass through the cathode region due to their inertia (thus the name IEC) and will begin to oscillate (they are confined). Amongst others, fusion collisions can occur between two fast ions or a fast ion and the background gas. The design of a typical fusor is shown in figure I.3.2.

Fusors have been built in a number of laboratories around the world [22, 23, 24, 25], and due to the relatively simple setup, the fusor is a popular device amongst fusion enthusiasts [26]. The University of Eindhoven has built its own device in 2013 [27]. Unfortunately, as Rider showed, fusors are unlikely to be operated in a regime with net energy gain [28]. His analysis concludes, amongst other things, that fast ions thermalise through collisions with other ions 2-3 orders of magnitude faster than they fuse. In an ideal fusor ions oscillate indefinitely until

they fuse and loose only little energy along the way. However, as Rider showed, thermalisation occurs on fast timescale and contrary to previous reports [29, 30], a non-Maxwellian energy distribution amongst ions cannot be sustained. This should not come as a surprise since no external drivers exist to hinder the ions from thermalising.

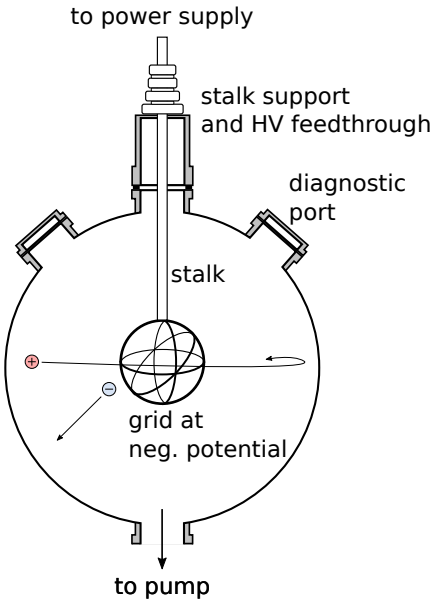

Figure I.3.2: Schematic of a fusor. Ions are attracted to the centre by the negative potential applied at the grid. If they do not collide with the grid, the ions can get confined on oscillatory trajectories.

Even though fusors may not be suitable as a fusion power plant, they may be used as compact neutron generators for industrial applications, when operated with deuterium as a fuel. Deuterium has a ≈50% probability to produce a neutron when fusing:

$$\mathrm{D} + \mathrm{D} \longrightarrow {}^{3}_{2}\mathrm{He}(0.82\ \mathrm{MeV}) + \mathrm{n}(2.45\ \mathrm{MeV}) \quad [50\%] \tag{I.3.1}$$

$$\mathrm{D} + \mathrm{D} \longrightarrow \mathrm{T}(1.01\ \mathrm{MeV}) + \mathrm{p}(3.02\ \mathrm{MeV}) \quad [50\%] \tag{I.3.2}$$

However, besides the already mentioned fast thermalisation, other loss mechanisms are limiting the performance of fusors: two of them are ion losses through neutralisation and an unfavourable ion velocity distribution. The high charge exchange cross section will, at typical operating pressures, only allow for a few oscillations before ions are neutralised. Secondly, spectroscopic measurements suggest that the majority of the ions are created close to the cathode and thus only gain a fraction of the available potential energy. The slow ions will use-up a large fraction of the supplied power, but only make a small contribution to the reaction rate (a more detailed description of both loss mechanisms is provided in section B.1.3).

Research question and approach

To improve the performance in IEC devices, the losses must be reduced and the number of fast ions must be increased. As part of this research, two approaches are pursued:

(i) Performance optimisation of IEC devices

Thermalisation and neutralisation losses are difficult to reduce because they are determined by the (fixed) cross sections and pressure required for plasma breakdown. Secondly, the low number of fast ions, caused by a peaking of the ion birth radius towards the cathode can be influenced. As part of this research on increasing the performance in a fusor, it is investigated whether ...

... the ion birth radius, and thus the ion velocity distribution, can be influenced by experimental parameters?

To answer the question, model and experimental results are analysed to understand the influence of the pressure, cathode potential and cathode radius on the ion velocity distribution, and furthermore the influence of the stalk on the symmetry of the vacuum electric field is evaluated.

(ii) Design reconception to reduce intrinsic losses

Energy losses via Coulomb scattering and fast ion losses through charge exchange collisions are difficult to mitigate because the working principle of a fusor relies on a high gas pressures for ion creation. To reduce these losses, a new confinement principle in an electron free system is proposed. The second part of the IEC research tackles the questions, whether ...

... oscillating, colliding, pure ion bunches can be sustained at a non-Maxwellian velocity distribution?

Herefore a design is proposed which uses pulsed electric fields to compress ion bunches in real- and velocity-space during every oscillation. The design hinders thermalisation and also reduces charge exchange losses by using external ion sources in a high vacuum system. The feasibility of such a system is demonstrated with particle simulations.

Part B of the thesis is structured as follows: after an introduction to IEC devices in section B.1, the experimental setup at TU/e as well as the research on shifting the ion velocity distribution is summarised in section B.2. The feasibility of the confinement of non-Maxwellian ion bunches is demonstrated in section B.3, followed by the conclusions in section B.4.

Part A:
q-profile reconstruction using the motional Stark effect diagnostic

A.1 Introduction to tokamaks and the safety factor

The most successful and advanced concept for an energy producing fusion reactor is the tokamak. Tokamaks are designed to confine a deuterium-tritium plasma at approximately 150.000.000°C with magnetic fields. The tokamak was invented by soviet physicists Igor Tamm and Andrei Sakharov in the 1950's in Russia. After its outstanding performance was confirmed by western physicists, tokamaks were built in laboratories around the world. The tokamak principle is depicted in A.1.1. The plasma is confined inside a donut shaped vacuum vessel by a helical magnetic field. The field is generated in part by toroidal field coils encircling the plasma and in part by a current carried by plasma. Only the toroidal component of the magnetic field, generated by the toroidal field coils, can be measured directly. The poloidal magnetic field is not known, because the current distribution in the plasma, i.e. the current density profile $\boldsymbol{j}$, is the result of the self-organisation in the plasma which is not controlled externally [31].

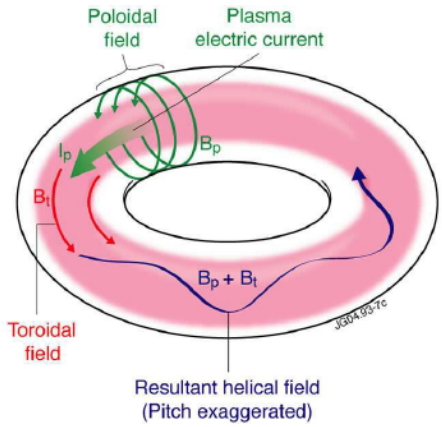

Figure A.1.1: Magnetic field required to confine a plasma in a tokamak. A helical field is required for the confinement of ions and electrons. The toroidal component is generated by external magnetic coils, the poloidal component is generated by a current which is induced in the plasma. Reprinted from [32].

Knowledge of the magnetic field is important for tokamak research, as will be explained via the safety factor q. Instead of evaluating the magnetic fields or current density, its derived quantity, the safety factor $q(\psi)$ is used as a figure of merit in tokamak research:

$$q(\psi) = \frac{1}{2\pi} \oint \frac{1}{R} \frac{B_\phi}{B_p} \mathrm{d}l, \tag{A.1.1}$$

with toroidal magnetic field B_ϕ and poloidal magnetic field B_p, poloidal magnetic flux ψ (introduced later in this section), and major radius R (the distance

from the geometric centre of the tokamak to the geometric centre of the vacuum vessel). The integration is carried out over one poloidal turn on a flux tube, see figure A.1.3. In a circular tokamak the safety factor can be approximated as $q = m/n \propto 1/j$, where m and n are the number of toroidal and poloidal turns a field line makes before closing on itself.

The safety factor q is preferred over the current density j for a number of reasons:

Stability: As the name implies, q is an important figure for plasma stability. Magnetic islands can form rational values of q, which reduce plasma confinement. If the central q-value approaches unity, the so-called sawtooth instability occurs, which periodically expels the hot plasma core [33, 8]. If q at the edge drops below 2 the plasma will disrupt, i.e. a sudden loss of confinement occurs, which can lead to structural damages in future devices.

Performance: In a "classical" tokamak discharge (the current is only inductively driven resulting in a high temperature and large current density in the plasma centre), the safety factor monotonically decreases from the edge to the centre. Advanced operation modes (AT) have been discovered which have improved confinement, leading to higher temperatures in the plasma core. In these advanced scenarios, regions within the plasma exist in which radial transport is suppressed by so-called internal transport barriers (ITB). ITB's occur in regions with low, zero, or reversed magnetic shear s, defined as $s = r/q \cdot dq/dr$. In AT operation, the q-profile does not decrease monotonically, but is flat or has a minimum as shown in figure A.1.2. To access advanced operation modes, the q-profile is modified by heating and current drive actuators. To study the phenomena of radial transport suppression, access advanced operation modes, and later control the current distribution, knowledge (and control) of the q-profile is required.

Dimensionless parameter: The pitch of the magnetic field, expressed in the safety factor, is a dimensionless parameter and is useful to compare different tokamaks. The same stability criteria apply to all machines, making q a good figure of merit.

q-profile reconstruction

No direct measurement of q, J, or is available, and direct measurements of the magnetic field are typically not available, but in principle possible [34]. To calculate the safety factor, the magnetic field structure is required, which in combination with the pressure profile is commonly referred to as the plasma equilibrium. The plasma equilibrium is obtained by solving the force balance in the plasma, for which numerous numerical solvers exist [35, 36]. The force balance states that at any point in the plasma, the plasma pressure p must be balanced by the magnetic pressure:

$$\nabla p = \boldsymbol{j} \times \boldsymbol{B}, \tag{A.1.2}$$

with current density $\boldsymbol{j}$ and magnetic field $\boldsymbol{B}$. For axisymmetric equilibria (i.e. equilibria independent of the toroidal angle), the magnetic field lines lie in nested toroidal magnetic surfaces, so-called flux tubes or flux surfaces (the magnetic flux within a flux tube is constant), shown in figure A.1.3. From equation A.1.2 it is clear that $\boldsymbol{B}\cdot\nabla p = 0$ and $\boldsymbol{j}\cdot\nabla p = 0$, i.e. the pressure and the current are constant on a flux tube. When analysing tokamak equilibria the poloidal flux $\psi = \iint_S B\,\mathrm{d}s_z$ is commonly used as radial coordinate. The poloidal flux is also a flux quantity. i.e. $\iint_{S1} B\,\mathrm{d}s_z = \iint_{S2} B\,\mathrm{d}s_z$.
With this knowledge and by using Ampere's law, H. Grad, H. Rubin (1958), and Vitalii Dmitrievich Shafranov (1966) reformulated equation A.1.2 for 2D equilibria

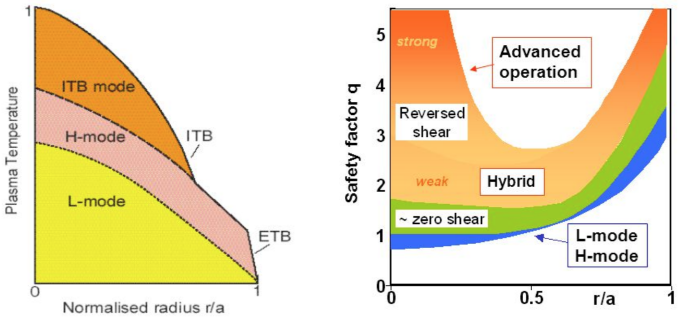

Figure A.1.2: The core temperature can be elevated by the formation of external (ETB) or internal transport barriers (ITB), i.e. zones of reduced radial transport. ETB's lead to the formation of the so-called H-mode and occur if enough power is deposited in the plasma. ITB's form in advanced scenarios which typically require a zero or reversed shear q-profile. Reprinted from [37, 38]

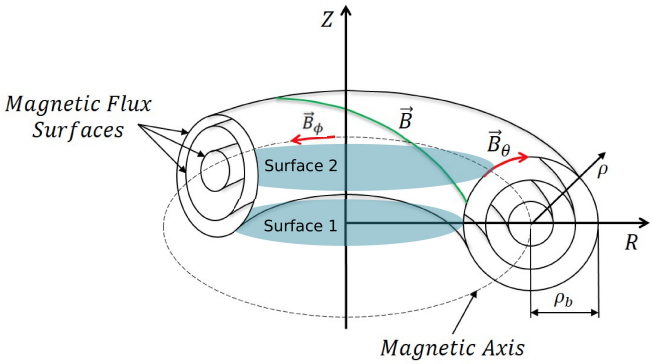

Figure A.1.3: Illustration of magnetic fields and flux surfaces in a tokamak plasma. The flux tubes are, amongst others, surfaces of constant current, pressure and poloidal flux . Adapted from [39]

in an axisymmetric torus [40, 41]:

$$\Delta^* \psi = -\mu_0 R^2 \frac{dp}{d\psi} - \frac{1}{2}\frac{dF^2}{d\psi}, \tag{A.1.3}$$

(A.1.4)

with the elliptic operator

$$\Delta^* \psi = R^2 \vec{\nabla} \cdot \left(\frac{1}{R^2} \vec{\nabla} \psi \right). \tag{A.1.5}$$

Here, μ_0 is the magnetic permeability, $p(\psi)$ the pressure and $F(\psi) = RB_\phi$ (major radius times toroidal magnetic field).
Equation A.1.3 is the [famous] Grad-Shafranov (GS) equation, which any plasma equilibrium reconstruction code must solve. The solution of the GS equation is determined by the free functions p and F, which can, in principle, be arbitrarily chosen[1]. These internal profiles are parametrised based on physical modelling and experience, and must be constrained by measurements to obtain experimentally correct results. Reconstructing the plasma equilibrium involves solving a least square problem of the type

$$\min_{p', FF'} ||y - h(\psi(r,z))|| \tag{A.1.6}$$

where p' and FF' are minimised by fitting a measurement y to an expected measurement h in order to best match the pressure balance and parametrised internal profiles.
A whole family of Grad-Shafranov solvers are available, for example EFIT [36], IDE [42], or LIUQE [43], to name only three. The measurement constraints on the solution can be grouped into internal and external measurements. External measurements are, for example, magnetic coils on the plasma edge or vacuum chamber. With external measurements the equilibrium can be reconstructed with good accuracy at the plasma edge, but they do not provide information on the profiles in the plasma centre. Internal measurements, for example temperature, density or polarimetry measurements from the Motional Stark Effect (MSE) diagnostic are required to constrain the profiles in the plasma. Without them, the reconstructed profiles are only as good as the initial guesses and they can in principle take any form. Grad-Shafranov solvers are typically constrained by measurements from the MSE diagnostic to reconstruct the current density and q-profile.
Part A of this thesis focuses on equilibrium reconstruction using the MSE diagnostic, which is described in the next section.

[1] In practice appropriate p and F are chosen, depending on the analysed discharge.

A.2 The Motional Stark Effect (MSE) diagnostic

The most common local measurements to constrain the q-profile during equilibrium reconstruction is the Motional Start Effect (MSE) diagnostic. In a nutshell, MSE systems measure the pitch of the magnetic field by analysing the visible emission of neutral particles, which are injected into the plasma. Through interaction with the plasma, the injected neutrals get excited and emit light. The particles experience a Lorentz electric field $\boldsymbol{E}' = \boldsymbol{v}_{\text{beam}} \times \boldsymbol{B}$, causing the emission to be degenerate and polarised due to the Stark effect. Measurements of the polarisation angle at the points of emission are used to locally constrain the q-profile in the equilibrium reconstruction. The outlined processes will now be explained in detail.

A.2.1 The Stark effect

As the name implies, the MSE diagnostic exploits the Stark effect to provide a constraint on the magnetic field. The Stark effect describes the splitting of degenerate emission lines in an external electric field. MSE systems commonly image the emission of the Balmer alpha lines, i.e. the emission generated from $n = 3 \rightarrow 2$ transition, n being the principal quantum number. The Balmer-α lines are favoured because they are the most intense in the visible spectrum for hydrogen, allowing the use of standard optical components. The nine emission lines are shown in figure A.2.1.

The lines are split into two groups, so-called π– and σ–lines. When viewed transversely to the applied electric field, the σ-lines are polarised perpendicular and π-lines parallel to it. The polarisation is exploited to measure the direction of the magnetic field inside the plasma.

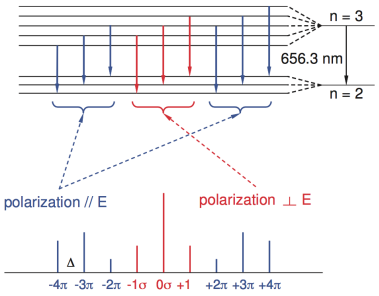

Figure A.2.1: Degeneration of the Balmer-α emission in an electric field due to the Stark effect. The single emission line is split into 9 lines, which are polarised parallel or perpendicular to the electric field. Reprinted from [44]

A.2.2 Principle of the MSE diagnostic

Due to the high temperatures, the plasma is fully ionised and no line emission of hydrogen (or hydrogen isotopes) is measured (except at the plasma edge). For the MSE diagnostic, fast neutral hydrogen isotopes are injected into the plasmas. Therefore either dedicated diagnostic beams are used, but commonly the emission from particles injected by the neutral beam (NBI) heating system is imaged. As the neutral particles enter the plasma, they emit light along their propagation direction due to collisional excitation and charge exchange reactions between beam neutrals and plasma ions. The particles experience a Lorentz electric field, described by

$$\boldsymbol{E}' = \boldsymbol{E_r} + \boldsymbol{v} \times \boldsymbol{B}, \tag{A.2.1}$$

where $\boldsymbol{E_r}$ is the background electric field in the plasma, $\boldsymbol{v}$ is the particle velocity and $\boldsymbol{B} = \boldsymbol{B_\phi} + \boldsymbol{B_p}$ is the magnetic field, composed of the toroidal and poloidal field, respectively. In first approximation the contribution of $\boldsymbol{E}_r$ can be neglected: Neutral particles from the NBI system enter the system with a velocity of $\approx 10^6$ m/s and today's tokamaks have a magnetic field of ≈ 3 T, resulting in Lorentz electric fields on the order of $3 \cdot 10^6$ V/m. In comparison, $E_b \approx 1 \cdot 10^5$ V/m [45][2].

The injected particles experience an electric field proportional the magnetic field according to equation equation A.2.1. The equilibrium reconstruction can be constrained by the measured polarisation angle in combination with the (known) velocity vector.

Although the plasma itself does not emit any visible light in the centre, the cooler plasma edge does radiate strongly. The light emitted by the injected fast neutrals is Doppler-shifted, separating it from the high intensity background. Figure A.2.2 shows a measured spectrum from the KSTAR tokamak. Three Stark multiplets are visible, originating from D_1, D_2 and D_3 molecules, which are created and injected by NBI system. Due to their different masses and resulting different velocities, the multiplets are Doppler shifted by different wave lengths. Typically, the emission of atomic deuterium is analysed because it has the highest intensity.

To reconstruct the magnetic pitch angle, the polarisation angle of one of the π- or σ-triplets must be measured. The challenge of the MSE system is to provide a fast and accurate measurement of the polarisation angle. Levinton [11, 47] proposed an elegant solution for this: Instead of measuring the polarisation angle directly, it is converted to an intensity modulated signal by photoelastic modulators (PEM) and a linear polariser.

[2] It was shown that neglecting radial electric field components can lead to high uncertainties in advanced scenarios [46]

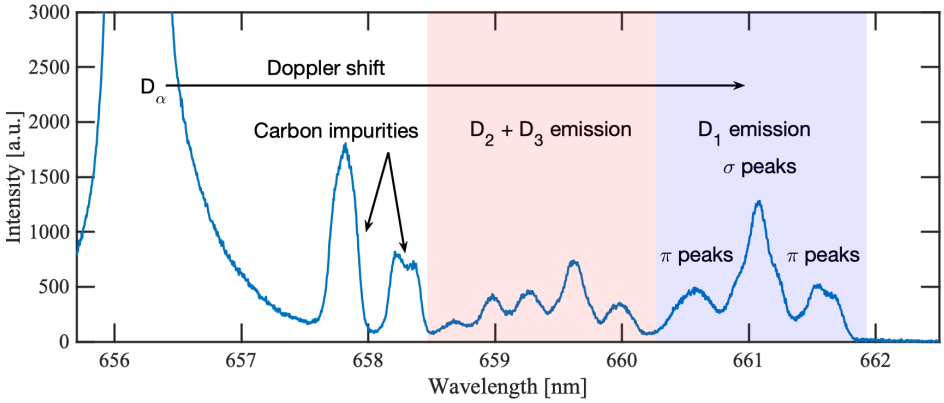

Figure A.2.2: Recorded spectrum of shot #12640 at KSTAR: Visible are the Stark multiplets from atomic and molecular deuterium (the molecular Stark peaks partly overlap). The MSE system at KSTAR measures the polarisation of the blue shifted π peak at $\lambda \approx 660.5$ nm.

A PEM is composed of a transparent crystal (typically fused silica) which is connected to a piezoelectric transducer. The transducer is tuned to the resonance frequency of the crystal. The underlying principle of a PEM is the photoelastic effect: A mechanically stressed material becomes birefringent depending on the strain on the material. This causes a time-varying phase shift between the x- and y- direction of the electric field of electromagnetic waves traveling through the crystal, or in other words, a time varying rotation of the polarisation. A linear polariser placed behind the PEM converts the rotation of the polarised light into an intensity modulation. The process is illustrated in figure A.2.3.

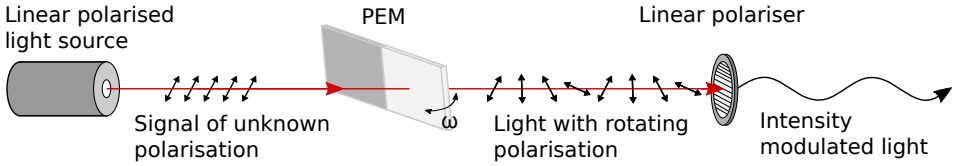

Figure A.2.3: Principle of the MSE diagnostic: The polarisation of linear polarised light is rotated in time by the time depending retardance of the PEM crystal. It transformed into an intensity modulated signal with an amplitude $A(t) = A_0 \sin(\omega t)$ by a linear polariser. Through knowledge of the optical system the polarisation angle can be reconstructed.

The intensity modulated signal can easily be guided by optical fibres for data recording. The sought polarisation angle can be reconstructed from knowledge of the optical system (the reconstruction process is explained in section A.4). The practical implementation of an MSE system is explained on the example of the

KSTAR diagnostic.

A.2.3 MSE diagnostic as KSTAR

As part of the research, an MSE diagnostic was commissioned at the KSTAR tokamak in 2015. Figure A.2.4 shows an equatorial cut of the reactor. The optics for the MSE system are located in the "M"-port of the vacuum vessel, imaging the emission from particles of the neutral beam injector NBI-1.
Because polarisation preserving guidance of light is difficult and the space in the port is limited, the PEM setup is contained in the port with as few optical elements between the port window and the PEMs as possible. The system is sketched in figure A.2.5. The emission entering the port is focussed through two photoelastic modulators followed by the linear polariser before it is imaged onto an array of 25 fibre bundles, each representing one radial channel. The resulting measurement span across the magnetic axis, ranging from $R = 1.74$ m to 2.28 m with a spacing of 2 cm.
The PEMSs are mounted in an angle of $\beta = 45°$ with respect to each other and oscillate with 23 kHz and 20 kHz. The linear polariser is rotated by $\alpha = 22.5°$ with respect the first PEM. The angles are chosen to simplify the mathematical description of the system, which is in detail explained in appendix .

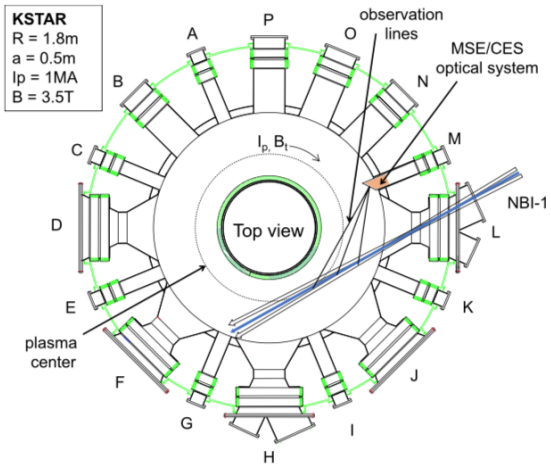

Figure A.2.4: Equatorial cut of the KSTAR vacuum vessel. Schematically drawn are the NBI trajectories (three NBI injectors are present at KSTAR) and the lines of sight of the MSE diagnostic.

The amplitude of the modulated light can be either proportional to the sine or cosine of the angle of polarisation of the incident light, depending on the orientation to the PEM. Two PEMs at slightly different frequencies and different angles are

used to measure both the sine and cosine of the polarisation angle simultaneously. The transmitted intensity I is

$$I \propto \sin(2\gamma)\cos(2\omega_1 t) - \cos(2\gamma)\cos(2\omega_2 t) + ..., \tag{A.2.2}$$

with polarisation angle γ and oscillation frequencies of the two PEMs ω_1 and ω_2.

To obtain γ from the intensity modulated light, the light leaving the fibres is guided through a wave-length tuneable, 2 cavity Lorentzian shaped, 4 Å FWHM bandpass filter before being focused onto an avalanche photo diode (APD) with a sampling rate of 2 MHz. The narrow bandpass filter is tuned to block all radiation except the blue shifted π-lines of the Stark spectrum. At KSTAR, this is the only Stark component which is not overlapping with emission from other neutral beams. The wavelength of the bandpass filter must be adjusted to match the Doppler shift of the emission, which depends on energy of the neutral beam, the applied magnetic field, and the angle between the NBI and the line of sight.

After a lengthy calculation[3] it can be shown that γ can be obtained from the harmonics of the recorded signal (see equation A.2.2):

$$\tan(2\gamma) \propto \frac{I_{2\omega_1}}{I_{2\omega_2}}. \tag{A.2.3}$$

The intensity of the signal harmonics $I_{2\omega_1}$ and $I_{2\omega_2}$ are determined from the recorded signal with a digital lock-in amplifier (described in section A.4.1). The polarisation angle γ can then be used to constrain the current density profile in the equilibrium reconstruction, explained next.

[3]The detailed calculations to derive equation A.2.3 are included in appendix .

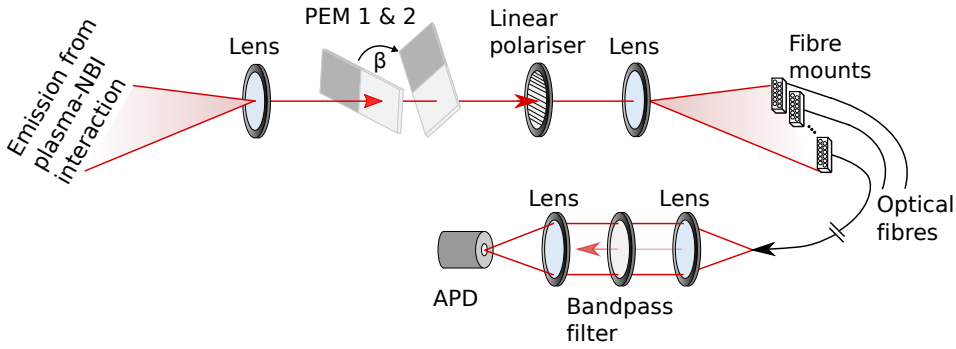

Figure A.2.5: Setup of the MSE diagnostic. The light emitted from the fast neutrals is guided through 2 PEMs which are rotated by $\beta = 45°$ to each other. The modulated light passes through a linear polariser which converts the polarisation modulated signal to an intensity modulated signal before the light is imaged onto fibre optic cables. In the diagnostic laboratory, two lenses guide the light through a tuneable bandpass filter and focus it on an APD for recording. In the figure only one recording unit is shown, in reality each of the 25 fibre bundles has its own APD setup. A detailed description of the optical setup has been published in [48].

A.2.4 MSE constrained q-profile reconstruction

The MSE diagnostic measures the polarisation angle γ of the emitted light, relative to the Lorentz electric field experienced by the injected neutral particles. Taking the geometry of the system into account, it can be shown that the polarisation angle is directly proportional to the magnetic pitch angle γ_m, defined as:

$$\tan(\gamma_m) = \frac{B_z}{B_\phi}. \tag{A.2.4}$$

To derive the relation between the polarisation angle and magnetic pitch angle, the geometry of the diagnostic setup in the tokamak must be known. Important are the angle between the NBI beam and the toroidal unit vector, as well as the angle between the lines of sight of the diagnostic and the NBI trajectory. The geometric relationship between the polarisation angle and the magnetic field can be written as[4] [50]:

$$\tan\gamma = \frac{A_0 B_z + A_1 B_r + A_2 B_\phi}{A_3 B_z + A_4 B_r + A_5 B_\phi}. \tag{A.2.5}$$

In equation A.2.5, the A-coefficients reflect the geometry of the diagnostic and

[4]Note that the A-coefficients can vary depending on the used equilibrium solver. For EFIT, they are described in [49].

contain information about the radial electric field E_r, B_z is the vertical component of the magnetic field, B_r the radial and B_ϕ the toroidal component.
Equation A.2.5 can be simplified if the neutral beam injectors and viewing optics are located on the mid-plane and by neglecting the radial electric fields to

$$\tan\gamma = \frac{A_0}{A_5}\tan\left(\gamma_m\right), \tag{A.2.6}$$

directly relating the polarisation angle to the magnetic pitch angle.

To reconstruct the q-profile, GS solvers are constrained by MSE measurements via equation A.2.5, following the approach described in section A.1. Since the MSE diagnostic only measure the local direction of the magnetic field but not the magnitude, the q-profile cannot be calculated directly from γ, but it does provide a strong constraint on the solution of the GS equation.

A.3 Challenges and recent developments

Challenges
The MSE diagnostic is the default diagnostic to constrain the q-profile during equilibrium reconstruction. Routine operation is, however, often challenging due to the high requirements on the measurement accuracy. The requirements depend on the investigated physics, and whether a qualitative or quantitative analysis is required. A perfect example for the difficulty is the sawtooth instability: During a sawtooth crash the hot core of the plasma gets expelled leading to a drop in the core temperature, causing increased resistivity and thus a rise of q in the plasma centre [33]. Theoretical models have been developed to explain the instability, however, one key question for model validation remains unanswered: What is the evolution of the safety factor at the magnetic axis, q_0, during a sawtooth crash? Specifically, whether it relaxes above unity or not during the crash [51, 52]. As Ko showed, q_0 is extremely sensitive to changes in γ and measurement accuracies of $\Delta\gamma < 0.1°$ are required to detect changes of $\Delta q = 0.1$ [53], which is difficult to achieve. Since the MSE diagnostic was first available, this question has been tried to be answered, but no conclusive results have been found, yet [54, 55, 56, 57, 58, 12]. Another example with similar requirements on the accuracy are advanced scenarios with low or zero magnetic shear. One envisioned future scenario is a low magnetic shear q-profiles with ITB formation and q_0 close to, but above unity. To control impurity accumulation, q_0 is periodically lowered to trigger a sawtooth instability to expel the hot plasma core with the accumulated impurities. This requires accurate tuning of the q-profile with precise tuning of the available actuators, for which high quality sensors (i.e. MSE) are required.

Sources of measurement uncertainties
Sources for measurement uncertainties of the MSE systems are manifold and make

accurate q-profile reconstruction a challenging task. The most important sources of uncertainty are:

Polarisation changes due to optical components: Until the signal has been transformed into an intensity modulated signal, any change in polarisation caused by the optical components in the optical path lead to deviations in the analysed signal. By performing an in-vessel calibration, the response function of the optical system can be determined. At KSTAR, a light source of known, tuneable polarisation was placed on a rail aligned in the path of the NBI inside the vacuum chamber. At the position of each MSE channel, the MSE diagnostic was illuminated with light from the polarised light source and the response function for various incident polarisation angles measured [48]. The calibration results are provided in section A.4.3. The recorded calibration can change during operation due to stresses on the window originating from evacuating the vacuum vessel or temperature changes during operation, which cannot be accounted for at KSTAR.

Faraday rotation: The Faraday effect describes a change of polarisation in light passing through media at the presence of magnetic fields. In tokamaks, the strong magnetic fields lead to changes in polarisation angle above acceptable levels as the light passes through the vacuum windows and mirrors. At KSTAR a polarised light source opposite of the MSE optics is used to record the changing polarisation angle during the ramp-up of the magnetic field. With this, a decrease of $\Delta\gamma_{\mathrm{FR}} \approx 1.5°$ was measured when changing B_ϕ from $0-2$ T [59]. Similar findings are reported at DIII-D [60]. Changes due to the poloidal field are expected to be one order of magnitude less and cannot be corrected for.

A-coefficients: The A-coefficients, see equation A.2.5, required for the q-profile reconstruction are calculated from the geometry of the setup. They depend on the lines of sight of the individual MSE channels as well as the injection angle of the NBI. The accuracy with which the A-coefficients can be determined depends on how precisely the geometry is known, but also on the volume of the imaged neutral beam.

Radial electric field: Going back once more to the A-coefficients in formula A.2.5, it was already mentioned that they include dependencies on the radial electric field E_r. These contribution are usually neglected, because measurements of E_r are often unavailable and E_r is expected to be a factor of 10 weaker than the Lorentz electric field. However, Rice showed that the effect of E_r can be far greater in advanced scenarios. In his analysis the reconstructed q-profile dropped by 0.3 when taking the radial electric field into account [46].

Signal noise Statistical noise is depending on the integration time of the measurement. The MSE system at KSTAR was designed to have a statistical uncertainty of $\Delta\gamma \leq 0.1°$ for 10 millisecond averaging intervals.

Signal contamination: Signal contamination due to background polarised light has been identified as the major problem at the CMOD and ASDEX Upgrade tokamaks, which both have been equipped with fully metallic walls. It was shown that reflections on the walls opposite of the diagnostic port can lead to contamination of the signal to the point where it can no longer be used for q-profile reconstruction [61, 62].

To correct for the uncertainties at KSTAR, a calibration technique has been developed which is presented in section A.4.3 and A.6.

Recent developments in MSE polarimetry
In addition to the described "classical" MSE system, a number of variants have been developed to tackle the described problems.

MSE polychromator: The measurement principle of the MSE polychromator is identical to the standard MSE system. Looking at figure A.2.5, the difference is in the last stage of the setup where the wavelength selection and data recording take place. The MSE polychromator was developed at the C-MOD tokamak, where polarised reflections from the metallic wall opposite to the MSE viewport render the recorded signal unusable. The polychromator setup measures multiple wavelength bands simultaneously on each channel, typically the π and σ component, as well as two wavebands red- and blue-shifted of the Stark multiplet to measure the background polarisation. Assuming a uniformly polarised background, the Stokes vector can be corrected by subtraction of the background polarisation [63]. Similar problems have been reported at ASDEX Upgrade [61], where a polychromator is being tested as well [64].

Spectral MSE: Besides measuring the pitch angle from the polarisation of the emitted light, γ can also be obtained from the MSE spectrum. The MSE-LS diagnostic, short for MSE Line Shift, measures the line shift between individual emission lines of the Stark spectrum to calculate γ [65]. Advantageous of the MSE-LS diagnostic are the reduced requirements on the optical system, since no care on polarisation conservation must be taken. This makes it suitable for next generation tokamaks where long distances with many optical elements between the vacuum window and the imaging of the emission onto optical fibres are expected. Unfortunately, due to spectral broadening, individual lines cannot be observed individually. Accurate models of the spectral emission are required to fit the spectrum, which can introduce uncertainties and make the analysis more time consuming and challenging for real-time applications.

Imaging MSE: The imaging MSE (IMSE) diagnostic does not filter out a spectral component of the Stark spectrum, instead it uses a combination of Savart plates and a delay plates to create a 2D interference pattern of the π and σ

peaks on a CCD camera [66]. IMSE provides a 2D measurement of the magnetic pitch angle, requires only a single calibration (rather than a channel-by-channel calibration), does not require the magnetic field and beam dependent filter calibration, and because the full spectrum is used, a brighter signal is recorded. IMSE systems are being investigated at AUG [67] and KSTAR [68]

Laser polarimetry: The laser polarimetry diagnostic is not based on the Stark effect, but will be mentioned for completeness since it is capable of constraining the current density profile in the plasma centre. Polarised laser light transmitted through the plasma experiences a change in polarisation $\Delta\gamma$ due to the Faraday effect. Measuring $\Delta\gamma$ provides information about the magnetic field, however, unlike the MSE diagnostic the laser polarimetry is not a local, but an integrated measurement.

The future of MSE

For future tokamaks, such as ITER, polarimetry based MSE system are more difficult to implement. The high neutron flux from the burning plasma requires a thick blanket where no direct lines of sight between plasma and the outside are permitted. As a result, viewports to the plasma are connected to the outside world via long pathways with multiple turns to provide adequate neutron shielding. Light collected by the MSE diagnostic has to be guided through this labyrinth by optical elements. The influence of mirrors on the polarisation must be known in order to obtain accurate measurements. These polarisation changes are difficult to calibrate because the optical properties of the plasma facing mirror(s) are expected to change due to plasma depositions in such extent, that the polarisation could change during shots.

Damages and deposition to the mirrors have been studied theoretically and experimentally. Experiments performed in 2004 used an MSE setup similar to the one at JET [69]. Measurements were performed with fresh mirrors and mirrors that were exposed to plasmas at Tore Supra for twelve hours. The experiments concluded that mirror erosion cannot be neglected and that if an MSE system based on polarisation measurement is used, an in-situ calibration is required [70]. A theoretical analysis performed in 2008 used the latest labyrinth design to analyse the effect of various impurities on the reflectivity and polarisation conversation of the first mirrors [71]. It was concluded that the LLNL-4b labyrinth design [72] reduced all particle fluxes significantly and the critical species to consider is Helium. How severe the influence on the polarisation angle is could not be concluded with significant accuracy and further research is required. If a labyrinth can be designed which reduces the incoming particle fluxes to acceptable levels, and an in-situ calibration is available to recalibrate the system, background polarised light similar to the findings at C-MOD and AUG is expected to induce high uncertainties in the measurement. For this, Thorman proposed a variation of the MSE polarimetry for

ITER which eliminates broadband background polarisation by using a birefringent delay plate which creates a sinusoidal spectral filter [73].
As already described earlier, spectral MSE is being investigated as an alternative since it does not require polarisation conserving optics. Moreover, the larger magnetic fields at ITER will lead to a larger line splitting, increasing the accuracy of the line splitting MSE.

A.4 Polarisation angle reconstruction algorithm

The MSE diagnostic measures light emitted by fast neutral particles which are injected into the plasma. The particles experience a Lorentz electric field, and due to the Stark effect the Balmer-α emission is degenerated into nine different lines. The emitted light is polarised with respect to the direction of the magnetic field. The diagnostic is composed of two photoelastic modulators (PEM) and a linear polariser, which converts the polarised emission into an intensity modulated signal which is recorded using avalanche photodiodes (APD).
This section describes the algorithm used to calculate the polarisation angle γ from the recorded signal.

A.4.1 Signal processing using digital lock-in technique

Digital lock-in amplifier
The modulation of the polarisation induced by the PEMs into the emission of the neutral beam particles is converted into an intensity modulated signal by the linear polariser. As already stated in section A.2.3 and calculated in appendix , the polarisation angle can be calculated from the intensity of the harmonics of the recorded signal. The recorded signal is generally low in intensity and noisy. To retrieve the signal harmonics, a digital lock-in amplifier is used.

Lock-in amplifiers [74, 75] are used to extract low intensity signals of a known carrier wave from noisy data. The principle is illustrated in figure A.4.1 on the example of an ideal sine wave.
First, the input signal V_{in}, shown in A.4.1(a) is multiplied by a known reference signal V_{ref}, shown in A.4.1(b). The output, equivalent to the recorded signal V_{rec}, is the product of two sine waves:

$$V_{\text{rec}} = A_{\text{sig}} A_{\text{ref}} \sin\left(\omega_{\text{in}} \cdot t + \varphi_{\text{in}}\right) \cdot \sin\left(\omega_{\text{ref}} \cdot t + \varphi_{\text{ref}}\right) \tag{A.4.1}$$

$$= \frac{1}{2} A_{\text{sig}} A_{\text{ref}} \cos\left([\omega_{\text{in}} - \omega_{\text{ref}}] \cdot t + \varphi_{\text{in}} - \varphi_{\text{ref}}\right) + \frac{1}{2} A_{\text{sig}} A_{\text{ref}} \cos\left([\omega_{\text{in}} + \omega_{\text{ref}}] \cdot t + \varphi_{\text{in}} + \varphi_{\text{ref}}\right) \tag{A.4.2}$$

To reconstruct the original signal, the recorded signal is multiplied by the carrier signal, resulting in A.4.1(d), the downshifted or rectified signal V_{DS}. This process

is also called heterodyne detection.

$$V_{\mathrm{DS}} = V_{\mathrm{rec}} \cdot V_{\mathrm{ref}} \tag{A.4.3}$$

$$= -\frac{1}{2}\left[\sin\left(\omega_{\mathrm{in}} x + \varphi_{\mathrm{in}}\right) \cdot \cos\left(2\omega_{\mathrm{ref}} x + 2\varphi_{\mathrm{ref}}\right) + \sin\left(\omega_{\mathrm{in}} t + \varphi_{\mathrm{in}}\right)\right] \tag{A.4.4}$$

The input signal is equal to the envelope of the downshifted signal. It is obtained by applying a convolution filter to the data. In our case, a Hann filter is used [76].

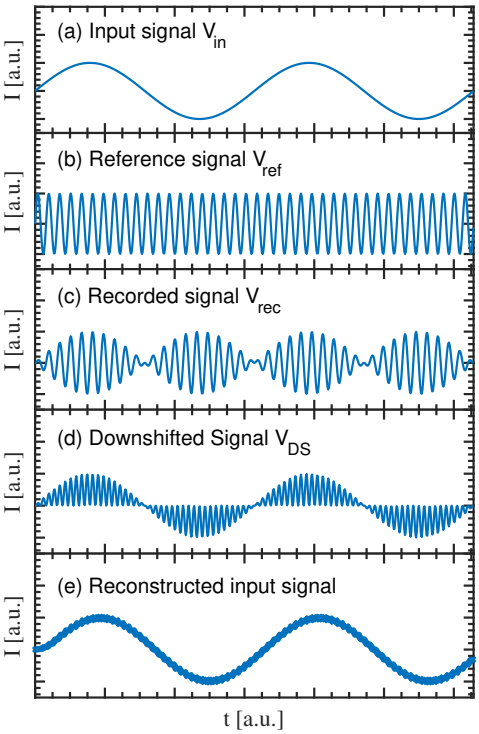

Figure A.4.1: Principle of the lock-in technique. The input signal is modulated by a known reference signal. To reconstruct the input signal from the recorded signal, the recorded signal is multiplied by the reference signal. The envelope is equivalent to V_{in}. A convolution filter is used to determine the envelope of the downshifted signal.

In the case of the MSE diagnostic, the emission of the NBI is modulated by the PEMs and the linear polariser. This results in the recorded signal V_{rec}. The reference signal, i.e. the oscillation frequency of the PEMs, is recorded from the PEM controllers. Phase shifts between the controller signal and the actual oscillation of the PEMs, originating from transmission delays, must be corrected.
These steps and the calculation of the polarisation angle γ are described next.

Determination of the reference signal
The crystals of the PEMs are set to oscillate with a fixed frequency, which is defined at the PEM controllers. The PEM controllers send a rectangular signal to the PEMs which induces a sinusoidal oscillation of the birefringent crystal. The controller signal is recorded by the data acquisition system (DAQ) for every shot, an example

is shown in A.4.2.

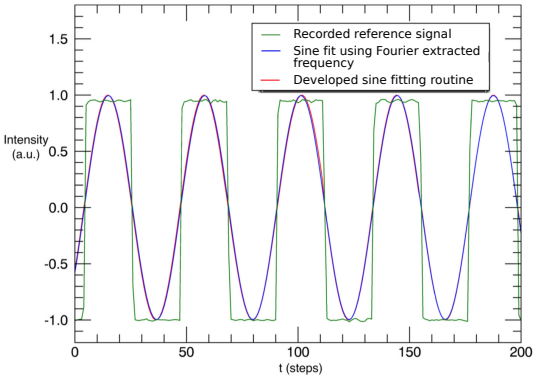

Figure A.4.2: Reconstruction of the PEM reference signal. The signal sent to the PEMs from the controllers is a square wave, leading to a sinusoidal oscillation of the PEM's crystal. The motion of the crystal is reconstructed by fitting a sine wave to the square wave. This can be done by Fourier analysis of the square wave to obtain the frequency and calculating the matching sine (——). Extracting the average frequency throughout the whole shot proved to be inaccurate. A new sine fitting routine has been developed, which fits a sine to the reference signal by analysing the zero-crossings of the signal, producing fast and accurate results (——).

The carrier wave signal, i.e. the sinusoidal motion of the crystals in the PEMs, has the same frequency as the signal sent from the controller. Although the frequency is in principle known (it is set at the PEM controller), deviations between the configured and the actual signal can occur. For this reason, the carrier signal is reconstructed directly from the recorded reference signal.
Since the frequency is roughly known, the reconstruction is typically done by Fourier transforming the recorded carrier signal and finding the strongest frequency component in the vicinity of the frequency set at the PEM controller. After the frequency has been determined, a sine wave is fit to the recorded signal (——) in figure A.4.2).
At KSTAR, minor variations were found to occur in the controller signal during a shot, which lead to increased uncertainties if only a single Fourier analysis was used to determine the average oscillation frequency throughout the full shot. Instead of determining the frequency for a full shot, small samples of the signal (similar to the way a spectrogram is created) can be Fourier transformed and the sinusoidal fit can be made for each sample. This was tested and accurate results were obtained, but the process proved computationally too expensive. For this reason, a new signal reconstruction routine has been developed:
First, all downwards zero-crossings of the reference signal are determined. Next, the signal is chopped into blocks, each containing 100 zero-crossings. For each

block, the frequency and phase for a sine wave matching the zero-crossings is calculated and a the matching sine wave is calculated for each sample. With this method, accurate results are achieved and computation time reduced (— in figure A.4.2).

Calculation of the signal harmonics

The polarisation angle γ is calculated from the Stokes vector S, which is calculated from the harmonics of the recorded signal I. The Stokes vector is used to describe the polarisation state of light and has the form $S = (S_0, S_1, S_2, S_3)$. The individual components are:

$$S_0 = I \tag{A.4.5}$$
$$S_1 = I \cdot p_l \cdot \cos(2\gamma)\sin(2\chi) \tag{A.4.6}$$
$$S_2 = I \cdot p_l \cdot \sin(2\gamma)\sin(2\chi) \tag{A.4.7}$$
$$S_3 = I \cdot p_l \cdot \sin(2\chi) \tag{A.4.8}$$

Here I is the total intensity, p_l the linear polarisation fraction, γ is the polarisation angle with respect to the horizontal axis and χ the polarisation angle with respect to the vertical axis. The Stokes vector can be visualised in the Poincaré sphere, shown in figure A.4.3.

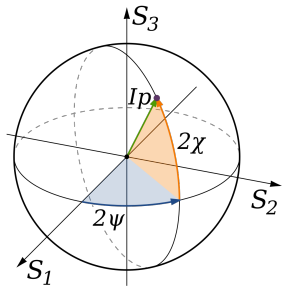

Figure A.4.3: Poincaré sphere visualising S_1, S_2 and S_3. Reprinted from [77].

From equations A.4.6 and A.4.7 the sought polarisation angle γ can be calculated as:

$$\gamma = \frac{1}{2}\tan^{-1}\left(\frac{S_2}{S_1}\right) \tag{A.4.9}$$

As demonstrated in appendix , the Stokes vector can be reconstructed from the harmonics of the recorded signal, resulting in

$$\gamma = \frac{1}{2}\tan^{-1}\left(\frac{J_2(|A_2|)I_{2\omega_1}}{J_2(|A_1|)I_{2\omega_2}}\right) \tag{A.4.10}$$

$$= \frac{1}{2}\tan^{-1}\left(\frac{J_4(|A_2|)I_{4\omega_1}}{J_4(|A_1|)I_{4\omega_2}}\right). \tag{A.4.11}$$

Here, J_i is the i-th Bessel function, A_k is the retardance of the 1st or 2nd PEM and $I_{j\omega_k}$ is the j-th harmonic of the recorded signal of the 1st or 2nd PEM.

The harmonics are extracted from the signal using the previously introduced digital lock-in amplifier. Because the phase information must be preserved, the calculated controller signal is first converted to a complex signal before being multiplied with the recorded signal, resulting in the complex downshifted signal. The complex amplitude is determined using a Hann filter, which was found to be a suitable solution as it combines properties of a Gaussian and Rectangle filter: low leakage and frequency cut-off, respectively.

Phase correction

Equation A.4.10 & A.4.11 requires signed amplitudes, otherwise the polarisation angle can only be determined between 0 and $\pi/2$. Sign changes of γ, which occur when crossing the magnetic axis, can otherwise not be resolved.
The recorded signal is out of phase with the reference signal due to propagation delays in the transmission lines. This phase difference must be corrected. The phase correction is done by "rotating" the complex harmonics to the real axis - the rotation angle is equal to the phase difference between reference and input signal. The rotation is performed as follows:
The first harmonic is shifted by π and it is checked whether the original or π shifted signal is closer to a guessed phase-shift. Next, since all harmonics experience the same phase lag, the process is repeated for all other harmonics to improve the accuracy. Here, the degeneracy of the harmonics, described by

$$\phi = \frac{\phi_{\text{measured},n} + k\pi}{n} \tag{A.4.12}$$

must be considered. In equation A.4.12, $\phi_{\text{measured},n}$ is the measured phase for the n-th harmonic, and $k \in [-n, n]$. k is chosen such that the resulting ϕ is closest to the guessed value.
The phase is determined for each channel individually, then weighted depending on the signal amplitude of the channel and combined into a single phase per PEM. An example of the original complex amplitude and the phase corrected amplitude is given in figure A.4.4. In the graph, the uncorrected complex amplitudes of all channels and all times are drawn in red. The phase is equal to the angle between the real axis and the complex amplitude. The determined average phase is drawn

in green and the phase corrected amplitudes in blue. In this example one measurement channel was disconnected (circled in pink). Channels which phase lies outside of 0.5° of the determined median phase are ignored in the analysis.

With the phase corrected harmonics and the Bessel function of the PEM retardance the polarisation angle can be calculated. The PEM retardance is set on the PEM controller, however it was found that the set retardance can deviate from the actual retardance of the PEM. To improve the accuracy, the retardance of the PEMs is calculated from the harmonics, described next.

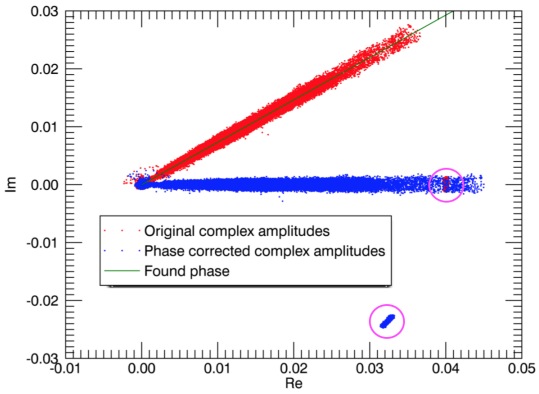

Figure A.4.4: Original and phase corrected complex amplitude. The complex amplitude of the reconstructed signal for all channels and all times is drawn in red. The phase, the angle between the real-axis and complex amplitude is used to shift all data points to the real-axis. In the shown example one channel of the MSE diagnostic was disconnected (circled in pink). Channels are excluded from the analysis if their phase differs by more than 0.5° from the determined average phase.

A.4.2 Determination of the PEM retardance

For an accurate calculation of γ, precise knowledge of the retardance of the PEMs is required, see equations A.4.10 and A.4.11.
Furthermore, the amplitudes of the signal harmonics itself depend on the set retardance. For example,

$$I_{2\omega_1} = -\frac{J_2|A_1|}{\sqrt{2}} I_{p_l} \sin(2\gamma). \tag{A.4.13}$$

Similar relations hold for the other harmonics (see appendix for the complete list). Figure A.4.5 shows the first four Bessel functions for retardances from $[0, 2\pi]$. The polarisation angle can be calculated using either the 2nd or the 4th harmonics of the signal, whose intensity depends on the 2nd and 4th Bessel function, see equation A.4.10 and A.4.11. In practice, γ is calculated using both sets of harmon-

ics, and the average weighted, depending on the amplitude of the harmonics. By optimising the product of J_2+J_4 the overall signal-to-noise ratio can be maximised. From figure A.4.5, the maximum of J_2+J_4 is determined at $A_{\text{opt}} = 207°$, which is the configured retardance of the PEM's.

The retardance configured at the PEM controller can differ from the true retardance of the PEM, which was demonstrated at KSTAR by measuring the retardance of the PEMs in a test setup [78]. Instead of relying on the retardance configured at the PEM controllers, it can be determined from the recorded signal using the relations:

$$\frac{J_1(|A_1|)}{J_3(|A_1|)} = -\frac{I_{\omega_1}}{I_{3\omega_1}}, \tag{A.4.14}$$

$$\frac{J_2(|A_1|)}{J_4(|A_1|)} = -\frac{I_{2\omega_1}}{I_{4\omega_1}}, \tag{A.4.15}$$

$$\frac{J_1(|A_2|)}{J_3(|A_2|)} = -\frac{I_{\omega_2}}{I_{3\omega_2}}, \tag{A.4.16}$$

$$\frac{J_2(|A_2|)}{J_4(|A_2|)} = -\frac{I_{2\omega_2}}{I_{4\omega_2}}. \tag{A.4.17}$$

Through an iterative process, the retardance of the PEM controller was stepwise adjusted until the calculated retardance was approximately equal to A_{opt}. The retardances calculated from the signal are shown in figure A.4.6 for all 25 channels. Achieving a uniform retardance for all channels is unfortunately not possible, because the light corresponding to the individual channels passes through the PEM crystals at different radial positions and the retardance is not constant throughout the crystal [78].

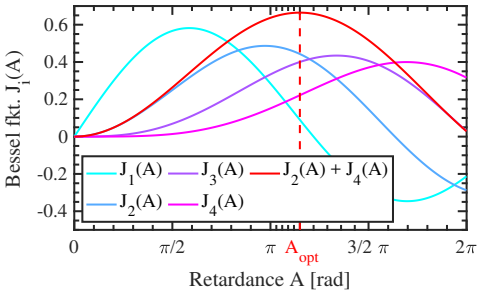

Figure A.4.5: First to fourth Bessel function. The 2nd and 4th Bessel function are used for the calculation of γ. The signal intensity is maximised by choosing the maximum of J_2+J_4. The ideal PEM retardance is $A_{\text{opt}} = 207°$.

This concludes the reconstruction routine of the polarisation angle. In summary:

By using a digital lock-in amplifier the input signal is extracted from the recorded noisy signal. From the harmonics of the signal the PEM retardance is calculated and the PEM controllers are tuned to maximise the signal intensity. The polarisation angle γ is calculated from the weighted, averaged 2nd and 4th harmonics.
Before the reconstructed polarisation angle can be used for the reconstruction of the q-profile, it must be corrected for systematic uncertainties arising from the setup by using an in-vessel calibration and correcting for Faraday rotation caused by the strong magnetic field. Both processes are described next.

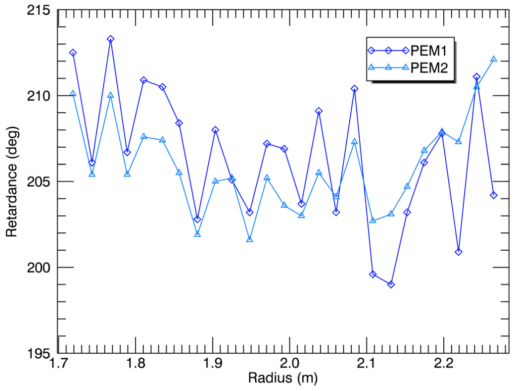

Figure A.4.6: Measured retardance for PEM 1 & 2 at KSTAR shot *#13689*. The set retardance at the PEM controller is 305° and 290° for PEM1 and PEM2, respectively. The measured retardance $A_{\text{meas}} \approx A_{\text{opt}} = 207°$ differs from the configured retardance at the PEM controller. For an accurate reconstruction of γ knowledge of the true retardance, calculated from the signal, is important.

A.4.3 Correction of γ for systematic uncertainties

In section A.4.1 the harmonics extraction from the recorded signal has been explained with which the polarisation angle γ can be calculated. To eliminate systematic uncertainties, an in-vessel calibration was performed and the polarisation angle is corrected for polarisation changes caused to Faraday rotation.

In-vessel calibration
As already outlined in section A.3, misalignment or imperfections in the optical elements, which are not included in the description of the optical system can result in differences between the true and measured polarisation angle.
To correct for these effects, an in-vessel calibration is performed. While the Tokamak was accessible during maintenance time (no vacuum and no magnetic field), a rail was placed in the path of the NBI. A light source with known, variable polarisation was placed on the rail and moved through all radially imaged MSE

locations. At each measurement location the light source was positioned to illuminate the MSE viewport at the emission angle expected from the NBI emission. The polarisation angle of the light source was varied from $60° - 120°$ and compared to the reconstructed angle by the MSE system, shown in figure A.4.7. A non-linear response function is visible for which the measurements are corrected during operation: During plasma operation, the polarisation angle (= input polarisation angle) is interpolated from the measured polarisation angle (= output polarisation angle) using the calibration curve.

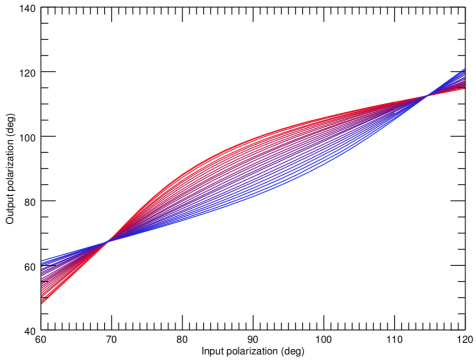

Figure A.4.7: In-vessel calibration curves. A linear polarised light source of known and variable polarisation ("input polarization") was shined on the port window of the MSE diagnostic. The "Output polarization" is the from the recorded signal reconstructed polarisation angle. The calibration curves for all 25 channels are shown. The transition from red to blue corresponds to channels from the plasma centre to the plasma edge. During plasma operation the true polarisation angle (=input angle) is interpolated from the reconstructed polarisation angle (=output angle).

Faraday correction

The Faraday effect describes the change in retardance of optical elements, which are exposed to a magnetic field. The previously determined in-vessel calibration was performed without any applied magnetic field and does not compensate for this effect. To calibrate for changes in transmitting materials, a polarised light source is installed opposite of the MSE port. During the ramping-up of the magnetic field γ is measured over time. Figure A.4.8 shows the changes in γ as the magnetic field is increased from 0 T to 2 T. The calibration curve can be recorded daily and is used to correct the recorded polarisation angles, depending on the set toroidal magnetic field.

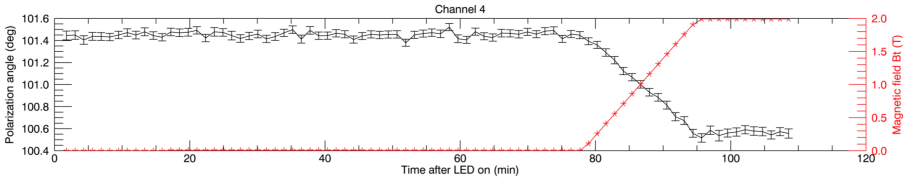

Figure A.4.8: Magnetic field dependent changes in γ over time during the ramping-up of the magnetic field. γ changes over 1° when the field is increased to $\Delta B = 2$ T.

A.5 Evolution of the central safety factor during stabilized sawtooth instabilities at KSTAR

Messmer M.C.C., Ko J. Chung J. Woo M. H., Lee K.-D. and *Jaspers R.J.E*

This chapter is published in Nuclear Fusion, Volume 58, Number 1, 2017

Abstract:
A Motional Stark Effect (MSE) diagnostic has recently been installed in the KSTAR tokamak. A difficulty faced at KSTAR and common to other MSE diagnostics is calibration of the system for absolute measurements. In this report we present our novel calibration routine and discuss first results, evaluating the evolution of the the central safety factor during sawtooth instabilities. The calibration scheme ensures that the bandpass filters typically used in MSE systems are aligned correctly and identifies and removes systematic offsets present in the measurement. This is verified by comparing the reconstructed safety factor profile against various discharges where the locations of rational q surfaces have been obtained from MHD markers. The calibration is applied to analyse the evolution of q_0 in a shot where the sawteeth are stabilized by neutral beam injection. Within the analysed sawtooth periods q_0 drops below unity during the quiescent phase and relaxes close to or slightly above unity at the sawtooth crash. This finding is in line with the classical Kadomtsev model of full magnetic reconnection and earlier findings at JET.

A.5.1 Introduction

One of the outstanding challenges in tokamak research is the control of the current density profile for plasma control and its optimisation for high performance discharges. To resolve the internal magnetic field structure in a tokamak and reconstruct the current density profile, optical spectroscopy measuring the light emitted by fast neutral particles injected into the plasma is used. The technique proposed by Levinton [11] exploits the Stark Effect and is dubbed the Motional Stark Effect (MSE) diagnostic. It enables a direct, local measurement of the magnetic pitch angle $\gamma_m(r) \equiv \tan^{-1}(B_\theta(r)/B_\phi(r))$, where B_θ and B_ϕ denote the poloidal and toroidal components of the magnetic field, respectively. From γ_m in combination with a Grad-Shafranov equation solvers, such as EFIT [36], the current density profile can be reconstructed. KSTAR recently showcased its capabilities by setting a new record for long pulse H-mode operation [79], however to support the ITER project in exploring advanced scenarios, current profile measurements are of essence. For this reason, a 25 chord MSE polarimeter has been installed

in 2015 [48] and commissioned during the 2015 plasma campaign. Owing to the digital data acquisition system combined with digital lock-in analysis, the full Stokes vector is reconstructed on a millisecond timescale. From this the magnetic pitch angle can be calculated with a statistical uncertainty below 0.2° on 10 ms time averages, resulting in an accuracy of the safety factor at the magnetic axis of $\Delta q_0 \approx 0.1$ [53]. In this report, after giving an overview of the experimental setup at KSTAR, a generic two-step calibration and verification method is presented: First the bandpass filters used to single out the red-shifted Stark peak are calibrated such, that the measured pitch angle displays a physically reasonable slope. In the second step it is investigated whether systematic offsets are present by comparing the reconstructed q-profile (constrained by MSE) against rational q-values obtainable from independent diagnostics during MHD instabilities in the plasma. After successful calibration, the q-profile evolution of a sawtooth crash is analysed in section A.5.4.

A.5.2 Experimental Setup

The MSE system at KSTAR has been installed prior to the 2015 plasma campaign during which it was commissioned. It measures the emission of high velocity neutral deuterium particles injected by one of KSTAR's neutral heating beams. A detailed report of the setup, including a description of the in-vessel calibration and correction of the Faraday rotation, can be found at [48, 80, 13]. A brief overview of the setup will be given for completeness. Figure A.5.1 shows an equatorial cut of the tokamak torus and the three available heating beams. Due to the different injection angles and the induced doppler shift, the Balmer-α emission of NBI-1 can be separated from the other beams and the background emission. The emitted light is captured by collection optics located in the M-port of the vessel. It is guided through two photoelastic modulators (PEM) oscillating at 23 kHz and 20 kHz and after passing through a linear polariser projected onto 25 fibre bundles. The resulting 25 radial channels span across the magnetic axis to the plasma edge, from R=1.74 m to 2.28 m with a spacing of 2 cm. Through the fibres, the light is transmitted to the optics laboratory for signal processing. It propagates through wavelength-tuneable 2 cavity Lorentzian shaped, 3 Å FWHM bandpass filter and is recorded by APD's with 2 MHz sampling rate. For the reconstruction of the Stokes vector and calculation of the magnetic pitch angle, the polarisation of the red-shifted π-peak is calculated. This line is chosen as it provides the lowest overlap with emission from the other neutral beams. The filters are initially rotated such that their central wavelength (CWL) matches the wavelength were we expect the highest emission intensity in the π spectrum, shown in figure A.5.2. This position is forth on denoted as λ_0 or 0° offset. Deviations from λ_0 will be denoted as offsets $\Delta\lambda_{\mathrm{Off}}$. First measurements showed that the initial filter position λ_0 was leading to unphysical results and thus a more elaborate calibration is required. The system is calibrated using a two-step approach: First, the optimal CWL of the bandpass filters is found, based on the linear polarisation fraction of the recorded signal (section A.5.3) and second it is ensured that no systematic

offsets are present in the recorded signal by cross-calibrating the reconstructed q-profile against independent diagnostics available at KSTAR (section A.5.3).

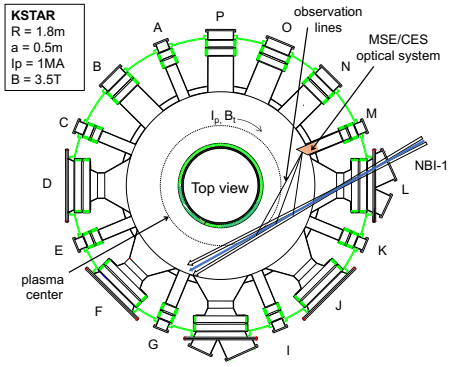

Figure A.5.1: Equatorial cut of the KSTAR vessel including NBI-1 marked in blue and the MSE lines of sight. Adapted from [80].

A.5.3 Calibration of the MSE system

Alignment of the bandpass filters

Of crucial importance for the performance of the system is the correct alignment of the bandpass filters. From figure A.5.2 one expects better signal-to-noise ratio by blue-shifting the filter function, but at the cost of signal quality as the recorded light will be contaminated by emission from the σ-peaks. To find the optimum filter position, four calibration shots with equal plasma equilibrium at a magnetic

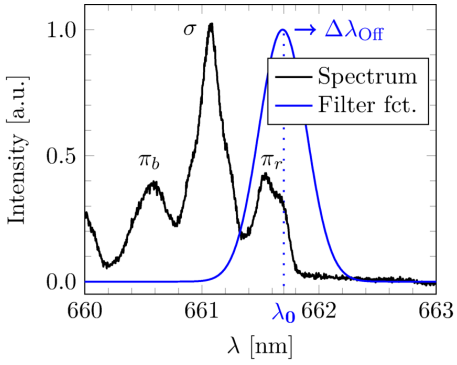

Figure A.5.2: Recorded spectrum of shot *#12692*, channel 12 and filter function of the bandpass filter. To calibrate the bandpass filters, the CWL of the filters are stepwise red-shifted from their initial position λ_0 by increasing offsets $\Delta\lambda_{\text{Off}}$.

field strength B_ϕ = 2.9 T and NBI acceleration voltage U_{NBI} = 100 keV were performed. In these L-mode discharges only NBI-1 beam was active and the CWL of the filter was incrementally red shifted between the shots. To increase the number of calibration points, the filter's CWL was additionally changed in the middle of each shot. Figure A.5.3 shows the time evolution of the polarisation angle of shot *#13691*, where the filter position was shifted by $\Delta\lambda_{Off}$ = 1 Å at t ≈ 4.5 s. Although the plasma equilibrium did not change during the measurement, a clear shift in the recorded polarisation angle during the time of the filter rotation can be observed.

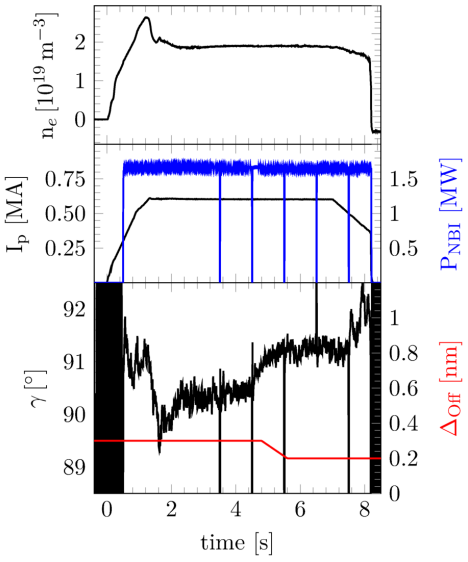

Figure A.5.3: Time evolution of shot *#13691*. Top: line averaged density. Middle: Plasma current and injected NBI power. Bottom: polarisation angle and filter offset of channel 6. *Note:* The blips in the neutral beam are for charge exchange measurements.

This behaviour has been observed for all channels throughout the calibration discharges. The effect on the radial profile is shown in figure A.5.4, which displays the measured polarisation angle profile for shot *#13691* shortly before and after the filter was rotated. Aside the described shift in polarisation angle, the profiles show an oscillating pattern in the central and outer channels, whereas one would expect a smooth gradient from the nature of the plasma equilibrium.

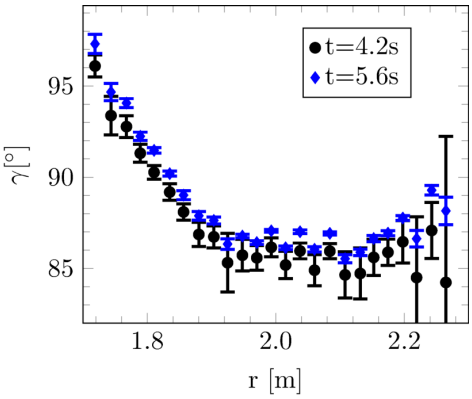

Figure A.5.4: Radial polarisation angle profile of shot *#13691* before (4.2 s) and after (5.6 s) the filter rotation.

To calibrate the system, we make use of the digital data acquisition system, with which the full Stokes vector can be reconstructed. From this, the linear polarisation fraction (LPF) $\sqrt{S_1^2 + S_2^2}/S_0$, where the S_i are the i-th component of the Stokes vector $S = (S_1, S_2, S_3, S_4)$, can be calculated. The LPF is evaluated for each offset $\Delta\lambda_{\text{Off}}$ and each channel. Figure A.5.5 shows the LPF and total intensity over the filter offsets for channel 6[†].

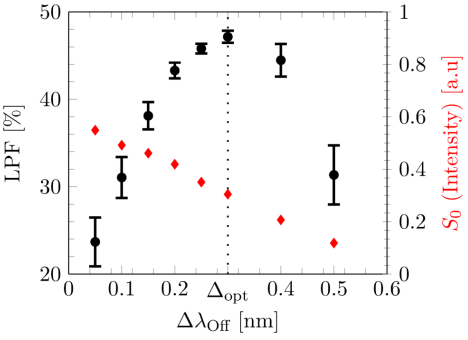

Figure A.5.5: Linear polarisation fraction (circles) and total intensity S_0 (diamonds) of channel 6, shot *#13691* over $\Delta\lambda_{\text{Off}}$. The signals are been averaged over 300 ms.

As expected, the total intensity decreases by red-shifting the CWL of the filter. The LPF displays a quadratic dependence on the filter rotation (as it is expected from

[†]Alternatively it would be possible to use a non-MSE-constrained equilibrium solver to calculate the q-profile (and the magnetic pitch angle) for each shot and each time step and compare it to the measured magnetic pitch angle to find the optimum. However, since the q-profile obtained by an equilibrium solver such as EFIT without MSE is even in L-mode shots only an educated guess, a different method has been chosen.

simulations [81]) and has its maximum, for channel 6, at $\Delta\lambda_{\text{Off}} \approx 0.3$ nm. A second order approximation is used to determine the optimum offset, defined as the position where the LPF has its maximum, for each channel. The obtained filter calibration was tested two consecutive shots with identical plasma equilibrium. Here, the optimal filter settings were applied only to the later shot to see the effect of the calibration in comparison to the original filter settings, used at the first shot. Figure A.5.6 compares the polarisation angle profile of the two at similar times of the discharge.

By optimising the filter rotation we almost completely eliminated the oscillations in the pitch angle profile. The measured radial profile has a continuous gradient and reduced uncertainties compared to the non-optimised discharge, giving confidence in the calibration method.

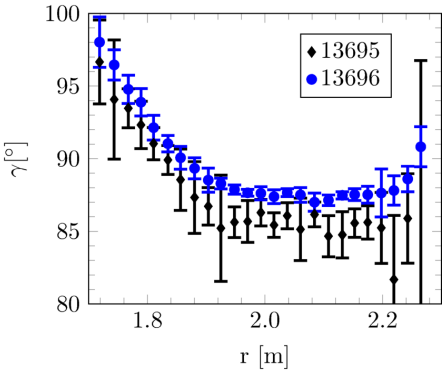

Figure A.5.6: Polarisation angle profile for shots *#13695, #13696* at t = 1.65 s. The calculated, optimal filter settings have been applied to shot *#13696*, resulting in a smooth pitch angle profile with reduced uncertainties.

Post-shot calibration algorithm

The calibration of the filters was completed mid-campaign, which meant that roughly half of the campaign shots are have been recorded using misaligned bandpass filters. To enable an analysis of these shots an algorithm has been developed to correct for the filter misalignment. The algorithm is illustrated in figure A.5.7. The graph shows an analysis of the calibration shots similar to figure A.5.5, but instead of plotting the dependency of the LPF on the filter rotation, the polarisation angles (averaged over the intervals of constant filter rotation) are plotted over the filter rotation. The graph shows a linear dependence of the polarisation angle over the offset, assuming that all shots have a similar plasma equilibrium over time. From physical intuition a flattening of the curve for higher values of $\Delta\lambda_{\text{Off}}$ is expected, once none of the light emitted by the σ-peaks overlaps with the envelope of the bandpass filters. However, this relationship cannot be deduced from the recorded data due to the low signal strength and increasing uncertainties at big filter offsets.

To re-calibrate the polarisation angle of an incorrectly calibrated shot, the polarisation angle matching the determined ideal offset and the one matching the set offset of the shot are interpolated from the calibration curve in figure A.5.7, marked exemplary by the dotted and dashed line. The recorded polarisation angles of the discharge are then corrected by $\Delta\gamma$.
The correction algorithm is demonstrated on one of the four calibration shots in figure A.5.8. The top figure shows the effect of the correction algorithm on the time evolution of γ. Here, the polarisation angle is now at a constant value before and after the change in filter rotation, lasting from $t \approx 4.4\,s - 5.5\,s$, and lowered by approximately one degree. Note that the jump of the corrected polarisation angle at $t = 5\,s$ is due to the change in the correction factor $\Delta\gamma$. Because of the change in filter rotation, the set offset must be adapted in the algorithm, which has been done at an arbitrary time point during the filter rotation. The re-calibrated γ-profile is shown in figure A.5.8(b). In contrast to the profile shown in figure A.5.6, the uncertainty in the measurement is not reduced due to the interpolation mechanism.

Determination of systematic offset

After calibrating the bandpass filters to achieve physically sensitive measurements, the last step in the calibration procedure is to ensure that no systematic offsets are present in the recorded data. These could arise from inaccurate determination of the measurement location in the vessel or from changes in the refractive index of the port window due to stress on the material induced from evacuating the vessel. To validate our measurements we compare the plasma equilibrium against tearing modes (TM) of known mode number and location. The plasma equilibrium is reconstructed with the Grad-Shafranov solver EFIT [36], which can be constrained by magnetic pitch angle measurements to reconstruct the current density profile. Initial attempts to reconstruct the MSE-constrained plasma equilibrium did not re-

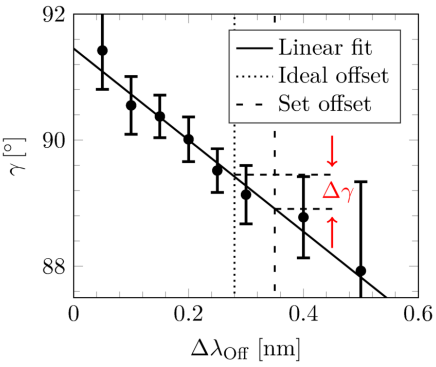

Figure A.5.7: Dependence of the measured polarisation angle γ from channel 6 on the filter offsets in the calibration shots.

sult in a converging solutions, which lead to the hypothesis of a systematic offset in the measurement. To determine the offset we repeatedly analysed the same shot with varying, channel independent offsets and compared the mode number and location of rational q-surfaces (determined by Mirnov Coils and ECE analysis) against the reconstructed equilibria. With this method a systematic offset of $-1.95°$ was found. A detailed description of the analysis is presented in appendix A.5.7. This finding has been verified by evaluating the position of the magnetic axis (which can be determined directly from the pitch angles) against the axis position determined by magnetics only EFIT. The result, shown in figure A.5.9, shows good agreement between the magnetic axis location determined by EFIT (∗ ∗ ∗) and the axis position reconstructed from the polarisation angle measurements after the filter rotation correction and systematic offset correction have been applied (——). The full description of the analysis is included in appendix A.5.7.

A.5.4 Evaluation of q_0 during sawtooth instabilities

After having successfully calibrated and verified the results obtained by the MSE diagnostic, the evolution of q_0 during sawtooth instabilities [33] is evaluated as a first application of the commissioned system. Despite tremendous effort, the underlying physics of the sawtooth instability have still not been fully understood and in the past 40+ years since its discovery various models have been proposed. Kadomtsev [51] explained the phenomena with full magnetic reconnection, however his model falls short of explaining the fast timescales of the sawtooth crash. Wesson [52] later suggested that a destabilising potential builds up during the ramp phase, which is released by a magnetic trigger and reconnection does not

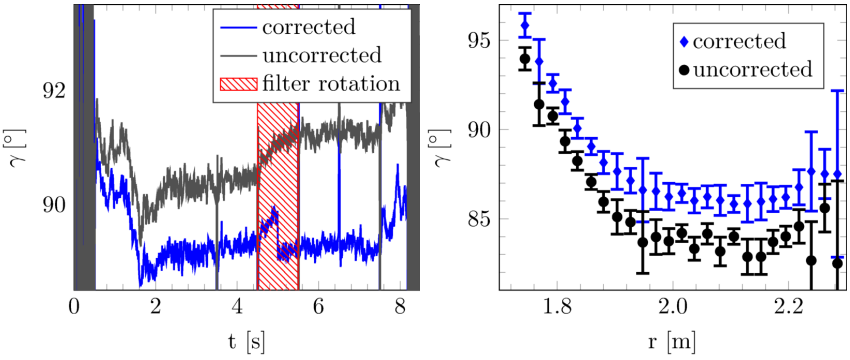

(a) Time evolution of the recorded and post-shot corrected polarisation angle of channel 6. **(b)** Radial polarisation angle profile at $t = 3$ s.

Figure A.5.8: Post-shot filter correction for shot *#13691*. In the time evolution (a) the times during which the filter rotation was changed is shaded in red. In (b) the uncorrected data has been shifted by $-2°$ for improved readability of the graph.

take place during the crash, but rather during the current ramp phase. Both models assume q_0 to rise to or above unity, however initial polarimetry measurements by Soltwisch [54] resulted in q_0 remaining well below unity on Textor. Measurements at TFTR [55] and JET [56] (and again Textor [57]) confirmed Soltwisch's findings. DIII-D initially reported similar results [58], but later claimed q_0 rising to unity after the sawtooth collapse [12].
Various other models have been proposed, however none was able to fully explain the measured observations. The presented analysis is focused on the investigation of the principal question, whether the evolution of the central safety factor evolves to or around unity during the sawtooth cycle. The short sawtooth period at KSTAR of typically 5 ms complicates spectroscopic analysis of the safety factor evolution, however a suitable discharge with a sawtooth period of $\tau_s \approx 150\,\text{ms} - 300\,\text{ms}$ (see fig. A.5.10, A.5.11) has been identified.
The characteristics of the increased sawtooth period are similar to the monster sawteeth reported by Campbell [82], where a stabilisation of the sawteeth by NBI injection was observed. In the analysed discharge the fast particle pressure p_{fast} was estimated from the injected NBI power, acceleration voltage and slowing down time. With a back-of-an-envelope calculation p_{fast} is estimated to account for up to 10% of the total pressure. This non-negligible fast particle pressure may be the reason for the relatively long sawtooth period in this particular discharge. However, the presented method of deducing the q-profile and magnetic axis does not rely on the fast particle content, but only on the total pressure.
In Campbell's analysis the evaluation of the safety factor was limited to magnetic measurements by which q_0 was determined to approximately $0.9 - 1.0$ during the quiescent time.
This can be compared to the reconstructed evolution of safety factor at KSTAR,

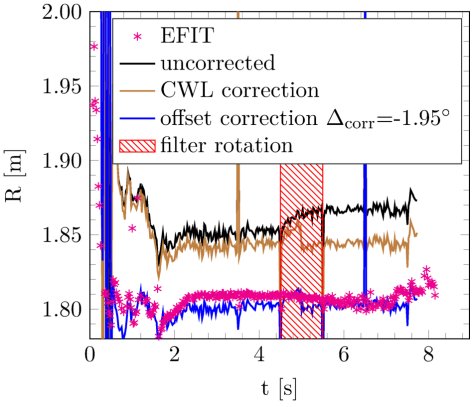

Figure A.5.9: Comparison of the magnetic axis calculated from MSE measurements against the position obtained from magnetics only EFIT. The MSE measurements have been corrected by the post-shot filter rotation correction and the determined systematic offset of −1.95°.

shown in figure A.5.11, where q_0 has been reconstructed using three different analysis methods: the curves marked as polynomial (—) and spline (—) result from the equilibrium reconstruction using EFIT, where for the first a second order polynomial is used to describe the basis function of the current density profile and for the later three splines have been chosen as basis function. The spline location is chosen at the plasma centre, at the edge and roughly at the location of the sawtooth inversion radius. The remaining parameters have been kept constant during the EFIT analysis. The third curve labelled analytical (—) is the analytical solution of q_0 derived by Petty [83]:

$$q_0 = -\frac{\kappa}{\mathrm{R}_0}\left(\frac{\partial}{\partial R}\tan(\gamma_m)\right)^{-1}\Big|_{\mathrm{R}=\mathrm{R}_m}. \tag{A.5.1}$$

Here, κ is the plasma elongation, R_0 the major radius and γ_m is the magnetic pitch angle at the magnetic axis R_m. κ has been obtained by reconstructing the plasma equilibrium using EFIT only constrained by magnetic measurements, which is believed to give the most accurate solution for the plasma boundary. For the analytical analysis a three point moving mean filter has been applied to the MSE data and for all three analysis methods the polarimetric data is averaged over 10 ms.
The three solutions follow the evolution of the electron temperature closely, a sharp increase of q_0 can be observed at the time of the sawtooth crash followed by a steady decline until the next expulsion of the plasma core. The polynomial and analytical solutions match well in absolute value, whereas $\mathrm{q}_{0,\mathrm{spline}}$ is raised by $\Delta\mathrm{q}_0 \approx 0.04$. Independent of the analysis method, q_0 drops well below unity between the sawtooth crashes. However, since the error on q_0 is estimated to be on the order of $\Delta\mathrm{q}_0 = 0.1$ no definite conclusion can be drawn whether q_0 stays below unity during the entire sawtooth cycle. It is important to point out that this result appears to be in contradiction with results published earlier at KSTAR [53],

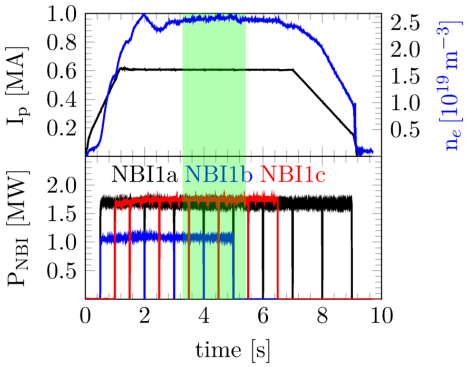

Figure A.5.10: Time evolution of shot *#16499*. Top: Plasma current and line averaged density. Bottom: NBI power. The sawtooth evaluation is limited to the area shaded in green.

where q_0 has been determined to stay above or close to unity by using the analytical solution. Possible explanations for this difference include: a) a difference in the discharge regime. b) in reference [53], κ was calculated by KSTAR's real-time version of EFIT, which is considered to be less accurate than the post-shot analysis version. c) possible the treatment of the radial electric field, which was assumed to be negligible in [53].

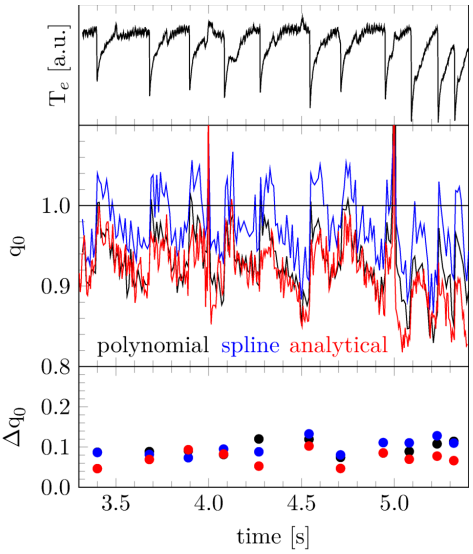

Figure A.5.11: Top: Time evolution of the electron temperature from a central ECE channel. Centre: q_0 determined form EFIT reconstruction and analytical solution. Bottom: Change in q_0 at the sawtooth crash. Note that the q-profile cannot be reconstructed during the NBI blips at $t = 3.5, 4.0, 4.5, 5.0$ s.

As the last analysis step, the location of the sawtooth inversion radius is compared between the reconstructed q-profile and ECE measurements. Figure A.5.12(a) shows the time evolution of the normalised temperature profile using KSTAR's ECE system from which the inversion radius is determined to $r_{i,\mathrm{ECE}} = 1.92$ m. Figure A.5.12(b) shows the q-profile before and after a sawtooth crash (polynomial basis functions), which is in good agreement with the inversion radius determined by ECE. The analysis shows a broadened safety factor profile, similar to observations by Mc Cormick *et al.* at the ASDEX tokamak [84], where sawteeth were stabilised with Lower Hybrid Current Drive (LHCD). However, in Mc Cormick's analysis q_0 relaxed to values above unity after the sawtooth crash, whereas our analysis is in agreement with the q_0 evolution at JET's stabilized sawteeth [82]. An important difference between the experiments at KSTAR and JET compared to ASDEX is the amount of non-inductive driven current which was reported to be almost fully non-inductive at ASDEX, but negligible at KSTAR and JET. Dedicated experiments are required to check whether a change in sawtooth behaviour can be observed at

KSTAR during non-inductive operation.

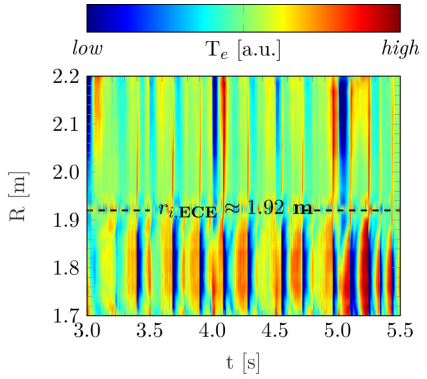

(a) Normalized time evolution of the electron temperature profile. The inversion radius has been determined from the graph to $r_{i,\mathrm{ECE}} = 1.92$ m, the position at which the change in temperature at the sawtooth crash inverses.

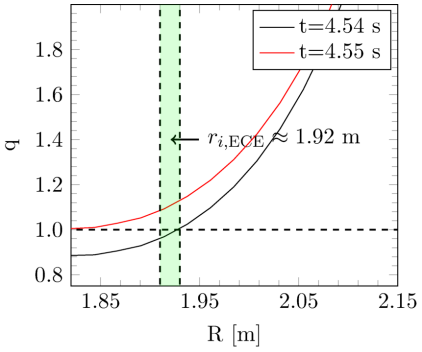

(b) Reconstructed q-profile (polynomial method) before and after a sawtooth crash. The green shaded area marks the approximate location of the sawtooth inversion radius determined from (a).

Figure A.5.12: Comparison of the sawtooth inversion radius determined from ECE analysis (a) and q-profile reconstruction (b).

A.5.5 Conclusion

In conclusion we have shown that with a two-step calibration procedure the MSE diagnostic at KSTAR provides physically sensible magnetic pitch angle measurements with a resolution of 10 ms and an accuracy of $0.1° - 0.5°$. The diagnostic is now ready for routine operation and has been used to measure the evolution of the central safety factor of a discharge with sawteeth instability with exceptionally long sawtooth periods. The MSE measurements show an increase in q_0 from 0.9 to 1 at the time of the sawtooth crash, where the uncertainty of q_0 is estimated to be $\Delta q_0 \approx 0.1$. This is in line with the reconnection model proposed by Kadomtsev, however it was shown that the analysis is very sensitive to the choice of the basis functions used to describe the current density. For the future a more in-depth analysis of the sawtooth behaviour at KSTAR is required to gain further insight on the evolution of the current density profile. The focus should clearly be on the analysis of multiple shots to get a higher statistical confidence in the result, the analysis of non-stabilized sawteeth as well as the sawteeth behaviour during non-inductive operation to see if a raised q-profile, similar to the results measured at ASDEX is obtained.

A.5.6 Acknowledgement

M.C.C. Messmer would like to thank Dr. Hyun-Seok Kim and Dr. Sang-hee Hahn of NFRI for the many fruitful discussions and support with the equilibrium recon-

struction.
This work was supported by the research programs funded by the Ministry of Science and ICT in Korea.

A.5.7 Appendix

Detailed description of the determination of the systematic offset

Section A.5.3 briefly described the determination of a systematic offset in the measured polarisation angles. The detailed procedure is described here. As afore mentioned, a reconstruction of the current density profile using the equilibrium solver EFIT constrained by polarisation angle measurements was initially unsuccessful due to non-convergence of EFIT. This has been attributed to an unaccounted systematic offset in the measurement. A channel independent, constant offset is assumed due to the shape of the polarisation angle profiles obtained after the bandpass filter calibration in section A.5.3, which imply physically sensible measurements.
To verify the hypothesis of the systematic offset, the plasma equilibrium of a shot is calculated with varying systematic offsets applied to the MSE data. The resulting q-profiles are compared to tearing modes of known mode number and location. The ideal offset is found where the best match is made.

Tearing mode analysis

Reference values for the by EFIT reconstructed, expected q-profile are obtained by an independent tearing mode (TM) analysis. The MHD mode numbers are determined by analysis of Mirnov Coil (MC) signals and the location of the instability is obtained by cross-correlating electron cyclotron emission (ECE) measurements with the MC data. The result of the analysis is shown in figure A.5.13, where the spectrogram of one of the toroidal MC is plotted, labelled with the determined mode numbers and locations. A 2/1 mode at approximately 1.98 m is present between $1.5\,\mathrm{s}-3\,\mathrm{s}$ and a 3/2 mode at 1.93 m has been observed between $7\,\mathrm{s}-9\,\mathrm{s}$. In the intermediate time interval the modes were suppressed by ECRH.

Determination of the systematic offset

To determine the systematic offset in the polarisation angle measurements, a stepwise increasing, channel independent correction factor $\Delta_{\mathrm{corr}} \in [-3.8°, +2.4°]$ is added to the measured polarisation angles. For each step in Δ_{corr} the plasma equilibrium is reconstructed and the following quantities are evaluated:

1. The difference Δr_{q} between the MHD mode location obtained from MC+ECE analysis and the location of the q-surface from the EFIT reconstructed q-profile.

2. The convergence of EFIT, reflected by the fit value χ^2 (lower is better).

3. The number of time steps for which EFIT converged.

4. The value of safety factor at the plasma edge q_{95}, more precisely the difference $\Delta q_{95} = |q_{95,mag} - q_{95,MSE}|$. Here, $q_{95,MSE}$ is the value of q_{95} determined by MSE constrained EFIT and $q_{95,mag}$ the edge safety factor determined by magnetics only EFIT. This is an important benchmark quantity as magnetics only EFIT is expected to give accurate results for the plasma edge.

For the analysis a combined total of 61 time points for the 2/1 and 3/2 TM are evaluated, where for each time the measurement signals are averaged over 50ms. For the final evaluation of the four criteria listed above, the 61 individual time steps are averaged for each correction factor.
The analysis has been performed for correction factors $\Delta_{corr} \in [+2.4°, -3.8°]$, however only the results of the analysis from $-2.4°$ to $-1.6°$ are discussed as it has been found to be the relevant interval. Figure A.5.14 shows Δr_q as well as χ^2 and the number of time steps for which EFIT converged over Δ_{corr}; Δq_{95} over $\Delta_{corr}$is plotted in figure A.5.15.

The difference in the tearing mode location Δr_q has a minimum of $\Delta r_{q,min} \approx 2.7$ cm at $\Delta_{corr} = -1.85°$, showing good agreement between MSE EFIT and the TM location determined via MC and ECE. However, Δq_{95} has a minimum at $\Delta_{corr} = -2.3°$, which is in line with the observation that χ^2 decreases for smaller values of Δ_{corr}. For offsets greater than $-1.6°$, χ^2 rises rapidly and EFIT is unable to find a converging solution.
From the analysis no conclusive ideal offset can be determined and thus a compromise solution was made and $\Delta_{corr,\,opt} = -1.95°$ has been selected as the ideal

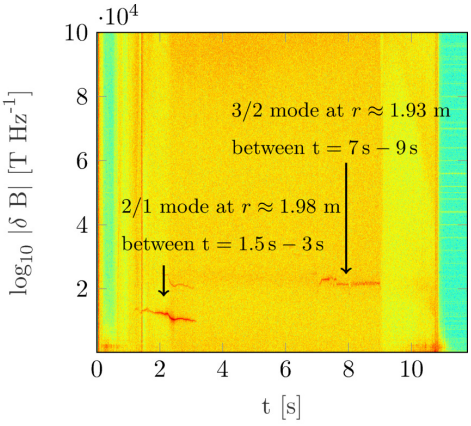

Figure A.5.13: Spectrogram of one of the toroidal MC of shot *#13728*: From Mirnov Coil and ECE analysis a 2/1 mode between 1.5 s – 3 s and a 3/2 mode between 7 s – 9 s has been determined. The MHD activity was suppressed from 3 s – 7 s by ECRH.

correction factor. With this, Δr_q is close to its minimum, the difference in Δq_{95} is acceptable low and EFIT shows good convergence.

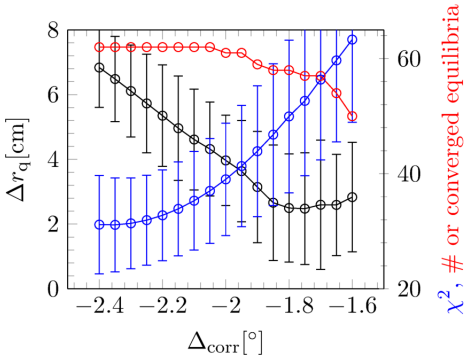

Figure A.5.14: Calibration analysis for shot *#13728*: Difference in boundary Δr_q, χ^2 and the number of time steps for which EFIT was able to converge are plotted over the systematic correction factor Δ_{corr}. The uncertainties are above what one would expect by purely looking at the spread of the data for both quantities, however they do represent the statistical spread of the data and no systematic error could be determined.

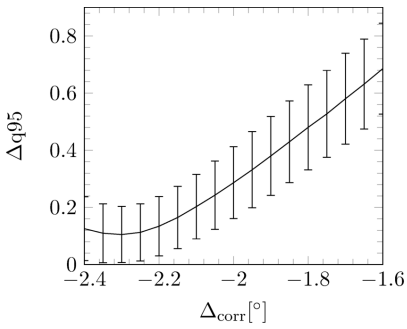

Figure A.5.15: Calibration analysis for shot *#13728*: Difference in Δq_{95} over the systematic correction factor Δ_{corr}. Δq_{95} as a minimum at $\Delta_{corr} \approx -2.3°$.

Applying the determined optimal correction factor to the recorded polarisation angles, figure A.5.16 shows the comparison of the MSE constraint and magnetics only reconstructed q-profile for t = 1.9 s of the calibration shot. The location of the 2/1 TM is in good agreement with the MSE EFIT reconstructed q-profile.
To further verify that the chosen offset does indeed provide sensible results, the now fully calibrated system is tested by comparing the location of the magnetic axis calculated from the measured polarisation angles against the axis location determined from magnetic probes.

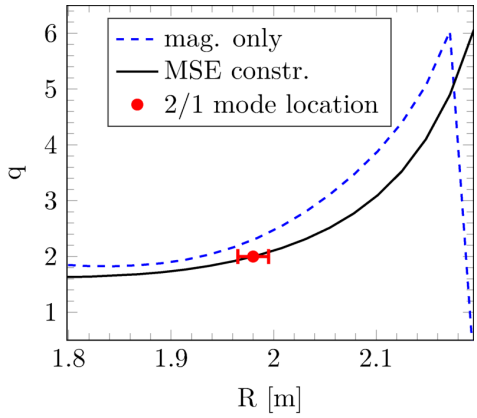

Figure A.5.16: Comparison of reconstructed q-profile for shot *#13728* at t = 1.9s with and without MSE constraint. The indicated location of the 2/1 mode (red) is the position determined by MS+ECE diagnostic.

Independent verification of Δ_{Off} and Δ_{corr}

For an independent test of the filter rotation calibration and the determined systematic offset in the polarisation angles, the position of the magnetic axis is verified by comparing the location calculated from the polarisation angle profiles against magnetics only EFIT. For the comparison, one of the MSE calibration shots described in section 2 is evaluated. For this L-mode discharge magnetics only EFIT is expected to provide accurate results. The position of the magnetic axis from the MSE data is obtained by interpolation the zero crossing of a third order polynomial fit to the first 10 channels neighbouring the magnetic axis as shown in figure A.5.17. A third order fit was chosen as it resembles the shape of the measured profile, although a second order fit provides similar results.

Figure A.5.18 compares of the time evolution of the magnetic axis with the two corrections applied to the MSE data: — marks the time evolution obtained from the uncorrected pitch angles. The measured data was first corrected to account for the incorrect filter rotation (described in section A.5.3), resulting in the — graph. Secondly, the pitch angles are corrected to account for the systematic $-1.95°$ offset, resulting in the — graph. This is in excellent agreement with the EFIT result ***, giving confidence in both filter calibration and the determined systematic offset.

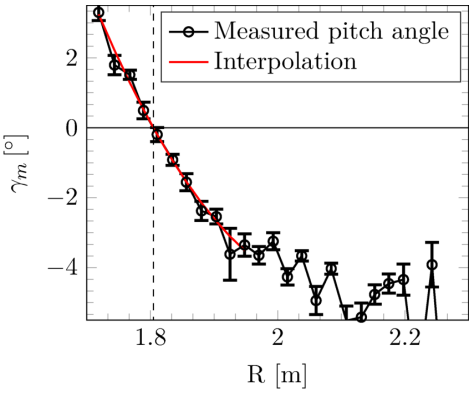

Figure A.5.17: Determination of the magnetic axis. The 10 innermost channels are interpolated by a third order polynomial fit from which the magnetic axis can be derived by calculating the intersection of the fit with the x-axis, indicated by the dashed line.

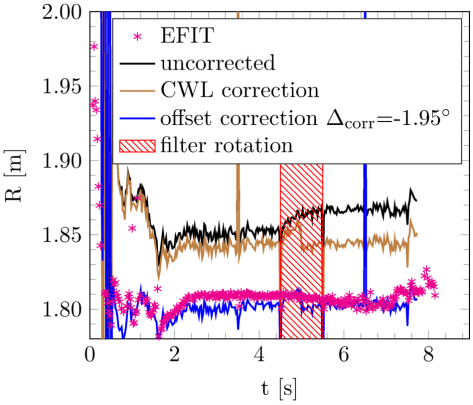

Figure A.5.18: Comparison of the magnetic axis for shot *#13691* between MSE analysis and the axis location reconstructed from magnetics only EFIT. The MSE measurements are corrected to account for the incorrectly set CWL of the band-pass filter and the systematic offset.

A.6 Optimal MSE polarisation angle and q-profile estimation using Kalman Filters and the plasma simulator RAPTOR

Messmer M.C.C., Felici F., Sauter, O., Teplukhina, A.A., Loenen J.P.G., Reich M., Fischer R., Rittich D., Jaspers R.J.E., the ASDEX Upgrade Team and *the EUROfusion MST1 team*

This chapter is published in Plasma Physics and Controlled Fusion, Volume 61, Number 3, 2019

Abstract:
Accurate q-profile reconstruction is of importance for the development of advanced scenarios, but continues to be a challenge in tokamak research. To constrain the q-profile in the plasma centre the Motional Stark Effect diagnostic (MSE) is often used, however achieving routine measurements with the required accuracy proves to be difficult in many devices. We present a novel approach to obtain accurate estimates of the q-profile using an observer-based approach. The observer combines MSE measurements with model-based prediction of the system. For this the plasma transport simulator RAPTOR is coupled with a fixed boundary equilibrium solver to create a model-based prediction of the MSE measurements. An Extended Kalman Filter (EKF) is used to merge profile evolution predictions from the RAPTOR code with measurements. Using synthetic data we demonstrate accurate q-profile estimations in situations where the model is purposely disturbed and only erroneous MSE measurements are available. For shots at ASDEX Upgrade we show that by constraining RAPTOR with MSE measurements, the evolution of the model's q-profile is in close proximity to reference profiles of reconstructed equilibria from an integrated diagnostic suite.

A.6.1 Introduction

Of the available concepts for nuclear fusion reactors, the most matured one is the Tokamak. It confines the plasma by a helical magnetic field which is created by external coils and a current running through the plasma. The externally applied toroidal component of the magnetic field is known, however the field components generated by the plasma current are difficult to measure and manipulate. Tailoring the plasma's current density profile J, or its derived quantity, the q-factor $q = d\Phi/d\psi$, with toroidal magnetic flux Φ and poloidal magnetic flux ψ, is essential for plasma stability and performance [8].

Unfortunately, no direct measurement of q (or J) is available. The plasma equilibrium, specifically the distribution of poloidal flux ψ(R,Z) and the free functions $p'(\psi)$, $FF'(\psi)$, are estimated using (real-time) equilibrium reconstruction codes that solve the 2D Grad-Shafranov equation, a two-dimensional, nonlinear, elliptic partial differential equation describing the force balance in the plasma [35, 36]. This process usually involves parametrising the internal profiles and solving a least-square problem constrained by internal and external measurements of the plasma. External measurements are magnetic probes, flux loops and Rogowski coils, internal measurements are for example temperature and density measurements. By using magnetic probes, the plasma equilibrium can be reconstructed with good accuracy at the plasma boundary, however in order to constrain the internal current distribution, knowledge of the internal magnetic field is required. In the plasma centre, Grad-Shafranov solvers are typically constrained by measurements from the Motional Stark Effect (MSE) diagnostic [11] or polarimetric measurements [85]. MSE systems locally measure the polarisation angle γ of light emitted by externally injected neutral particles, which is aligned with respect to the magnetic field. A continuous challenge of the MSE diagnostic is to record data with sufficient accuracy for a good q-profile reconstruction. For a precise reconstruction, for example to accurately resolve the evolution of the central safety factor during sawtooth events, a measurement accuracy of 0.1° on a millisecond timescale is required [53, 86].

In this article we propose a novel way to use a model-based observer to obtain accurate estimates of the magnetic pitch angles. This approach results in higher quality estimates than can be achieved by using only measurement or model data and can also complement situations where direct measurements from MSE are not available. The observer combines MSE measurements with model-based prediction of the system for better estimates of the state of the system. This provides:

- a check of the measurement quality (or the simulation quality),
- better estimates of the state of the model by combining the real and predicted measurement,
- a real-time capable filtering solution,
- a constraint on the q-profile by the model in cases where MSE data is not available,
- a correction of the model in case of model mismatch.

As a physics model describing the process, we use the poloidal flux diffusion equation and electron transport equation [87], implemented in the RAPTOR code [88].

A recently developed approach, similar to the one described in this paper, is implemented in the IDE code [42, 89]. In this approach, a Bayesian approach is used to merge diagnostic measurements related to the core current density with a one-step-ahead prediction based on the poloidal flux diffusion equation. Important

differences between both approaches are that RAPTOR is capable to run in real-time and the physics model in IDE only includes the poloidal flux diffusion equation, while the kinetic core profiles are obtained from a Bayesian reconstruction using several diagnostics for individual time slices. The approach of combining RAPTOR with an Extended Kalman Filter contains a predictive model for the electron temperature (with future versions including also ion temperature and particle transport equations [90]), allowing the EKF approach to be applied to reconstruct all the core profiles. At the same time, it is important to realise the similarities between the Bayesian approach of IDE and the Kalman Filter approach in this paper. Indeed, it can be shown that the Kalman Filter can be written as a special case of a Bayesian estimator assuming the noise is Gaussian [91]. The great advantage of Kalman Filter above more general Bayesian reconstruction is its speed, which allows real-time implementation. In previous work [92], RAPTOR has been used on TCV to estimate the core electron temperature and q-profile, constrained by measurements of core density and temperature. The code is also used at AUG [93], JET [90] and ITER [94].
In this work, we show for the first time that RAPTOR can be constrained by MSE measurements to accurately model the q-profile evolution. A prediction of γ is not possible from the state of the model (RAPTOR) alone, but requires knowledge of the 2D magnetic field structure. To be able to calculate γ, RAPTOR has been coupled to a Grad-Shafranov solver (CHEASE [95]) in a self-consistent way, which ensures that the geometry-dependent terms that enter the current diffusion equation (CDE) evolve consistently with the 2D equilibrium, and at the same time the equilibrium is correctly constrained by the q-profile from the CDE. This coupling allows a fast and accurate calculation of γ from the current density profile given by the CDE in combination with the plasma equilibrium.
In the future we want to couple RAPTOR to a real-time capable equilibrium solver for real-time q-profile prediction and control. Then, instead of constraining the GS solver by RAPTOR's q-profile, the filtered polarisation angle would be used as a constraint to ensure consistent q-profiles between RAPTOR and the equilibrium solver.

The remainder of this article is structured as follows:
Section 2 introduces the EKF, followed by a description of the RAPTOR code and a brief outline of the MSE diagnostic and the difficulties present at the ASDEX Upgrade Tokamak. In section 3 the EKF is first tested on a virtual MSE diagnostic, where γ is calculated from the model, and lastly the EKF is used to constrain RAPTOR's q-profile with MSE measurements from ASDEX Upgrade. The conclusions are presented in section 4.

A.6.2 Methodology

Extended Kalman Filter

To provide the best estimate of the state of a system, an Extended Kalman Filter (EKF) can be used to filter real measurements with model predicted measurements

of the system. The EKF, the non-linear extension of the Kalman Filter (which is used for systems described by linear ODE's), has been described in literature extensively [96]. The EKF has the advantage that it not only takes the measurement and model into account, but it is also recursive, fast and can handle asynchronous measurements. Only the main concepts of the EKF algorithm are outlined here, the interested reader is referred to [96, 97] for a more detailed description.
The EKF algorithm is illustrated in figure A.6.1. For every time step k, the EKF algorithm consists of 4 steps. Our notation follows the one of Simon [96], the hat denotes a predicted quantity from the model and the subset, e.g. $k|k-1$, denotes that the quantity is evaluated for time k, taking into account the history of the quantity up to time $k-1$.

Step 1: The EKF uses a model of the system in the form of a nonlinear ODE $x_k = f(x_{k-1}, u_{k-1}, w_{k-1})$, where x_k describes the state of the system, u are inputs to the model and w is the noise vector of the state. First, the partial derivatives of the model function are calculated

$$F_{k-1} = \left.\frac{\partial f_{k-1}}{\partial x}\right|_{\hat{x}_{k-1}}, \tag{A.6.1}$$

$$G_{k-1} = \left.\frac{\partial f_{k-1}}{\partial w}\right|_{\hat{x}_{k-1}}. \tag{A.6.2}$$

$$\tag{A.6.3}$$

Step 2: Predict the state estimate and estimation-error covariance matrix:

$$\hat{x}_{k|k-1} = f(\hat{x}_{k-1}, u_{k-1}, 0), \tag{A.6.4}$$

$$\Sigma_{k|k-1} = F_{k-1}\Sigma_{k-1}F_{k-1}^T + G_{k-1}Q_{k-1}G_{k-1}^T. \tag{A.6.5}$$

Here, Σ is the estimation-error covariance matrix and Q_k is the covariance matrix of the model.

Step 3: Calculate the partial derivatives of the predicted measurement function $\hat{y}_k = h(\hat{x}_k, v)$:

$$H_k = \left.\frac{\partial h_k}{\partial x}\right|_{\hat{x}_{k|k-1}}, \tag{A.6.6}$$

$$M_k = \left.\frac{\partial h_k}{\partial v}\right|_{\hat{x}_{k|k-1}}, \tag{A.6.7}$$

with v being the noise vector of the measurement.

Step 4: Update the state and error covariance estimate:

$$L_k = \Sigma_{k|k-1} H_k^T \left(H_k \Sigma_{k|k-1} H_k^T + M_k R_k M_k^T \right)^{-1}, \tag{A.6.8}$$

$$\hat{x}_{k|k} = \hat{x}_{k|k-1} + L_k \left(y_k - h_k(\hat{x}_{k|k-1}) \right), \tag{A.6.9}$$

$$\Sigma_{k|k} = (I - L_k H_k) \Sigma_{k|k-1}, \tag{A.6.10}$$

where L_k is the so-called Kalman gain and y_k the real measurement of the system. For a smooth initialisation of the EKF, the Kalman gain is multiplied with a time dependent function:

$$L'_k = L_k \cdot \exp\left(-0.12 \cdot (t - t_0)\right), \tag{A.6.11}$$

where t_0 is the first active time step of the observer and the factor 0.12 was chosen to provide a smooth initialisation.

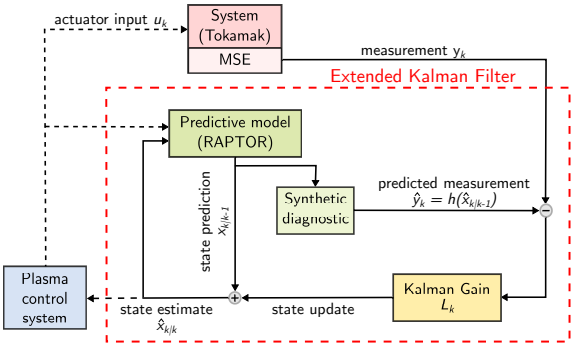

Figure A.6.1: Overview of the Extended Kalman Filter: The predictive model (RAPTOR) simulates the state of the system from which the measurement (polarisation angles γ) is predicted. In combination with the real measurement the EKF updates the state to obtain an improved estimate.

The system is described by the current diffusion equation and heat transport equations, implemented by the transport simulator RAPTOR. The state of the model $\hat{x}$ is a representation of the poloidal flux ψ and the electron temperature T_e, from which various plasma parameters - for this article most importantly the safety factor q - can be derived. As measurements y_k, the polarisation angle measurements from the MSE diagnostic are used. The model, measurement and measurement prediction, will be explained in the following sections.

A central quantity for the EKF algorithm are the noises of the state and measurement, w_k and v_k respectively, from whose covariance matrices the Kalman Gain L_k is calculated (equation A.6.8). The covariance matrices are essential for the performance of the EKF. They determine the weighting of the model, or measurement, and are used to tune the EKF.

The process covariance matrix Q_k of the model has previously been defined in [97]. It is designed to enforce a high correlation between neighbouring spatial points based on physical and numerical consideration of the problem.
The covariance matrix of the measurement is a diagonal matrix containing the square of the standard deviation of each measurement channel as diagonal entries. It is described in more detail in section A.6.2.

Plasma evolution model: RAPTOR

The observer is based on a model of the system (the tokamak), which provides estimates of the state of the system from which the expected measurement can be derived. The system is modelled by the transport simulator RAPTOR. This faster than real-time capable code solves the coupled 1D poloidal flux (ψ), electron- and ion- temperature (T_e, T_i) equations, as well as particle transport equations for electrons and multiple ion species [90]. For the present work, we solve only the equations for ψ (equation A.6.12) and T_e (equation A.6.13).

$$\sigma_{||}\left(\frac{\partial\psi}{\partial t}\Big|_{\hat{\rho}} - \frac{\hat{\rho}\dot{\Phi}_b}{2\Phi_b}\frac{\partial\psi}{\partial\hat{\rho}}\right) = \frac{F^2}{16\pi^2\mu_0\Phi_b^2\hat{\rho}}\frac{\partial}{\partial\hat{\rho}}\left[\frac{g_2 g_3}{\hat{\rho}}\frac{\partial\psi}{\partial\hat{\rho}}\right] - \frac{B_0}{2\Phi_b\hat{\rho}}V'_{\hat{\rho}}\left(j_{\text{aux}} + j_{\text{bs}}\right) \quad \text{(A.6.12)}$$

In equation A.6.12, $\sigma_{||}$ is the neoclassical conductivity, j_{aux} is the non-inductive driven current by auxiliary systems, j_{bs} the bootstrap current, and g_2, g_3, F, $V'_{\hat{\rho}}$ define the geometry of the simulation and are calculated from magnetic equilibria.
The electron energy transport equation is written as:

$$\begin{aligned}\frac{3}{2}\left(V'_{\hat{\rho}}\right)^{-5/3}&\left(\frac{\partial}{\partial t}\Big|_{\hat{\rho}} - \frac{\dot{\Phi}_b}{2\Phi_b}\frac{\partial}{\partial\hat{\rho}}\hat{\rho}\right)\left[\left(V'_{\hat{\rho}}\right)^{5/3} n_e T_e\right] \\ &+ \frac{1}{V'_{\hat{\rho}}}\frac{\partial}{\partial\hat{\rho}}\left(-\frac{g_1}{V'_{\hat{\rho}}}n_e\chi_e\frac{T_e}{\partial\hat{\rho}} + \frac{5}{2}T_e\Gamma_e g_0\right) = P_e \end{aligned} \quad \text{(A.6.13)}$$

With electron temperature, density, thermal diffusivity, convective flux T_e, n_e, χ_e, Γ_e and geometric terms g_0, g_1. P_e denotes the sum of the power density sources and sinks. Φ_b, $\hat{\rho} = \sqrt{\Phi/\Phi_{\text{edge}}}$, and B_0 are the toroidal flux enclosed by the LCFS, the normalised square root of the toroidal flux and toroidal magnetic field at the magnetic axis, respectively. The particle flux Γ_e is neglected in this work.
Equation A.6.12 and A.6.13 follow the notation of [90], where a detailed description of the individual terms is provided.

The equations are solved on a radial grid corresponding to the normalised toroidal flux and are depending on the plasma and flux surface shape.
The thermal transport coefficient χ_e is provided by a gradient based empirical transport model [93] with free parameters tuned to match the temperature profiles calculated by the IDE code. The equilibrium calculated by IDE is taken as reference for this analysis.

MSE diagnostic

Equilibrium solvers reconstruct the magnetic equilibrium in the plasma by solving the Grad-Shafranov equation, constrained by various measurements. As a constraint for the current density in the plasma centre, the Motional Stark Effect (short MSE) diagnostic is commonly used. It provides a measure for the local magnetic pitch angle γ_m, the angle between B_ϕ and B_θ. The MSE diagnostic measures the light emitted by neutral particles, which are injected into the plasma. Typically, the radiation of the particles injected by the neutral beam injectors is analysed. Due to the Stark effect the emitted light is polarised relative to the magnetic field; measurements of the polarisation angle γ can be linked to the pitch angle of the magnetic field projected in a plane perpendicular to the diagnostic's line of sight [11]. The MSE diagnostic at AUG can measure the polarisation angles at 8 different radial positions, with up to two channels per radius. The diagnostic measures the radiation of the Balmer-α line, which, due to the Stark effect, is degenerate into a total of 9 lines with different polarisations. The lines can be grouped in two components: π- and σ-lines, which are polarised perpendicular and parallel to the electric field vector. The setup at AUG allows simultaneous measurement of both spectral components at similar radial and vertical positions [98, 99, 61].

The configuration of the MSE channels for the shot analysed in this article is shown in figure A.6.2. 6 channels of the diagnostic are configured to record the σ lines of the stark spectrum and 2 the π emission. The measurement location of the π channels are in proximity to the σ channels. In a shot with high quality MSE data, the relationship $\sigma_n \approx \pi_n - 90°$ holds, where $n = 1,2$ refers to one of the two channel pairs marked in purple in figure A.6.2.
A challenge at AUG is the contamination of the recorded signal with background

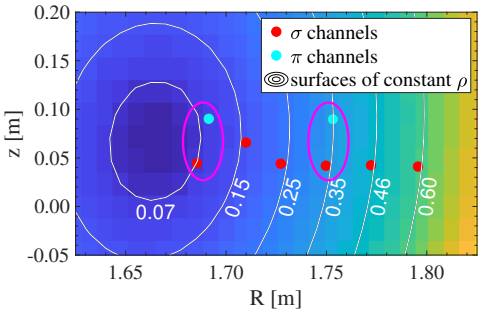

Figure A.6.2: Poloidal plane, CHEASE flux surfaces and corresponding toroidal ρ values. Plotted are the spatial locations of the MSE channels and contour lines of constant ρ intersecting the MSE channels. Note that the values of ρ are subject to change during the shot, shown is the reconstructed grid for $t = 3.7$ s, shot *#33134*. The q-profile cannot be constrained by MSE signals in the vicinity of the plasma edge. No MSE channels are available here, however q_{95} is constrained by the total plasma current.

polarised light, originating from reflections on the inner metallic wall of the device. This background polarised light can render the recorded signals unusable in discharges where the line averaged central electron densities exceeds $\langle n_e \rangle \gtrapprox 5{\cdot}10^{19}$ [61] (a shot-by-shot analysis is required to determine the quality of the MSE signal). One extreme example of a contaminated measurement is shown in figure A.6.3: The diagnostic was configured to record five $\pi - \sigma$ measurement pairs simultaneously, which should display a 90° difference. During the shot, this can only be observed within the first 1.7 s, after which the density is increased and the lines begin to diverge [61], rendering the measurement unusable[¶].

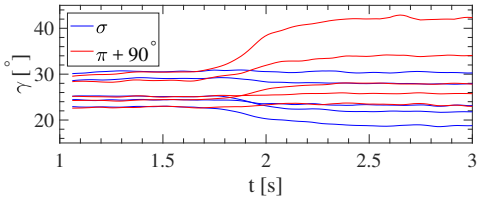

Figure A.6.3: Example of the high-noise contaminated MSE measurements, recorded in AUG shot *#31313* (adapted from [61]).

The simultaneous measurement of π and σ lines is used to derive a time-varying estimate of the variance of each MSE measurement: The measurement covariance matrix R_k, required by the EKF (equation A.6.8), is calculated from the two available $\pi - \sigma$ pairs (see figure A.6.2) by calculating their time averaged difference:

$$\Delta\gamma(t) = \frac{1}{2}\sum_{n=1}^{2}\overline{\left|\left(\gamma_n^{\sigma} - \left(\gamma_n^{\pi} - 90°\right)\right)\right|} \tag{A.6.14}$$

$$\equiv \frac{1}{2}\overline{\Delta\Gamma}, \tag{A.6.15}$$

where the overline denotes that for each time t, $\Delta\Gamma$ is averaged over the previous 20 ms (the averaging window was chosen to provide statistically relevant results for simulations where the time step is one millisecond, but proved to work well in simulations with a time step of 5 ms). The diagonal elements of the covariance matrix, corresponding to the covariances of the individual MSE channels, are then $R_k = (\Delta\gamma)^2$.

[¶]For completeness we like to mention that similar problems have been reported at Alcator C-Mod, whereas a solution the MSE polychromator has been developed [100]. The MSE polychromator measures the $\pi+\sigma$ emission as well as the background polarisation in wavebands close to the measurement wavelengths for every channel. The polarisation angles are then corrected by subtraction of the background.

Measurement prediction

The EKF requires the calculations of the predicted measurement from the model. The polarisation angle is calculated by

$$\gamma = \tan^{-1}\left(\frac{a_0 B_z + a_1 B_r + a_2 B_\phi}{a_3 B_z + a_4 B_r + a_5 B_\phi}\right), \tag{A.6.16}$$

where the a_i are known device specific geometric coefficients, that depend on the setup of the MSE diagnostic. $B_z(r,z)$ and $B_r(r,z)$ are the vertical and radial components of the poloidal magnetic field B_θ, and $B_\phi(r,z)$ is the toroidal magnetic field at the measurement location r,z[||].
From equation A.6.16 it is clear that γ cannot be derived from the RAPTOR state alone, since RAPTOR calculates 1D profiles and does not reconstruct the 2D equilibrium. The plasma equilibrium, constrained by RAPTOR's q-profile, must be calculated in order to calculate the predicted measurement. Then, by rewriting the poloidal magnetic field as

$$B_\theta = e_\phi \times (2\pi R)^{-1} q^{-1} \nabla\Phi, \tag{A.6.17}$$

the polarisation angle can be calculated by using $\Phi = \Phi_{\mathrm{EQ}}$ (i.e. the toroidal flux is obtained from the plasma equilibrium) and $q = q_{\mathrm{RAPTOR}}$. The required coupling between RAPTOR and an equilibrium solver is described next.

Coupling between RAPTOR and CHEASE

The RAPTOR code does not evolve the plasma geometry, but instead assumes it to be fixed throughout the simulation. A time dependent coupling between RAPTOR and an equilibrium reconstruction code is required to calculate the spatial distribution of magnetic fields required to estimate γ locally. This requires constraining an equilibrium solver with RAPTOR's q-profile and updating geometry terms in the transport equations from the calculated equilibrium before continuing the iteration of the transport equations. In practice this can be achieved by constraining both codes with the same MSE angles. Since the flux surface shape and Φ changes slowly compared to ψ, and thus q, updates of the plasma equilibrium are not required with every iteration of the CDE.
For the presented analysis, RAPTOR has been coupled to CHEASE [95], a fixed-boundary equilibrium solver, which solves the GS equation using specified boundary conditions and internal profiles. The last-closed flux surface and magnetic fields are used as inputs by CHEASE and are directly provided by RAPTOR. The pressure profile in terms of normalised toroidal flux $p(\hat{\rho})$ can also be used as input profile. The use of $\hat{\rho}$ allows a direct coupling with RAPTOR, since it is RAPTOR's

[||] Note that equation A.6.16 is a reduced form which neglects contributions from electric fields, which can lead to high uncertainties in advanced plasma scenarios [46]. The radial electric fields cannot be obtained from RAPTOR. For improved accuracy E_r can be estimated from ion pressure profiles and toroidal and poloidal velocities [101].

radial coordinate, and is less sensitive to changes in the q-profiles. This requires CHEASE to transform internally to profiles with respect to the poloidal flux, a solution of the GS equation. Another new option has recently been introduced in CHEASE, namely to provide the $q(\hat{\rho})$ profile as input [102]. In this case CHEASE computes the current density profile I^*, related to j_ϕ, such as to match the input q-profile and iterates until convergence (see equation 50 in [102]). This usually leads to a finite current density at the plasma boundary which can be reduced by slightly modifying the radial derivative of q near the edge. This is sometimes used to study the sensitivity of plasma stability on the edge current density, for example, but it is not needed for this routine since the $I^*(q_{\text{target}})$ matching performed by CHEASE provides the target q-profile without unphysical edge surface currents. Also, CHEASE can use the previous equilibrium as an initial guess which will significantly accelerate the equilibrium calculation.

The implementation allows dynamic updates of the geometry at arbitrary time steps of the simulation; it is illustrated in figure A.6.4. The implemented coupling calculates the plasma equilibrium based on RAPTOR's q- and pressure profiles every n-th RAPTOR iteration **. The equilibrium update frequency is chosen by the user. Too few updates can cause jumps in the calculated polarisation angle, a high update frequency leads to long simulation times. For the presented work it was found sufficient to update the equilibrium every 5th RAPTOR time step.
From the calculated equilibrium, the geometry, i.e. the shape of the poloidal flux surfaces as well as the toroidal flux they enclose (in detail terms g_1, g_2, g_3, V' and F in equation A.6.12, A.6.13) are calculated and updated in RAPTOR before the iteration of the transport equations is continued. This asynchronous implementation allows for a fast and accurate calculation of the polarisation angle, which can be used in offline and real-time simulations alike.
The importance of the equilibrium update is shown figure A.6.5. Here, RAPTOR was run twice with identical simulation parameters, however, in one case the geometry was prescribed and fixed throughout the simulation, and in the second case the geometry terms were updated during the simulation.
The geometry updates do not change the q-profile evolution, but result in corrections of γ of multiple degrees, essential for a sensitive analysis.

A.6.3 Implementation of the MSE observer

EKF tuning using synthetic data

The MSE observer is implemented and the performance is evaluated with synthetic data. The aim is to test and validate the implementation and investigate the effect of various settings of the EKF. For this, artificial MSE measurements are generated by simulating an AUG shot with RAPTOR, used in purely predictive mode,

**Technically CHEASE was constrained by the parallel current density $j_{||}$ and p, which is computational easier and available from RAPTOR. We verified that constraining CHEASE with $j_{||}$ or q results in similar results.

as in [93]. Matching plasma equilibria are calculated with CHEASE. From the simulation result and equilibria, the expected polarisation angles are calculated as

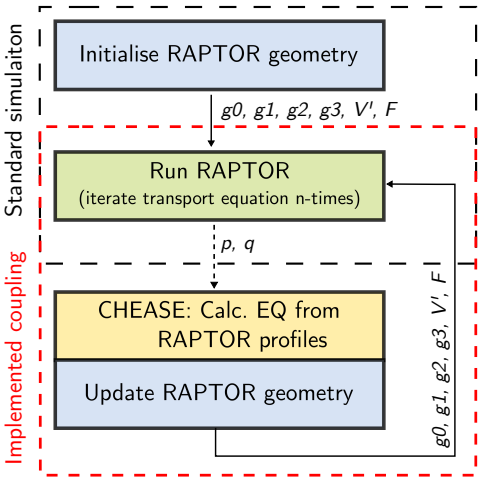

Figure A.6.4: Flow diagram of the implemented coupling between RAPTOR and CHEASE.

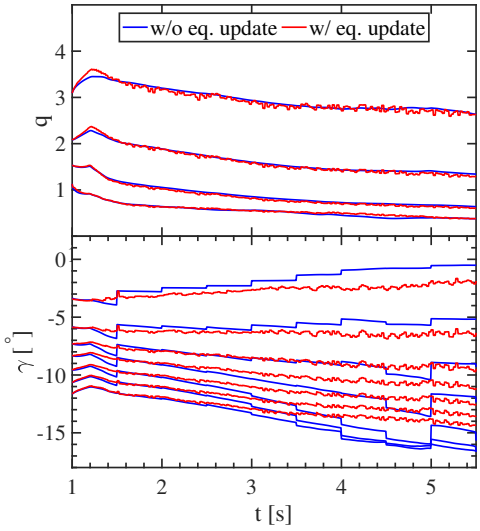

Figure A.6.5: RAPTOR simulations with and without equilibrium update: Top: q values for different ρ values. Bottom: calculated γ. No simulation parameters were changed resulting in the equal evolution of q. The a priori calculated geometry (—) is based on equilibria from IDE which were loaded in half-second intervals. This is manifested in step-wise changes in γ. In the coupled simulation (—) the geometry is updated every 5th simulation step.

described in section A.6.2 and A.6.2. This simulation and synthetic diagnostic are assumed to correspond to the true evolution of the plasma profiles (q, T_e, ...) and corresponding true measurements, i.e. the nominal case.
A normal distributed random noise with standard deviation of $\Delta\gamma = 0.5°$ is added to the polarisation angles to simulate the effect of measurement noise. This noise level is arbitrarily chosen and approximately 5 times higher than the acceptable error margins on MSE signals. Furthermore, the model used by the EKF is perturbed with respect to the nominal simulation: Firstly, the q-profile used to initialise the simulation at $t_0 = 1.5$ s is elevated, see figure A.6.6 (d) and A.6.7 at t_0. Additionally, the electron temperature transport coefficient is reduced by 30%, which yields a higher temperature, higher conductivity and correspondingly different q-profile evolution.
The input to the EKF are the perturbed simulation and noisy polarisation angles. The q-profile is evaluated to verify that the EKF is able to provide a good estimate of the nominal q-profile.
The time evolution of various quantities of the nominal and observer simulation are shown in figure A.6.6. The model mismatch due to the reduced transport is clearly visible in the central electron temperature evolution in figure A.6.6 c). For the observer case, the initially perturbed q-profile, figure A.6.6 d), converges within ≈ 80 ms to the q-profile of the nominal simulation, only a slight mismatch is visible at the q values towards the plasma centre, which is the most affected by the reduced heat transport.
The innovation sequence $\mathfrak{I} = z_k - h(\hat{x}_{k|k-1})$, the difference between measured and model predicted MSE data, shown in fig. A.6.6 e), is expected to be zero mean if the underlying system is linear. For the non-linear case it still serves as an indication on the performance of the EKF. In the analysed scenario $\mathfrak{I}$ does not converge to a zero mean, but stays close to zero. This implies that a constant correction from the observer on the q-profile is required. Contradictory to [97], no disturbance estimation is required due to the relatively large timescales of the current diffusion time.
The q-profile of the nominal and perturbed simulation as well as the observer results are compared for various time steps in figure A.6.7.
The observer corrects the perturbed q-profile to closely approximate the nominal case. The difference in q for each time step between the nominal case and the observer/perturbed case is calculated using the standard deviation figure of merit [103, 104]

$$\sigma(t) = \sqrt{\int_{\rho=0}^{1} d\rho\,(q_{\mathrm{obs,pert}} - q_{\mathrm{nom}})^2} \Big/ \sqrt{\int_{\rho=0}^{1} d\rho\, q_{nom}^2}. \tag{A.6.18}$$

Averaged over all times $t > 75$ ms, $\overline{\sigma}_{\,\mathrm{nom|obs}} = 0.02$ (between the nominal and observer simulation) is very low compared to $\overline{\sigma}_{\,\mathrm{nom|pert}} = 0.19$ (between the nominal and perturbed case).
The convergence time depends on the choice of the covariance matrix, which is used to tune the EKF. To illustrate the influence of the model covariance, figure

A.6.8 shows the innovation sequence for varying σ_J, the value of the diagonal elements of the model covariance matrix Q_k (see equation A.6.5). Decreasing covariance results in an increase convergence time. Tuning of the covariance (matrix) is crucial for the operation of the EKF.

q-profile reconstruction of AUG discharge

After the initial verification using synthetic measurements, the q-profile of a full AUG discharge is reconstructed using the MSE observer. A shot with low noise MSE signals is analysed, for which a reference equilibria (reconstructed by MSE constrained IDE [89]) is available. IDE is a GS solver, which, apart from being constrained by the measurements, also evolves the poloidal flux diffusion equation in-between consecutive equilibria reconstructions. The evolved current density profile is used to constrain the next equilibrium solution. The goal of this analysis is for the observer to obtain a q-profile comparable with the IDE reference. For the analysis, RAPTOR's heat transport model, non-inductive current density deposition profiles from ECRH and NBI as well as the non-inductive driven currents

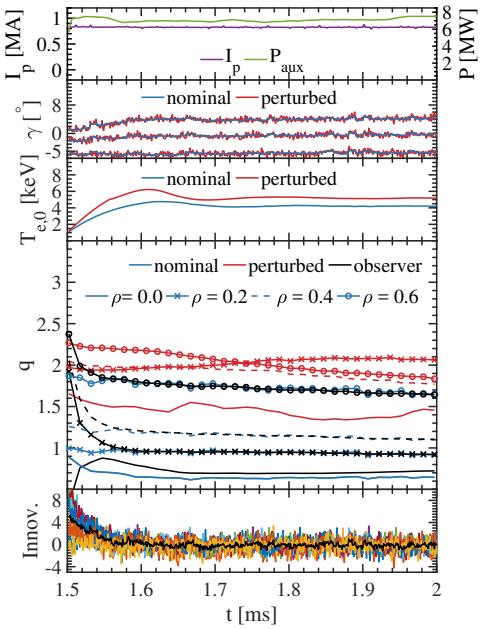

Figure A.6.6: Summary of the MSE observer results using synthetic MSE data (based on AUG shot *#33134*). a) Plasma current and aux. power. b) calculated polarisation angle without (—) and with 0.5° noise (—). c) central electron temperature of the nominal and perturbed simulation. d) comparison of the q-value evolution at $\rho = 0, 0.2, 0.4, 0.6$ between the nominal simulation, perturbed simulation and MSE observer. e) Innovation sequence, the difference between measured and model predicted MSE data.

have been tuned to approximate IDE estimates. The density profiles are fixed to match IDE. A comparison between IDE and the RAPTOR simulation without the EKF is shown in figure A.6.9. Here, q_{edge} matches well due to the constraints at the plasma boundary, however, in the plasma centre, RAPTOR diverges from the reference.

The MSE observer is run with the same RAPTOR configuration used to create figure A.6.9 and the measured polarisation angles of shot *#33134*. The goal of the analysis is to obtain a q-profile matching the IDE analysis. The safety factor evolu-

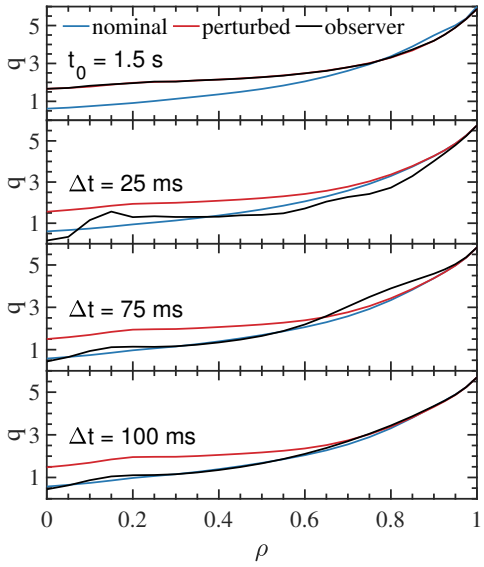

Figure A.6.7: q-profile for the reference (—) and perturbed (—) simulation, as well as the q-profile resulting from the observer (—). q-profiles are plotted for t_0 and $\Delta t = 25, 75, 100$ ms after the begin of the simulation. The model of the observer is the perturbed simulation, input measurements are the noisy polarisation angles.

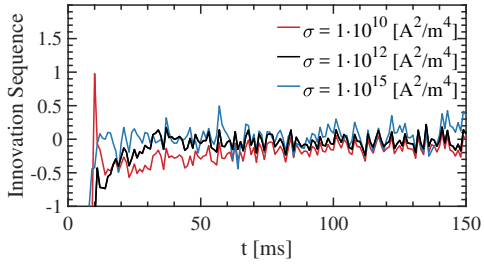

Figure A.6.8: The convergence of the EKF, measured by the innovation sequence $\mathfrak{I}$, can be tuned by the covariance σ_J.

tion of the MSE observer is shown in figure A.6.10. The observer is active between 1.2 s – 7 s, the time during which MSE measurements are available.

The q-profile evolution estimated by the MSE observer is in good agreement with the IDE reference. Only in the vicinity of the magnetic axis, where the difference between the pure RAPTOR simulation and IDE is highest, a significant deviation from the IDE reference is notable. At the plasma edge, a match in q between RAPTOR and IDE is guaranteed by the boundary conditions.
The q-profiles are compared in figure A.6.11 at four times. The q-values in the vicinity of the magnetic axis differ by $\Delta q \approx 1$ between the RAPTOR simulation without MSE and IDE. The MSE observer corrects the q-profile significantly. To compare the correction, the standard deviation figure of merit (see equation A.6.18) is calculated. Since the observer only corrects the q-profile in the plasma centre, the integral in equation A.6.18 is evaluated like $\int_{\rho=0}^{0.7}$ (for larger values of ρ, no

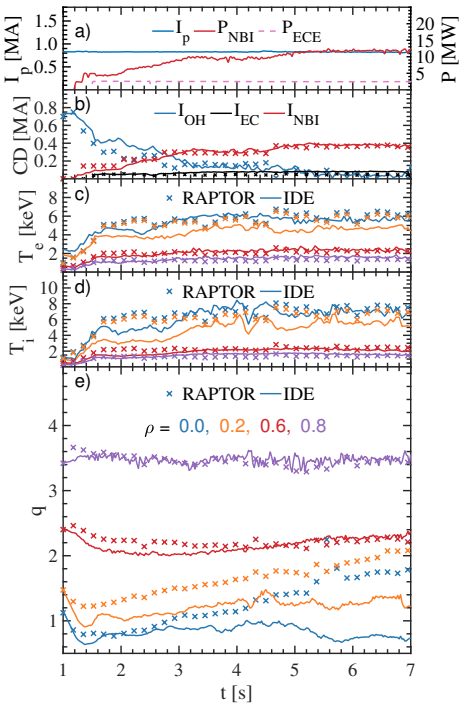

Figure A.6.9: Comparison of IDE analysis and RAPTOR simulation (with deactivated observer) of AUG shot *#33134*: a) Plasma current and aux. power. b) Current sources from IDE (solid) and RAPTOR (crosses). c), d): Electron and ion temperature at different ρ. e) q-value evolution at different ρ. Temperature and q-values are plotted for $\rho = 0, 0.2, 0.6, 0.8$. Note that the shot is not sawtoothing and that due to the high uncertainty of the q-profile reconstruction around the magnetic axis no assessment can be made whether q_0 drops below one.

MSE channels are available and the observer result matches the RAPTOR simulation without MSE.). As it was previously done, the resulting $\sigma(t)$ are averaged over all times. We find a significant improvement from $\overline{\sigma}_{\text{OBS|IDE}} = 0.05$ (difference between observer and IDE reference), compared to $\overline{\sigma}_{\text{RAP|IDE}} = 0.19$ (disabled observer and IDE reference).

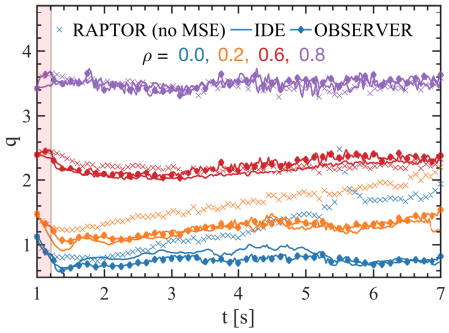

Figure A.6.10: q-profile evolution at $\rho = 0, 0.2, 0.6, 0.8$. Compared are three cases: RAPTOR without MSE, the reference IDE solution and the observer result. The times where the observer is inactive are shaded in red, here no MSE measurements are available. The RAPTOR time resolution is 5ms; every 35th time step is plotted for improved visibility.

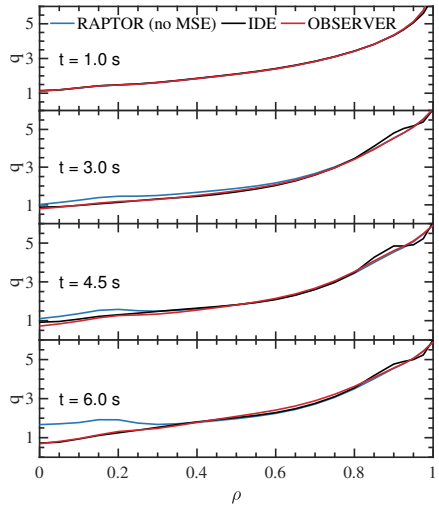

Figure A.6.11: q-profile comparison between the nominal simulation (——), IDE (——) and MSE observer (——). Due to the high number of constraints, IDE is able to resolve the plasma edge more accurately than RAPTOR, leading to the divergence of q for $\rho > 0.8$.

Observer behaviour at signal loss

Lastly, the behaviour of the MSE observer after the loss of the MSE signal is analysed. The previous scenario is repeated, but the MSE input to the observer is cut at $t = 5$ s. The resulting time evolution of q is shown in figure A.6.12. Immediately after the loss of the measurement signals, the q-profile of the observer begins to converge towards the non MSE-constrained case.
An advantage of using the MSE observer is the constant availability of polarisation angles which can be passed to a (real-time) Grad-Shafranov solver. In the worst case, i.e. no valid measurements are available, the q-profile is predicted solely by the model, whose information of the transport in the plasma can greatly enhance the equilibrium reconstruction. In other words: with the approach described in this article almost any GS solver can easily be constrained by the evolution of the poloidal flux calculated by RAPTOR.

A.6.4 Conclusion & outlook

In this article we have shown that RAPTOR can be constrained by polarisation angle measurements to provide an improved estimation of the q-profile. The implemented observer is able to accurately estimate the q-profile in simulations where both the measurement and model have been perturbed. Furthermore, it was shown, that in shots where reliable MSE data is available, the MSE observer constrains RAPTOR's q-profile to match reference equilibria with minimal offsets. The MSE diagnostic at ASDEX Upgrade suffers from parasitic polarised reflections from the metallic walls, which can render the diagnostic unusable in several scenarios. Due to the setup of the MSE system, which can simultaneously measure π and σ emission at the same radial location, an (real-time capable) estimate of the measurement quality is obtained. With this, the observer continuously updates the covariance matrices and it can provide estimates of the polarisation angle measurements to a GS solver in any discharge scenario, even if physical measurements

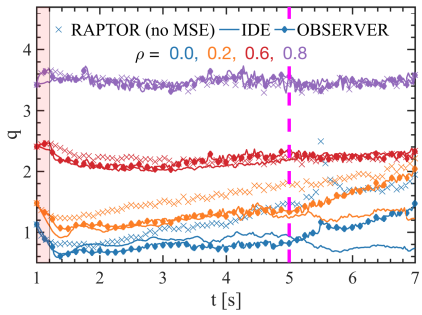

Figure A.6.12: q-profile evolution at $\rho = 0, 0.2, 0.6, 0.8$. At $t = 5$ s the measurement input to the observer is disabled and the simulation continues without being constraint by MSE measurements.

are unavailable.

While the work presented here uses the CHEASE equilibrium code, which is fixed-boundary solver and not capable to run in real-time, this approach can readily be ported to a real-time capable equilibrium code such as LIUQE [105] or JANET [106]. Then, instead of using RAPTOR's q-profile, the filtered polarisation angles can be used to constrain the q-profile of the equilibrium reconstruction. In principle, this allows any Grad-Shafranov solver to be constrained by the current diffusion, heat and particle transport between consecutive equilibria reconstruction by coupling it to RAPTOR via a virtual MSE diagnostic. The only requirement is that the GS solver can be constrained by MSE measurements.

In the future we plan to implement the observer in AUG's real-time control system, where the RAPTOR code is already implemented, a real-time capable MSE diagnostic is installed and the real-time equilibrium reconstruction code JANET [106] are readily available. For this, the observer must be converted to a Simulink model prior to execution in RT and the corrected MSE signals from the observer passed to JANET, which is already capable of MSE constrained equilibrium reconstruction. Once implemented, a model-based q-profile controller can be designed, similar to the already implemented electron temperature controller at ASDEX Upgrade [107], or a plasma profile controller developed for ITER [108]. The RAPTOR code has no constraint on the plasma scenario and can be used to model (and control) monotonic and advanced (e.g. reversed shear) q-profiles, using real-time estimates of the driven current from codes such as RT-TORBEAM for electron cyclotron heating [109, 110] and RABBIT for NBI [111]. In advanced scenarios, it is important to follow and control the q-profile evolution close to the magnetic axis. Here, small uncertainties on the MSE signal can lead to large uncertainties in the q-profile reconstruction. The model-based approach can help to gain more accurate insight and control in advanced scenarios. To reduce uncertainties, a central DCN polarimetry channel [112] could possibly be added to the observer, this is however currently not planned.

A.6.5 Acknowledgement

This work has been carried out within the framework of the EUROfusion Consortium and has received funding from the Euratom research and training programme 2014-2018 under grant agreement No 633053. The views and opinions expressed herein do not necessarily reflect those of the European Commission. This work was supported in part by the Swiss National Science Foundation.

A.7 Conclusions A

Tokamaks are the leading type fusion reactors for future power plant designs. They confine a thermal plasma at millions of degrees Celsius using magnetic fields. The magnetic field structure, or its derived quantity, the q-profile, is in general not known accurately, because it is in part generated by a current of unknown spatial distribution running through the plasma. Knowledge of the q-profile is important for the stability and performance of the plasma and the first step towards controlling the current distribution through external actuators.
In this work the feasibility of the MSE diagnostic for use as a real-time measurement of the q-profile of a tokamak, with a view on using it as the sensor for real-time q-profile control, has been assessed.
The central conclusion is that the MSE diagnostic does indeed provide valuable information that can be used to advantage in such a scheme, especially if it is combined with a real-time equilibrium solver, i.e. if the MSE data is used in consort with e.g. magnetic measurements to constrain the equilibrium reconstruction.
In order for such an application of MSE to be successful, it is necessary that several data processing steps are taken in order to suppress the effects of systematic errors from polarisation changes due to optical components and experimental influences on the optics, which are difficult to approximate a-priori. In this work a calibration routine has been developed which consists of an in-vessel calibration, correction of Faraday rotation caused by the magnetic field, a filter calibration based on maximising the linear polarisation fraction of the transmitted light, as well as a cross-validation against known MHD modes determined by secondary diagnostics. While these corrections are complex, once established the results can in principle be reused and no recalibration is required. Only polarisation changes caused by depositions on the transmitting vacuum window throughout the plasma campaign must be corrected for, which can be detected by the daily available Faraday calibration measurement. The calibration routine was developed for the commissioning of the newly installed MSE system at the KSTAR tokamak where polarisation angles with accuracies of $\Delta\gamma = 0.2°$ over 10 ms averages are obtained. With the newly installed diagnostic, changes in the central q-value (q_0) during the monster sawtooth instability were evaluated, and it is shown that the change in q_0 is in line with the Kadomtsev model of magnetic reconnection. These findings were later confirmed by a follow-up investigation which is not part of this thesis [113].

As a step towards real-time q-profile reconstruction it is shown that the q-profile reconstruction can be significantly improved by using filter techniques from control theory on the MSE data. An extended Kalman filter (EKF) is implemented at ASDEX Upgrade which combines predicted measurements from the RAPTOR code and measurements from the MSE diagnostic. The EKF is able to reduce the error in the reconstructed q-profile from 19% to 5% (compared to established reference equilibria). For the measurement prediction, RAPTOR, a 1D plasma transport sim-

ulator, is coupled to a predictive equilibrium solver. The coupling allows updates of the magnetic topology, and consequently the geometry on which RAPTOR solves the transport equations, in between simulations steps, which was previously not possible. Instead, the geometry (including, among other parameterisations, the shape of the poloidal flux surfaces) used to be based on reference equilibria of similar plasma scenarios and be fixed throughout the simulation. The new coupling allows dynamic, asynchronous updates of the geometry. This can result in a more accurate prediction of the plasma profiles, which is essential for the calculation of the polarisation angles.
The connection between RAPTOR and the equilibrium solver can in principle be ported to any other Grad-Shafranov solver, as long as it is constrainable by polarisation angle measurements. Using RAPTOR in conjunction with an equilibrium solver in situations where no MSE measurements are available, or even at devices without an MSE diagnostic, will allow for more accurate reconstruction of the q-profile, because the internal profiles are no longer only constrained by predefined profiles and magnetic measurements at the plasma edge, but also by the evolution of the poloidal flux diffusion modelled by RAPTOR.

From the research it is evident that implementing a polarimetry based MSE system on today's tokamaks is challenging and will be more so for the next generation device, ITER. Like ASDEX Upgrade, ITER will feature a fully metallic wall [114] and stray radiation can be an issue. Therefore, implementing a classical MSE system (i.e. polarimetry based) could be challenging, possibly requiring an MSE polychromator setup. This will, however, not be able to correct inter-shot drifts of the signal caused by depositions on the first mirror, the severity of which requires further investigation. If it proves that these depositions cannot be ignored, it must be investigated whether an observer is able to provide accurate estimates in the case of a signal with unknown drift. An alternative can be the line-shift MSE (MSE-LS), which is being investigated by the US (tasked with implementing the MSE system at ITER) [65]. MSE-LS systems require reliable and fast models of the spectrum to extract the shift between the individual emission lines from the broadened spectrum. Spectral models have been created at ASDEX Upgrade [115], KSTAR [116] and MAST [117] and as part of the MSE-LS study for ITER [65], showing promising first results. However, further investigations are required on the achievable accuracy of both line-shift and polarimetry based MSE systems.

Even though further research is required for the next generation devices, the conducted research is of value for current generation tokamaks with a view on ITER, for which the plasma scenarios are still being developed. The presented research is the first step towards the final goal of real-time q-profile control. At ASDEX Upgrade, RAPTOR is already able to run as a plasma controller and a real-time capable MSE diagnostic, as well as a real-time equilibrium solver, are available. The following next steps are proposed to advance the implemented observer to a real-time q-profile controller at ASDEX Upgrade:

Model validation: In high-density scenarios at ASDEX Upgrade the MSE diag-

nostic is so error prone, that the data cannot be used as an input to the Grad-Shafranov solver. In these situations a real-time observer can complement the q-profile reconstruction by constraining the equilibrium solver with the model predicted polarisation angle. For a routine operation, a validation of RAPTOR in a broad range of plasma scenarios is required to determine the applicable parameter space and ensure consistent results.

Conversion to real-time observer: The developed observer currently only works offline. For real-time operation the algorithm must be converted to a Simulink model, which is compatible with the plasma control system, and the link between real-time diagnostic and the observer must be established.

MSE polychromator: Due to the high uncertainties of the MSE diagnostic, an upgrade to a polychromator based system is currently carried out. With the new system reliable polarisation angles measurements are expected for a wide range of plasma scenarios. Once the hardware upgrade is complete, the real-time polarisation angle reconstruction algorithm must be adapted and an improved uncertainty estimator should be implemented in the observer.

Part B:
Performance optimisation of inertial electrostatic confinement machines

B.1 Introduction

B.1.1 Inertial electrostatic confinement machines

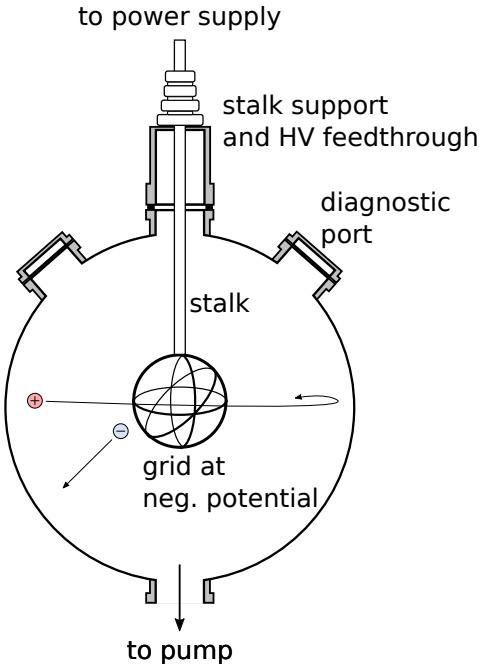

Figure B.1.1: Schematic drawing of a fusor. Fusors consist of a grounded spherical or cylindrical vacuum vessel in which a transparent grid is centred. Plasma breakdown is achieved by applying high negative potentials to the grid. The electric field accelerates ions towards the device centre where they can fuse with other ions or neutral gas particles. Ions missing the grid oscillate until they get neutralised, fuse, or collide with the grid or stalk. The working principle is in more detail explained in section B.2.

Fusors, a type of inertial electrostatic confinement (IEC) machine have been an active topic of research since the 1960s. Compared to thermonuclear, or (laser) inertial confinement devices, they are appealing due to their small size and comparably simple design. In an IEC device ions are accelerated and confined with static electric fields. They can be categorised into two classes:

Gridded devices: The most common type of IEC experiments, and the focus of this research, consists of a vacuum vessel in which a transparent grid is centred. The concept is sketched in figure B.1.1. A negative potential is applied to the grid, the electric field accelerates ions towards the centre and electrons to the vacuum vessel. Ions and electrons are created by filling the vacuum vessel with the fuel (for example deuterium) at low pressures and applying high enough potential on the cathode for plasma breakdown to occur. A more detailed explanation of the principle, as well as an overview of the experimental setup at TU/e, is given in section B.2.

Virtual electrode devices: A disbenefit of the gridded design are losses due to ions colliding with the grid or stalk. To reduce the losses, gridless machines have been developed which create a virtual cathode by trapping electrons. Two

variations are an original design by Farnsworth [118], which can best be described as a classical fusor with reversed polarity (creating a virtual cathode via converging electrons), and the Polywell [119], which forms a virtual cathode by magnetically trapping electrons in a quasi-spherical-cusp.

Fusion mechanisms in IEC devices

The fusor theory assumes that fast ions will converge towards centre of the device and move on oscillatory trajectories through the device until they collide with the grid or are neutralised. Fusion collisions can occur, amongst others, by collisions between two fast ions (beam-beam fusion), the collision between a fast ion and a neutral gas particle (beam-gas fusion), or the collisions between ions and fuel particles embedded or absorbed in the grid (embedded fusion). To estimate which of these collisions is dominant, the reaction rate R, used to calculate the number of reactions per unit time, is estimated:

$$R = \iiint f_1(\mathrm{v}_\mathbf{1}) f_2(\mathrm{v}_\mathbf{2}) \sigma(|\mathrm{v}_\mathbf{2} - \mathrm{v}_\mathbf{1}|) |\mathrm{v}_\mathbf{2} - \mathrm{v}_\mathbf{1}| \mathrm{d}\mathrm{v}_\mathbf{1} \mathrm{d}\mathrm{v}_\mathbf{2} \mathrm{d}V \tag{B.1.1}$$

$$= n_1 n_2 \langle \sigma v \rangle V, \tag{B.1.2}$$

Here, the f_i are the distribution functions of the two reactants with densities n_i, $\sigma(v)$ the velocity dependent cross section and v the relative velocity. The reaction rate is estimated assuming deuterium as a fuel. The density of species one is proportional to the current of the fast ions, $n_1 \propto I_{\mathrm{fast}}$, and the density n_2 is collision dependent:

$$\begin{aligned} \text{beam-beam fusion:} &\quad n_2 \propto I_{\mathrm{fast}} \\ \text{beam-gas fusion:} &\quad n_2 \propto p_{\mathrm{gas}} \\ \text{embedded fusion:} &\quad n_2 \propto n_{\mathrm{emb}} \end{aligned}$$

Figure app.2.1 shows the calculated reaction rate for increasing grid currents, assuming a gas pressure $p_{\mathrm{gas}} = 0.2$ Pa ($n_{\mathrm{gas}} \approx 10^{19}$ m^{-3}) and an embedded deuterium density in the cathode grid $n_{\mathrm{emb}} = 1 \cdot 10^{25}$ m^{-3}. The calculation is described in appendix .

Typically, fusors are operated with tens to hundreds of milliamperes of current, for which beam-beam fusion is negligibly low. In the analysis, the contributions of beam-gas and embedded fusion differ by one order of magnitude, however, it must be stressed that tuning of the free parameters, for example the embedded density, can lead to significant shifts in the reaction rate. Whether embedded fusion plays a dominant role in fusors is unclear because results in literature vary. Measurements from Krupakar Murali show that beam-gas fusion and collisions between neutralised fast ions with gas particles are the dominant contribution to the reaction rate [120], whereas a recent publication by Bowden-Reid suggests that 80%

of the fusion rate originates from the grid surface [121]. Preliminary results from the TU/e fusor show no evidence of a large contribution from embedded fusion and it is not further considered in the remainder of this thesis.

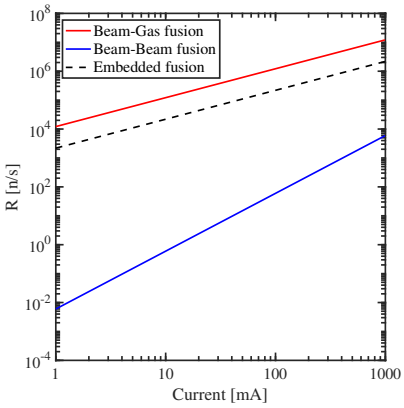

Figure B.1.2: Estimated reaction rate for beam-beam, beam-gas and embedded fusion. Beam-beam fusion is negligibly low for fusor typical currents of tens to hundreds or milliamperes. Whether embedded fusion plays a dominant role is not fully understood and requires further research. The model used to calculate the reaction rate R is described in appendix .

In theory, thermal fusion can also play a (significant) role in a fusor: The central potential focusses ions to the centre of the cathode, where one or more virtual electrodes can form. In the resulting potential structure a thermal plasma can be confined. More information is provided in section B.2.1, including a visual representation of the potential structure in figure B.2.2. For the confinement of a thermal plasma with a significantly contributes to the reaction rate, potential wells with tens of keV are required. These have experimentally not been observed and thus thermal fusion is neglected for the remaining discussion.

B.1.2 Applications and global research

Even though, as Rider showed, fusors are likely not suitable as a fusion power plant because bremsstrahlung losses are prohibitively large and thermalisation of the fuel leads to too high fast-particle losses [28], a number of industrial applications are foreseen as a compact neutron generator. Some applications are shown in figure B.1.3. Noteworthy developments are a compact landmine detector [122] and PHOENIX*, a spin-off from the IEC research department in Wisconsin-Madison, which after research on fusors shifted to the production of linear accelerators producing up to $3 \cdot 10^{11}$ n/s.

*https://phoenixwi.com

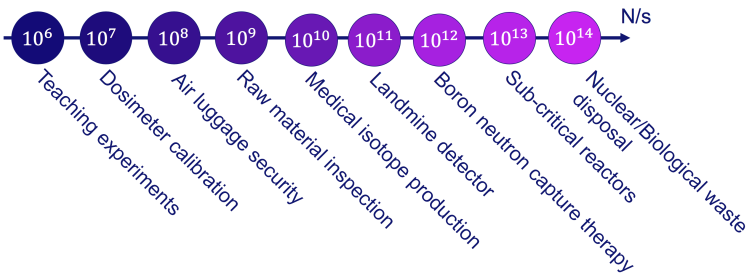

Figure B.1.3: Industrial applications for various neutron fluxes. Currently fusors can produce up to 10^9 neutrons / s.

The main research contributors to field of IEC are the Tokyo Institute of Technology, the university of Wisconsin-Madison, the university of Illinois and the university of Sydney. A summary of fusor research until 2014 is given in a book by Miley and Krupaker Murali [123]. Selected research topics of the different groups are:

Tokyo Institute of Technology Four IEC devices, a spherical, a cylindrical, a coaxial double cylinder, and a magnetically assisted device were built [124]. Yamauchi et al. developed a pulsed system for landmine detection with a maximum neutron yields of $2 \cdot 10^8$ n/s [122].

University of Wisconsin-Madison The University of Wisconsin-Madison is running a fusor program since 1991. The group developed the eclipse disk diagnostic with which the source of D-^{3}He fusion was determined to be embedded fusion and D-D fusion was determined to originate from volume processes [125]. The group also built a steady-state D-^{3}He reactor producing up to $7 \cdot 10^6$ protons/s [126].

University of Illinois The group at the University of Illinois has been exploring the viability of IEC devices as space thrusters for over 20 years [127, 128, 129] and as part of their fundamental research on IEC devices was able to measure the formation of a virtual cathode within the inner grid [130].

University of Sydney Amongst other research, the IEC group in Sydney did a variety of research on Polywell type devices, in which electrons get confined to form a virtual electrode [131, 132].

B.1.3 Performance limitations of IEC devices

The IEC theory assumes that ions are confined on oscillatory trajectories by static electric fields until they collide with the grid, get neutralised, or fuse. To gain a better understanding of the severity of different loss mechanisms, the mean free path $\lambda_{\text{mfp}} = 1/(\sigma n)$, and from it the number of possible oscillations, is estimated for them. For the calculations, the parameters of a typical discharge at the TU/e fusor are taken: pressure $p = 0.2$ Pa (from which the density is calculated to $n \approx 3.6 \cdot 10^{19}$

m^{-3}), applied potential $U = -50$ kV, fusor radius $r_f = 25$ cm, cathode radius $r_c = 5$ cm, grid transparency $\eta = 95\%$, and a partially ionised plasma within the cathode grid with 1% ionisation degree and a temperature of 1 eV.

Mean free path for fusion collisions:
The mean free path until a fusion reaction occurs is calculated under the assumption that the dominant fusion process is the collision of fast ions with gas particles. For a kinetic energy $E_{\text{fast}} = 50$ keV, the cross section is $\sigma = 1 \cdot 10^{-30}$ m^2, resulting in $\lambda_{\text{fusion}} \approx 2.8 \cdot 10^{10}$ m, or the equivalent of $N_{\text{pass}} = 5.6 \cdot 10^{10}$ passes through the fusor at maximum energy. Note that N_{pass} is a low estimate since not all ions reach the maximum energy (resulting in a lower cross section), and also ions are only at their maximum energy while transversing the grid.

Grid losses:
With a grid transparency of $\eta = 95\%$ an ion can make statistically $\Gamma = \eta/(1-\eta^2) \approx 10$ oscillations before colliding with the grid. Note that here only the geometric transparency is considered and effects such as micro channeling are neglected, which can lead to higher effective transparencies [133].

Neutralisation via charge exchange:
From the ALADDIN database [134], the cross section for the reaction $H^+_{2,\text{fast}} + H_2 \rightarrow H_{2,\text{fast}} + H^+_2$ is evaluated[†]. To provide an upper estimate for the mean free path, the lowest cross section $\sigma_{\text{min}} = 1.55 \cdot 10^{-20}$ m^2 for ion energies between $E_{H^+_2} = 1 - 50$ keV is used for the calculation. With this, $\lambda_{\text{mfp}} = 1.8$ m. Thus, before an ion is neutralised it can do at most ≈ 3.5 oscillations. Note that ions spend a significant time at low energies, for which the cross section is higher.

Thermalisation via Coulomb scattering:
During every oscillation the fast ions travel through the cathode region where a weakly ionised plasma exists. With the made assumptions, and following the approach of Freidberg (ch. 9) [8], the energy loss over time $\mathrm{d}E/\mathrm{d}t$ of a 50 keV deuterium ion passing through a 1 eV plasma with density $n_e = n_i = 0.01 \cdot n_{\text{gas}}$ is calculated.
It is assumed that an ion does no longer contribute to the reaction rate once the fusion cross section drops by a factor of 10 from the initial cross section at $E_{\text{ion}} = 50$ keV, which happens after the ion has travelled a distance of 1.05 m through the plasma. Assuming the plasma is approximately confined within the cathode grid ($2 \cdot r_c = 0.1$ m path length per oscillation), approximately ≈ 10 oscillations are possible until the ion has thermalised.

Unfavourable ion birth radius:
For the estimation of the mean free path it is assumed that ions travel constantly

[†]From the considered reactions the charge exchange collision has the highest cross section.

at $E_{\mathrm{kin}} = 50$ keV. Besides the fact that ions only reach the full potential energy after accelerating from the anode to the cathode, spectroscopic measurements show that the majority of the ions do not accelerate through the full potential and only reach a low velocity when arriving at the cathode. The peaking of the ion birth radius close to the cathode is modelled in section B.2.3. In summary, the peaking is caused by the increasing ionisation cross section for collisions between ions and neutrals with increasing ion energies, and the decreasing ionisation cross section for collision between electrons and neutrals with increasing energies.

These estimates show that the basic principle of an IEC device, the assumption that ions move on oscillatory trajectories through the device only holds for few oscillations. The majority of the ions is created close to the cathode and cannot reach the full potential energy and ions with larger birth radius will quickly thermalise or neutralise through charge exchange collisions.

B.2 Influence of experimental and geometric parameters on the fast ion distribution in IEC devices

Messmer M.C.C., Rouwette S.M.M., Huisman A., Alers B., Hermans E.C.G., Oosterbeek J. W., de Jong H.M.M. and *Jaspers R.J.E*

This chapter will be submitted to Fusion Science and Technology

Abstract:
Fusion machines based on the concept of inertial electrostatic confinement have long attracted interest due to their simple design, however, elevating fusion rates to industry relevant levels proves to be difficult. The fusion group at TU/e has set up an IEC device in 2013 to study the performance-limiting physics experimentally and theoretically. This device has the classical fusor configuration, i.e. a spherical vacuum vessel (radius 25 cm) in which a single spherical grid (radius 5 cm, variable) is centred. The grid is at a negative potential (0 to -100 kV) w.r.t. the vacuum vessel, accelerating ions towards the centre of the device. In this article we present experimental and modelling results aimed at increasing the fast ion population. To gain a better understanding of the ion velocity distribution, the influence of experimental parameters (pressure, grid potential, grid radius) on the ion birth radius is modelled. The model shows a reduction of the number of slow ions for decreasing pressures, resulting in more current being available for fast particles. This scaling is verified experimentally by achieving so-called star-mode operation at, for our device, atypically low pressures, made possible by the injecting of ions at the anode. Here, a tripling of the neutron production rate is recorded. Other predictions made by the model are a marginal influence of the cathode potential on the ion birth radius and an increase of fast ions with increasing grid radius. An important component of IEC experiments is the stalk, connecting the grid to the power supply. Simulation of ion trajectories show that the concept of oscillating ions in the fusor does not hold if the stalk is not insulated (in this case the majority of the ions collide with the stalk), and we show that radial symmetry of the electric field is restored by dielectric shielding of the stalk. This is explained by charging-up of the insulator until the symmetry of the vacuum potential is restored.

B.2.1 Introduction

Inertial electrostatic confinement (IEC) devices, commonly referred to as fusors, are designed to accelerate, collide and confine ions using static electric fields. The design was proposed and patented by Farnsworth [20] and first built by Hirsch [21] in 1960 and 1967, respectively. The schematic of a fusor is shown in figure B.2.1. Fusors consist of a (typically) spherical vacuum vessel, which is electrically grounded. A spherical grid, which is connected to the cathode of a power supply through the high voltage feedthrough, the stalk, is centred in the vacuum vessel. The vacuum vessel is filled with the fusion fuel (e.g. deuterium gas) at low pressures. Plasma breakdown occurs when a high enough negative potential is applied to the grid, leading to the acceleration of ions towards the centre, and the acceleration of electrons towards the vacuum vessel.

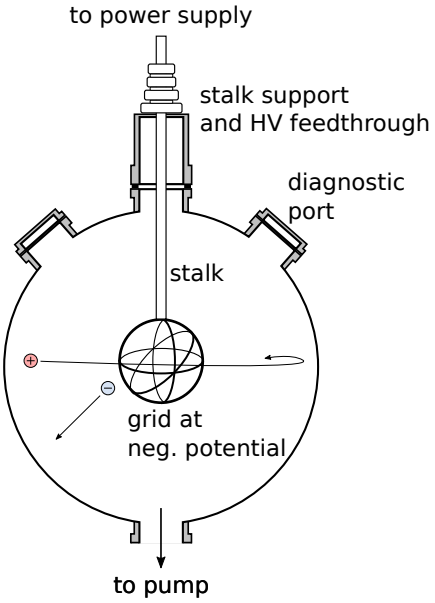

Figure B.2.1: Basic anatomy of a fusor: Within a grounded vacuum chamber a transparent grid is connected to the cathode of an external power supply. Ions are accelerated towards the centre of the device and may begin an oscillatory motion if they do not collide with the grid. Fusion reactions can occur through ion-ion or ion-gas collisions.

The number of fusion collisions R occurring per unit time of two colliding, monoenergetic species with densities n_1 and n_2 and relative velocity v is:

$$R = \int n_1 \cdot n_2 \cdot \sigma(v) \cdot v \cdot dV, \tag{B.2.1}$$

where $\sigma(v)$ is the velocity dependent cross section and the volume V depends

on the fusion mechanism. Above equation only holds for constant velocities, a more precise definition must take the velocity distribution into account, too. The densities depend on the participating reactants. The reactions occurring in a fusor can be grouped into five different categories:

Beam–Beam fusion (BB): Two accelerated ions collide (inside the cathode) and fuse. The reaction rate for beam-beam fusion is proportional to the square of the fast ion densities: $R \propto n_{\mathrm{i,f}}^2$. The fast ion density $n_{\mathrm{i,f}}$ is estimated by assuming all ions are focussed to a sphere of 5 mm radius inside the cathode [130]. Then, for an ion current $I_{\mathrm{ion}} = 100$ mA and cathode potential $U = -100$ kV, $n_{\mathrm{i,f}} = I/(evA) \approx 6.5 \cdot 10^{14}$ m^{-3}. Compared to a typical gas pressure $p \approx 0.2$ Pa in the fusor, the fast ion density is 5 orders of magnitude lower than the neutral density, making BB fusion negligible except for very high currents.

Beam–Gas fusion (BG): An accelerated ion collides with a neutral gas particle and they fuse. For BG fusion, the reaction rate is proportional to the fast ion density $n_{\mathrm{i,f}}$ and the gas pressure, which determines the density of neutrals n_{gas}: $R \propto n_{\mathrm{i,f}} \cdot n_{\mathrm{gas}}$. Due to the large value of n_{gas} compared to $n_{\mathrm{i,f}}$, beam-gas fusion is expected to make a large contribution to the total reaction rate.

Fast neutral–Gas (FN-G): An accelerated ion gets neutralised through a charge exchange collision, the resulting fast neutral collides and fuses with a gas particle. If the mean free path for charge exchange reactions $\lambda_{\mathrm{mfp}} = 1/(n_{\mathrm{gas}} \cdot \sigma_{cx})$ is on the order of, or shorter than the radius of the fusor, FN-G fusion can contribute significantly to the reaction rate, as the distance that fast neutrals travel is similar to the distance they have travelled as ions.

Embedded fusion: A high-density of the fusion fuel can accumulate in the cathode, stalk and wall of the vacuum vessel through ion bombardment, absorption and adsorption. Fast ions or neutrals colliding with the solid targets can fuse with embedded or adsorbed fuel. The reaction rate is proportional to the embedded density n_{emb} and the flux of ions hitting the target material. Depending on n_{emb}, embedded fusion can make a substantial contribution to the reaction rate. Preliminary results at our fusor showed no indication that embedded fusion makes substantial contribution to the reaction rate at our device and it is not further considered in this article.

Thermal fusion: At high currents, virtual electrodes can form inside the cathode grid, leading to a single or double potential well, illustrated in figure B.2.2. This process was postulated by Hirsch [21] and measured by Nadler and Miley [135, 136]. The virtual electrodes can confine a thermal plasma, which, depending on the plasma temperature, could contribute significantly to the reaction rate. In this article thermal fusion is neglected because we do not see evidence that it plays a significant role in our experiments. Spectroscopic measurements show no indication of a high temperature thermal plasma. Fitting a thermal distribution to the Doppler-broadened Balmer-α peak in our experiments has resulted in plasma temperatures of a few electron volt.

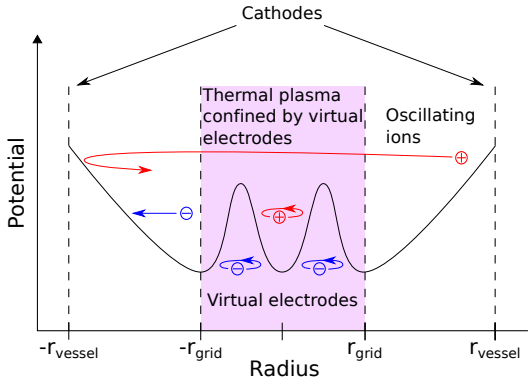

Figure B.2.2: Illustration of the potential structure in a fusor, including a double potential well inside the cathode grid formed by virtual electrodes. The virtual electrodes form due to the central vacuum potential, which focusses the ions to the centre of the cathode. A thermal plasma can be confined by the virtual electrodes, which, if at sufficient temperature, can contribute significantly to the fusion rate.

With this in mind, the operating principle of a fusor can be described as follows: if the applied potential is high enough, plasma breakdown occurs and ions get accelerated to the energy of the potential difference between anode and cathode. Reaching the centre, they fuse via one of the processes listed above. Due to the spherical symmetry of the device, all ions converge to the centre of the device. The ions which do not collide with the grid will oscillate through the device until they fuse, collide with the grid, or get neutralised via charge exchange.
Assuming BG or FN-G fusion is the dominant process, the fusion yield scales linearly with the background pressure since both reaction rates are proportional to n_{gas}.

However, experiments and simulations performed in our group show that the actual operation of a fusor is quite different from the simple picture:

- Spectroscopic measurements and modelling of the ion birth radius presented in section B.2.3 show that the bulk of the ions is created in the vicinity of the cathode and do not accelerate through the full potential. This leads to a low energy distribution of the ions, which will have a low fusion cross section. From the model we learn that the ion birth radius can be influenced by varying the applied potential, the gas pressure, or the cathode radii, however, these actuators are limited in their effectiveness.

- Due to the linear scaling of the reaction rate with the gas pressure, the fusion rate is expected to increase with increasing pressure. By installing an ion source at our fusor we are able to reduce the pressure at which plasma breakdown occurs, with the added ions acting as a kick-start for the plasma formation. Against expectations, the unlocked low-pressure regime shows

a tripling in the reaction rate. The results are presented and interpreted in section B.2.4

- Due to the stalk, which is at the same potential as the grid, the radial symmetry of the electric field is broken. We will demonstrate that a large fraction of the ions is accelerated towards the stalk and only ions created in the midplane are able to oscillate, if the stalk is not insulated by a dielectric. Simulations of the ion trajectories and experimental comparison of an insulated vs. a non-insulated stalk are presented in section B.2.5.

Before discussing the results of the experiments and simulations, a description of our experimental setup is given in B.2.2.

B.2.2 Experimental setup

Fusors have been built in a number of universities, for example the University of Wisconsin [22], Sydney [23], Kyoto [24], the MIT [25], and by numerous amateurs (including 12-year olds) [26]. The TU/e fusor was built in 2013. The current setup of the fusor lab is shown in figure B.2.3 and has the following specifications:

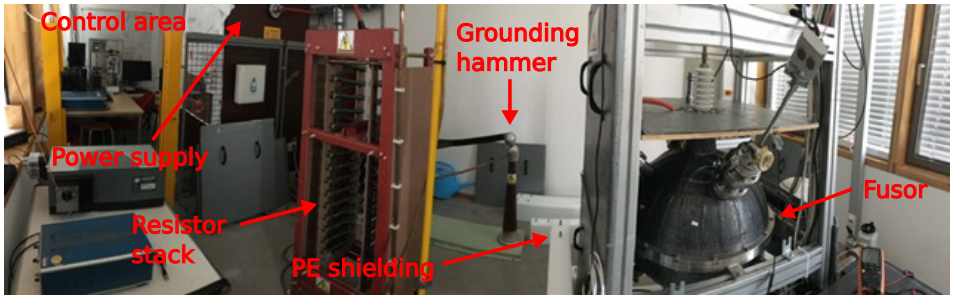

Figure B.2.3: View from within the fusor lab. Visible are the control area and safety fence, the power supply, resistor stack and grounding hammer, as well as the fusor and the disassembled polyethylene (PE) shielding. The PE shielding was disassembled when the picture was taken and normally surrounds the fusor on all sides which are facing the building.

Vacuum vessel

The vacuum vessel of the fusor is double walled with inner radius $R_{\text{in}} = 250$ mm and outer radius $R_{\text{out}} = 263$ mm. A water-cooling system is available to cool the vessel by pumping water through the double wall. The vessel has 10 access ports of which the top and bottom port are reserved for the high voltage feedthrough and vacuum pump, respectively.

Power supply and stalk

The power supply can supply a maximum of 12 kW at $U_{\text{max}} = -120$ kV. A 210

kΩ ballast resistor is connected in-series between the fusor and power supply to stabilize the discharge.
The design of the stalk connecting the cathode with the power supply is shown in figure B.2.4. The grid is connected to a stainless-steel pipe which is slid over a 5 mm steel rod. A spring is mounted inside the pipe, clamping the two together. The spring is tight enough for the pipe to be suspended on the rod but flexible enough to allow a manual translation of the grid. A quartz glass cylinder can be slid over the pipe for electrical insulation.

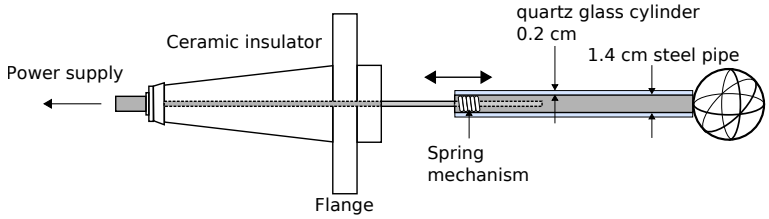

Figure B.2.4: Schematic drawing of the stalk and high voltage feedthrough of the TU/e fusor. All current carrying elements are drawn in grey. The power supply is connected to a copper tube outside the fusor. A ceramic insulator prevents arcing between the copper tube and the vacuum vessel. On the inside, a stainless steel rod with ⌀5 mm is attached to the copper tube. A steel pipe on which the grid is attached is slid over the rod. The rod and pipe are held together by a spring mechanism mounted inside the pipe, allowing the grid to be moved up and down to adjust for different grid sizes. A cylinder made out of quartz glass can be added to insulate the stalk.

Neutron detection and neutron shielding
The neutron counts are registered by a Boron-Trifluoride neutron counter and digitally recorded. The neutron counter is mounted in the midplane of the vacuum vessel. The neutron detector was calibrated with an Am^{241}-Be reference source. For the calibration the source was placed in a thin plastic gripper arm and lowered into the centre of the fusor to the position where the grid is normally placed. It is assumed that both the reference source and the fusor radiation are isotropic. The calibration factor is determined from the known total radiation of the Am^{241}-Be source and the measured neutron counts by the detector.
For radiation protection of the experimentalist, the fusor is surrounded by 10 cm thick blocks of polyethylene (which is almost completely disassembled in figure B.2.3). Furthermore, the vacuum vessel is covered in a lead blanket to absorb x-ray radiation produced by the fast electrons impacting on the vacuum vessel.

Diagnostics
The available diagnostics are the already described neutron detector, a webcam for optical observation of the plasma and a spectrometer. The spectrometer has F/6.5 aperture, a 1200 lines/mm grating and an entrance slit width of 50 μm, resulting in a maximal resolution of 0.06 nm. The experimental parameters are

digitally recorded for each discharge. The pressure is obtained from a pressure gauge, current and potential are directly read-out from the power supply.

Operating regimes

The fusor can be operated in three distinct operation modes called glow-, jet- and star-mode, which have also been reported on other IEC devices [123]. The three modes are shown in figure B.2.5.

(a) Glow-mode: occurring for pressures of tens of pascal to ≈ 0.5 Pa

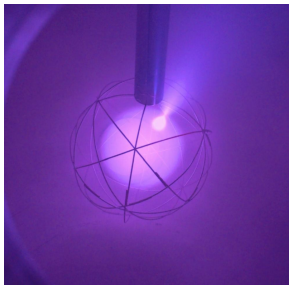

(b) Jet-mode: occurring for pressures of several pascal to ≈ 0.5 Pa

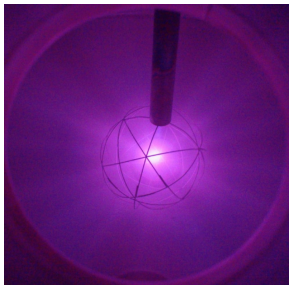

(c) Star-mode: occurring for pressures ($\lesssim 0.5$ Pa)

Figure B.2.5: The operating modes of the fusor are depending on the pressure inside the vessel. Star-mode is most commonly used in experiments, because here the highest neutron production rate can be achieved.

Similar to other IEC devices, the operation mode depends on the gas pressure. At high pressures, a uniform glow discharge from the emission of neutralised or excited hydrogen, in and around the cathode grid, is observed. This regime is called glow-mode. If the pressure drops, the discharge switches to jet-mode. In addition to a uniform glow inside the grid a single intense jet-like emission is observed. The jet is exiting the grid at the largest opening and is explained by electrons leaving the cathode region, forming a virtual cathode, dragging ions along with them [137, 138]. Further decreasing the pressure leads to star-mode, the switch occurs around 0.5 Pa. In star-mode a bright glow is observed in the centre of the grid and spokes of light emerge through the grid openings. The spokes have been attributed to ions, which are confined on oscillatory trajectories due to focusing caused by electric field inhomogeneities between the grid wires [123].

In our experiments, the highest fusion rates were achieved in star-mode, which is accessible for pressures between 0.15 Pa $\lessapprox p \lessapprox 0.5$ Pa over a large range of grid potentials and currents. An overview of the parameter space is given in figure B.2.6.

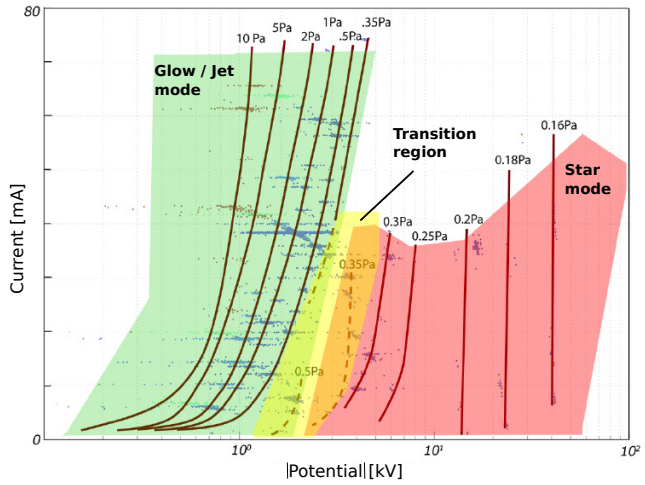

Figure B.2.6: Operation range of the TU/e fusor, provided by A. J. Wolf. Plotted are value pairs of (U,I) where plasma breakdown occurs, grouped by the set gas pressure. For pressures above 0.5 Pa the discharge is in glow- or jet-mode, for pressures below 0.5 Pa star-mode is accessible. Around 0.5 Pascal a transition region exists where all modes can be achieved depending on the grid potential and current.

B.2.3 Modelling the ion birth radius and current contributions

Model description

To increase the ion energy, and thus the fusion cross section and reaction rate, it is advantageous if gas particles get ionised close to the vessel wall. These ions accelerate through the full electric potential and reach the maximum possible energy. Unfortunately, this is not the case for most ions. Figure B.2.7 (a) shows the recorded spectrum of a hydrogen discharge with $U = -45.2$ kV.

The central peak at the Balmer-α wavelength, $\lambda_{B\alpha} = 656.28$ nm, originates from emission of the plasma in the cathode grid (compare with figure B.2.5 (c)). The line broadening stems from Doppler-shifted B_α emission of fast ions neutralised in the cathode. Marked in the figure is the maximum possible Doppler shift $\Delta\lambda_{\max}$ for H_2^+ which has accelerated through the full potential. The intensity at $\Delta\lambda_{\max}$ is close to the background noise; only a small fraction of the ions are accelerated through the full potential. In contrast, figure B.2.7 (b) shows the calculated spectrum for the (ideal) case where all ions gain the full potential energy. The spectrum is calculated under the assumption of a uniform angular influx of ions into the cathode, and that neutralisation and emission are a point source in the centre of the grid. The spectra is calculated from the non-relativistic Doppler-shifted wavelength λ_{DS}:

$$\lambda_{DS} = \lambda_{B\alpha}\left(1 - \beta\cos\theta\right), \tag{B.2.2}$$

with unshifted Balmer-α wavelength $\lambda_{B\alpha}$, $\beta = v/c$, ion velocity v, speed of light c, and the viewing angle between the line of sight and ion trajectory $\theta \in [0,360]°$ ($\theta = 0°$ corresponding to the case where the ion is moving away from the observer). The peaking at $\pm\Delta\lambda_{\max}$ results from the slope of the cosine whose gradient is lowest for $\theta \to 0$ (corresponding to $\lambda_{DS} \to \lambda_{B\alpha} \pm \Delta\lambda_{\max}$).

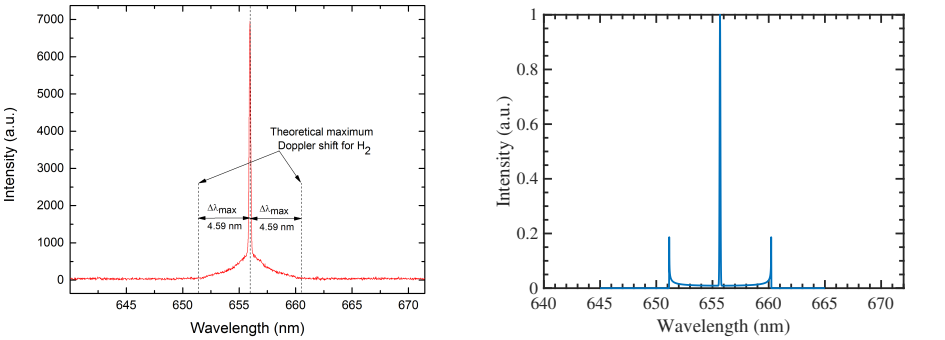

(a) Recorded spectrum

(b) Calculated spectrum for a mono energetic ions distribution and a thermal plasma

Figure B.2.7: Left: Spectrum of a hydrogen discharge with gas pressure $p = 0.13$ Pa and applied potential $U = -45.2$ kV. The central peak originates from emission of the low temperature plasma in the cathode region, the spectral broadening is caused by emission of neutralised fast ions. Right: Calculated spectrum for the case that all ions are created at the edge of the vacuum vessel and reach the centre with $E_{\text{kin}} = eU$. The doppler shifted emission is calculated under the assumption of a uniform angular distribution of ions. The central B-α peak is calculated for a 1 eV plasma. Note that the graph is normalised to the thermal emission, which has been arbitrarily scaled to be 5x higher in intensity than the maximum of the doppler shifted spectrum.

Not only the velocity distribution of the ions is unknown, but also their current. Only the total current measured at the power supply is known. According to Krupakar Murali, the oscillating ion current can be estimated from the measured current I_{meas} [139] via:

$$I_{\text{ion}} = \frac{\eta(I_{\text{meas}} - I_{\text{th}} - I_{\text{p}} - I_{\text{f}})}{(1-\eta^2)(1+\gamma)}. \tag{B.2.3}$$

Here, I_{ion} is the current of oscillating ions, I_{th} the thermic emission of the grid, I_{p} the photoemission of the grid, I_{f} the field emission, η the grid transparency and γ

the secondary electron emission (SEE) coefficient of the grid material. Equation B.2.3 gives an estimate of the oscillating ion current, but does not provide any information about the velocity distribution and, as we will see later, neglects an important contribution to the measured current.

No further experimental results or theoretical predictions of the ion velocity distribution and current fractions are found in literature. Therefore, a model based on the theory developed by Emmert and Santarius [140, 141] was created to determine the influence of experimental parameters on the ion birth radius, and understand how the individual current fractions contribute to the total current. Their formalism describes the interaction between ions and a neutral gas for the case of nearly transparent electrodes. We extended the original work with a more precise and self consistent model of the cathode current and temperature [142]. A full description of the original model from Emmert and Santarius is out of the scope of this article, but a summary is provided.

The model by Emmert and Santarius describes the ion flow between two nearly transparent electrodes in a spherical geometry. It assumes two classes of ions: Class I ions, which are created close to the vacuum vessel and class II ions, which are created by charge exchange or ionisation interaction of class I ions with the background gas. Class II ions may oscillate until they hit the cathode grid or have a collision with the background gas, while class I ions are considered lost after they reach the vessel opposite of their origin. Collisions between class II ions and the background gas lead to the next generation of class II ions, thus the model sums over an infinite number of passes and generations to obtain the total ion density. The model result is the source function S_f, radially specifying the number density of D^+ and D_2^+ ions created per incoming class I ion.
Our analysis extends the original work, by analysis of the ion birth radius and an extension of the model by including a self-consistent current model, including the thermal effect of the cathode.
Shortcomings of the model are the fixed electric potential at the vacuum value, i.e. no potential well inside the cathode is considered, and that no ionisation or neutralisation of ions through electrons are considered (similar to the original work). These are neglected because electrons gain energy quickly when leaving the cathode due to the inverse square scaling of the electric field. As a result, the cross section for ionisation and dissociation through electron collisions quickly drops below the corresponding ion-gas collisional cross sections for energies above 1 keV (see figure B.2.27).

The modelled interactions, the implemented current, and the temperature model are in detail described in appendix B.2.7. At this point only the results are presented, namely the scaling of the ion birth radius and an analysis of the current contributions. For the analysis, a nickel cathode (work function $W = 5.2$ eV) with 98% effective transparency is used in the model. The background gas is D_2 with an initial class I ion distribution of 10% D^+, 30% D_2^+ and 60% D_3^+ (taken from

[143]). The gas temperature is $T_{\text{gas}} = 300$ K. Due to limitations of the model, it is not known whether plasma breakdown occurs for the used parameters. Also, asymmetries in the electric field caused by the stalk are not included in the model. Analysed is the dependence of S_f on the grid potential, background pressure and cathode radius.

Results I: Dependence of S_f on the grid potential

Figure B.2.8 shows the source function S_f of D^+ and D_2^+ for varying cathode potentials at constant pressure $p = 0.5$ Pa, cathode radius $r_c = 5$ cm and fusor radius $r_f = 25$ cm. For both species S_f depends only weakly on the applied potential and drops quickly outside the cathode. With rising potentials a minor shift of S_f towards larger radii is observed, explained by the increased cross section for ion induced ionisation. From figure B.2.8 a small fraction of fast ions is expected, consistent with the spectroscopic measurements shown in figure B.2.7.

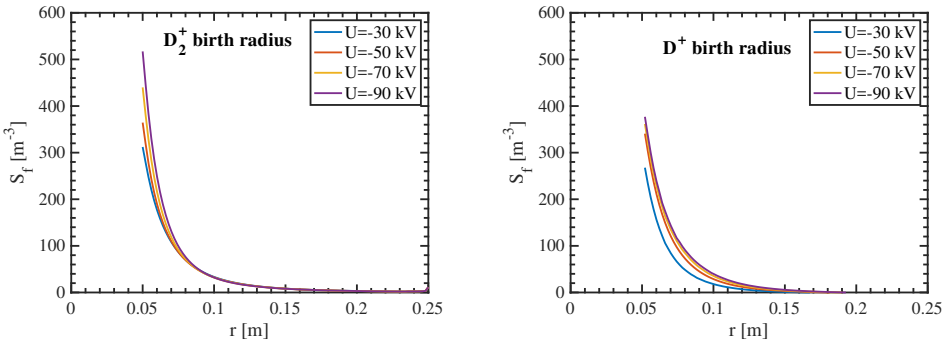

(a) D_2^+ source function for varying potentials

(b) D^+ source function for varying potentials

Figure B.2.8: Dependence of the ion birth radius for D_2^+ (left) and D^+ (right) on the grid potential U. The source function depends only weakly on the applied potential. Higher potentials are favourable because at similar birth radii the ions can reach higher energies increasing the fusion cross section.

From the model the individual contributions to the total current are obtained, shown in figure B.2.9. At low potentials, the dominant contribution to the total current is secondary electron emission, caused by D_3^+ ions hitting the cathode. With increasing potential, an increasing number of slow ions is created in the cathode region due to the increased cross section for

$$H_2^+ + H_2 \rightarrow 2H_2^+ + e, \tag{B.2.4}$$

making slow ion impact the dominant current contribution for $|U| > 50$ kV.
Overall, only a small fraction of the current is caused by the collision of fast ions

with the cathode and most of the available current is used by slow ion impact and secondary electron emission.
Comparing the results from figure B.2.9 to the relationship between the measured and fast ion current derived by Murali (see equation B.2.3), our results show that neglecting the slow ion current in Murali's work leads to an overestimation of the fast ion current.

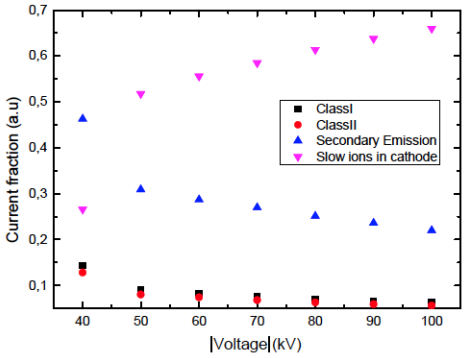

Figure B.2.9: Dependence of the four dominant current fractions on the grid potential. With increasing potential more slow ions are created inside the cathode due to the increasing ionisation cross section. The slow ions take up a large fraction of the total current, reducing the number of fast particles.

Results II: Dependence of S_f on the pressure

The pressure dependence is analysed at a grid potential $U = -50$ kV and the cathode and fusor radius are again $r_c = 5$ cm and $r_f = 25$ cm, respectively. S_f for D^+ and D_2^+ is shown in figure B.2.10.
With increasing pressure the total number of ions is increased due the reduced mean free path $\lambda_{\text{mfp}} = 1/(\sigma n(p))$. Increasing pressures result in an increase of the absolute number of ions created at larger radii. However, the large fraction of slow ions will take up a large fraction of the available total current I_{tot}. Experimentally it is observed that the NPR drops significantly for $p > 0.3$ Pa because the current limit of the power supply is reached which subsequently limits the grid potential because the total power is limited (see section B.2.4 for a detailed description).
To provide more qualitative insight, the area normalised source function $\left(\int_{r_c}^{r_f} S_f = 1\right)$ is plotted in figure B.2.11. This is motivated by the fact that the total current in the fusor is limited and the large amount of class II ions for increasing pressures is likely not sustainable by the power supply. The normalised source function shows a (weak) favourable shift of the ion birth radius for $r \gtrapprox 0.08$ m with decreasing pressures.

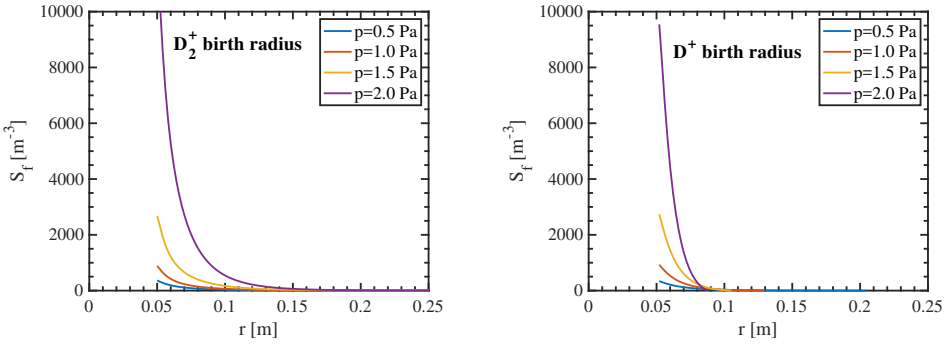

(a) D_2^+ source function for varying pressures **(b)** D^+ source function for varying pressures

Figure B.2.10: Pressure dependence of the ion birth radius. Left: source function for D_2^+, right: source function for D^+. The total number of ions increases with pressure due to the reduced mean free path for ionisation collisions.

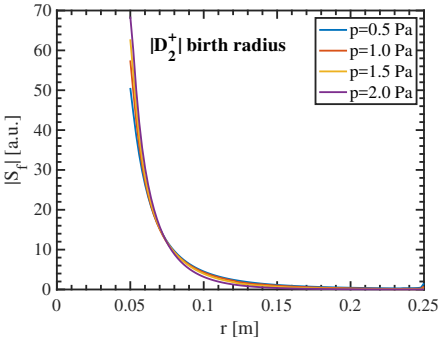

Figure B.2.11: Normalised D_2^+ birth radius: The source function is normalised such that $\int_{r_c}^{r_f} S_f = 1$, motivated by the limited total current. The minor shift of S_f to larger radii is likely insignificant in experiments.

The dependence of the current fractions on the pressure is plotted in figure B.2.12. Similar to the potential scan, the dominant contributions to the current are the secondary electron emission and slow ions current. The slow ion contribution increases with pressure due to the reduced mean free path $\lambda_{\text{mfp}} \propto 1/p$. For low pressures the class I & II current increases and a favourable scaling of the NPR.

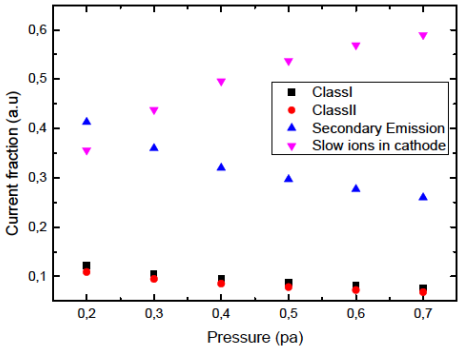

Figure B.2.12: Scaling of the current fractions for varying pressure. Higher pressures reduce the mean free path for ionising collisions, increasing the number of slow ions created in the cathode and thus the slow ion current. An increased NPR is expected at lower pressures due to the increase in class I & II current.

Results III: Dependence of S_f on the cathode radius

Lastly, the effect of varying cathode radii is examined. For the analysis $p = 0.5$ Pa, the cathode potential is -50 kV, and the fusor radius is again $r_f = 25$ cm. To compare different grid radii, the normalised source function ($\int_{r_c}^{r_f} S_f = 1$) is plotted in figure B.2.13 as a function of the ion energy.
For increasing cathode radii, more high energy D^+ and D_2^+ ions are created and an increase in the NPR is expected due to the increased cross section. In addition, with increasing grid radii ions will travel longer at their maximum energy, further increasing the NPR. An increased NPR with increasing cathodes has experimentally been observed by Wehmeyer. In his experiments with a fusor of radius 25 cm, a 20% increase in the NPR was observed when doubling the grid radius from 5 cm to 10 cm [144].

A feature not captured by the normalised source function is a drop of S_f for $r_g = 15$ cm, shown in figure B.2.14. For too large cathode radii S_f decreases, because the distance between grid and vacuum vessel is too short for sufficient ionisation events to occur. This can hinder plasma breakdown in experiments. In fact, in experiments not included in this article we were unable to achieve plasma breakdown using a grid with radius $r_{\text{grid}} = 15$ cm.

The changes in current fractions for varying cathode radius are shown in figure B.2.15. Increasing grid radii result in longer travel distances of ions within the cathode and a consequent increase in the creation of slow ion. Although smaller grid radii provide improvements in the class I & II ion current, the associated decrease of S_f is expected to outweigh the benefits of small grids on the current fractions.

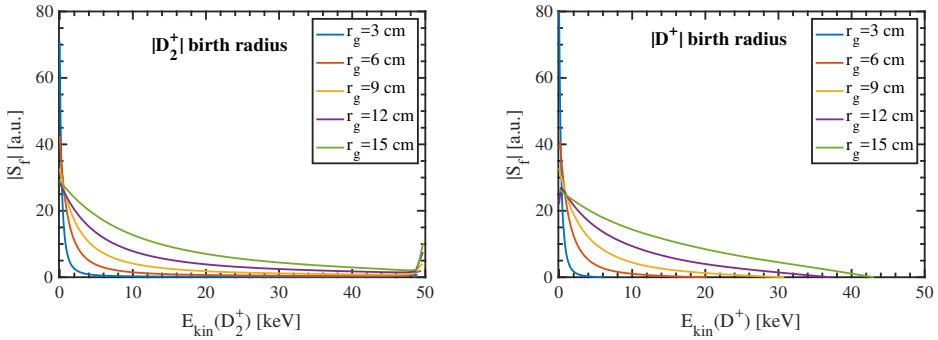

(a) D_2^+ source function for varying r_g **(b)** D^+ source function for varying r_g

Figure B.2.13: Source function for varying cathode radii r_g. To compare different radii, S_f is plotted over the ion energy, calculated from the birth radius. Left: source function for D_2^+, right: source function for D^+. Relatively more fast ions are created with increasing cathode radii. However, as is shown in figure B.2.14, the absolute number of ions drops for too large cathodes, possibly hindering plasma breakdown.

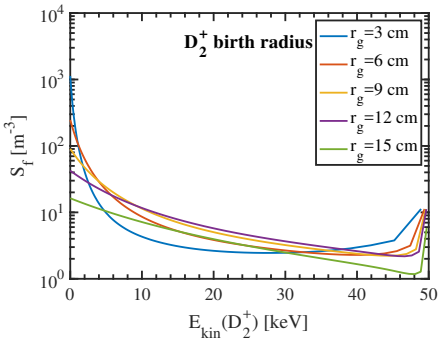

Figure B.2.14: Source function of D_2^+ as a function of the ion energy. $S_f(D_2^+)$ scales favourably for grid radii until $r_g = 0.12$ cm, for larger cathodes the spacing between grid and vacuum vessel is too short for sufficient ionisation reactions to occur and an overall decrease in $S_f(D_2^+)$ is observed.

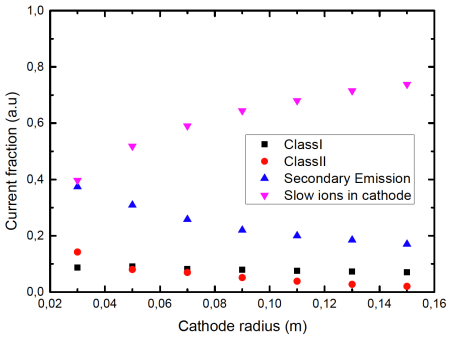

Figure B.2.15: Current fractions for increasing grid radii. The probability of ionising collisions between class I & II ions with gas particles in the cathode grid increases with larger radii, resulting in a higher slow ion current fraction for larger radii. The small improvements in class I & II ion current for smaller radii are not expected to compensate for the shift of S_f to lower energies.

B.2.4 Experimental scaling of the neutron production rate in low-pressure star-mode operation

As discussed in the introduction, if beam-gas or fast neutral-gas fusion are the dominant fusion mechanisms, a positive scaling of the fusion rate for rising background pressures is expected. However, the analysis of the ion birth radius showed an increasing fast ion current at reducing pressures.
To gain further insight, the dependence of the neutron production rate on the gas pressure p, the grid potential U, and the measured current I is investigated experimentally. The results are shown in figure B.2.16. In the graph, the size of the markers placed at (U, I, p) triplets represents the neutron yield, a higher neutron count corresponding to a larger sphere. All neutron measurements are taken in the star-mode operating regime. The figure shows an increased NPR with increasing potential and current, as it is expected from the reaction rate for beam-gas and fast neutral-gas fusion: $R \propto n_{\text{fast}}(I) \cdot v(U)$. Furthermore, the NPR scales favourably with decreasing pressures: Increasing pressures leads to increasing currents, which limit the performance by two effects: First, for too high currents, the grid potential is limited by the power supply, and second, in experiments where a high NPR is expected by the achievable combinations of a high current and a high potential, the grid quickly overheats and thus the NPR could not be measured.
These results are in line with the discussed pressure dependence of the ion birth radius (section B.2.3), where large pressures resulted in a manyfold increase of the total number of ions (limiting the available power), with a birth profile peaked at small radii (resulting in small contribution to R due to their low energy).

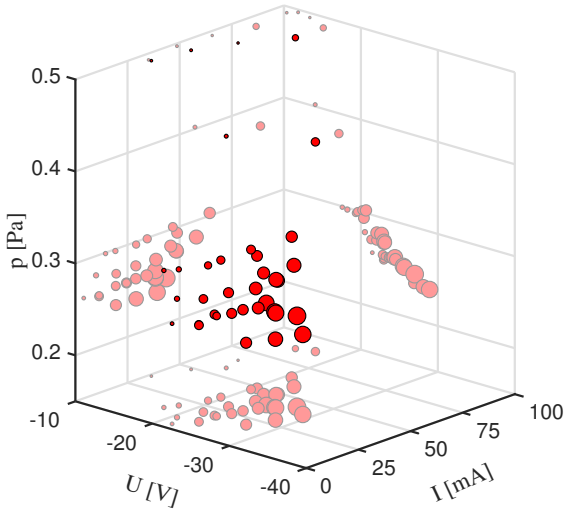

Figure B.2.16: Dependence of the NPR on the potential, current and pressure in star-mode operation. The size of the spheres indicates the relative neutron count; a larger diameter (linearly) corresponds to a higher NPR. Higher NPR's are observed for lower pressures. At large pressures the current limit of the power supply is reached and because the available power is fixed, the grid potential is reduced, subsequently reducing the ion energy which leads to the decreasing NPR.

In the experiments no stable star-mode discharge could be achieved for $p \lessapprox 0.24$ Pa. To extend the available parameter space and explore the scaling of the NPR at low pressures, an ion source has been installed. The commercially available ion source is capable of delivering a current of $6-10$ mA [145]. It is mounted at one of the lower ports, in the line of sight of the spectrometer, shown in figure B.2.17. The additional ions created at large radii (to be treated as class I ions in the model of chapter B.2.3) are expected to a) assist the plasma breakdown and enable star-mode operation at lower pressures; and b) add ions at large radii which will accelerate through the full potential and increase the NPR.

Spectroscopic analysis of fast ions

Prior to measuring the NPR in low pressure star-mode, the shift in the ion birth radius caused by the ion source is analysed. Therefore the fusor is operated at pressures too low for plasma breakdown to occur ($p = 0.13$ Pa for hydrogen, and $p = 0.17$ Pa for deuterium). At these settings a single light emitting beam is observed, originating from the ion source and passing through the grid, and a large fraction of the fast ions is expected to originate from the ion source. Figure B.2.18 compares recorded spectra in hydrogen and deuterium discharges.

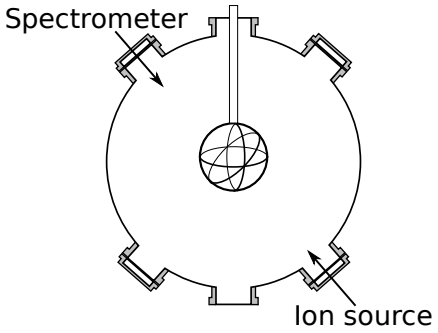

Figure B.2.17: Schematic setup of the ion source. The spectrometer measures the emitted light along the path of the fast ions.

To associate the peaks with particle species, the kinetic energy E_k of ions with atomic mass $m_u = 1,2,3,4$ is calculated from the recorded Doppler shift $\Delta\lambda$ and central wavelength λ_0 as:

$$E_k = \frac{1}{2}mc^2\left(\frac{\Delta\lambda^2 + 2\lambda_0\Delta\lambda}{\Delta\lambda^2 + 2\lambda_0\Delta\lambda + \lambda_0^2}\right)^2. \tag{B.2.5}$$

With this, we have identified peaks "1" and "2" of the hydrogen spectrum to belong to particles of mass H and H_2, respectively, and peaks "1" and "2" of the deuterium spectrum to be consistent with masses of D and D_2, respectively. To ensure that the peaks do truly originate from fast ions accelerating through the full potential, a scan of increasing grid potentials was performed which showed a linear shift of the peaks "1" and "2" with the applied potential, verifying the identified species.

With this knowledge, the hydrogen spectrum of figure B.2.18 can be interpreted. The blue shifted peaks correspond to particles moving from the ion source towards the spectrometer. The H^* emission is likely due to charge exchange processes between accelerated H^+ particles and neutral H_2 background gas. Since Balmer-α emission is only possible for atomic hydrogen peak "2" and it's plateau require the dissociation of H_2^+.
The plateau is interpreted as fast H_2^+ particles colliding with the background gas H_2 while accelerating towards the grid. The reaction with the shortest mean free path is

$$H^+_{2,\text{fast}} + H_{2,\text{bg}} \longrightarrow H^+ + H^* + H_2 \tag{B.2.6}$$

The peak corresponding to $E_{\text{kin}} = e \cdot U_{\text{fusor}}$ is likely due to dissociation of H_2^+ within the cathode region. Inside and surrounding the cathode a plasma is visible from optical observations. In this region, in addition to process B.2.6, the dissociation of H_2^+ through collisions with can H^+ occur:

$$H^+_{2,\text{fast}} + H^+ \longrightarrow H^+ + H^* + H^+ \tag{B.2.7}$$

The spectrum in figure B.2.18 shows that a large fraction of the ions is H_2^+. This can also be observed in a star-mode discharge, see figure B.2.7 (a), and in the model of the ion birth radius, compare figure B.2.8. H_2^+ will have a lower relative velocity at similar grid potentials compared to H^+ and thus a lower cross section. This must be considered in modelling efforts of the NPR.

Neutron production rate in low pressure star-mode operation
With the installed ion source, stable star-mode operation at lower pressures is possible. The previous parameter scan, see figure B.2.16, is extended and the results are presented in figure B.2.19. Again, the marker diameter symbolises the NPR, bigger spheres corresponding to higher NPR. The measurements are categorised into four sets:

red: Star-mode discharges without the ion source (same as figure B.2.16). The maximum measured neutron yield is $(0.50 \pm 0.05) \cdot 10^6$ n/s.

blue: The parameter space of (p, I, U) is similar to the **red** data set, but the

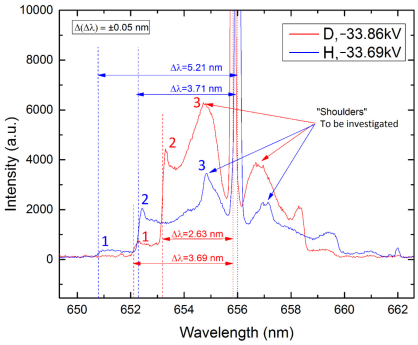

Figure B.2.18: Recorded spectra of a hydrogen and deuterium discharge. The gas pressure is low and only a single beam on the line of sight between the ion source and the spectrometer is visible. The discharge parameters are: a) for the hydrogen discharge: $p = 0.13$ Pa, $U = -33.7$ kV. b) for the deuterium discharge: $p = 0.17$ Pa, $U = -33.7$ kV [146]. The peaks labelled as 1 have been identified to belong to atomic hydrogen and deuterium, the peaks labelled as 2 belong to molecular hydrogen H_2^+ and deuterium D_2^+. Peaks 3 are assumed to originate from water impurities, but further analysis is required. The central wavelength corresponding to the B-α transition differs by 0.29 nm from the literature value for both Deuterium and Hydrogen. The difference between both peaks of 0.18 nm matches the literature, pointing to an error in the absolute calibration of the spectrometer. The calibration error is not further investigated since only relative wavelength measurements will be used.

ion source is operated at the maximum power. The maximum measured NPR is $(0.76 \pm 0.06) \cdot 10^6$ n/s. With higher currents the grid was observed to glow white-hot and is expected to melt at prolonged operation, which limits the available parameter space.

green: The ion source is used at low power. Its primary use is the stabilisation of the plasma in discharge regimes otherwise inaccessible. Without the ion source, star-mode either can't be achieved at all or is unstable, characterised by rapid drops in the current and an optical observed flickering of the discharge. In this region of the parameter space higher than usual voltages can be reached and the neutron yield is increased. The maximum measured NPR is $(1.43 \pm 0.34) \cdot 10^6$ n/s.

cyan: The pressure in the cyan data set is further reduced. Star-mode breakdown does not occur for potentials below 55 kV. For lower potentials only a single beam, originating from the ion source, is visible. The maximum measured neutron yield was $(0.88 \pm 0.34) \cdot 10^6$ n/s. At potentials below -60 kV arcing is observed and no stable discharge was achieved, limiting the recorded NPR. For pressures below 0.1 Pa no stable discharge could be achieved.

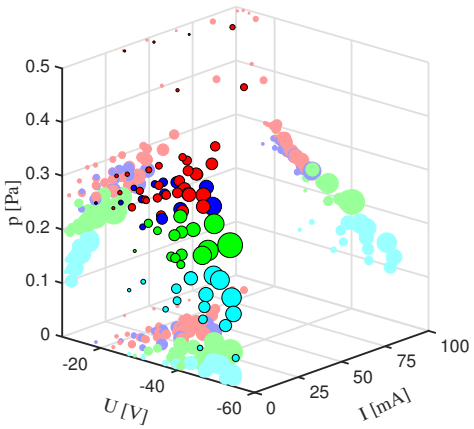

Figure B.2.19: NPR in star-mode operation, larger markers correspond to higher NPR (linear scaling). The different colours correspond to different discharge regimes: Red: star-mode without the ion source. Blue: star-mode operation in a similar parameter space as the red markers but the ion source is operated at maximum current. Green: lower pressure than red and blue with the ion source at a minimal current required to achieve a stable star-mode. Cyan: lowest pressure. Star-mode is only possible for potentials below -55 kV. The maximum NPR was achieved was $(1.43 \pm 0.34) \cdot 10^6$ n/s (green markers).

The unlocked low-pressure regime allows higher grid potentials before the current limit of the power supply is reached. Figure B.2.19 suggests that the NPR increases

for 0.1 Pa ≤ p ≤ 0.2 Pa and decreases for 0.2 Pa ≤ p ≤ 0.5 Pa.
To evaluate the pressure dependence of the neutron production rate, the NPR is decoupled from the current and potential by normalising it with the current I and potential dependent cross section $\sigma(E_{\text{ion}}(U)/2)$:

$$|\text{NPR}| = \frac{I_0}{I} \cdot \frac{\sigma_0}{\sigma(U/2)} \cdot \text{NPR} \tag{B.2.8}$$

A normalisation with I_0/I and σ_0/σ is chosen to preserve the units of the NPR in s^{-1}. $I_0 = 15$ mA and $\sigma_0 = \sigma(30\ [\text{keV}])$ have been chosen arbitrarily as these values are approximately centred in the experimental parameter space. The cross section is taken at half the grid potential, because we expect that most fusion reactions will be due to collisions of fast D_2^+ with the background gas (see figure B.2.18), whereas the cross sections are provided for D^+. The NPR is not normalised by the potential, because $R \propto v(U) \cdot n_{\text{fast}} \propto v(U) \cdot I/v(U)$, with fast ion density n_{fast}. For the determination of σ it is assumed that all ions have accelerated though the full potential and that beam-gas fusion is dominant. Note also, that the normalisation neglects any changes in the ion birth radius due to changes in U and p.
The normalised NPR is shown in figure B.2.20. Blue and cyan data points from figure B.2.19 are excluded, because they distort the NPR by the addition of a large amount of fast ions, or are not recorded in star-mode, respectively.
Assuming $R \propto n_{\text{gas}}$, the NPR is expected to increase by a factor of ×1.5 when the pressure is increased from 0.2 Pa to 3 Pa. The graph shows a better than expected tripling in the normalised NPR. The scaling can be explained with the ion birth radius model: The measurements at low pressures are obtained with the highest grid potentials, for which the model predicts a reduction of the fast ion current (see figure B.2.9), resulting in the lower than expected NPR for decreasing pressure.

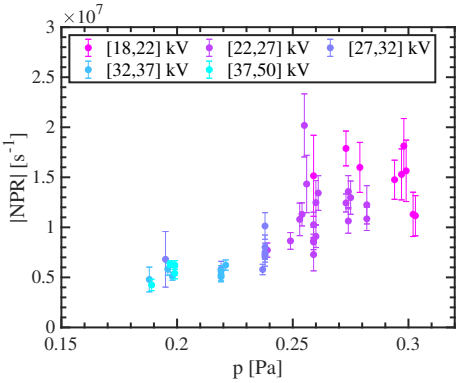

Figure B.2.20: Normalised neutron production rate as a function of p. The blue and cyan dataset of figure B.2.19 are excluded from the plot, since the large amount of fast ions may lead to inconclusive results. The normalised NPR scales favourably with increasing pressures, as it is expected for BG fusion.

The increase in absolute NPR (see figure B.2.19) is in line with the prediction of the ion birth radius model: For low pressures the number of slow ions created in the cathode region is reduced (see figure B.2.12) and an absolute decrease in low energy ions is expected (compare figure B.2.10). Thus, for low pressures, the current limit of the power supply is no longer reached due to the reduction of ions in the system and higher grid potential can be applied. For further reduction of the pressure (cyan data set in figure B.2.19) star-mode operation cannot be achieved, and rather a single ion channel between ion source and grid is visually observed. The drop of the NPR is attributed to the reduction of (fast) ions in the system, deduced from the low achievable currents and the absence of star-mode. It is unclear if the NPR can be further increased (compared to the green data set) by achieving star-mode, for example by adding more ion sources.

Scaling law for the neutron production rate

From the data points in figure B.2.19 a scaling law is derived to estimate the NPR from the experimental settings by approximating the free parameters in the reaction rate (see equation B.2.1). First, the reaction rate is multiplied with the volume and the energy dependent cross section of the neutron producing branch D(d,n)^{3}He, $\sigma_n(E)$, is used:

$$\mathrm{NPR} = n_i \cdot n_{\mathrm{gas}} \cdot \sigma_n(E) \cdot v \cdot V, \tag{B.2.9}$$

Assuming beam-gas fusion as the dominant fusion process, the densities are the fast ion density n_i and the gas density n_{gas}. The fast ion current is estimated from the ion birth radius model and the current model from Krupakar Murali (see equation B.2.3): Hereby the current of class I & II ions is (conservatively) estimated to 10% of the total current, with which equation B.2.3 is rewritten as

$$I_{\mathrm{fast}} = \frac{\eta(0.1 \cdot I_{\mathrm{meas}})}{1-\eta^2}. \tag{B.2.10}$$

At higher pressure ions can make less oscillations before they are neutralised by charge exchange. As a first-order approximation, the fast ion current is normalised with the pressure to account for the reduced mean free path.

$$I_{\mathrm{fast}} = \frac{\eta(0.1 \cdot I_{\mathrm{meas}})}{(1-\eta^2)} \cdot \frac{1[\mathrm{Pa}]}{p}. \tag{B.2.11}$$

To approximate the ion density, it is assumed that the fast ion current is carried in one single star-mode ion beam with beam diameter A:

$$n_i = \frac{I_{\mathrm{fast}}}{e v A}. \tag{B.2.12}$$

The gas density is estimated by using the ideal gas law $n_{\text{gas}} = p/(k_b T)$ with a constant gas temperature $T \approx 300$ K. The cross section is calculated using the R-matrix parametrisation from Bosch [147] and all ions are assumed at energy $E = eU$. The collisional energy is taken as half the kinetic energy, because it is assumed that the dominant ion fraction is molecular H_2^+ (see figure B.2.18). The volume is estimated as the grid diameter $d_{\text{grid}} = 0.1$ m times the beam diameter A.
Plugging all parameterisations in equations B.2.9, eliminating A, v and p, and using a grid transparency $\eta = 0.95$, the NPR is estimated as:

$$\text{NPR} = \frac{0.1 \cdot \eta \cdot d_{\text{grid}} \cdot I_{\text{meas}} \cdot \sigma(0.5eU)}{(1-\eta^2) \cdot e \cdot k_b \cdot T} \tag{B.2.13}$$

$$\approx 1.5 \cdot 10^7 \cdot I_{\text{meas}}[\text{mA}] \cdot \sigma(0.5eU)[\text{b}] \tag{B.2.14}$$

The NPR is calculated for every data point in figure B.2.19 from the discharge parameters I and U and compared against the measured NPR. the result is plotted in figure B.2.21. The colour of the points reflects the parameter space of the measurement point in figure B.2.19 and a 1:1 line is plotted, representing a perfect fit between model and measurement. The simple model gives a good estimate of the measured NPR, but it must be stressed that this can be purely coincidental because the assumptions ignore key physics which are unknown. For one, the cross section is calculated based on the assumption that all ions have accelerated through the full grid potential, which has previously been shown to be incorrect. Secondly, the cross section is underestimated by assuming all ions are D_2^+, which have a lower relative velocity, and thus a lower cross section, than D^+. Furthermore, the interaction volume is limited to the grid area, and collisions outside the grid are neglected. Lastly, an approximation of the fast ion current is made which can experimentally not be verified.

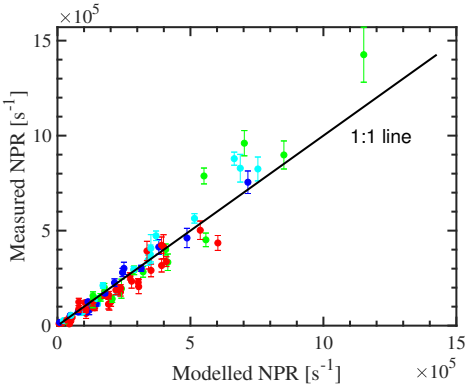

Figure B.2.21: Comparison between the calculated NPR (see equation B.2.14) and measured NPR for all data points from figure B.2.19. The simple model, which only depends on the current and potential, provides a good estimate of the measured NPR.

For the experiments at our device the scaling law provides a good expectation of the neutron production rate and it will be interesting to see how well this scaling holds at other devices.

B.2.5 Influence of the stalk on the ion trajectories

An aspect not considered by the model of the ion birth radius, and neglected by the simple picture of oscillating ions in a symmetric electric field, are field inhomogeneities caused by the stalk and consequent trajectory changes of ions. The asymmetry of the electric potential caused by the stalk is shown in figure B.2.22, as well as the force exerted on ions (red arrows). Looking at figure (b), the simple approximation made by the ion oscillation model becomes questionable: ions born in the upper half of the fusor seem to be accelerated towards the stalk and it is anticipated that ions created in the lower half of the fusor will pass through the grid only once before accelerating towards, and colliding with, the stalk.

A previous study by Kurt [148] and Ohnishi [149] showed an electric field perturbation similar to the results shown in figure B.2.22. Kurt's analysis focused on the field structure in the centre of the grid and did not consider the perturbations of the stalk on the symmetry of the vacuum field and the consequent changes in the ion trajectories. Ion losses to the stalk have been reported by Osawa [150], in the simulations 50% of the ions collided with the stalk, however the initial distribution is not clear from the presented results and no further assessments on the number of ion oscillations are made. This analysis follows-up on Osawa's work to provide more insight on the influence of the stalk on the ion confinement, and also shows how symmetry to the vacuum electric field can be restored by dielectric insulation of the stalk.

Ion trajectory simulations with unshielded stalk

Using the simulation suite Comsol [152] the influence of an uninsulated stalk on the ion trajectories is simulated with various grid sizes. The simulations are performed in 2D. Tracked are the total number of passes ions make cumulatively through the grid region. The geometry of our fusor is replicated in the simulation and 100 hydrogen ions (test particles with mass m_H, charge 1.6×10^{-19} C and initial energy $E_0 = 0$ eV) are initialised in a circle close to the wall with a uniform spacing between ions. The vacuum electric field inside the fusor is calculated for a grid and stalk potential of -60 kV, which was chosen because it is achievable with our experimental setup. At $t = 0$ s the ions are released, and their trajectory in the field simulated. The total number of passes through the grid is calculated from the trajectories. Ions colliding with the stalk are lost, the grid is assumed to be fully transparent and Coulomb interactions between particles are neglected. Figure B.2.23 shows the simulated geometry and particle trajectories after a few time steps. The colour indicates the ion energy, red corresponding to high kinetic energies.

The simulations are run for an arbitrarily chosen duration of 7 μs, in which a single ion can do at most 23 oscillations, allowing a maximum of 4600 cumulative passes through the grid. Simulated are three cathode grids with radius 5 cm, 9.5 cm, and 19 cm. The resulting number of passes for each grid is given in table B.2.1. Larger grids perform better in the simulation because the electric field in the northern hemisphere becomes more homogeneous, resulting in fewer particles being accelerated towards the stalk. To gain a better understanding of the results, figure B.2.24 shows a detailed analysis of the simulation with the 5 cm grid. Figure B.2.24 (a) shows the initial particle location, colour coded by the number of passes the ions made in the simulation. Here, a brighter colour corresponds to more passes. In the histogram in figure B.2.24 (b) the particles are grouped by the number of grid transitions they make in the simulated time. The majority of the particles makes 0 passes (22 particles), or 1 pass (32 particles). These correspond to the particles initialised in the upper and lower half of the fusor, respectively. Only few particles, the ones initialised close to the mid-plane, are able to oscillate multiple times.
Related results were experimentally obtained by Krupakar Murali [153]. In his experiments the NPR was measured for vertical translations of the grid. The ex-

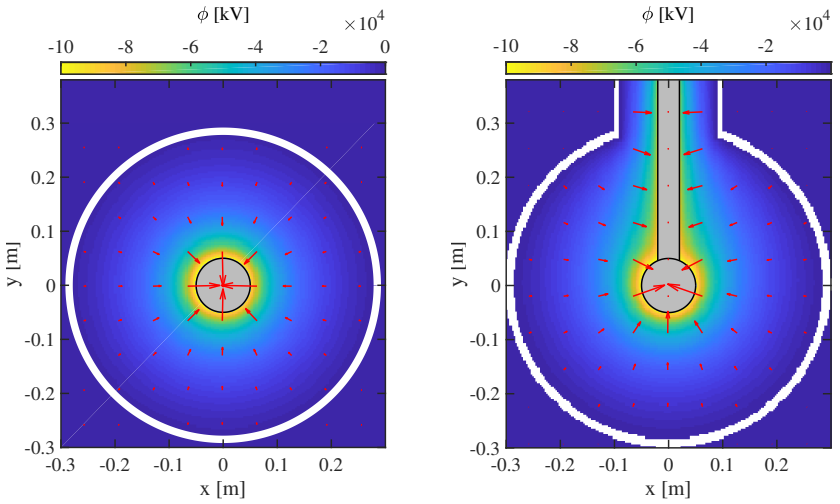

(a) Radial symmetric system **(b)** Field perturbations caused by the stalk

Figure B.2.22: Influence of the stalk on the electric potential. The vacuum vessel is drawn in white, the grid and stalk are coloured grey. For the calculations the cathode is approximated as a solid sphere. The figures show the strength of the electric potential, the red arrows represent the Coulomb force exerted on ions due to the electric field. The electric potential was calculated using CST Studio suite [151].

periments showed a maximum NPR when the grid was centred in the vacuum vessel. Comparing this result with the simulations, Murali's experiments can be interpreted such that only when the grid is placed in the midplane a symmetric field region capable of confining ions on oscillatory trajectories exists.

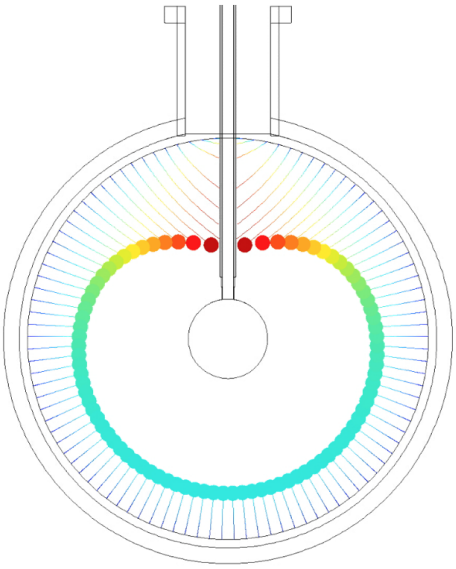

Figure B.2.23: Snapshot of a particle simulation. First, the vacuum electric field is calculated for a potential difference of -60 kV between the grid and vacuum vessel. 100 hydrogen-like ions are initialised in a circle in the vicinity of the wall with a uniform spacing. Their motion in the field is simulated, the grid is assumed to be fully transparent and ions colliding with the stalk are removed from the system. The cumulative number of passes of all particles through the grid is calculated for varying grid radii. In the plot the particles are colour coded by their energy, red representing high kinetic energies.

r_{grid} [cm]	Cumulative # of passes
5	176
9.5	706
19	3011

Table B.2.1: Cumulative number of passes for various grid sizes. The field asymmetry caused by the stalk reduces with increasing grid size, less ions are attracted to the stalk and the number of passes is increased.

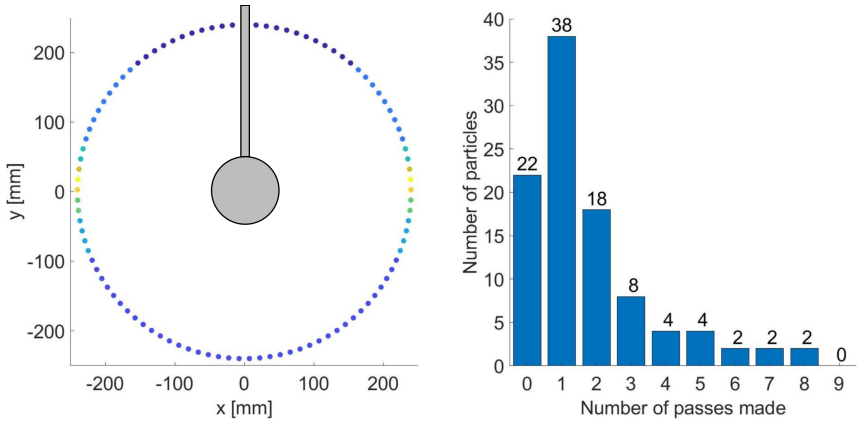

(a) Colour coded dependence of the number of oscillations on the initial particle location

(b) Histogram showing how many passes were made by how many particles.

Figure B.2.24: Detailed analysis of a simulation: The simulation results are shown for $r_{\text{grid}} = 5$ cm. (a): Correlation between initial particle location and the number of oscillations. Brighter colours correspond to a larger number of oscillations. Only particles initialised on the mid-plane are able to oscillate. Particles initialised in the upper hemisphere are accelerated directly towards the stalk, particles initialised in the lower hemisphere pass the grid once before being accelerated to the stalk. (b): Histogram summarising how many passes are made by how many particles.

Symmetry restoration through dielectric insulation of the stalk

In addition to the simulation of varying grid radii, different insulator materials (glass, alumina, air) surrounding the stalk were simulated to determine the effect of the dielectric on the ion confinement. In the simulations the number of ion oscillations was independent of the dielectric. We attribute this to the fact that the effect of (positive) charge build-up on the insulator caused by ion impact is not included in the simulations.

The influence of dielectric shielding of the stalk is tested experimentally. In the experiments a 3-ring grid made out of nichrome ($r_{\text{grid}} = 3$ cm, grid wire diameter 0.7 mm) was used. The NPR was measured with and without a quartz glass cylinder isolating the stalk (see figure B.2.4).

A doubling of the NPR was measured when the stalk was shielded, explained by the different operation modes of the fusor. Two distinct changes in the discharge characteristic were observed:

- Visual observation shows the plasma is only in star-mode when the stalk is isolated, shown in figure B.2.25.
- When the stalk is insulated, the grid temperature is strongly increased, deduced from a white-hot glow of the grid, which is not observed when the stalk is unshielded.

From the experiments we conclude that ions are attracted to the stalk and deposit their charge on the insulator until the built-up charge counteracts the electric potential of the stalk, and radial symmetry of the vacuum electric field is restored. This explains the strong heating of the grid when the insulator is installed: In the radial symmetric field all ions accelerate towards the grid on which the full power (caused by ion impact heating and ohmic heating) is deposited. If the stalk is not shielded, the power is distributed over the grid and stalk, which can be effectively cooled by radiative cooling due to the large surface. In this case, no star mode is achievable because ion micro channels are unable to form due to the strongly asymmetric field.

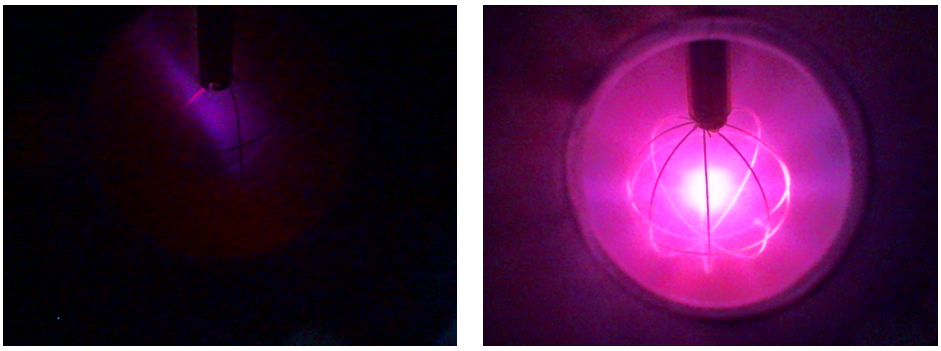

(a) Discharge without insulator **(b)** Discharge with insulator

Figure B.2.25: Comparison of the optical emission of two discharges. (a) Unshielded stalk. (b) Stalk is shielded by a quartz glass cylinder. In both discharges the pressure was 0.20 Pa, the measured current 11 mA, the potential 22 kV and the same grid was used. The ion source was used at the minimal required current to provide a stable discharge at 11 mA. In the discharge without quartz cylinder only a single beam of light is visible, likely caused by ions accelerating from the ion source towards the grid. If the stalk is insulated, star-mode operation is achieved and the NPR is doubled.

Assuming the energy distribution of ions colliding with the stalk or grid is similar for the insulated and non-insulated experiment, the increased NPR in the shielded configuration points towards beam-gas fusion as the dominant fusion process. In the radial symmetric field ions can oscillate, increasing the path length for BG fusion. If embedded fusion was the dominant process the number of oscillations would not matter.

B.2.6 Summary and Discussion

IEC devices do not operate at the idealised principle described by a non-Maxwellian distribution of oscillating ions in a spherically symmetric field with energies equiv-

alent to the potential energy supplied by the grid. In fact, spectroscopic measurements show that the majority of the ions are at a low temperature thermal distribution and calculations of the vacuum electric field show a strong asymmetry of the electric field caused by the stalk. To better understand these performance limiting factors we have developed a model to determine the influence of the experimental parameters (pressure, grid potential, and cathode radius) on the ion birth radius, investigated the scaling of the neutron production rate (NPR) at low pressures, and determined the influence of the stalk on the ion recirculation.
The ion birth radius is calculated by modelling the interaction between ions and a neutral gas background in a system with nearly transparent electrodes. The model predicts that the majority of ions are created in, or close to the cathode, qualitatively matching with experimental observations. The model shows only a minor influence of the grid potential and pressure on the ion birth radius, but favourable performance is predicted at low pressure because the number of slow ions created inside the cathode is reduced, and more current is available for fast ions. This has been verified experimentally. By installing a low current ion source, star-mode operation was achieved at lower than usual pressures. Here the power supply current is no longer saturated and higher potentials can be applied to the grid. Another prediction by the model is an increased fraction of fast ions for larger grid radii. In the work of Wehmeyer [144] and Egle [154] an increased NPR for increasing cathode radii was observed, however, no comparison between the emission spectra is provided and it is thus not immediately clear whether a shift in the birth radius is responsible for the performance increase, or if other effects play a role. Lastly, it is worth mentioning that a large fraction of the power supply current will be used up by secondary electron emission (SEE) caused by ion impact on the grid. In the model nickel grids were used. Comparison of the SEE coefficients found in literature, titanium is a favourable material having one of the lowest SEE (20% lower than Ni at 20 keV) [155, 156].
In addition, we've analysed the effects of the stalk, and dielectric shielding of the stalk, on the symmetry of the vacuum electric field. The central conclusion is that if the stalk is not surrounded by a dielectric, ions can only oscillate on the midplane of the device, and only if the grid is centred in the vacuum vessel. From measurements with and without dielectric shielding of the stalk we conclude that the dielectric will charge-up positively by ion impact until the electric potential of the stalk is cancelled out and symmetry of the electric field is restored. From this we conclude that simple stalk designs are sufficient, if insulated, and that advanced designs, such as condenser bushings or the conical-shaped stalk used in Kyoto and Illinois [149, 157] are of limited additional value.
These results are also interesting for the operation of fusors with pulsed power supplies, for which various laboratories have reported experimental results [158, 159, 160]. If too short pulses are applied and the stalk insulator does not have sufficient time to charge, oscillating ions will not exist in the device, leading to worse performance than anticipated.
Lastly, the findings are viewed in the context of embedded fusion, which was not considered in this article. For embedded fusion an uninsulated stalk can be ben-

eficial because the fusor can be operated at higher potentials and currents while keeping the target (grid and stalk) at a low temperature. The beneficing of low temperatures on embedded fusion has recently been reported by Bowden-Reid [121]. An uninsulated stalk will essentially turn the fusor into a linear collider, for which the ion birth radius profile should be re-evaluated. Whether a fusor-like design is of advantage over a linear machine will be left open for future investigations.

Acknowledgement

The current and cathode temperature model has been developed in collaboration with SPARC Industries SARL.

Appendix

B.2.7 Description of the current and cathode temperature model

We refrain from a complete description of the model and refer the interested reader to the original publications [140, 141]. Here, only the implemented current and cathode model expanding the original work are explained.

B.2.8 Modelled ion-gas interactions

Collisions between electrons and ions are not included and only collisions between charged deuterium ions D^+, D_2^+ and D_3^+ and the background neutral D_2 gas are taken into account because of the low ionisation and dissociation cross sections for electron with energies above 1 keV (see figure B.2.27 (c)). This is justified because for a cathode radius of 5 cm and vacuum vessel radius of 25 cm, electrons created at the grid will reach 1 keV after traveling 1 cm, whereas the mean free path for the ionisation of H_2 is over 30 m at $p = 0.2$ Pa, and increasing with energy. The initial isotope distribution is 10% D^+, 30% D_2^+ and 60% D_3^+, taken from experiments at the university of Wisconsin [143].
The collisions included in the model are:

D^+ impact on D_2

$$D^+ + D_2 \rightarrow D + D_2^+ \tag{B.2.15}$$
$$D^+ + D_2 \rightarrow D^+ + D^+ + D^+ + 2e \tag{B.2.16}$$
$$D^+ + D_2 \rightarrow D^+ + D_2^+ + e \tag{B.2.17}$$
$$D^+ + D_2 \rightarrow D^+ + D + D^+ + e \tag{B.2.18}$$
$$\tag{B.2.19}$$

D_2^+ impact on D_2

$$D_2^+ + D_2 \rightarrow D_2 + D_2^+ \tag{B.2.20}$$
$$D_2^+ + D_2 \rightarrow D_2^+ + D_2^+ + e \tag{B.2.21}$$
$$D_2^+ + D_2 \rightarrow D_2 + D_2^+ \tag{B.2.22}$$
$$D_2^+ + D_2 \rightarrow D^+ + D + D^2 \tag{B.2.23}$$
$$D_2^+ + D_2 \rightarrow D + D^+ + 2D^+ + 2e \tag{B.2.24}$$

D_3^+ impact on D_2

$$D_3^+ + D_2 \rightarrow D_3^+ + ... \tag{B.2.25}$$
$$D_3^+ + D_2 \rightarrow D^+ + ... \tag{B.2.26}$$
$$D_3^+ + D_2 \rightarrow D_2^+ + ... \tag{B.2.27}$$
$$\tag{B.2.28}$$

The cross sections for D^+ and D_2^+ are obtained from the Aladdin database [134], D_3^+ cross sections are taken from [161], and the +... is used to specify a cumulative cross section, e.g. in equation B.2.27 the sum of all cross section in which a D_2^+ is produced. The Aladdin database contains cross section for the interaction between H^+, H_2^+ and H_3^+ and neutral H_2. The same cross sections are used for the modelling of deuterium, however the corresponding energy was adjusted to account for the heavier Deuterium mass.
The modelled collisions are only the most relevant interactions. For completeness, all available cross sections from the Aladdin database and ref. [161] for hydrogen isotopes are given in figure B.2.27 and figure B.2.26.

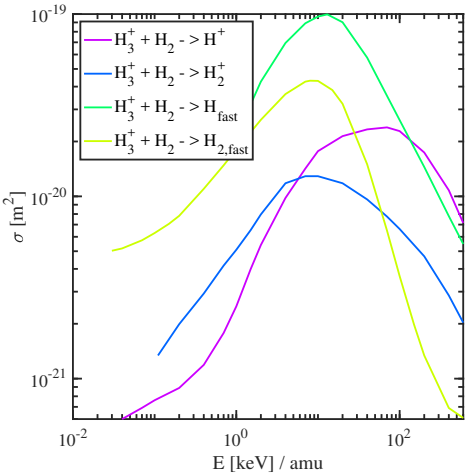

Figure B.2.26: Available cross sections for different collision processes between H_3^+ and H_2 [161]

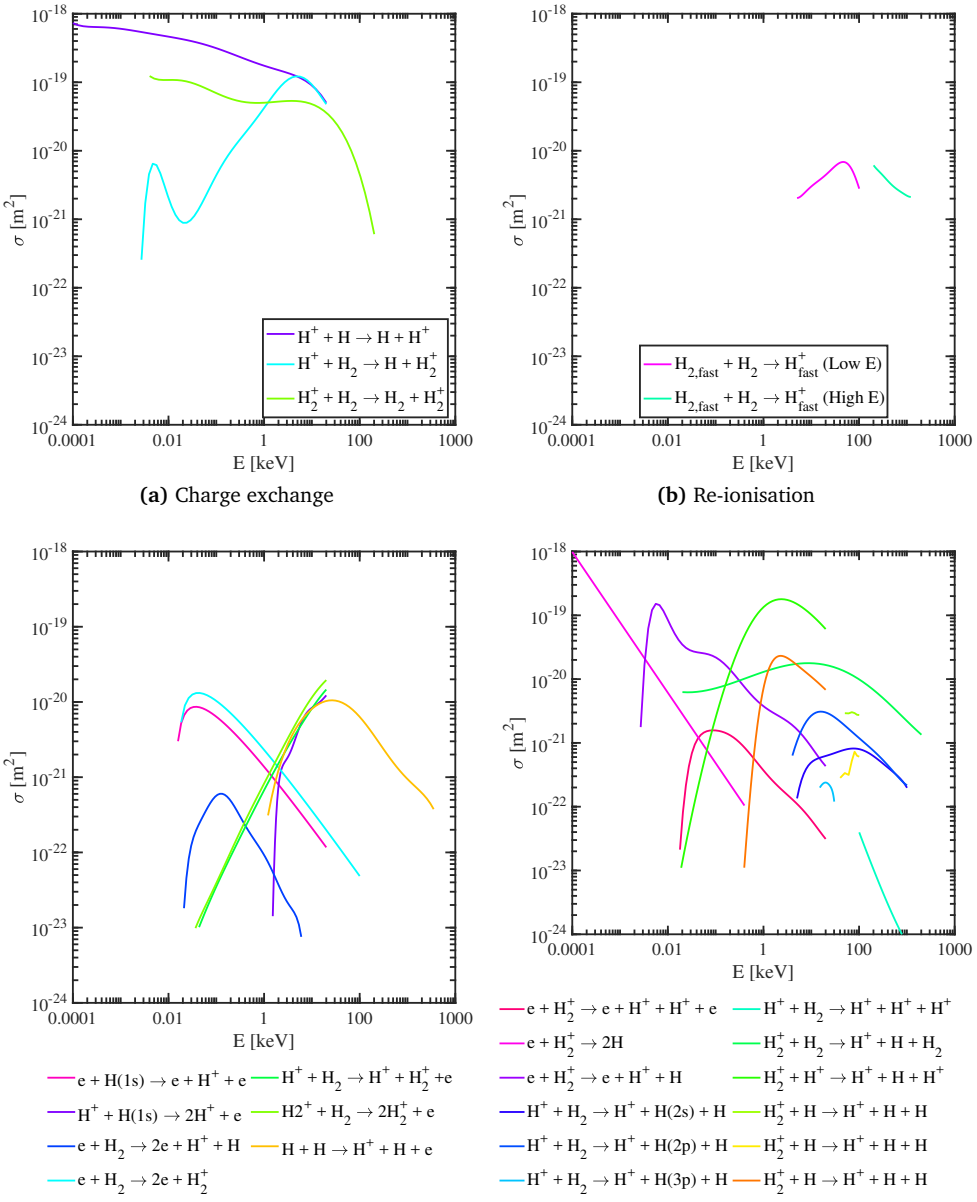

(a) Charge exchange

(b) Re-ionisation

(c) Ionisation

(d) Dissociation

Figure B.2.27: Comparison between all available atomic and molecular collisions of H and H_2 from the Aladdin database [134] as well as ref. [161]. All graphs have been scaled to the same x- and y-axis for better comparison of the dominant processes.

B.2.9 Current model

To analyse the ion birth radius knowledge of the different contributions to the total, i.e. measured current, is required. In the model the following contributions to the total current I_{tot} are taken into account:

$$I_{\text{tot}} = I_{\text{T}} + I_{\text{F}} + I_{\text{PISEE}} + I_{\text{Imp}} + I_{\text{EISEE}} + I_{\text{IISEE}}, \tag{B.2.29}$$

with

$I_{\mathbf{T}}$: thermionic emission current due to electrons leaving the cathode

$I_{\mathbf{F}}$: field emission current

$I_{\mathbf{PISEE}}$: photon induced secondary electron emission current

$I_{\mathbf{Imp}}$: ions implanted in the grid

$I_{\mathbf{EISEE}}$: electron induced secondary electron emission current

$I_{\mathbf{IISEE}}$: ion induced secondary electron emission current

The individual terms are calculated as follows:

Thermionic emission current $I_{\mathbf{T}}$
Thermionic emission occurs when the surface of the material reaches temperatures where electrons can have energies higher than the work function, allowing them to leave the material. The thermionic current is described by the Sommerfeld formula [162]:

$$J = \frac{4\pi m_e e k_b^2}{(2\pi\hbar)^3} \cdot T^2 \cdot (1-R) \cdot \exp\left(-\frac{W}{k_b T}\right). \tag{B.2.30}$$

Here, J is the current flux from the surface, m_e the electron mass, e the elementary charge, T the temperature of the material, R the internal reflection coefficient and W the work function. Figure B.2.28 shows an upper estimate of the thermionic emission by assuming $R = 0$.

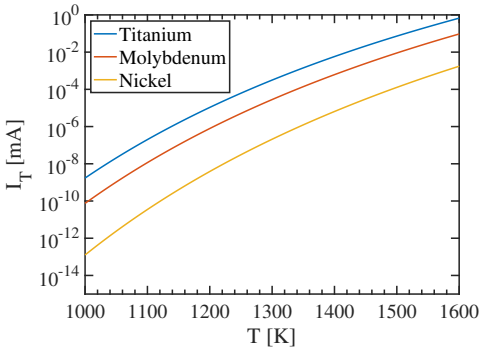

Figure B.2.28: Application of formula B.2.30. The used values for the work function W are taken from [163]. Equation B.2.30 gives the thermionic emission in units of A/m^2. For the calculation of I the surface area of one of our titanium grids was used - a 5 ring grid with wire diameter ⌀2 mm and grid diameter ⌀3 cm.

Even for grid temperatures above 1000 K, the calculated thermionic emission is orders of magnitude lower than the I_{tot}, which is typically above 10 mA. For completeness it is included in the model. I_{T} requires knowledge of the cathode temperature, which is calculated based on a power balance. The temperature model is described in section B.2.10.

Field emission current I_{F}

Depending on the strength of the electric field in the vicinity of a conductor, emission of electrons caused by strong electric fields occurs due to two different effects: Modification of the work function via the Schottky effect and, for fields $E > 10^8$ V/m, tunnelling of electrons through the potential barrier.
For fusor operating with grid potential of tens of kV, the electric field at the cathode is on the order 10^6 V/m and only the change in the work function W is considered [162]:

$$W = W_0 - 3.8 \cdot 10^{-4} \sqrt{(E[\text{V/cm}])}, \tag{B.2.31}$$

where W_0 is the work function without external electric fields. For the Titanium grid, this results in an increase in thermionic emission by a factor of $\approx 1.5 - 3$.

Electron induced SEE (EISEE) current I_{EISEE}

Electrons impacting on the cathode can transfer enough energy to electrons in the metal to overcome the work function. Lin and Joy developed a semi-empirical model to calculate the number of emitted secondary electrons, depending on the energy of the colliding electron [164]:

$$\frac{\delta}{\delta_m} = 1.28 \left(\frac{E_{PE}}{E_{PE}^m} \right)^{-0.67} \left(1 - \exp\left(-1.614 \left(\frac{E_{PE}}{E_{PE}^m} \right)^{1.67} \right) \right) \tag{B.2.32}$$

Here, δ is the secondary electron emission coefficient, δ_m the maximal secondary electron coefficient for a given maximum energy E_{PE}^m, and E_{PE} is the energy of the incoming electron. For molybdenum $\delta_m = 1.14$, $E_{PE}^m = 0.5$ keV [140].
In the fusor the electron current to the grid is limited to electrons originating from within the cathode. Due to the low plasma density within the cathode, the number of electrons hitting the cathode is estimated to be negligible. The EISEE formula is presented for completeness as it can be important for electrons colliding with the vessel. For a significant effect, electron energies in the keV range are required.

Photon induced SSE (PISEE) current I_{PISEE}
Photons produced due to CX processes or other excitation processes in the plasma with energies above the work function of the cathode material can free electrons from the cathode upon impact. The work function of different metals and corresponding wavelength is given in table B.2.2.

Metal	Work function W [eV]	Wavelength [nm]
Ti	4.33	268
Ni	5.15	240
Mo	4.6	270
W	4.78	260

Table B.2.2: Work function of different metals [163] commonly used as grid materials and corresponding photon wavelength.

I_{PISEE} is estimated under the assumption of a 1% ionisation degree of the gas in the cathode and an electron temperature between 1-6 eV. The excitation rate coefficients from electron impact on neutral hydrogen atoms are known from literature [134]. With this, the number of deexcitations, i.e. the photon emissions, per second with energies above 10 eV are estimated to 10^{18} $\mathrm{m^{-3}s^{-1}}$. Taking into account that not all photons produce an electron when hitting the cathode (e.g. the photon emission coefficient for molybdenum is 10% [165]) and the geometric transparency of the cathode, the PISEE current is estimated to be $I_{\mathrm{PISSE}} \approx 1 \cdot 10^{-2}$ mA, a negligible current compared to I_{tot}.

Ion induced currents
Ions impacting on the cathode get neutralised and can cause an electron to be emitted. No general formula describing the effect is available, however, measurements for a variety of target materials and impacting ion species are available. Figure B.2.29 shows the energy dependence of the secondary electron coefficient for H^+ and H_2^+ impacting on Titanium and Molybdenum.

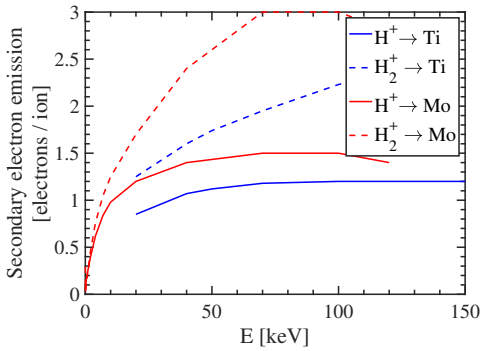

Figure B.2.29: Ion induced secondary electron emission for hydrogen ions colliding with titanium and molybdenum targets [166]

Furthermore, ions with energies below 1 keV can produce an Auger electron. The SEE coefficient γ_{aug} is [167]

$$\gamma_{\text{aug}} = 0.016 \cdot (E_b - 2W), \tag{B.2.33}$$

with binding energy E_b and work function W. For Molybdenum, $\gamma_{\text{aug}} = 0.07$.
All secondary electron emission coefficients are for the case of perpendicular impact. Due to the lack of data, e.g. surface roughening during operation, the effect of non-perpendicular impact has not been examined and it is assumed that all ions hit the cathode perpendicular.
To calculate the ion induced secondary electron emission, the energy distribution of impacting ions must be known. The approach by Emmert and Santarius is followed to calculate the distribution function for both cases of atomic and molecular hydrogen.

Neglecting Auger electrons, the ion current is made up of 6 different components: Implantation of class I and class II ions hitting grid, implantation of ions created in the cathode regions by class I and class II ions which collide with the grid and contributions from secondary electron emission due to fast class I and class II ions impacting on the grid. In case of molecular deuterium, the 6 terms have to be evaluated for D^+, D_2^+ and D_3^+.

B.2.10 Cathode temperature model

The remaining unknown in equation B.2.29 is the cathode temperature, required to calculate the thermionic emission I_T. The cathode is heated by ohmic heating and by class I and II ions hitting the surface. Cooling processes are convection, radiative cooling, secondary electron emission and thermionic field emission. With this, the power balance is

$$P_\Omega + P_{\text{ion}} + P_{\text{ISEE}} + P_{\text{TFE}} + P_{\text{rad}} + P_C = 0, \tag{B.2.34}$$

with ohmic heating power P_Ω, ion bombardment P_{ion}, secondary electron emission P_{ISEE}, thermionic field emission P_{TFE}, radiated power P_{rad} and convection P_C. The individual terms are modelled as follows:

Ohmic heating
The ohmic heating power P_Ω is calculated using Ohms law:

$$P_\Omega = \frac{l_c \rho}{A} I_{\text{tot}}^2, \tag{B.2.35}$$

with the total length of the cathode wire l_c, wire cross section A, resistivity ρ and cathode current I_{tot}. To describe the resistivity of molybdenum for temperatures $250\,\text{K} < T < 2894\,\text{K}$ the following parametrisation is used [168]:

$$\rho = -1.7021 + 2.3319 \cdot 10^{-2} \cdot T + 2.5507 \cdot 10^{-6} \cdot T^2 - 2.5930 \cdot 10^{-10} \cdot T^3. \tag{B.2.36}$$

Ion impact heating
From the current model described in the previous section B.2.9 the currents of class I and class II ions, I_i^I and I_i^{II}, hitting the cathode are determined. As a reminder, class I ions are ions created in the vicinity of the anode. Multiplying I_i^I with the acceleration voltage results is the power P^I transferred to the cathode. For class II ions, i.e. ions created in the region between the vessel and the cathode, the power delivered to the cathode is equal to the class II ion current times an accelerating voltage depending on their birth radius, $P^{II} \propto I_I^{II}(r) \cdot U(r)$.
The third contribution to ion impact heating is due to slow ions created in the cathode region which collide with the grid. Their average energy is estimated to be equal to the temperature of the background gas T_{gas}. The background current $I_{\text{slow ion}}$ is again obtained by the current model. The power is estimated to be $P_{\text{slow ion}} = 3/2 k_b T_{\text{gas}} I_{\text{slow ion}}$.
With this, the total power deposition on the cathode due to ion impact is

$$P_{\text{ion}} = P^I + P^{II} + P_{\text{slow ion}}. \tag{B.2.37}$$

Thermionic field emission cooling
The average energy released per electron E_e due to thermionic field emission is described by the Nottingham effect [169]:

$$E_e[\text{J}] = W_0 + 2 k_b T, \tag{B.2.38}$$

The total cooling due to thermionic field emission in electron volt is calculated

with

$$P_{\mathrm{TFE}} = \frac{1}{q}\frac{E_e}{I_{\mathrm{TF}}}, \tag{B.2.39}$$

with the thermionic field emission current I_{TF} (see equation B.2.30) using the reduced work function due to the Schottky effect (see equation B.2.31).

Radiative cooling
Assuming cathode temperatures above 1000 K, the cathode can be described as a black body radiator. The radiated power is described by the Stefan-Boltzmann Law:

$$P_{\mathrm{rad}} = \epsilon\sigma A_{\mathrm{eff}}\left(T^4_{\mathrm{vessel}} - T^4_{\mathrm{cathode}}\right). \tag{B.2.40}$$

Here, ϵ is the emissivity, σ is the Stefan-Boltzmann constant, A_{eff} the effective surface of the emitting surface, T_{vessel} and T_{cathode} the temperature of the vacuum vessel and cathode, respectively.
We define the effective cathode surface because radiation from the inner side of the cathode will in part radiate onto the cathode. To define A_{eff}, the cathode surface is divided into two halves: the outer half radiates towards the vessel. Radiation from the inner half has a chance equal to the geometric transparency η_{geom} to reach the vessel. With this, the effective geometry is

$$A_{\mathrm{eff}} = \frac{1+\eta_{\mathrm{geom}}}{2} A_{\mathrm{surf}}, \tag{B.2.41}$$

with the geometric surface area of the wires A_{surf}.

Convection
Convective cooling is expected to be insignificant for pressures below 1 Pa, but is included in the model to evaluate higher pressures. We follow the approach of Krupakar Murali [143], which, under the assumption of a collisional gas, estimates the power loss due to convection P_c as

$$P_c = 2kn_{\mathrm{gas}}\sqrt{\frac{kT_{\mathrm{gas}}}{2\pi m}}(T_{\mathrm{cath}} - T_{\mathrm{gas}})A_{\mathrm{surf}}. \tag{B.2.42}$$

The atom specific constants k and mass m for deuterium are: $k = 1{,}38\cdot10^{-23}$ J/K and $m = 4\cdot1{,}67\cdot10^{-27}$ kg.

Benchmark of the temperature model
The individual power contributions are plugged into equation B.2.34 to calculate the cathode temperature. Unfortunately, no cathode temperature measurements are available at our fusor, instead the model is tested against measurements from

Krupakar Murali [143]. Here, a spherical fusor was operated at various pressures with a constant cathode potential $U = -40$ kV and measured current $I = 30$ mA. The comparison is shown in figure B.2.30 and agrees within a few percent for pressures below 0.4 Pa. The model assumptions are less valid for higher pressures where an increasing mismatch to the measurement is observed, but the difference is still below 10%.

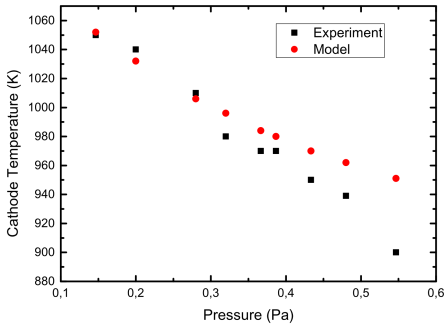

Figure B.2.30: Benchmark of the cathode temperature model against experiments from reference [143]. The model matches the measured temperature within a few percent, no measure for the uncertainty of the measurement is available.

B.3 Conceptual design of an electrodynamic confinement machine sustaining a non-Maxwellian ion populations with applications for nuclear fusion

Messmer M.C.C., Jaspers R.J.E and *Lopes Cardozo N.J.*

This chapter will be submitted to Physical Review Accelerators and Beams

Abstract:
Fusion machines are typically designed to confine a thermal plasma because Coulomb collisions between ions and electrons quickly thermalise the fusion fuel. The presented research explores the feasibility of a non-thermal fusion reactor by eliminating the dominating electron losses from the system. A novel concept is presented which confines a pure ion plasma. The ions are confined in oscillating bunches which remain longitudinally and transversally compressed by pulsed electric fields and the symmetry of the system, respectively. The design ensures that all ions remain at a monoenergetic velocity distribution and that different bunches collide at their maximum energy during every oscillation. We dub this concept BEACON, for Bunched ElectrodynAmic CONfinement. In this article the feasibility of confining a pure ion plasma is demonstrated by using particle tracing simulations. The simulations show that bunches with densities close to 10^{14} m^{-3} can be confined in the simulated geometry, which matches our calculated estimates within a factor of two. We find that, depending on the size of the device, ion densities up to 10^{15} m^{-3} can remain bunched for thousands of oscillations. The confinable densities are, however, more than 10^{7} orders of magnitude too small for break-even operation. This hurdle could be overcome by modifying the design to collide bunches with a solid density target in the device centre, which will also make the concept viable as a very efficient neutron generator for industrial applications.

B.3.1 Introduction

For decades the idea of constructing a machine able to achieve stable nuclear fusion and produce clean energy has spurred scientists. The fundamental physical challenge is to overcome the Coulomb repulsion between two ions, requiring large kinetic energies for them to come sufficiently close to each other. A less explored concept to achieve nuclear fusion is based on electrostatic confinement of ions. In so-called fusors, ions are confined by a static electric field on oscillatory trajectories. This concept can however not work as an energy source because Coulomb collisions with electrons lead to fast thermalisation of the ions. The dominating

power losses to electrons from Coulomb scattering vs. the power gain by fusion reactions are compared in figure B.3.1 for deuterium colliding with a stationary deuterium or tritium target[‡]. To make a fusor-like concept viable, a beam-like, non-maxwellian energy distribution maximising the cross sections is desired, and minimising the energy losses is required. This motivates a novel design of a spherical accelerator. Even though the concept stems from considerations made for fusion applications, the design is not limited for these, but applicable to all systems requiring high frequency, high flux collisions. All quantities will be derived in a general way, but solutions for fusion collisions between DT and DD are supplementary provided.

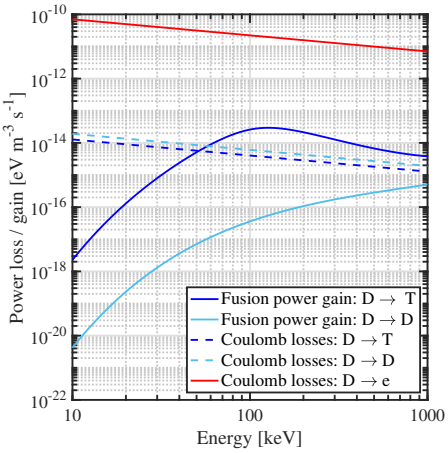

Figure B.3.1: Power gain from fusion reactions and losses due to Coulomb scattering in beam-target fusion. In a classical system (composed of electrons and ions), the losses to electrons always outweigh the gains due to the higher Coulomb cross section, resulting in fast thermalisation of the system.

Motivated by figure B.3.1, the Coulomb losses can be reduced by 3 orders of magnitude by removing the electrons, which in principle allows a positive power balance for DT collisions. Conceptually this can be realised by colliding ion beams, sketched in figure B.3.2 a).

[‡]A derivation of the Coulomb power losses and fusion power gain are given in appendix B.3.6

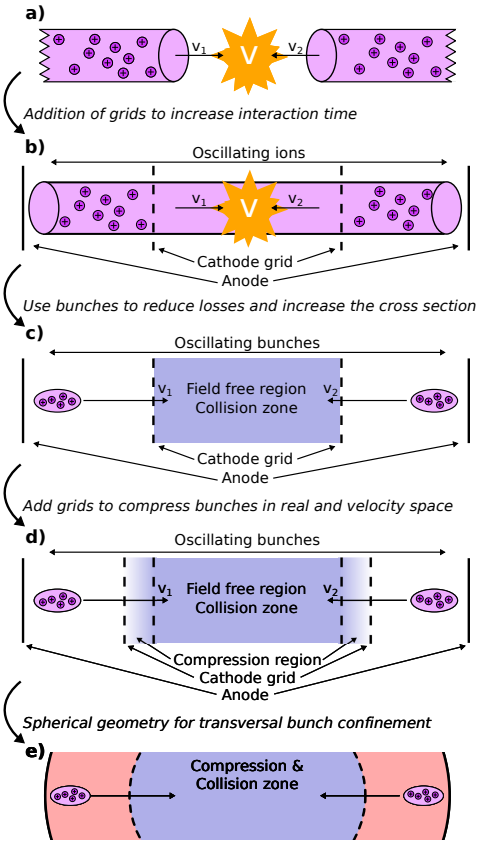

Figure B.3.2: Step-by-step build-up of the bunched, spherical accelerator, starting from two colliding ion beams (a). Cathode grids are added to increase the interaction time between ions (b), and instead of continuously oscillating ions beams, the ions are confined in non-thermal bunches to maximise the cross section and reduces losses (c). Additional grids are added to maintain the non-Maxwellian velocity distribution and keep the ions bunched (d). The linear design is adapted to a spherical one to circumvent radial expansion of the bunches (e).

In such a linear system, the reaction rate R is

$$R = n_1 n_2 \sigma(v) v V, \tag{B.3.1}$$

with beam densities n_1 and n_2, cross section σ, relative velocity $v = |v_1 - v_2|$, and interaction volume V. With colliding beams, different issues spring to mind:

1. The interaction volume is limited. The addition of grids and resulting oscillatory confinement of ions, sketched in figure B.3.2 b), increases the reaction

rate by N_{osz}, the number of oscillations ions can be confined in the system:

$$R = n_1 n_2 \sigma(v) v V \cdot N_{\mathrm{osz}} \tag{B.3.2}$$

2. Coulomb scattering between ions and the resulting thermalisation will lead to two effects: Fast ions in the tail of the velocity distribution can gain sufficient energy to overcome the confining potential and are lost by colliding with the anode. Secondly, slow ions have a low contribution to the reaction rate. By modifying the design to use non-thermal bunches which collide in a central, field free collision zone, both issues are overcome. The modified concept is sketched in figure B.3.2 c). For such a system, the reaction rate is

$$R = n_1 n_2 \sigma(v_{\mathrm{opt}}) v_{\mathrm{opt}} V_{\mathrm{bunch}} \cdot N_{\mathrm{osz}} \cdot \Delta t \cdot f \tag{B.3.3}$$

with oscillation frequency f and interaction time $\Delta t = L_{\mathrm{bunch}}/(2v)$; the time it takes for the bunches to pass through each other.

3. In the bunched design, the energy transfer in Coulomb collisions between ions in the collision zone will still lead to thermalisation and eventually debunching of the ions. To keep the ions bunched, additional grids are added to compress the bunches at every oscillation in real- and velocity-space. In section B.3.3 a multi-grided concept is worked out and the feasibility demonstrated, for now a sketch of the system is given in B.3.2 d).

4. In a linear pure ion plasma space charge effects will lead to radial expansion of the bunch necessitating an electric field which counteracts bunch expansion. As we will show in section B.3.2, and later confirm by particle simulations, this is achievable by moving to a spherical geometry, illustrated in figure B.3.2 e). In section B.3.2 an analytical model will be developed to estimate the maximum bunch density n_{bunch} to:

$$n_{\mathrm{bunch}} = \frac{2\epsilon_0 U}{q} \frac{1}{r_a^{-1} - r_c^{-1}} \cdot \frac{1}{\left(\sqrt{h_b^2 + z^2} - r_c\right)^2} \cdot \frac{1}{\sqrt{h_b^2 + z^2}}. \tag{B.3.4}$$

In equation B.3.4, U is the potential applied to the cathode grid, ϵ_0 the vacuum permittivity, q the elementary charge, r_a and r_c the anode and cathode radius, respectively, h_b the bunch width and z the radial bunch position. In the (later) simulated geometry we find a maximum sustainable density of $n_{\mathrm{bunch}} \approx 5 \cdot 10^{13}$ m^{-3}, which matches the analytical estimate within a factor of 2.

Moving to a spherical system has another advantage, namely that (small) angle scattering from Coulomb collisions no longer leads to particle losses, as long as the accelerating and compressing potentials ensure that ions converge in the collision zone simultaneously.

In this article, theoretical estimates for the reaction rate, the maximum sustainable bunch density and an energy gain criteria are derived in section B.3.2. Based on physical intuition a multi-grid structure capable of confining non-Maxwellian ion bunches is proposed in section B.3.3. Particle tracing simulations are used to simulate thousands of different combinations of timings and potentials of the pulsed grids to determine a suitable parameter range to compress ion bunches in real- and velocity-space. The determined parameters are used to demonstrate bunch sustainment for >150 oscillations with minimal losses for bunches close to the theoretical density limit. The results are used to reflect on the feasibility energy producing fusion reactor in section B.3.4 before concluding in section B.3.5.

B.3.2 Theoretical consideration

Expected fusion reaction rate

The reaction rate for two oscillating, colliding, cylindrical ion bunches is estimated in a linear geometry. In a spherical system no instructive solution for the time of flight for ions traveling from the anode to the cathode is available due to the inverse square scaling of the electric field $\mathscr{E} \propto r^{-2}$. The geometry is sketched in figure B.3.3, the full derivation is provided in appendix B.3.7. Here only the result is presented and discussed.

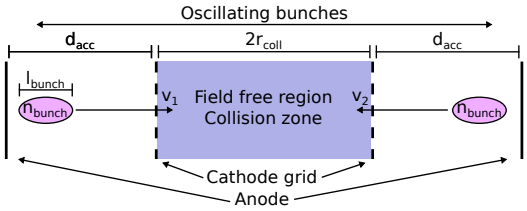

Figure B.3.3: The reaction rate R is derived based on two oscillating ion bunches in a linear system. Loss mechanisms are not considered and the ions are assumed to be monoenergetic.

The general reaction rate as well as the reaction rate for deuterium-deuterium and deuterium-tritium fusion are:

$$R = \sqrt{\frac{2e}{m}} \cdot \frac{\sigma(E_{\text{cm}}) E_{\text{bunch}}^{1/2} n^2 A_{\text{bunch}} l_{\text{bunch}}^2}{0.5\, r_{\text{coll}} + d_{\text{acc}}} \tag{B.3.5}$$

$$\overset{D\rightarrow D^*}{\approx} \frac{3\, E_{\text{bunch}}^{7/6}[eV] n^2 A_{\text{bunch}} l_{\text{bunch}}^2 \cdot 10^{-29}}{\left(d_{\text{acc}} + 0.5 r_{\text{coll}}\right)} \tag{B.3.6}$$

$$\overset{D\rightarrow T^\dagger}{\approx} \frac{2\, n^2 A_{\text{bunch}} l_{\text{bunch}}^2 \cdot 10^{-21}}{\left(d_{\text{acc}} + 0.5 r_{\text{coll}}\right)} \tag{B.3.7}$$

The reaction rate scales favourably with the density, bunch volume, and bunch length, equivalent to a larger number of particles in the bunch $N_{\text{part}} = nV$, and longer interaction times $\Delta t \propto l_{\text{bunch}}$. Larger systems lead to smaller oscillation frequencies decreasing R, reflected by the denominator.

Density limit of the bunches

The bunch density n_{bunch} is a central quantity for the performance of the collider. For the proposed spherical design no expression on the maximum bunch density is found in literature. We estimate it by analysing the force balance on bunched ions, and later verify the derived expression with particle simulations.
A thin 2-D bunch of ions moving with velocity v on the z-axis towards the cathode is sketched in figure B.3.4. The cathode with radius r_c and applied potential U is centred in the vacuum vessel with radius is r_v. The position of the bunch along the z-axis is denoted as z. The bunch is accelerated in the region $r_c < r < r_v$ [§].
The electric field E_{acc} in the acceleration region at radius r is well known from spherical capacitors:

$$E_{\text{acc}} = \frac{U}{r_v^{-1} - r_i^{-1}} \cdot \frac{1}{r^2}. \tag{B.3.8}$$

Bunch expansion along the z-axis will not be considered in this analysis, the longitudinal compression will be determined by the particle simulations in section B.3.3.

[*] For deuterium energies between 150 keV - 400 keV

[†] For a centre of mass energy $E_{\text{cm}} \approx 110$ keV, where the cross section is highest.

[§] The compression region with $r < r_c$ is excluded from the analysis, because it is yet to be specified. Assuming no transversal bunch compression occurs in the compression region, the electric field in the acceleration region has to compensate for bunch expansion while the bunch travels through the cathode.

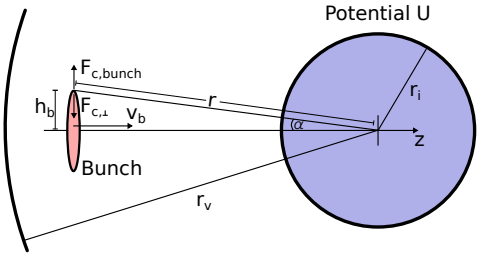

Figure B.3.4: Sketch of the geometry used to estimate the maximum bunch density.

Transversal bunch expansion will occur due to Coulomb force $F_{C,\text{bunch}}$ caused repulsion between the ions, and the bunch will be compressed due to the radial character of the accelerating electric field. The field component balancing $F_{C,\text{bunch}}$ is denoted as $F_{acc,\perp}$. The bunch will not expand when the force balance

$$F_{C,\perp}(h_b, z) = F_{C,\text{bunch}}(h_b). \tag{B.3.9}$$

is fulfilled. Equation B.3.9 is analysed for an ion at the edge of the bunch at distance h_b from the z-axis, where the $F_{C,\text{bunch}}$ is strongest.
The compressing force $F_{C,\perp}$ experienced by a particle at distance h_b perpendicular to the oscillatory direction at distance z from the centre is obtained from equation B.3.8 and geometric considerations from figure B.3.4:

$$\begin{aligned} F_{C,\perp}(h_b, z) &= q \cdot E_{\text{acc}} \cdot \sin(\alpha) && \text{(B.3.10)} \\ &= q \cdot \frac{U}{r_v^{-1} - r_i^{-1}} \cdot \frac{1}{(r - r_i)^2} \cdot \frac{h_b}{r} && \text{(B.3.11)} \\ &= q \cdot \frac{U}{r_v^{-1} - r_i^{-1}} \cdot \\ &\quad \frac{1}{\left(\sqrt{h_b^2 + z^2} - r_i\right)^2} \cdot \frac{h_b}{\sqrt{h_b^2 + z^2}}, && \text{(B.3.12)} \end{aligned}$$

where q is the elementary charge. To estimate $F_{C,\text{bunch}}(h_b)$, the bunch is approximated as a cylinder with charge density n_{bunch}, length l and radius h_b. Using Maxwell's equation, the electric field in the bunch for $h < h_b$ is readily calculated to

$$E_{\text{bunch}}(h) = \frac{q n_{\text{bunch}} h_b}{2\epsilon_0}, \tag{B.3.13}$$

where ϵ_0 is the vacuum permittivity.

Combining equations B.3.12 & B.3.13 in equation B.3.9 results in the sought relation between the ion density n_{bunch} and geometric parameters of the system:

$$n_{\text{bunch}} = \frac{2\epsilon_0 U}{q} \frac{1}{r_v^{-1} - r_i^{-1}} \cdot \frac{1}{\left(\sqrt{h_b^2 + z^2} - r_i\right)^2} \cdot \frac{1}{\sqrt{h_b^2 + z^2}} \tag{B.3.14}$$

The derived expression for n_{bunch} scales favourably with the applied potential U, but is inversely proportional to the bunch width h_b. For increasing h_b the confinable bunch density decreases due to the increased Coulomb repulsion between particles and the increasing radial distance between the outermost ions and the device centre, leading to a decrease in the compressing field $F_{C,\perp}$. However, a decrease in h_b will lead to a decrease in the number of particles in the bunch and consequently lower reaction rates.
Aside from increasing the applied potential, n_{bunch} can be increased by decreasing $r_v^{-1} - r_i^{-1}$, i.e. the distance between vacuum vessel and compression region, which is limited by the bunch length. Too short grid spacing might hinder longitudinal compression.
The calculated limit on the bunch density will be used in section B.3.4 to estimate whether an engineering design of a power producing fusion reactor is feasible.

Energy gain criterium

Due to the low losses the concept is interesting for applications in nuclear fusion and an interesting question is if, and under which conditions, the design could produce net energy.
For the derivation of an energy gain criteria, the energy balance is evaluated. For break-even operation, the energy generated by a fusion reaction must exceed the losses:

$$W_{\text{fusion}} > W_{\text{loss}} \tag{B.3.15}$$

The generated fusion energy per fusion collision $W_{\text{fusion}} = E_f \cdot f_{\text{bu}}$ equals the released energy per reaction E_f times the burn-up fraction f_{bu}, the probability that a particle will fuse before it is lost. Looking at a single bunch ion colliding with an oncoming bunch with length L and density n_{bunch} (see figure B.3.5), the single pass burn-up fraction f_{sp} is

$$f_{\text{sp}} = n_{\text{bunch}} \cdot L \cdot \sigma_f, \tag{B.3.16}$$

where σ_f is the fusion cross section.

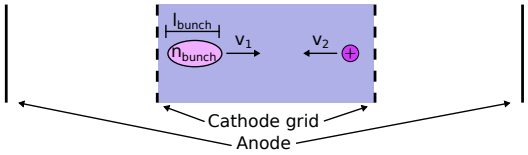

Figure B.3.5: Single ion colliding head-on with a bunch of density n_{bunch} and length L. The single pass burn-up fraction, i.e. the probability of the ion f, is $f_{\text{sp}} = n_{\text{bunch}} L \sigma_f$.

The energy loss of an ion W_{loss} is the energy E_{ion} used to accelerate the ion plus the bremsstrahlung losses E_b from trajectory changes due to Coulomb collisions. Additionally, Coulomb collisions cause a transfer of energy ΔE_c between colliding ions, which must be compensated for by the compressing electric fields to keep the ions bunched. The bremsstrahlung losses of an ion transversing through a colliding ion bunch are derived by integrating the power losses P_b of a single ion-ion interaction over all scattering events and impact parameters occurring between the ion and the bunch. The derivation closely follows the approach of Freidberg [8], chapter 3 (not all steps are reproduced in this work, all units are in SI units unless stated otherwise).
The radiated power of an accelerated or decelerated particle is calculated with the Larmor formula [170].

$$P_b = \frac{q^2 a^2}{6\pi\epsilon_0 c^3}, \tag{B.3.17}$$

with charge q, acceleration a, vacuum permittivity ϵ_0, and speed of light c. From the radiated power P_b, the energy loss per ion-ion collision is obtained: $W_b = P_b \cdot \Delta t$. The generalised reaction rate per unit volume and per unit time, w, is obtained by integrating the energy change W of a single ion-ion collision over the distribution functions of all particle species and scattering angles:

$$w = 2\pi \int W(v,b) f_1(\boldsymbol{v_1}) f_2(\boldsymbol{v_2})\, v\, b \,\mathrm{d}b \,\mathrm{d}\boldsymbol{v_1} \,\mathrm{d}\boldsymbol{v_2} \tag{B.3.18}$$

Here f_i are the distribution functions, $v = |\boldsymbol{v_1} - \boldsymbol{v_2}|$ the relative velocity, and b the impact parameter. Assuming two colliding ion bunches with density n_1 and n_2 and a constant ion velocity distribution with $v_{\text{ion},1} = -v_{\text{ion},2}$, the integration is straight forward. The energy loss E_b of a single ion passing through a colliding bunch with length L is:

$$E_b = w_b \cdot t \tag{B.3.19}$$

$$= \frac{Z^2 q^6 n L}{12\pi h \epsilon_0^3 c^3 m_{\text{ion}}} \quad \text{[J]}, \tag{B.3.20}$$

with charge Z, density n, Planck constant h, and ion masses m_{ion}. A deuterium ion traveling $L = 1$ m through a target at solid state density $n \approx 1 \cdot 10^{28}$ m^{-3} will only radiate $E_b \approx 1$ eV. Thus, the bremsstrahlung losses are negligible compared to E_{ion}.

The second loss mechanism is due to energy transfer in Coulomb collisions between colliding bunches (the energy transfer in a single ion-ion collision is calculated in appendix B.3.6). The net energy loss in a system of colliding bunches is however argued to be zero: transversal energy transfer results in a fast and a slow ion after the collision. When compressing the bunches, the energy required to speed up the slow particle is equal to the energy gained by the system when slowing down the fast particle.

With this, the energy loss W_{loss} is:

$$W_{\text{loss}} = E_{\text{ion}}, \tag{B.3.21}$$

and equation B.3.15 becomes

$$n \cdot L \cdot N_{\text{pass}} > \frac{E_{\text{ion}}}{E_f \sigma_f} \tag{B.3.22}$$

$$\overset{(D\rightarrow D)_{\min}}{\gtrapprox} 3.7 \cdot 10^{27}\,\text{m}^{-2} \tag{B.3.23}$$

$$\overset{(D\rightarrow T)_{\min}}{\gtrapprox} 5.9 \cdot 10^{24}\,\text{m}^{-2} \tag{B.3.24}$$

The requirements on $n \cdot L \cdot N_{\text{pass}}$ in equation B.3.22 are plotted in figure B.3.6 for various ion energies E_{ion}. The minimal values (see equation B.3.23 and B.3.24) are determined from the graph. An estimate for the achievable values of the density, bunch length and number of passes will be made in section B.3.4, after a concept for a non-Maxwellian, bunched, confinement device, and its feasibility, is shown in the next section.

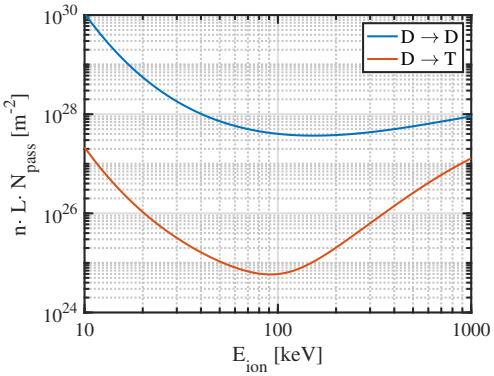

Figure B.3.6: Energy dependent minimal values of $n \cdot L \cdot N_{\text{pass}}$ required for energy break-even for colliding deuterium and deuterium-tritium bunches at different energies.

B.3.3 Feasibility study

Conceptual design

Based on the previous considerations, a design is proposed to investigate the feasibility of a device confining oscillating ion bunches. The design is based on an idealised spherical vacuum vessel in which three grids of different radii are used to accelerate and compress the ions. An illustration of the concept is given in figure B.3.7. The vacuum vessel (at ground potential) has a radius r_v in which the three spherical grids with radius r_1, r_2, r_3, henceforth referred to as inner, middle, and outer grid, are centred.
Ions are injected into the system by two ion guns, placed on the equatorial plane. A constant potential is applied on the outer grid to accelerate the ions to their target energy (acceleration region shaded in red). The inner and middle grid are initially at the same potential as the outer grid, creating a field free region in the compression area (purple shaded area). Three grids area required for bunch compression to create a symmetric electric field between the middle and outer, and between the middle and inner grid, when a pulsed potential is applied to the middle grid. When applying a pulsed potential at grid 2 at the right time, the fast, leading ions of the bunch will decelerate between grid 2 and grid 3, while slow, trailing ions accelerate between grid 1 and grid 2. If the timing and applied potential is set correctly, the slower ions are expected to catch-up with the fast ones and the ions remain bunched.

The motion of an ion bunch through the vessel can be described in 4 steps, which are marked in figure B.3.7:

1 **Injection & acceleration:** The potential of the three inner grids are at equal negative potential. Particles are injected into the system and accelerate to their maximum energy between the vessel and outer grid.

2 **Constant motion:** The potentials of the inner, middle and outer grid remain constant, creating a field free region within the outer grid. Particles travel with constant energy through the inner grid and collide with oncoming bunches.

3 **Compression:** After the passage through the inner grid, the potential of the middle grid is pulsed in such a way that the ions remain in a bunched state and that all bunches arrive simultaneously in the centre of the device during their next oscillation.

4 **Deceleration & acceleration:** After leaving the outer grid, the particles get decelerated and begin to accelerate back towards the centre of the device.

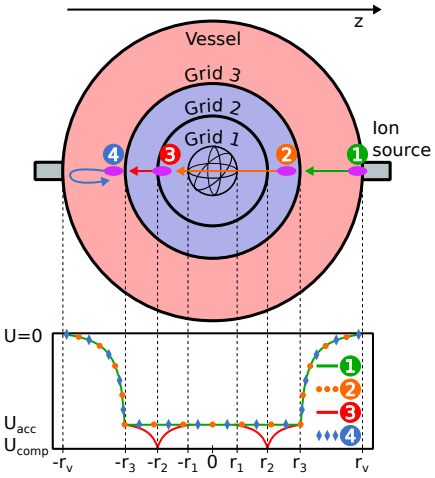

Figure B.3.7: Top: The working principle of the proposed design. Ions are injected at the edge and accelerate until they reach grid 3. After having passed through grid 1, a pulsed potential is applied to grid 2 to compress the bunch. The requirements on the pulsing will be explored in section B.3.3. In this sketch only one ion bunch is drawn to clarify the individual steps. In an actual implementation more bunches are required for bunch collisions in the centre. Bottom: The electric potential required to accelerate and compress the bunch(es). The figure is scaled for the simulations of sections B.3.3 & B.3.3.

The feasibility of this concept is evaluated in two steps: First, by simulating low density bunches without Coulomb interactions between particles, the timing and strength of the pulsed potential required for transversal bunch compression are determined in section B.3.3 (step 3). Second, we evaluate whether the ions remain radially bunched (as calculated in section B.3.2). For this, simulations where Coulomb interactions between particles are taken into account are performed for

bunches with initial densities up to $n_b = 1 \cdot 10^{17}$ m^{-3} in section B.3.3.

Determination of the pulse parameters for bunch compression

The conceptual design is implemented in the particle tracer GPT [171] with the goal to numerically determine the viability of keeping an ion bunch compressed and at a non-maxwellian velocity distribution. GPT is a commercially available 3D particle tracer which can track the trajectories of particles in external electric and magnetic fields. It includes modules for particle-particle interaction via the Coulomb force and can be extended with custom modules. The code uses a 5th order Runge-Kutta driver with adaptive stepsize control to ensure fast and accurate computation. GPT was originally developed for the design of accelerators and beam lines for which a number of components are built in. Due to its modularity the software can be extended for a wide variety of problems [172].

Figure B.3.8 shows the expected averaged ion motion along the z-axis of a single bunch. A pulsed electric potential (simulated as a block wave; simulation step & potential shape 3 in figure B.3.7) is applied to the middle grid while the bunch passes through the compression region. The unknowns to be determined by the simulation are the strength of the electric potential and the timing of the pulse. The probed timing parameters are visualised in figure B.3.8. A numerical parameter scan is used to determine the starting time t_s of the first pulse, the period T, the duration of the pulse Δt and the strength of the potential ΔU. The goodness of a simulation is evaluated by the transversal bunch length at the end of the simulation, where a lower bunch length along the direction of propagation corresponds to a better bunch compression.

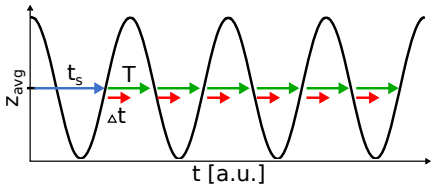

Figure B.3.8: Expected average ion motion of a bunch along the z-axis. A parameter scan is made to determine the time t_s when the potential ΔU is first applied at the middle grid, with which period T, and the duration of the pulse Δt.

The geometry of the simulation is based on an available vacuum chamber in our group, which can provide a future testbed for the device. The radii of the three grids and vacuum vessel are: $r_1 = 0.05$ m, $r_2 = 0.10$ m, $r_3 = 0.15$ m, and $r_v = 0.3$ m (which is the radius of the available vacuum vessel). The scaling of the grids is shown in figure B.3.7. An equal spacing between the inner, middle and outer grid is chosen to obtain symmetric electric fields in the compression region. The distance between outer grid and vacuum vessel was chosen 3× the distance between

the inner grids to obtain small gradients of the electric field for $r \to r_v$ (later, the potential required for longitudinal bunch compression will be estimated based on this).
The vacuum vessel is at ground potential, grids 1, 2, and 3 are initially at $U_0 = -10$ kV. The chosen U_0 is too low to obtain appreciable fusion rates, instead it is based on the premise of designing an easy to implement first experiment to demonstrate the feasibility of sustaining oscillating ion bunches.

For the determination of the pulsed field parameters only a single bunch is simulated. The particle bunch is initialised at $(x_0, y_0, z_0) = (0, 0, 0.25)$ m at $t = t_0 = 0$ s. The bunch has a dimension of $\Delta x = \Delta y = 10\,\mu$m and $\Delta z = 0.01$ m and consists of 100 hydrogen ions which are uniformly distributed in the volume. Coulomb interactions between ions are disabled to decrease the computation time (high-density simulations with particle-particle interactions are analysed in section B.3.3).

The electric field $E(r)$ acting on the particle is equivalent to the field inside a spherical capacitor and calculated analytically for each particle at each simulation step:

$$E(r) = U \cdot \frac{r_b - r_a}{r_a \cdot r_b} \cdot \frac{1}{r^2}, \tag{B.3.25}$$

with the diameter of the larger sphere r_b, diameter of the smaller sphere r_a and radial location of the particle r. The fields are calculated in the same way for both the acceleration region between the outer grid and vacuum vessel and the compression region within the outer grid.

As an initial guess for ΔU the potential difference between leading and tailing particle (bunch length $\Delta z = 1$ cm) is taken. The starting time t_s is chosen to allow the particles one oscillation before the first pulse is applied, the period T is estimated from the oscillation frequency of the bunch and the duration Δt is estimated from the time it takes a particle to travel the distance between the inner and outer grid. The evaluated parameter ranges are:
The duration of each simulations is $t = 10\,\mu$s (the equivalent of 16 oscillations), this short simulation time was chosen to complete the simulations in a reasonable time.

For all simulations the figure of merit, the bunch length at the end of the simulation, has been calculated. Only the result with the best bunch compression is presented in figure B.3.9. Shown is the averaged ion motion of the bunch along the z-axis (top) and the evolution of the particle density function (PDF) for eight different times when the bunch crosses the centre of the device at $z = 0$ m. Two evolutions of the PDF are shown: In b): the evolution of the PDF for a static accelerating field between the vessel and outer grid and no pulsed compression potential. A spread of the bunch over the whole volume is observed within a few

Parameter	Start	End	n_{steps}
ΔU [V]	226	254	14
t_s [ns]	990	1010	10
T [ns]	620	640	10
Δt [ns]	0	40	20
Total # simulations: 28000			

Table B.3.1: Evaluated parameter ranges of the electric potential and the timing of the potential. Each parameter range was discretised into n_{steps} equal steps, resulting in a total of 28000 simulated combinations.

oscillations due to the finite initial bunch length, leading to different oscillation times of the ions. In c): the evolution of the PDF with active compression for the numerically determined ideal parameters of the pulsed potential. The determined parameters are: $\Delta U = 254$ V, with timing $t_s = 1002$ ns, $T = 628$ ns $\rightarrow f = 1/T \approx 1.6$ MHz and $\Delta t = 38$ ns. The ions remain bunched throughout the whole simulation and only a spread in length to approximately the inner grid diameter is observed.

In addition to the compression along the z-direction the ions must also remain bunched transversal to the oscillatory direction. Figure B.3.10 shows the evolution of the bunch width in the x and y direction. Within the simulation time the bunch stays compressed, with 84% of the particles remaining within an 80 μm diameter after 16 oscillations.

To conclude this section, figure B.3.11 shows the energy distribution of the particles from the reference simulation and compressed simulation. In the reference simulation the majority of the particles has the maximum energy during the last zero crossing of the bunch, due to the large diameter of the outer grid within which all particles are at the maximum energy. As expected from the spread of the particles along the z-direction in the bunched simulation, all particles are at their maximum energy at the last pass when the compression field is activated (the visible spread is due to the finite bunch length).

High-density simulation with Coulomb interactions between particles

The previously determined parameters are used to investigate whether bunches can be sustained if Coulomb interactions between ions are included in the simulation. The GPT code is used to determine the maximum sustainable charge density in a bunch, and whether bunches at the density limit can be sustained for longer times than previously simulated.
The applied potential, grid geometry and initial bunch geometry are equivalent to the simulations in the previous section. Varied are only the number of particles initialised in the bunch volume.

Density scan

In section B.3.2 a theoretical limit on the maximum bunch density was derived. Now, bunches with different initial charge densities are simulated and compared to the calculated density limit.

In figure B.3.12, the theoretical limit on the bunch density, calculated by equation B.3.14, is plotted for various bunch widths h_b, depending on the radial location of the bunch in the acceleration region. The density converges for $h_b \to 0$ m to $n_{\mathrm{b,max}} \approx 4.9 \cdot 10^{13}$ m^{-3} at $z = r_v = 0.3$ m. During the acceleration from the edge to the centre, the compressing Coulomb force $F_{C,\perp}$ increases, which is expected to partly compensate for the bunch expansion in the compressing region.

The compressing electric field is in its shape similar to the electric field in the compression region (central field, $\mathscr{E} \propto r^{-2}$), but due to low potential required to

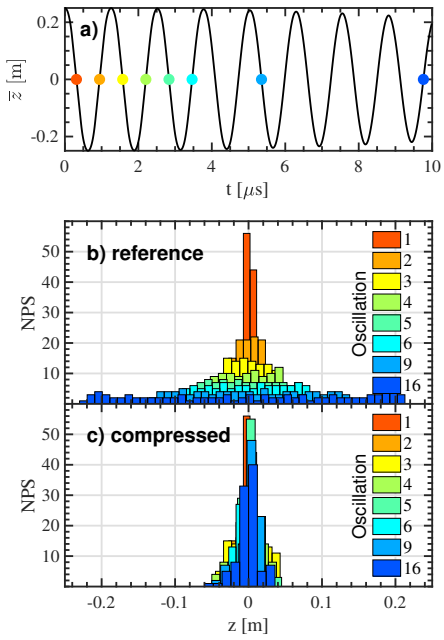

Figure B.3.9: Determined field parameters using GPT to maintain an oscillating ion bunch. a) Averaged z-coordinate of all particles over time. The bunch oscillates along the z-axis of the device. b) and c): Particle density function (PDF) without and with the pulsed electric field in the compression region. The PDFs are plotted for eight different times when the bunch crosses the centre of the device. The colour of the PDFs corresponds to the times marked in a). The bunch compression in c) is obtained with $\Delta U = 254$ V, $t_s = 1002$ ns, $T = 628$ ns, and $\Delta t = 38$ ns. These field parameters resulted in the lowest bunch length along the z-axis at the end of the simulated time.

compress the bunches and short pulse duration it will not significantly contribute to the transversal compression.
To test the developed formalism for the maximum bunch density, bunches with varying initial charge density n_0 are simulated. Simulated is a single bunch consisting of 1000 macro particles for $\delta t = 5\,\mu$s, the equivalent of 4 full oscillations. The charge of the macro particles is adjusted to match the desired initial charge density of the bunch. The density n_{end} and volume V_{end} of the bunch at the end of the simulation are compared to the initial density n_0. The results of the simulations are shown in figure B.3.13. For starting densities up to $n_0 = 10^{17}$ m^{-3} the bunch volume increases in order to equilibrate n_{end} below $n_{\text{b,max}}$. In the graph, the maximum bunch density $n_{\text{b,max}}$ is plotted for $h_b \to 0$ m and $z = 0.25$ m (the initial bunch location), see equation B.3.14 and figure B.3.12. It was verified that the bunch length, i.e. the spread of particles in the direction of motion, remains almost constant due to the longitudinal bunch compression, and that the increased volume is due to a larger bunch width. For $n_0 > 10^{17}$ m^{-3} the ions can no longer be transversally confined, leading to debunching characterised by an increase in

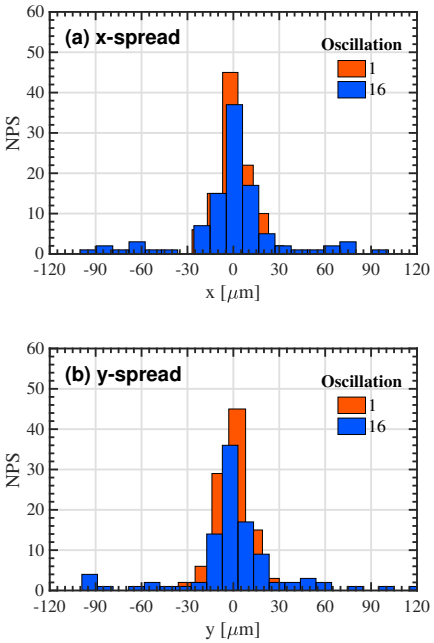

Figure B.3.10: GPT results showing the bunch spread in the x- and y-direction of the compressed simulation at the first and last oscillation. The majority of the ions are confined within $\Delta x = \Delta y = 30\,\mu$m, a three times increase compared to the initial bunch width of $10\,\mu$m. The small radial expansion is attributed to the lack of Coulomb interaction between the ions.

volume and a drop in n_{end}.

Long-time, high-density simulation with colliding ion bunches
The density scan only simulated a single bunch for a total of 4 oscillations to investigate transversal bunch confinement. Now, the bunching is evaluated for

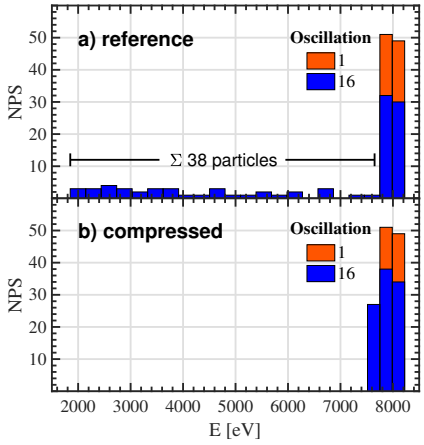

Figure B.3.11: Energy spread of the reference and the compressed simulation at the first and last oscillation (compare to figure B.3.9). In the compressed simulation all particles are at the maximum energy. In the reference simulation all particles within the outer grid are at the maximum energy.

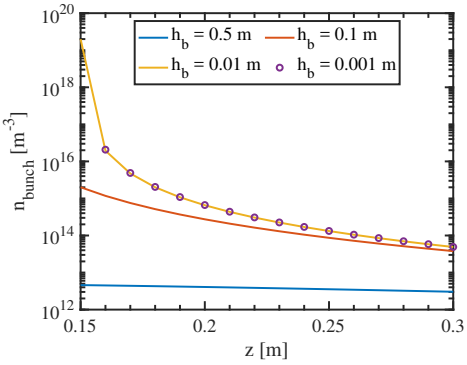

Figure B.3.12: Analysis of the derived density limit (see equation B.3.14). Plotted is the calculated limit on the bunch density n_{bunch} for various bunch widths h_b as the bunch moves from the vacuum vessel to the outer grid. Due to the falloff of the electric field the sustainable bunch density decreases for larger z. Due to the lower total charge slimmer bunches can sustain higher densities (see equation B.3.13).

colliding ion bunches over longer simulation times.
Two bunches are initialised at $z = \pm 0.25$ m, the bunch dimensions are equivalent to the bunch dimension in the previous sections. As in the density scan, each bunch consists of 1000 macro particles. Each macro particle has a charge of 10.000.000 q, resulting in an initial bunch density of $n = 10^{16}\,\mathrm{m}^{-3}$. Coulomb interactions between all particles are calculated by the GPT code at every time step. The system is simulated for $100\,\mu$s, approximately 160 oscillations.
The simulation results are presented in figure B.3.14 and B.3.15. Figure B.3.14 shows the PDF of the two colliding bunches along their trajectory of motion. The PDFs show that both bunches remain bunched throughout the entire simulation with a final bunch length of ≈ 10 cm. Throughout the simulated time, no change in bunch length is observed and it can be assumed that longer confinement is feasible.
Figure B.3.15 shows the spread of the ions in the x- and y-direction. Compared to the simulation without space charge effects (see section B.3.3), a larger transversal spread is observed. The increased spread is already visible in the first oscillation and attributed to Coulomb repulsion of the particles. The transversal spread remains constant throughout the simulated time.
In summary, the simulations show that colliding ion bunches can be sustained with minimal losses over a long period of time with densities close to the theoretical limit.

Macro particle validation
In the simulation macro particles are used to reduce the computational time. However, the use of macro particles in GPT is known to give inaccurate estimates of the Coulomb interaction. To verify that the use of macro particles does not falsify

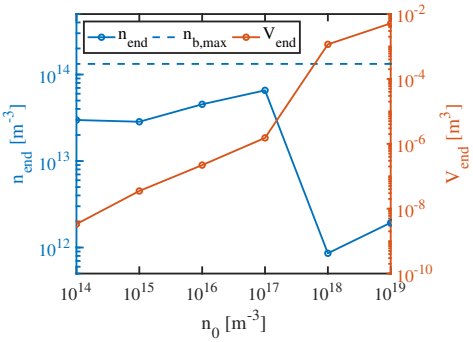

Figure B.3.13: Comparison of the bunch density n_{end} and bunch volume V_{end} of a bunch after 4 oscillations for varying initial bunch densities n_0. For $n_0 < 10^{17}$ m^{-3} the bunch volume increases, keeping the density below the calculated maximum density $n_{\mathrm{b,max}}$. For initial bunch densities of $n_0 > 10^{17}$ m^{-3}, transversal bunch confinement is no longer possible, characterised by a large increase in bunch volume and a corresponding drop in n_{end}.

the presented results, three checks have been performed comparing the behaviour of ion bunches with 100.000 real particles against ion bunches composed of 1.000

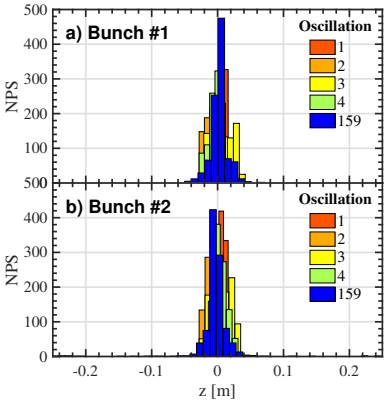

Figure B.3.14: Evolution of the PDF of the two simulated high-density bunches along the z-axis at the first 4 and the last oscillation. The initial bunch density is $n = 10^{16}\,\mathrm{m}^3$ and Coulomb interactions between particles are simulated. Both bunches remain bunched with a bunch length of ≈ 0.1 m. The parameters for the timing of the pulsed fields and electric potential are $\Delta U = 254$ V, $t_s = 1002$ ns, $T = 628$ ns and $\Delta t = 38$ ns, equivalent to the ideal parameters determined in section B.3.3. At the 159th oscillation, 986 particles of bunch #1 and 976 particles of bunch #2 remain within an interval $\Delta z = [-0.05, 0.05]$ m.

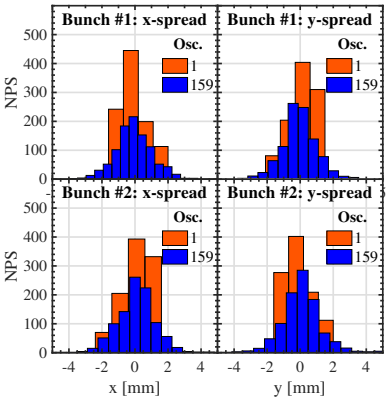

Figure B.3.15: Spread of the two bunches in the x- and y-direction. Most of the particles remain bunched. Compared to the simulation without space charge effects a larger expansion is visible due to the Coulomb repulsion between ions. At the 159th oscillation, 991 particles of bunch #1 and 985 particles of bunch #2 remain within the plotted interval $\Delta x = \Delta y = 10$ mm.

macro particles with total charge 100.000 q, resulting in equal charge densities for both cases. In the three described simulations no external fields are present and the resulting trajectories of all ions are due to Coulomb interactions between particles.
First, the radial expansion of a stationary ion cloud with initial radius $r = 0.01$ m (equivalent to the initial bunch length in the previous simulations) is simulated. The average particle displacement in the macro particle simulation was overestimated by 7%.
Second, the scattering of two colliding bunches was simulated to estimate the effect on the scattering angle during collisions in the centre of the device. The simulated bunches have the same dimensions as the ones used to demonstrate the bunching of high-density bunches in this section ($\Delta x = \Delta y = 0.00001$ m and $\Delta z = 0.01$) and collide head-on. Compared was the averaged scattering angle of all ions after the collision. On averaged the scattering angle was overestimated by $\approx 35\%$ in the macro particle simulation.
Third, for a simulation time of $10\,\mu$s, using the parameters for the pulsed electric field determined in section B.3.3, the simulation was run with 10.000 macro particles and a charge of 100.0000 q. The result was compared to the simulation with 1000 macro particles of equal total charge and no significant difference was found in the bunch spread along the x, y and z direction.
The three simulations show an overestimation of the Coulomb interaction when macro particles are used. In the performed simulation of the colliding bunches, smaller scattering effects from the ion-ion interaction are expected when no macro particles are used - a desirable result. It is concluded that the simulations give a good indication that the macro particle simulations are valid.

Sensitivity study

In the initial determination of the ideal field configuration for bunch sustainment number of other timings and field strengths were found which confined the bunches, but at worse performance (i.e. a larger transversal spread of the bunches). For an experimental implementation it is important to know how accurately the determined parameters must be met. A Monte Carlo scan is performed to map the parameter space where bunching occurs. Varied parameters are the electric potential ΔU, the pulse period T and the duration of the pulses Δt.

As previously shown, the results achieved with a single bunch of 100 ions without particle-particle interaction provided results which are directly transferable to high-density simulations with space charge effects enabled. To obtain a fast, first estimate, the simulations in the Monte Carlo analysis are again run with only a single bunch of 100 particles and without space charge effects. The simulations are run for $10\,\mu$s.

A total of 1000 simulations were run and checked whether the ions remain bunched. A simulation is said to be bunching if the bunch length along oscillatory direction,

i.e. the z-axis, does not exceed the inner grid diameter, i.e. $\Delta z_{\text{bunch}} < 0.10$ m, at the end of the simulation. This criteria was chosen because the bunch length at the end of the simulation in both the parameter scan (section B.3.3) and the high-density simulation (section B.3.3) was comparable to the inner grid diameter.

The Monte Carlo scan showed that a large parameter window exists in which bunching occurs. Electric potentials as low as 100 V and up to 800 V are able to compress the bunch, the compression period T can be varied 600 ns - 640 ns, and the pulse duration Δt can vary between 30 ns - 130 ns. Note, that the parameters are interlinked and not all combinations are possible.
These findings allow for some freedom in an experimental implementation and further more let us assume that the pulses can have a finite rise and fall time, unlike the perfect rectangle pulse shape used in the simulations. The results of the Monte Carlo scan will not be presented in further detail because they are not relevant for the conceptual study presented in this work.

B.3.4 Application to an energy producing fusion reactor

After having shown the feasibility of maintaining colliding ion bunches with a non-Maxwellian velocity distribution, the energy gain criteria derived in section B.3.2 is revisited to discuss the requirements on an energy producing fusion machine.

The proposed concept uses a symmetrical triple grid configuration to compress the bunches during each oscillation, requiring an equal oscillation period of all ions. This limits the available fuel to a single species. For energies below ≈1 MeV, deuterium-deuterium fusion has the highest cross section. For D-D fusion reactions, the minimum requirements on the density, bunch length and number of oscillations have been determined to (see equation B.3.23):

$$n \cdot L \cdot N_{\text{pass}} = 3.7 \cdot 10^{27}\,\text{m}^{-2}, \tag{B.3.26}$$

at a centre of mass energy $E_{\text{cm}} \approx 130$ keV. Based on the simulations, a maximum value for N_{pass} is estimated and the maximum density is calculated based on the theoretical considerations from section B.3.2. With $N_{\text{pass,max}}$ and $n_{\text{b,max}}$ the requirements on the bunch length L are determined.

Maximum number of oscillations N_{pass}: The maximum number of possible passes are estimated from the high-density simulations (see figure B.3.14). Here, ≈ 2% of the particles were lost after 160 oscillations. We verified that the decrease in particles is approximately linear in the simulated time. Assuming a continued linear loss of particles in the bunch, all particles will be lost after ≈ 8000 oscillations, resulting in an average $N_{\text{pass,max}} = 4000$ oscillation per ion before it lost.

Density n: In section B.3.2 an estimate for the maximum achievable bunch density per unit length was developed, which is recited here for convenience:

$$n_{\text{bunch}} = \frac{2\epsilon_0 U}{q} \frac{1}{r_v^{-1} - r_i^{-1}} \cdot \frac{1}{\left(\sqrt{h_b^2 + z^2} - r_i\right)^2} \cdot \frac{1}{\sqrt{h_b^2 + z^2}} \tag{B.3.27}$$

The maximum density n_{max} is estimated under the assumption that the aspect ratio between the vacuum vessel and outer grid is 0.5 (equivalent to the simulated design). With this condition, equation B.3.27 is evaluated for different r_v and h_b, the result show in figure B.3.16. In the figure, no data points are calculated for $r_v < h_b$. As previously shown, n_{b} has its minimum at r_v, for which the values $n_{\text{b,max}}$ are calculated. Because the electric field $E \propto 1/r^2$, the maximum bunch density increases with decreasing chamber radius r_v.

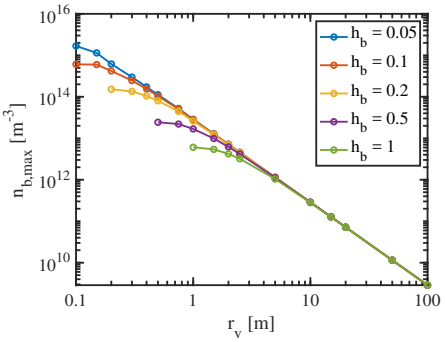

Figure B.3.16: Calculated maximal transversally compressible bunch density $n_{\text{b,max}}$ depending on the radius of the vacuum vessel r_v. It is assumed that $r_i = r_v/2$. $n_{\text{b,max}}$ is plotted for various bunch widths h_b. The graph shows an increase in $n_{\text{b,max}}$ for smaller r_v due to the increasing gradients of the electric field for $z \to r_v$.

Bunch length L: By plugging $N_{\text{pass,max}}$ into equation B.3.26, we find

$$n \cdot L = 9 \cdot 10^{23}\,\text{m}^{-2} \tag{B.3.28}$$

Comparing with figure B.3.16 it is clear that no achievable combination of L and n can fulfil equation B.3.28.

With the proposed concept of a bunched spherical particle collider, achieving net

energy gain with deuterium–deuterium collisions is not possible. A way to relax the criteria for net energy is to switch to deuterium-tritium as a fuel. Then,

$$n \cdot L \cdot N_{\text{pass}} \overset{(D\rightarrow T)_{\min}}{=} 5.9 \cdot 10^{24}\,\text{m}^{-2} \tag{B.3.29}$$

However, even then the achievable density and bunch length would not suffice.
A solution to increase the density could be to modify the concept to accelerate deuterium bunches through a stationary tritium target, for example a cryogenic hydrogen jet, which have been reported with radii as low as $5\,\mu$m [173]. These targets are however not electron free and the fundamental limitation of beam-target fusion (i.e. dominating Coulomb power losses - see figure B.3.1) will prevent net energy gain unless a way is found to remove the electrons. Assuming one is able to remove the electrons during the time the oscillating ions pass through the target, e.g. by pulsed lasers, and if the remaining pure ion plasma remains close to solid state density due to the inertia of the ions while the bunches pass through the target, net energy gain could be possible. An in-depth analysis is required to evaluate the feasibility of such a system, which is outside the scope of this work.

B.3.5 Discussion

In this article a novel concept for a fusion machine based on electrodynamic confinement of ion bunches is proposed. Analytical estimates of the expected fusion rate, maximum bunch density and requirements on the bunches for net energy gain are made. By using a particle tracing code, it is shown that ions can remain longitudinally and transversally bunched over 160+ oscillations with only 2% particle losses while remaining at a non-Maxwellian energy distribution in an electron free system.
Using both the energy gain criteria and simulation results, the requirements for break-even operation of a fusion reactor based on deuterium-deuterium fuel is made. However, with the proposed concept achieving break-even conditions are not possible because the confinable density is over 8 orders of magnitude too low. A more efficient design could be a storage ring, which can fulfil the energy gain criteria due to the increased confinement time and higher focus density[¶]. However, due to the overall low number of particles and bunch volume, a storage ring cannot produce a substantial amount of fusion power. In future investigations for a collider-type fusion power plant, increasing the density and volume are of paramount importance.
Due to the low losses the concepted design could be implemented as an efficient neutron generator, however the absolute neutron yield will again be limited by the low densities and the low duty cycle compared to a steady state device.
For a practical implementation particle losses to the grid must be investigated and mechanisms derived on how to minimise them. The so-called star-mode of inertial

[¶]The evaluation of the energy gain criteria and resulting power output on the example of the Large Hadron Collider is included in appendix B.3.8

electrostatic confinement (IEC) devices is proposed as a possible solution: in IEC devices, which are a type of gridded spherical accelerators, good ion confinement with low grid collision has been reported through the formation of microchannels, in which the ions are confined on oscillatory trajectories with low grid collisionality [174]. Furthermore, an actual implementation will require connectors between the grids and power supply, which will, similar to a fusor, introduce an asymmetry in the vacuum electric field. If the stalk is surrounded by a dielectric, charge deposition of ions colliding with it will mitigate the perturbing field in the acceleration region. In the compression region the field asymmetry will play a lesser role because of the tighter grid spacing and the low strength of the compressing field.

Appendix

B.3.6 Coulomb power losses and fusion power gain in a beam-target experiment

Coulomb power losses

The power loss due to Coulomb collisions of a charged particle traveling through a stationary target is calculated. In the derivation, first the energy losses between two interacting particles are calculated from which the power loss of an ion traveling through a target with density n is derived.
The scattering between a particle with mass m_1, velocity v_1 and charge q_1, and a particle at rest with mass m_2, velocity $v_2 = 0$ and charge q_2 is sketched in figure B.3.17.

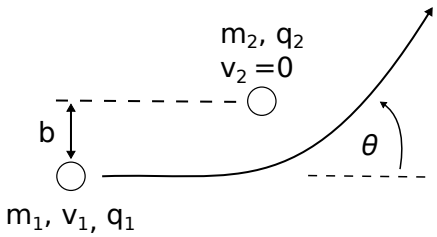

Figure B.3.17: Coulomb scattering between a moving and a stationary particle.

Depending on the impact parameter b, particle one will not only change its trajectory, but also transfer energy ΔE to particle two [175]:

$$\Delta E = \frac{1}{2} m_1 v_1 \frac{2 m_1 m_2}{(m_1 + m_2)^2} (1 - \cos(\theta)) \tag{B.3.30}$$

Using the relation

$$\tan(\theta/2) = \frac{q_1 q_2}{4\pi\epsilon_0} \frac{1}{m_r v_1^2 b}, \tag{B.3.31}$$

equation B.3.30 can be rewritten as

$$\Delta E = 2\frac{m_r^2}{m_2}\frac{v_1^2}{1+K^2 m_r^2 v^4 b^2} \tag{B.3.32}$$

$$= \frac{2\Delta E_{c,90^\circ}}{1+(b/b_{90})^2} \tag{B.3.33}$$

with $K = 4\pi\epsilon_0/(q_1 q_2)$, relative mass $m_r = (m_1 m_2)/(m_1 + m_2)$, and $b_{90} = 1/(K m_r v^2)$

To calculate the power loss of two colliding ion bunches, equation B.3.33 is plugged into equation B.3.18:

$$P_c = 2\pi \int W(v,b) f_1(\boldsymbol{v_1}) f_2(\boldsymbol{v_2})\, v\, b\, \mathrm{d}b\, \mathrm{d}\boldsymbol{v_1}\, \mathrm{d}\boldsymbol{v_2} \tag{B.3.34}$$

$$= \frac{4\pi m_r^2}{m_2} \int \frac{v_1^3 b}{1+K^2 m_r^2 v^4 b^2} f_1(\boldsymbol{v_1}) f_2(\boldsymbol{v_2})\, \mathrm{d}b\, \mathrm{d}\boldsymbol{v_1}\, \mathrm{d}\boldsymbol{v_2} \tag{B.3.35}$$

For the case of an ion beam with velocity $v_x = v_y = 0$, and $v_z = v_0$ impacting on a stationary target, $v = |\boldsymbol{v_1} - \boldsymbol{v_2}| = v_0$, the integral $\int f_2(\boldsymbol{v_2})\mathrm{d}\boldsymbol{v_2} = n_2$, and furthermore $f_1(\boldsymbol{v_1}) = f_1(\delta v_x = 0, \delta v_y = 0, \delta v_z = v_0)$. With this, equation B.3.35 becomes

$$P_c = \frac{4\pi m_r^2}{m_2} n_1 n_2 \int_0^\infty \frac{v_0^3 b}{1+K^2 m_r^2 v_0^4 b^2}\, \mathrm{d}b \tag{B.3.36}$$

$$= \frac{4\pi m_r^2}{m_2} n_1 n_2 \frac{v_0^3}{2k^2 m_r^2 v_0^4} \ln\left(1 + 2k^2 m_r^2 v^4 b_\infty\right) \tag{B.3.37}$$

For $b \to \infty$ the logarithm diverges and b must be cut-off. This is done in the usual way by limiting the impact parameter to the Debye length λ_D. With $\ln(1 + \lambda_D^2/b_{90^\circ}^2) \approx 2\ln(\lambda_D/b_{90^\circ}) \equiv \ln(\Lambda)$, equation B.3.37 is rewritten as

$$P_c = \sigma_c \Delta E_{c,90^\circ} n_1 n_2 v_0 \tag{B.3.38}$$

where the Coulomb cross section has been defined as $\sigma_c = \ln(\Lambda)\left(q_1^2 q_2^2\right) / \left(4\pi\epsilon_0^2 m_r^2 v_0^4\right)$ and the energy loss for perpendicular scattering is $\Delta E_{c,90^\circ} = m_r^2 v^2 / m_2$. Note that equation B.3.38 was derived under the assumption of quasi neutrality, i.e. an equal electron and ion density $n_e = n_i$. In the case of a pure ion (or electron) plasma, the Debye length changes as $\lambda_{D,pure} = 0.5\lambda_D$ [176].

Fusion power gain

The fusion power gain is calculated via

$$P_f = E_f n \sigma v, \tag{B.3.39}$$

where E_f is the released energy per fusion reaction (summed over all reaction channels), n the density, σ_f the velocity dependent fusion cross section and v the centre of mass velocity. Values for σ_f are taken from [177].

B.3.7 Derivation of the reaction rate in a linear system with oscillating bunches

The reaction rate is estimated in a linear system with two oscillating ion bunches. The geometry is sketched in figure B.3.18: The ions are accelerated between the anode and cathode and collide in a field free region in the centre.

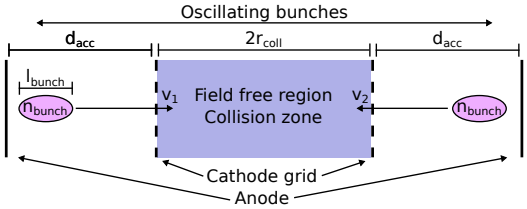

Figure B.3.18: Linear geometry used to estimate the reaction rate of two colliding, oscillating ion bunches.

The reaction rate R in this system is:

$$R = C_{\text{pass}} \cdot f \quad [\text{s}^{-1}] \tag{B.3.40}$$

Where C_{pass} are the number of collisions during one oscillation and f the oscillation frequency. C_{pass} is calculated in the usual way:

$$C_{\text{pass}} = n_1 n_2 \sigma(v) v V_{\text{bunch}} \Delta t \tag{B.3.41}$$

Here, n_i are the densities of two colliding beams, $\sigma(v)$ the cross section, $v = |v_1 - v_2|$ the relative velocity, V_{bunch} the bunch volume and $\Delta t = l_{\text{bunch}}/(2v)$ the collision time between the bunches, i.e. the time it takes an ion with velocity v to transverse through the oncoming bunch with length l_{bunch}.
Assuming the bunches have equal density $n_1 = n_2 \equiv n$, equal velocity $v_1 = -v_2$ and approximating the bunches as cylinders, (the bunch volume is expressed as bunch length l_{bunch} times bunch cross section A_{bunch}), equation B.3.41 becomes:

$$C_{\text{pass}} = \sigma(v)\, n^2 A_{\text{bunch}} l_{\text{bunch}}^2 \tag{B.3.42}$$

The frequency can be expressed as

$$f = (t_{\text{coll}} + 2t_{\text{acc}})^{-1}, \tag{B.3.43}$$

where t_{acc} is the time the bunches spend accelerating between the anode and cathode and t_{coll} the time of flight through the collision region.
The calculation of t_{coll} is straight forward:

$$t_{\text{coll}} = \frac{2r_{\text{coll}}}{\sqrt{2E_{\text{bunch}}/m}}, \tag{B.3.44}$$

where the velocity has been substituted for the kinetic energy E_{bunch}. In the linear design, the accelerating electric field is equivalent to the field of plate capacitor $\mathscr{E} = U/d_{\text{acc}}$, with potential difference U and distance d_{acc} between the electrodes. With acceleration $a = qU/(md)$, t_{acc} becomes

$$t_{\text{acc}} = \sqrt{\frac{2md_{\text{acc}}^2}{eU}}, \tag{B.3.45}$$

resulting in

$$f = \sqrt{\frac{2eE_{\text{bunch}}}{m}} \left(0.5\, r_{\text{coll}} + d_{\text{acc}}\right)^{-1} \tag{B.3.46}$$

Combining equation B.3.42 and B.3.46 leads to the final expression for the reaction rate:

$$R = \sqrt{\frac{2e}{m}} \cdot \frac{\sigma(E_{\text{cm}}) E_{\text{bunch}}^{1/2} n^2 A_{\text{bunch}} l_{\text{bunch}}^2}{0.5\, r_{\text{coll}} + d_{\text{acc}}} \tag{B.3.47}$$

$$\overset{D\rightarrow D}{\approx}{}^{*} \frac{3\, E_{\text{bunch}}^{7/6}[eV] n^2 A_{\text{bunch}} l_{\text{bunch}}^2 \cdot 10^{-29}}{\left(d_{\text{acc}} + 0.5 r_{\text{coll}}\right)} \tag{B.3.48}$$

$$\overset{D\rightarrow T}{\approx}{}^{\dagger} \frac{2\, n^2 A_{\text{bunch}} l_{\text{bunch}}^2 \cdot 10^{-21}}{\left(d_{\text{acc}} + 0.5 r_{\text{coll}}\right)} \tag{B.3.49}$$

*For energies 150-400 keV the D-D cross section can be approximated within 10% by $\sigma_{DD} = 2 \cdot 10^{-33} \cdot E_{\text{cm}}^{2/3}$, with centre of mass energy E_{cm}.

†The maximum D-T cross section is $\sigma_{DT}^{\max} \approx 5 \cdot 10^{-28}$ m^{-2} at $E_{\text{cm}} \approx 110$ keV was used.

B.3.8 Energy gain criteria and power generation in a storage ring

The analysis in section B.3.4 concluded that design modifications are required to achieve a positive energy balance. An example for devices having excellent ion confinement and high focus densities are storage rings. On the example of the Large Hadron Collider (LHC) we will examine whether such a device fulfils the energy gain criteria and how much power output could be achieved.
For the analysis the LHC geometry and its bunch parameters will not be changed, only the bunch energy is adapted to maximise the fusion cross section. Because LHC has two beamlines, we assume that deuterium and tritium can be used as a fuel, one species per beamline. For simplicity it is assumed that both species have approximately the same kinetic energy $E_{\mathrm{kin}} \approx 50$ keV and equal velocity. No modifications of the energy gain criteria (derived in section B.3.2) is required, which, for colliding deuterium and tritium bunches is:

$$n \cdot L \cdot N_{\mathrm{pass}} \gtrapprox 5.9 \cdot 10^{24}\ \mathrm{m}^{-2}. \tag{B.3.50}$$

First, the density n, bunch length L and number of oscillations N_{pass} for LHC are given to evaluate whether equation B.3.50 can be fulfilled before calculating the possible power generation. All values for LHC are taken from the [178, 179, 180, 181].

Evaluation of the energy gain criteria at an LHC-like device

Bunch length L and density n
At LHC, each bunch is composed of $N_{\mathrm{ion}} = 1.15 \cdot 10^{11}$ protons and has a length of $L = 30$ cm. When colliding, the bunches are focussed to 3.5 μm diameter, resulting in a density of $n \approx 3.1 \cdot 10^{22}\ \mathrm{m}^{-3}$.

Number of turns N_{pass}
The bunches at the LHC are confined for 10 h and make 11245 turn / second (at 7 TeV) in the 27 km long ring. At $E_{\mathrm{kin}} = 50$ keV, ions make ≈ 81 turns / second. Assuming an equal confinement time of 10 h for our DT bunches, $N_{\mathrm{pass}} \approx 2.9 \cdot 10^6$.

Energy gain criteria
The minimal required density n_{min} for energy gain is calculated by plugging N_{pass} and L into equation B.3.50, resulting in:

$$n_{\mathrm{min}} = 6.7 \cdot 10^{18}\ \mathrm{m}^{-3}, \tag{B.3.51}$$

which is four orders of magnitude lower than the bunch density during collisions at LHC. Thus, by using an LHC like setup energy gain is, in principle, possible.

Whether substantial fusion energy can be produced by a storage ring is calculated next.

Fusion power generation in an LHC-like storage ring

To calculate the generated fusion power, first the number of fusion collisions (see equation B.3.41) per bunch collision is calculated. The equation is repeated here for convenience:

$$C = n_1 n_2 \sigma(v) v V_{\text{bunch}} \Delta t \tag{B.3.52}$$

The densities of the deuterium and tritium bunch, n_1 and n_2 are assumed to be equal and have already been calculated to $n = 3.1 \cdot 10^{22}$ m^{-3}. The velocity and bunch volume are calculated from the energy and beam dimensions, the interaction time is $\Delta t = L/(2v) = 6.9 \cdot 10^{-8}$ s. With this, the number of fusion collisions per bunch collision C is:

$$C \approx 2 \cdot 10^5. \tag{B.3.53}$$

At LHC, there are 2808 bunches confined simultaneously in one beamline. To calculate the power, C is multiplied with the number oscillations per second, the number of bunches per beamline and the power gain per fusion collision (17.9 MeV), resulting in

$$P = 0.1 \text{ Watt}. \tag{B.3.54}$$

Although LHC could be turned into a fusion power plant, the output is low compared to the power required to keep the device running. The bottleneck is the small number of particles per bunch, which, could result in a viable concept if it can be increased. As an example: using the same design parameters to generate 100 MW would require $\approx 3 \cdot 10^{15}$ particles / bunch.

B.4 Conclusion B

So-called fusors are a type of fusion machines based on the principle of inertial electrostatic confinement (IEC). In IEC devices, ions are accelerated and trapped with static electric fields. They typically consist of a spherical, grounded vacuum vessel in which a transparent cathode grid at negative potential is centred. Ions accelerate towards the centre where they may fuse with other ions or gas particles. Fusors are attractive thanks to their small size as well as their cheap and robust design, but they experience high particle and energy losses caused by, among others, geometric effects, neutralisation of fast ions through charge exchange collisions, thermalisation of ions and bremsstrahlung losses by electrons. The research investigated the influence of experimental parameters (pressure, cathode potential, ion current) and the experimental configuration (cathode size and the influence of the stalk) on the performance of the TU/e fusor.
The research concludes that improving the performance of IEC devices is challenging and it is unclear whether substantial gains, required to make industrial IEC devices with a neutron production rate above the current record of 10^9 n/s are possible. The limiting factors are the unfavourable velocity distribution of ions, caused by a peak in the ion birth radius close to the cathode grid, as well as high losses of fast ions and quick thermalisation due to the large operating pressure.

Because most ions are created close to the cathode, they will accelerate to energies below the grid potential resulting in low fusion cross sections, decreasing their contribution to the reaction rate. A model of the ion birth radius, which has been qualitatively validated by experiments, shows that experimental parameters (pressure, cathode potential and cathode radius) have a minor influence on the birth radius. A significant shift of the birth radius towards the anode requires an external ion source and operation at low pressure. At high pressure, a large number of slow ions are created through ionisation and dissociation collisions within the cathode, which take up a significant fraction of the total current and limit the effectiveness of an external ion source. These results also show that an approximation of the fast ion current by Krupaker Murali [139] overestimates the oscillating ion current by neglecting the impact of these slow ions on the cathode. Furthermore, high pressure causes fast neutralisation (through charge exchange collisions) and thermalisation (through Coulomb collisions with electrons) of the ions. As a result, ions are only able to make a few oscillations before they are lost.

To increase the NPR, these limitations must be overcome. If a fusor should be operated as intended, i.e. confining fast ions at, or close to, a non-Maxwellian velocity distribution, it must be operated at low pressures to enable ions to perform a meaningful number of oscillations. Low gas pressures will also reduce scattering between ions and electrons, resulting in slower thermalisation of the ions. However, as the experiments in this work showed, plasma breakdown is increasingly difficult to achieve. Lower pressures will require one or more strong ion sources and, without star-mode breakdown, the current will be limited by the available

ion source power.
Operating the fusor at pressures where the current from ionising gas collisions is limited also increases the need for ion re-circulation. A large number of grid collisions would diminish the positive effects of low pressures and thus grid designs are required which allow a high number of ion oscillations. Current literature provides only a limited insight into the influence of the grid on the ion confinement: Wehmeyer investigated whether symmetric, latitudinal or longitudinal alignment of the grid wires influences the neutron production, however only minor differences were found [144]. Egle measured the changes in NPR for different combinations of cylindrical and spherical anodes and cathodes. In these experiments spherical grids in spherical cathodes outperformed cylindrical configurations [154], and Krupaker Murali showed that symmetric grids increase the NPR [182]. Further research is clearly required, for example investigating the effect of different grid shapes.
It is, however, not immediately clear how much lowering the pressure will increase the NPR, because the assumed dominant fusion collision, the collision between fast ions and neutral gas particles, scales unfavourably with decreasing pressure. Assuming good ion confinement, the increased number of ions (due to the decreased charge exchange losses) and reduction in the NPR might balance out. In this case, gains in the NPR are expected due to the more favourable ion birth radius (the gross of the ions are injected at the anode) and the reduced thermalisation.

Building on the gained knowledge, a new confinement principle is proposed to reduce the fundamental loss mechanisms of IEC devices. Similar to a fusor, the conceptual device accelerates ions with static electric fields in a spherical geometry towards the centre, but it distinguishes itself by confining pure ion bunches in an electron-free system. Periodic pulsed electric fields spatially compress the ion bunches during each oscillation, sustaining them at a non-Maxwellian velocity distribution. Named after the pulsed nature of the electric fields, the confinement principle is dubbed electrodynamic confinement (EdC). This scheme reduces ion losses through neutralisation, actively suppresses thermalisation caused by ion-ion scattering, and mitigates Coulomb power losses by 3 orders of magnitude due to the absence of electrons. In addition, the fusion cross section is increased by accelerating all ions through the full grid potential.
Particle tracing simulations in an idealised, gridless geometry show that a system confining pure ion bunches can be realised by using three concentric cathode grids of which the middle grid is pulsed. The bunches are compressed during every oscillation as they pass-through the inter-grid region. The simulated design is able to maintain and confine the ion bunches for thousands of oscillation through the active compression. Depending on the device and bunch geometry, this scheme is able to confine ion bunches with densities up to 10^{15} m^{-3}.
The low losses make the design come into question for a power plant feasibility study. Similar to a tokamak, the energy gain criteria for oscillating colliding ion bunches depends on the bunch density and confinement time, i.e. the number

of oscillations ions perform before they are lost, and also on the bunch length. When applying the simulation results for bunch length and confinement time, the required bunch density is 9 orders of magnitude higher than the confinable density. This is in part due to the requirements on the fuel: The EdC principle only allows the confinement of bunches composed of equal mass ions. For different fuel components, such as the favoured deuterium-tritium mix, the varying oscillation times will cause the ions to debunch. This limits the fuel to pure deuterium or helium-3, which, even at high energies, have a more than 10× lower fusion cross section than D-T. A workaround for this limitation could be to oscillate bunches, which are each composed of only one species, at different oscillation frequencies and to collide them at their smallest common transition period. For example, for deuterium-tritium at $2 \times 3 = 6$ times the hydrogen oscillation frequency. This requires adjustments on the pulsing of the grids and ions would not collide at the ideal collisional during every oscillation, but the increases in the reaction rate would be substantial. For this scheme to work adjustments on the geometry can be required to ensure that only one species resides in the compression region at any given time.
Apart from using different species to increase the reaction rate, required to make the design viable as a high-performance neutron source (or a fusion power plant), the density must be increased. Only marginal increases can be achieved by scaling the device and design modifications of the concept are required. An advantage of IEC devices, which are essentially a type of beam-target collider, is the high target density, i.e. the density of the background gas. On the other hand, the EdC concept relies on beam-beam fusion where the density is low. For future research it should be investigated whether a combination of both concepts is possible, i.e. an EdC device with a high-density target. For thin targets injected in the centre, e.g. pellets, drops, or liquid jets, the bunching mechanism is still applicable as long as the energy lost during the transition of the target can be replenished. This will not only result in a manyfold increase of the reaction rate, but also enable fuels composed of different species, such as DT, or advanced fuels such as proton-boron.

Appendix 1: Reconstruction of the polarisation angle from the signal

The polarised emission of the injected neutral particles is guided through two PEMs and a linear polariser. Each PEM has a time varying retardance $A = A_0 \cos(\omega t)$, with amplitude A_0 (typically a halve wave) and oscillation frequency ω. The PEMs are mounted under an angle of $\beta = 45°$ with respect to each other and the polariser is at an angle $\alpha = 22.5°$ with respect to the first PEM.

The by the system induced changes in polarisation of the incoming light are evaluated with the Müller formalism. In Müller calculus, each optical element is described by a Müller matrix M_i. The changes in the Stokes vector after light has passed through an optical element are obtained by matrix multiplication: $S_{\text{out}} = M_i \cdot S_{\text{in}}$. The Müller matrices required to describe the MSE system are:

Rotator
A rotator M_α describes an optical element that changes the polarisation angle of incoming light by an angle α:

$$M_\alpha = \begin{bmatrix} 1 & 0 & 0 & 0 \\ 0 & \cos(2\alpha) & -\sin(2\alpha) & 0 \\ 0 & \sin(2\alpha) & \cos(2\alpha) & 0 \\ 0 & 0 & 0 & 1 \end{bmatrix} \quad \text{(app.1.1)}$$

Rotators can also be used to calculate the Müller matrix of an optical element which is aligned at an arbitrary angle, when their Müller matrix is given with respect to the horizontal axis. The Müller matrix, rotated by an angle φ with respect to the horizontal axis, can be written as $M_y = M_\varphi \cdot M_x \cdot M_{-\varphi}$.

Retarders
Retarders (e.g. waveplates, PEMs, ...) describe optical elements that cause a phase shift between the orthogonal components of the transmitted light. The Müller matrix is:

$$M_r(A) = \begin{bmatrix} 1 & 0 & 0 & 0 \\ 0 & 1 & 0 & 0 \\ 0 & 0 & \cos(A) & \sin(A) \\ 0 & 0 & -\sin(A) & cos(A) \end{bmatrix} \quad \text{(app.1.2)}$$

Polarisers
The Müller matrix of a polariser, transmitting light along the horizontal axis, is:

$$M_p = \frac{1}{2}\begin{bmatrix} 1 & 1 & 0 & 0 \\ 1 & 1 & 0 & 0 \\ 0 & 0 & 0 & 0 \\ 0 & 0 & 0 & 0 \end{bmatrix} \quad \text{(app.1.3)}$$

Müller matrix for the KSTAR MSE system
At KSTAR two PEMs and one linear polariser are used to encode the polarisation of the incoming light into an intensity modulated signal. The calculation can be simplified by choosing angles between the PEMs and the polariser that simplify the Müller matrix of the rotator. At KSTAR, the first PEM is mounted along the horizontal axis, the angle between the two PEMs is $\beta = 45°$ and the angle between the first PEM and the polariser is $\alpha = 22.5°$. With this, the Müller matrix describing the system becomes:

$$M_{\mathrm{MSE}} = M_{\pi/8} \cdot M_p \cdot M_{-\pi/8} \cdot M_{\pi/4} \cdot M_r(|A_2|\cos(\omega_2 t)) \cdot M_{-\pi/4} \cdot M_r(|A_1|\cos(\omega_1 t))$$

$$= \frac{1}{2}\begin{bmatrix} 1 & \frac{\cos(A_2)}{\sqrt{2}} & \frac{\sin(A_1)\sin(A_2)+\cos(A_1)}{\sqrt{2}} & \frac{\sin(A_1)-\cos(A_1)\sin(A_2)}{\sqrt{2}} \\ \frac{1}{\sqrt{2}} & \frac{\cos(A_2)}{2} & \frac{\sin(A_1)\sin(A_2)+\cos(A_1)}{2} & \frac{\sin(A_1)-\cos(A_1)\sin(A_2)}{2} \\ \frac{1}{\sqrt{2}} & \frac{\cos(A_2)}{2} & \frac{\sin(A_1)\sin(A_2)+\cos(A_1)}{2} & \frac{\sin(A_1)-\cos(A_1)\sin(A_2)}{2} \\ 0 & 0 & 0 & 0 \end{bmatrix} \quad \text{(app.1.4)}$$

Multiplying equation app.1.4 with the incoming stokes vector (see equation A.4.5 - A.4.8) results in the total intensity after the light has passed through the MSE system:

$$I_{\mathrm{MSE}} = \frac{I}{2}\Big(1 + \frac{\cos\big(|A_2|\cos(\omega_2 t)\big)}{\sqrt{2}} p_l \cos(2\gamma) \quad \text{(app.1.5)}$$

$$+ \frac{\sin\big(|A_1|\cos(\omega_1 t)\big)\sin\big(|A_2|\cos(\omega_2 t)\big) + \cos\big(|A_1|\cos(\omega_1 t)\big)}{\sqrt{2}} p_l \sin(2\gamma) \quad \text{(app.1.6)}$$

$$+ \frac{\sin\big(|A_1|\cos(\omega_1 t)\big) - \cos\big(|A_1|\cos(\omega_1 t)\big)\sin\big(|A_2|\cos(\omega_2 t)\big)}{\sqrt{2}} p_c\Big) \quad \text{(app.1.7)}$$

The modulated signal contains terms $\sin\big(X\cos(\omega)\big)$ and $\cos\big(X\cos(\omega)\big)$ which are expanded into their harmonics:

$$\sin\big(X\cos(\omega t)\big) = \sum_{n=1}^{\infty} (-1)^{(n-1)} J_{2n-1}(X)\cos\big((2n-1)\omega t\big), \quad \text{(app.1.8)}$$

$$\cos\big(X\cos(\omega t)\big) = J_0(X) + 2\sum_{n=1}^{\infty} (-1)^n J_{2n}(X)\cos(2n\omega t), \quad \text{(app.1.9)}$$

where $J_n(X)$ is the $n-$th order Bessel function. The amplitudes up to the four harmonic of the intensity modulated signal are:

$$I_0 = \frac{I}{2}\left(1 + J_0(|A_1|)\frac{p_l \sin(2\gamma)}{\sqrt{2}} + J_0(|A_2|)\frac{p_l \cos(2\gamma)}{\sqrt{2}}\right) \tag{app.1.10}$$

$$I_{\omega_1} = \frac{IJ_1(|A_1|)}{\sqrt{2}} p_c \tag{app.1.11}$$

$$I_{\omega_2} = \frac{IJ_0(|A_1|)J_1(|A_2|)}{\sqrt{2}} p_c \tag{app.1.12}$$

$$I_{2\omega_1} = -\frac{IJ_2(|A_1|)}{\sqrt{2}} p_l \sin(2\gamma) \tag{app.1.13}$$

$$I_{2\omega_2} = -\frac{IJ_2(|A_2|)}{\sqrt{2}} p_l \cos(2\gamma) \tag{app.1.14}$$

$$I_{3\omega_1} = -\frac{IJ_3(|A_1|)}{\sqrt{2}} p_c \tag{app.1.15}$$

$$I_{3\omega_2} = -\frac{IJ_0(|A_1|)J_3(|A_2|)}{\sqrt{2}} p_c \tag{app.1.16}$$

$$I_{4\omega_1} = \frac{IJ_4(|A_1|)}{\sqrt{2}} p_l \sin(2\gamma) \tag{app.1.17}$$

$$I_{4\omega_2} = -\frac{IJ_4(|A_2|)}{\sqrt{2}} p_l \cos(2\gamma) \tag{app.1.18}$$

(app.1.19)

From this, the original Stokes vector is calculated:

$$I = 2I_0 + \frac{J_0(|A_1|)}{J_2(|A_1|)} I_{2\omega_1} + \frac{J_0(|A_2|)}{J_2(|A_2|)} I_{2\omega_2} \tag{app.1.20}$$

$$Q = -\frac{\sqrt{2}}{J_2(|A_2|)} I_{2\omega_2} = \frac{\sqrt{2}}{J_4(|A_2|)} I_{4\omega_2} \tag{app.1.21}$$

$$U = -\frac{\sqrt{2}}{J_2(|A_1|)} I_{2\omega_1} = \frac{\sqrt{2}}{J_4(|A_1|)} I_{4\omega_1} \tag{app.1.22}$$

$$V = \frac{\sqrt{2}}{J_1(|A_1|)} I_{\omega_1} = -\frac{\sqrt{2}}{J_3(|A_1|)} I_{3\omega_1} \tag{app.1.23}$$

$$= \frac{\sqrt{2}}{J_0(|A_1|)J_1(|A_2|)} I_{\omega_2} = -\frac{\sqrt{2}}{J_0(|A_1|)J_3(|A_2|)} I_{3\omega_2} \tag{app.1.24}$$

The polarisation angle γ is calculated by:

$$\begin{aligned}\gamma &= \frac{1}{2}\arctan\left(\frac{U}{Q}\right) \\ &= \frac{1}{2}\arctan\left(\frac{J_2(|A_2|)I_{2\omega_1}}{J_2(|A_1|)I_{2\omega_2}}\right) = \frac{1}{2}\arctan\left(\frac{J_4(|A_2|)I_{4\omega_1}}{J_4(|A_1|)I_{4\omega_2}}\right)\end{aligned} \tag{app.1.25}$$

Furthermore, the retardance of the PEMs can be calculated from the harmonics which is expected to be more accurate than the retardance specified at the PEM controller:

$$\frac{J_1(|A_1|)}{J_3(|A_1|)} = -\frac{I_{\omega_1}}{I_{3\omega_1}} \tag{app.1.26}$$

$$\frac{J_2(|A_1|)}{J_4(|A_1|)} = -\frac{I_{2\omega_1}}{I_{4\omega_1}} \tag{app.1.27}$$

$$\frac{J_1(|A_2|)}{J_3(|A_2|)} = -\frac{I_{\omega_2}}{I_{3\omega_2}} \tag{app.1.28}$$

$$\frac{J_2(|A_2|)}{J_4(|A_2|)} = -\frac{I_{2\omega_2}}{I_{4\omega_2}} \tag{app.1.29}$$

Appendix 2: Estimation of the neutron production rate in a fusor

The NPR is estimated for beam-beam (BB), beam-gas (BG) and embedded fusion (EMB). Therefore the reaction rate R is evaluated for the three processes. R is defined as:

$$R = n_1 \cdot n_2 \cdot \sigma(v) \cdot v \cdot V, \tag{app.2.1}$$

with densities n_1 and n_2, cross section σ, relative velocity v and interaction volume V. Deuterium is used as a fuel gas with pressure $p = 0.2$ Pa for which, using the ideal gas law, the density is calculated to $n_{\text{gas}} = 3.6 \cdot 10^{19}$ m^{-3}. Furthermore, mono-energetic ions with energy $E_{D^+} = 100$ keV, a grid transparency of $\eta = 95\%$, and an embedded density $n_{\text{emb}} = 1 \cdot 10^{25}$ m^{-3} is assumed. For the three collision types, the reaction rate is calculated as:

$$R_{\text{BB}} = n_{\text{fast,osc}}^2 \cdot \sigma(v) \cdot v \cdot V_{\text{bb}} \tag{app.2.2}$$

$$R_{\text{BG}} = n_{\text{fast,osc}} \cdot n_{\text{gas}} \cdot \sigma(v) \cdot v \cdot V_{\text{bg}} \tag{app.2.3}$$

$$R_{\text{emb}} = n_{\text{fast,grid}} \cdot n_{\text{emb}} \cdot \sigma(v) \cdot v \cdot V_{\text{emb}} \tag{app.2.4}$$

The parameters are approximated as:

Oscillating ion density $n_{\text{fast,osc}}$
Assuming all fusion collisions occur inside the cathode grid, the fast ion density is approximated as

$$n_{\text{fast,osc}} = \frac{I_{\text{fast,osc}}}{e\nu A}, \tag{app.2.5}$$

with fast ion current $I_{\text{fast,osc}}$, elementary charge e, area $A = 4/3\pi r^3$. For beam-gas fusion it is assumed that all fusion processes take place in the cathode and $r = r_{\text{grid}} = 5$ cm, for beam-beam fusion it is assumed that all ions are focused to a sphere of radius $r = 0.5$ cm in which the collisions take place.

Oscillating ion current $I_{\text{fast,osc}}$
From the experiments only the total measured current is known. The oscillating ion current is calculated following Krupaker Murali [139] as

$$I_{\text{fast,osc}} = \frac{\eta \cdot I_{\text{fusor}}}{(1-\eta^2)(1+\gamma)}, \tag{app.2.6}$$

with measured current I_{fusor}, grid transparency η and secondary electron emission $\gamma = 2$.

Grid-impact ion current density $n_{\text{fast,grid}}$
The current density of ions colliding with the grid is required for the calculation of R_{emb}. The current of ions colliding with the grid is approximated as $I_{\text{impact}} = I_{\text{fusor}}/\gamma$, with which the current density is calculated:

$$n_{\text{fast,grid}} = \frac{I_{\text{impact}}}{e\nu A_{\text{grid}}}. \tag{app.2.7}$$

Here, $A_{\text{grid}} = A_{\text{C}} \cdot (1-\eta)$ is the surface area of the grid wires.

Interaction volume V
The calculation of the interaction volume depends on the collision type:

beam-beam fusion: For the calculation it is assumed that all fast ions are focused to a sphere of radius 0.5 cm where the fusion collisions take place.

beam-gas fusion: The beam-gas fusion processes are assumed to take place inside the cathode grid, thus $V = 4/3\pi r_{\text{grid}}^3$.

embedded fusion: It is assumed that an ion does no longer contribute to the reaction rate once the cross section has dropped by a factor of 10 from its initial value at $E_{D^+} = 100$ keV. Applying the Bethe-Bloch formula [183, 184] to a titanium grid results in a penetration depth of $\mathrm{dx} \approx 0.6$ μm until the ion energy is reduced to 30 keV, at which $\sigma \approx 0.1 \cdot \sigma_0$. The volume is calculated from the grid wire surface and penetration depth: $V = \mathrm{dx} \cdot A_{\text{grid}}$

Results

With the above assumption, equation app.2.1 is calculated for increasing fusor currents. The result is plotted in figure app.2.1.

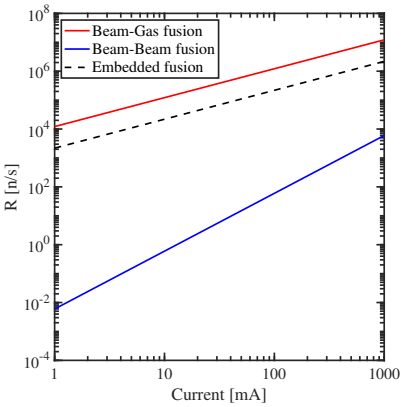

Figure app.2.1: Dependence of the reaction rate of beam-beam, beam-gas and embedded on the fusor current.

Bibliography

[1] P. C. Budassi. *Observable universe logarithmic illustration*. URL: https://commons.wikimedia.org/wiki/File:Observable%7B%5C_%7Duniverse%7B%5C_%7Dlogarithmic%7B%5C_%7Dillustration.png (visited on July 3, 2018).

[2] *Wikipedia: List of solar deities*. URL: https://en.wikipedia.org/wiki/List%7B%5C_%7Dof%7B%5C_%7Dsolar%7B%5C_%7Ddeities (visited on July 1, 2018).

[3] A. S. Eddington. "On the Radiative Equilibrium of the Stars". In: *Mon. Not. R. Astron. Soc.* 77.1 (1916), pp. 16–35.

[4] A. S. Eddington. "The Internal Constitution of the Stars". In: *Sci. Mon.* 11.4 (1920), pp. 297–303.

[5] H. A. Bethe. "Energy Production in Stars". In: *Phys. Rev.* 55.1 (1939), pp. 103–103.

[6] *Britannica: The First Hydrogen Bombs*. URL: https://www.britannica.com/technology/nuclear-weapon/The-first-hydrogen-bombs (visited on Jan. 9, 2019).

[7] J. Wesson. *Tokamaks*. 3rd ed. Oxfort: Oxford University Press, 2004.

[8] J. P. Freidberg. *Plasma Physics and Fusion Energy*. 1st ed. New York: Cambridge University Press, 2007.

[9] *EUROfusion: Tokamak Principle*. URL: https://www.euro-fusion.org/de/news/n/detail/News/tokamak-principle/ (visited on Jan. 3, 2019).

[10] E. M. Hollmann et al. "Status of research toward the ITER disruption mitigation system". In: *Phys. Plasmas* 22 (2015), p. 021802.

[11] F. M. Levinton et al. "Magnetic Field Pitch-Angle Measurements in the PBX-M Tokamak Using the Motional Stark Effeect". In: *Phys. Rev. Lett.* 63.19 (1989), pp. 2060–2063.

[12] D. Wróblewski and L. L. Lao. "Polarimetry of motional Stark effect and determination of current profiles in DIII-D (invited)". In: *Rev. Sci. Instrum.* 63.10 (1992), pp. 5140–5147.

[13] J. Chung et al. "Initial operation of a newly developed multichord motional Stark effect diagnostic in KSTAR". In: *Rev. Sci. Instrum.* 87.11 (2016), p. 503.

[14] B. C. Stratton et al. "Instrumentation for the joint European torus motional Stark effect diagnostic". In: *Rev. Sci. Instrum.* 70.1 (1999), p. 898.

[15] N. Bretz et al. “A motional Stark effect instrument to measure q(R) on the C-mod tokamak”. In: *Rev. Sci. Instrum.* 72.1 (2001), p. 1012.

[16] M. Reich et al. “Real-time diagnostics and their applications at ASDEX upgrade”. In: *Fusion Sci. Technol.* 58.3 (2010), pp. 727–732.

[17] T. Suzuki et al. “Off-axis current drive and real-time control of current profile in JT-60U”. In: *Nucl. Fusion* 48 (2008), p. 045002.

[18] J. R. Ferron et al. “Real time equilibrium reconstruction for tokamak discharge control”. In: *Nucl. Fusion* 38.7 (1998), pp. 1055–1066.

[19] S. Woodruff. “An overview of tokamak alternatives in the US fusion program with the aim of fostering concept innovation”. In: *J. Fusion Energy* 23.1 (2004), pp. 27–40.

[20] P. T. Farnsworth. *US Patent 3258402A*. 1960.

[21] R. L. Hirsch. “Inertial-electrostatic confinement of ionized fusion gases”. In: *J. Appl. Phys.* 38.11 (1967), pp. 4522–4534.

[22] J. F. Santarius et al. “Overview of University of Wisconsin inertial-Electrostatic Confinement Fusion Research”. In: *Fusion Sci. Technol.* 47.4 (2005), pp. 1238–1244.

[23] J. Khachan, D. Moore, and S. Bosi. “Spatial distribution of ion energies in an inertial electrostatic confinement device”. In: *Phys. Plasmas* 10.3 (2003), pp. 596–599.

[24] T. Takamatsu et al. “Spatial Distribution of D-D Neutrons from a Compact Water-Cooled Inertial Electrostatic Confinement Device”. In: *Fusion Sci. Technol.* 52.4 (2007), pp. 1114–1118.

[25] C. C. Dietrich, J. E. Leslie, and J. S. Raymond. “Experimental Verification of Enhanced Confinement in a Multi-grid IEC Device”. In: *44th AIAA/ASME/SAE/ASEE Jt. Propuls. Conf. Exhib.* Hartfort, CT, 2008.

[26] *Online community*. URL: `http://www.fusor.net/board/` (visited on Sept. 8, 2018).

[27] E. C. G. Hermans. “The Design and Optimization of an Inertial Electrostatic Confinement Fusion Device”. Master thesis. Technical University Eindhoven, 2013. URL: `repository.tue.nl/759014`.

[28] T. H. Rider. “A general critique of inertial-electrostatic confinement fusion systems”. In: *Phys. Plasmas* 2.6 (1995), pp. 1853–1872.

[29] R. Bussard. “Some Physics Considerations of Magnetic Inertial Elecostatic Confinement : A New Concept for Spherical Converging-Flow Fusion”. In: *Fusion Technol.* 19.2 (1991), pp. 273–293.

[30] M. Rosenberg and N. A. Krall. “The effect of collisions in maintaining a non-Maxwellian plasma distribution in a spherically convergent ion focus”. In: *Phys. Fluids B* 4 (1992), p. 1788.

[31] A. A. Harms et al. *Principles of Fusion Energy*. New Delhi: Allied Publisher Limited, 2002.

[32] J. Mlyná et al. *Focus On: JET The European Centre of Fusion Research*. Tech. rep. Prague, 2007, p. 208.

[33] S. von Goeler, W. Stodiek, and N. Sauthoff. "Studies of Internal Disruptions and m = 1 Oscillations in Tokamak Discharges with Soft-X-Ray Techniques". In: *Phys. Rev. Lett.* 33.20 (1974), pp. 1201–1203.

[34] E. L. Foley and F. M. Levinton. "Progress on the motional Stark effect with laser-induced fluorescence diagnostic (invited)". In: *Rev. Sci. Instrum.* 77 (2006), 10F311.

[35] V. Mukhovatov and V. D. Shafranov. "Plasma equilibrium in a Tokamak". In: *Nucl. Fusion* 11 (1971), p. 605.

[36] L. L. Lao et al. "Equilibrium analysis of current profiles in tokamaks". In: *Nucl. Fusion* 30.6 (1990), p. 1035.

[37] C. Gormezano et al. "Chapter 6: Steady state operation". In: *Nucl. Fusion* 47.6 (2007).

[38] A. C. Sips. "Advanced scenarios for ITER operation". In: *Plasma Phys. Control. Fusion* 47.5 A (2005), pp. 18–40.

[39] J. E. Barton et al. "Simultaneous closed-loop control of the current profile and the electron temperature profile in the TCV tokamak". In: *Proc. Am. Control Conf.* Chicago, 2015, p. 3316.

[40] V. D. Shafranov. "On Magnetohydrodynamical Equilibrium Configurations". In: *J. Exptl. Theor. Phys.* 6.33 (1958), p. 545.

[41] H. Grad and H. Rubin. "Hydromagnetic equilibria and force-free fields". In: *Proc. Second United Nations Conf. Peac. uses At. Energy*. Geneva, 1958, p. 190.

[42] R. Fischer et al. "Magnetic equilibrium reconstruction using geometric information from temperature measurements at ASDEX Upgrade". In: *Proc. 40th EPS Conf. plasma Phys.* Ed. by V. Naulin. Espoo, Finland, 2013, P2.139.

[43] F. Hofmann and G. Tonetti. "Tokamak equilibrium reconstruction using Faraday rotation measurements". In: *Nucl. Fusion1* 28 (1988), p. 1871.

[44] J.-S. Ko. "Current Profile Measurements Using MSE on Alcator C-Mod". PhD thesis. Massachusetts Institute of Technology, 2009.

[45] B. W. Rice et al. "Direct Measurement of the Radial Electric Field in Tokamak Plasmas using the Stark Effect". In: *Phys. Rev. Lett.* 79.14 (1997), pp. 2694–2697.

[46] B. W. Rice, K. H. Burrell, and L. L. Lao. "Effect of plasma radial electric field on motional Stark effect measurements and equilibrium reconstruction". In: *Nucl. Fusion* 37.4 (1997), pp. 517–522.

[47] F. M. Levinton et al. “Magnetic field pitch angle diagnostic using the motional Stark effect (invited)”. In: *Rev. Sci. Instrum.* 61 (1990), pp. 2914–2919.

[48] J. Ko, J. Chung, and M. Messmer. “Diagnostic development for current density profile control at KSTAR”. In: *Fusion Eng. Des.* 109-111 (2016), pp. 742–746.

[49] B. W. Rice et al. “Simultaneous measurement of q and E r profiles using the motional Stark effect in high-performance DIII-D plasmas (invited)”. In: *Rev. Sci. Instrum.* 70.1 (1999), pp. 815–820.

[50] M. D. Bock. *Relation between polarisation angle, magnetic field and radial electric fiel*. Tech. rep. 2011, pp. 1–16.

[51] B. B. Kadomtsev. “Disruptive instability in Tokamaks”. In: *Sov. J. Plasma Phys.* 1 (1975), p. 389.

[52] J. A. Wesson. “Sawtooth Oscillations”. In: *Plasma Phys. Control. Fusion* 28.1A (1986), pp. 243–248.

[53] J. Ko. “Sensitivity of magnetic field-line pitch angle measurements to sawtooth events in tokamaks”. In: *Rev. Sci. Instrum.* 87.11 (2016), 11E541.

[54] H. Soltwisch. “Measurement of current-density changes during sawtooth activity in a tokamak by far-infrared polarimetry (invited)”. In: *Rev. Sci. Instrum.* 59.8 (1988), pp. 1599–1604.

[55] M. Yamada et al. “Investigation of magnetic reconnection during a sawtooth crash in a high-temperature tokamak plasma”. In: *Phys. Plasmas* 1.10 (1994), pp. 3269–3276.

[56] J. O’Rourke. “The change in the safety factor profile at a sawtooth collapse”. In: *Plasma Phys. Control. Fusion* 33.4 (1991), pp. 289–296.

[57] H. R. Koslowski. “Overview of current density measurements and sawtooth studies on TEXTOR”. In: *Fusion Sci. Technol.* 47.2 (2005), pp. 260–265.

[58] D. Wróblewski and L. L. Lao. “Determination of the safety factor in sawtoothing discharges in DIII-D”. In: *Phys. Fluids B Plasma Phys.* 3.10 (1991), pp. 2877–2881.

[59] K. Lee et al. “Design of a multi-channel polarization-preserving optical system for the KSTAR motional Stark effect diagnostic”. In: *Fusion Eng. Des.* 121 (2017), pp. 301–307.

[60] D. Wróblewski and L. L. Lao. “Polarimetry of motional Stark effect and determination of current profiles in DIII-D (invited)”. In: *Rev. Sci. Instrum.* 63.10 (1992), pp. 5140–5147.

[61] A. Bock et al. “Non-inductive improved H-mode operation at ASDEX Upgrade”. In: *Nucl. Fusion* 57.12 (2017).

[62] R. T. Mumgaard. “Lower Hybrid Current Drive on Alcator C-Mod: Measurements with an Upgraded MSE Diagnostic and Comparisons to Simulation”. PhD Thesis. Massachusetts Institute of Technology, 2015.

[63] R. T. Mumgaard, S. D. Scott, and M. Khoury. “The multi-spectral line-polarization MSE system on Alcator C-Mod”. In: *Rev. Sci. Instrum.* 87.11 (2016), p. 527.

[64] M. Reich et al. “Upgrade of the MSE diagnostic at ASDEX Upgrade”. In: *44th EPS Conf. Plasma Phys.* Belfast, 2017.

[65] E. L. Foley et al. “The motional Stark effect diagnostic for ITER using a line-shift approach”. In: *Rev. Sci. Instrum.* 79.10 (2008).

[66] J. Howard. “Snapshot-imaging motional Stark effect polarimetry”. In: *Plasma* 50.125003 (2008).

[67] O. P. Ford et al. “Imaging motional Stark effect measurements at ASDEX Upgrade”. In: *Rev. Sci. Instrum.* 87.11E537 (2016).

[68] J. Chung et al. “Motional Stark Effect Diagnostics for KSTAR”. In: *J. Korean Phys. Soc.* 65.8 (2014), pp. 1257–1260.

[69] M. Kuldkepp et al. “First mirror contamination studies for polarimetry motional Stark effect measurements for ITER”. In: *Rev. Sci. Instrum.* 75 (2004), p. 3446.

[70] M. Kuldkepp et al. “First mirror contamination studies for polarimetry motional Stark effect measurements for ITER”. In: *Rev. Sci. Instrum.* 75.3446 (2004).

[71] J. N. Brooks and J. P. Allain. “Particle deposition and optical response of ITER motional Stark effect diagnostic first mirrors”. In: *Nucl. Fusion* 48.045003 (2008).

[72] S. Allen et al. *Evaluation of ITER MSE Viewing Optics*. Tech. rep. 2007, PPPL 73501DD1533A.

[73] A. Thorman et al. “A photoelastic-modulator-based motional Stark effect polarimeter for ITER that is insensitive to polarized broadband background reflections”. In: *Rev. Sci. Instrum.* 87.073504 (2016).

[74] C. R. Cosens. “A balance-detector for alternating-current bridges”. In: *Procc. Phys. Soc* 46 (1934), p. 818.

[75] W. C. Michels and N. L. Curtis. “A pentode lock-in amplifier of high frequency selectivity”. In: *Rev. Sci. Instrum.* 12 (1941), p. 444.

[76] R. B. Blackman and J. W. Tukey. *The measurement of power spectra*. Toronto, 1958, pp. 98–99.

[77] *Wikipedia: Poincaré sphere*. URL: `https://en.wikipedia.org/wiki/Stokes%7B%5C_%7Dparameters%7B%5C#%7D/media/File:Poincar%C3%A9%7B%5C_%7Dsphere.svg` (visited on Mar. 24, 2019).

[78] M. F. M. De Bock et al. “Real-time MSE measurements for current profile control on KSTAR”. In: *Rev. Sci. Instrum.* 83.10D524 (2012).

[79] Y.-K. Oh et al. “Overview of the KSTAR Research in Support of ITER and DEMO”. In: *26th IAEA Fusion Energy Conf. Proc.* Kyoto, 2016, OV/2–4.

[80] J. Chung et al. “Instrumentation for a multichord motional Stark effect diagnostic in KSTAR”. In: *Rev. Sci. Instrum.* 85.11 (2014), p. 827.

[81] M. F. M. De Bock et al. “Ab initio modeling of the motional Stark effect on MAST”. In: *Rev. Sci. Instrum.* 79.10 (2008), 10F524.

[82] D. J. Campbell et al. “Stabilization of sawteeth with additional heating in the JET tokamak”. In: *Phys. Rev. Lett.* 60.21 (1988), pp. 2148–2151.

[83] C. C. Petty, P. A. Politzer, and Y. R. Lin-Liu. “Direct measurement of neoclassical currents using motional Stark effect polarimetry”. In: *Plasma Phys. Control. Fusion* 47.7 (2005), pp. 1077–1100.

[84] K. McCormick et al. “Temporal behavior of the plasma current distribution in the ASDEX tokamak during lower-hybrid current drive”. In: *Phys. Rev. Lett.* 58.5 (Feb. 1987), pp. 491–494.

[85] J. Blum, C. Boulbe, and B. Faugeras. “Reconstruction of the equilibrium of the plasma in a Tokamak and identification of the current density profile in real time”. In: *J. Comput. Phys.* 231.3 (2012), pp. 960–980.

[86] M. C. C. Messmer et al. “Evolution of the central safety factor during stabilized sawtooth instabilities at KSTAR”. In: *Nucl. Fusion* 58.1 (2018), p. 016030.

[87] F. L. Hinton and R. D. Hazeltine. “Theory of Plasma Transport in Toroidal Confinements Systems”. In: *Rev. Mod. Phys.* 48.2 (1976), pp. 239–308.

[88] F. Felici et al. “Real-time physics-model-based simulation of the current density profile in tokamak plasmas”. In: *Nucl. Fusion* 51.8 (2011), p. 083052.

[89] R. Fischer et al. “Coupling of the flux diffusion equation with the equilibrium reconstruction at ASDEX Upgrade”. In: *Fusion Sci. Technol.* 69.2 (2016), pp. 526–536.

[90] F. Felici et al. “Real-time-capable prediction of temperature and density profiles in a tokamak using RAPTOR and a first-principle-based transport model”. In: *Nucl. Fusion* 58.9 (2018).

[91] G. Kitagawa and W. Gersch. “Linear Gaussian State Space Modeling BT - Smoothness Priors Analysis of Time Series”. In: ed. by G. Kitagawa and W. Gersch. New York, NY: Springer New York, 1996, pp. 55–65.

[92] F. Felici et al. “Real-time Model-based Reconstruction and Control of Tokamak Plasma Profiles”. In: *IAEA Conf. 2012*. 2012, EX/P3–12.

[93] A. A. Teplukhina et al. “Simulation of profile evolution from ramp-up to ramp-down and optimization of tokamak plasma termination with the RAPTOR code”. In: *Plasma Phys. Control. Fusion* 59.12 (2017), p. 124004.

[94] J. Van Dongen et al. “Numerical optimization of actuator trajectories for ITER hybrid scenario profile evolution”. In: *Plasma Phys. Control. Fusion* 56.12 (2014).

[95] H. Lütjens, A. Bondeson, and O. Sauter. “The CHEASE code for toroidal MHD equilibria”. In: *Comput. Phys. Commun.* 97.3 (1996), pp. 219–260.

[96] D. Simon. *Optimal State Estimation*. 1st ed. Hoboken, New Jersey, USA: John Wiley & Sons, Inc, 2006.

[97] F. Felici, M. D. Baar, and M. Steinbuch. “A dynamic state observer for real-time reconstruction of the tokamak plasma profile state and disturbances”. In: *Am. Control Conf.* 2014, pp. 4816–4823.

[98] R. Reimer et al. “Motional Stark effect spectra simulations for Wendelstein 7-X”. In: *Contrib. to Plasma Phys.* 50.8 (2010), pp. 731–735.

[99] R. C. Wolf et al. “Motional Stark Effect measurements of the local magnetic field in high temperature fusion plasmas”. In: *J. Instrum.* 10 (2015), P10008.

[100] R. T. Mumgaard, S. D. Scott, and M. Khoury. “The multi-spectral line-polarization MSE system on Alcator C-Mod”. In: *Rev. Sci. Instrum.* 87.11E527 (2016), pp. 87–90.

[101] B. W. Rice et al. “Simultaneous measurement of q and Er profiles using the motional Stark effect in high-performance DIII-D plasmas”. In: *Rev. Sci. Instrum.* 70.1 (1999), p. 815.

[102] L. Blondel and O. Sauter. “Axisymmetric Tokamak Equilibria computed with a Predefined Safety Factor Profile as CHEASE input”. Master project. EPFL, 2016.

[103] C. Holland. “Validation metrics for turbulent plasma transport”. In: *Phys. Plasmas* 23.060901 (2016).

[104] “ITER Physics Expert Group on Confinement and Transport et al”. In: *Nucl. Fusion* 39 (1999), p. 2175.

[105] J. M. Moret et al. “Tokamak equilibrium reconstruction code LIUQE and its real time implementation”. In: *Fusion Eng. Des.* 91 (2015), pp. 1–15.

[106] L. Giannone et al. “A data acquisition system for real-time magnetic equilibrium reconstruction on ASDEX Upgrade and its application to NTM stabilization experiments”. In: *Fusion Eng. Des.* 88.12 (2013), pp. 3299–3311.

[107] F. Felici and E. al. “Subitted”. In: *Nucl. Fusion* (2018).

[108] S. H. Kim and J. B. Lister. “A potentially robust plasma profile control approach for ITER using real-time estimation of linearized profile response models”. In: *Nucl. Fusion* 57.7 (2012).

[109] M. Reich et al. “Real-time beam tracing for control of the deposition location of electron cyclotron waves”. In: *Fusion Eng. Des.* 100 (2015), pp. 73–80.

[110] E. Poli et al. “TORBEAM 2.0, a paraxial beam tracing code for electron-cyclotron beams in fusion plasmas for extended physics applications”. In: *Comput. Phys. Commun.* 225 (2018), pp. 36–46.

[111] M. Weiland et al. “RABBIT: Real-time simulation of the NBI fast-ion distribution”. In: *Nucl. Fusion* 58.8 (2018).

[112] A. Mlynek et al. “Fringe jump analysis and implementation of polarimetry on the ASDEX Upgrade DCN interferometer”. In: *Rev. Sci. Instrum.* 85.11 (2014).

[113] Y. B. Nam et al. “Validation of the ’full reconnection model’ of the sawtooth instability in KSTAR”. In: *Nucl. Fusion* 58.6 (2018), p. 066009.

[114] S. Carpentier et al. “Modelling of beryllium erosion – redeposition on ITER first wall panels”. In: *Proc. 19th Int. Conf. Plasma-Surface Interact. Control. Fusion*. Vol. 415. SAN DIEGO, 2011, S165–S169.

[115] A. Dinklage et al. “Forward Modeling of Motional Stark Effect Spectra”. In: *Fusion Sci. Technol.* 592.2 (2011), pp. 406–4017.

[116] J. Ko and J. Klabacha. “Improved spectral analysis for the motional Stark effect diagnostic”. In: *Rev. Sci. Instrum.* 83.10D513 (2012), p. 513.

[117] M. F. M. D. Bock et al. “Ab initio modeling of the motional Stark effect on MAST”. In: *Rev. Sci. Instrum.* 79.10F524 (2008), p. 524.

[118] P. T. Farnsworth. *Electric discharge device for producing interactions between nuclei*. Patent US3258402A, 1966.

[119] N. A. Krall. “The Polywell™: A Spherically Convergent Ion Focus Concept”. In: *Fusion Technol.* 22.1 (1992), pp. 42–49.

[120] S. Krupakar Murali et al. “Study of fusion regimes in an inertial electrostatic confinement device using the new eclipse disk diagnostic”. In: *Phys. Plasmas* 13.5 (2006), pp. 1–7.

[121] R. Bowden-Reid et al. “Evidence for surface fusion in inertial electrostatic confinement devices”. In: *Phys. Plasmas* 25.11 (2018), p. 112702.

[122] K. Yamauchi et al. “Pulsed operation of a compact fusion neutron source using a high-voltage pulse generator developed for landmine detection”. In: *Fusion Sci. Technol.* 47.4 (2005), pp. 1229–1232.

[123] G. H. Miley and S. Krupaker Murali. *Inertial Electrostatic Confinement (IEC) Fusion*. New York: Springer, 2014.

[124] E. Hotta et al. “Overview of IEC Research at Tokyo Tech.” In: *15th US-Japan Work. IEC Fusion*. Kyoto, Japan, 2013.

[125] S. Krupakar Murali et al. “Study of fusion regimes in an inertial electrostatic confinement device using the new eclipse disk diagnostic”. In: *Phys. Plasmas* 13.5 (2006).

[126] R. P. Ashley et al. “Steady-State D-3He Proton Production in an IEC Fusion Device”. In: *Fusion Technol.* 39.2P2 (2001), pp. 546–551.

[127] G. Miley et al. “Scaling of the Inertial Electrostatic Confinement (IEC) for near-term thrusters and future fusion propulsion”. In: *AIP Conf. Proc.* 420.1998 (1998), pp. 1373–1376.

[128] G. H. Miley et al. “IEC thrusters for space probe applications and propulsion”. In: *AIP Conf. Proc.* 1103 (2009), pp. 164–174.

[129] R. L. Burton et al. “Fusion Ship II - A Fast Manned Interplanetary Space Vehicle Using Inertial Electrostatic Fusion”. In: *AIP Conf. Proc.* Vol. 654. 2003, p. 553.

[130] Y. Gu and G. H. Miley. “Experimental study of potential structure in a spherical IEC fusion device”. In: *IEEE Trans. Plasma Sci.* 28.1 (2000), pp. 331–346.

[131] M. Carr and J. Khachan. “The dependence of the virtual cathode in a Polywell on the coil current and background gas pressure”. In: *Phys. Plasmas* 17.5 (2010).

[132] S. Cornish et al. “The dependence of potential well formation on the magnetic field strength and electron injection current in a polywell device”. In: *Phys. Plasmas* 21.9 (2014).

[133] J. M. DeMora and R. A. Stubbers. “Study of Ion Microchannels and IEC Grid Effects Using the SIMION Code”. In: *Proc. 16th Int. Symp. Fusion Eng.* Champaign, IL, USA, 1995, pp. 1486–1489.

[134] *ALADDIN*. URL: `https://www-amdis.iaea.org/ALADDIN/` (visited on Nov. 3, 2018).

[135] J. H. Nadler, Y. B. Gu, and G. H. Miley. “Potential profile measurements using a collimated proton detector in spherical inertial-electrostatic plasma confinement”. In: *Rev. Sci. Instrum.* 63.10 (1992), pp. 4810–4812.

[136] G. H. Miley and Y. Gu. “IEC Neutron Source Development and potential well measurement”. In: *Curr. Trends Int. Fusion Res.* Ed. by E. Panarella. Washington, 1997, p. 177.

[137] G. H. Miley et al. “Inertial-Electrostatic Confinement Neutron/Proton Source”. In: *AIP Conf. Proc. 299*. Vol. 299. 1. 1994, pp. 675–689.

[138] G. H. Miley et al. “IEC thrusters for space probe applications and propulsion”. In: *AIP Conf. Proc.* 1103 (2009), pp. 164–174.

[139] S. K. Murali, J. F. Santarius, and G. L. Kulcinski. “Consolidated electron emission effects in an IEC device”. In: *Plasma Sources Sci. Technol.* 19.4 (2010), p. 045029.

[140] G. A. Emmert and J. F. Santarius. “Atomic and molecular effects on spherically convergent ion flow. I. Single atomic species”. In: *Phys. Plasmas* 17.013502 (2010).

[141] G. A. Emmert and J. F. Santarius. “Atomic and molecular effects on spherically convergent ion flow. II. Multiple molecular species”. In: *Phys. Plasmas* 17.013503 (2010).

[142] S. M. M. Rouwette. “Modelling of the Ion Birth Radius in an Inertial Electrostatic Confinement Device”. Master thesis. Technical University Eindhoven, 2015.

[143] S. Krupakar Murali et al. “Effects of chamber pressure variation on the grid temperature in an inertial electrostatic confinement device”. In: *Phys. Plasmas* 17.10 (2010), p. 102701.

[144] A. L. Wehmeyer, R. F. Radel, and G. L. Kulcinski. “Optimizing neutron production rates from D-D fusion in an inertial electrostatic confinement device”. In: *Fusion Sci. Technol.* 47.4 (2005), pp. 1260–1264.

[145] Anode Layer Ion Source. *https://techplasmas.com/anode-layer-ion-source*. URL: `https://techplasmas.com/anode-layer-ion-source` (visited on Aug. 7, 2018).

[146] A. E. Huisman. “Optimization of the neutron yield in TU/e FUSOR”. Master thesis. Technical University Eindhoven, 2017.

[147] H.-S. Bosch and G. M. Hale. “Improved formulas for fusion cross-sections and thermal reactivities”. In: *Nucl. Fusion* 32.4 (1992), p. 611.

[148] E. Kurt and S. Arslan. “An inertial electrostatic confinement (IEC) device modeling and the effects of different cathode structures to the fields”. In: *Energy Convers. Manag.* 63 (2012), pp. 55–62.

[149] M. Ohnishi et al. “Studies of Inertial Electrostatic Confinement Fusion Neutron Source”. In: *Fusion Technol.* 34.3P2 (1998), p. 1071.

[150] H. Osawa et al. “Effects of cathode structure on neutron production in IEC device”. In: *US-Japan Work. 9–10 Oct*. 2002.

[151] *CST*. URL: `https://www.cst.com/` (visited on Mar. 28, 2019).

[152] *Comsol*. URL: `https://www.comsol.nl/` (visited on Mar. 27, 2019).

[153] S. K. Murali, J. F. Santarius, and G. L. Kulcinski. “Effects of displaced grids on the fusion reactivity of an Inertial Electrostatic Confinement device”. In: *J. Fusion Energy* 29.3 (2010), pp. 256–260.

[154] B. J. Egle, J. F. Santarius, and G. L. Kulcinski. “Comparison of spherical and cylindrical cathode geometries in inertial electrostatic confinement devices”. In: *Fusion Sci. Technol.* 52.4 (2007), pp. 1110–1113.

[155] P. C. Zalm and L. J. Beckers. “Secondary electron yields from clean polycrystalline metal surfaces bombarded by 5-20 keV hydrogen or noble gas ions”. In: *Philips J. Res.* 39.3 (1984), pp. 61–76.

[156] L. N. Large and W. S. Whitlock. “Secondary Electron Emission from Clean Metal Surfaces Bombarded by Fast Hydrogen Ions”. In: *Proc. Phys. Soc. Second.* 79 (1962), p. 148.

[157] G. H. Miley. “A portable neutron/tunable X-ray source based on inertial electrostatic confinement”. In: *Nucl. Instruments Methods Phys. Res. A* 422 (1999), pp. 16–20.

[158] Y. Gu et al. “Pulsed operation of spherical inertial-electrostatic confinement device”. In: *Fusion Technol.* 30.3P2B (1996), pp. 1342–1346.

[159] J. H. Nadler et al. “High-current pulsed operation of an inertial-electrostatic confinement (IEC) device”. In: *18th IEEE/NPSS Symp. Fusion Eng. Symp. Proc. (Cat. No.99CH37050)*. Albuquerque, NM, 1999, pp. 209–212.

[160] K. Yamauchi et al. “Pulsed operation of a compact fusion neutron source using a high-voltage pulse generator developed for landmine detection”. In: *Fusion Sci. Technol.* 47.4 (2005), pp. 1229–1232.

[161] C. F. Barnett. *Atomic Data for Fusion volume 1: Collision of H, H2, He, and Li atoms and ions with atoms and molecules*. Tech. rep. ORNL–6086/V1. Oak Ridge, Tenessee: Oak Ridge National Laboratory, Oak Ridg, Tenessee, 1990.

[162] A. Fridman. *Plasma Chemistry*. New York: Cambridge University Press, 2008.

[163] J. Holzl and F. K. Schulte. *Solid Surface Physics - Work Functions of Metals*. Berlin Heidelberg: Springer-Verlag, 1979.

[164] Y. Lin and D. C. Joy. “A new examination of secondary electron yield data”. In: *Surf. Interface Anal.* 37 (2005), pp. 895–900.

[165] A. Fridman and L. A. Kennedy. *Plasma Physics and Engineering*. New York: Taylor & Francis, 2004.

[166] E. W. Thomas. *Atomic Data for Fusion volume 3: "Particle interactions with surfaces"*. Tech. rep. Oak Ridge, Tennessee: Oak Ridge National Laboratory, Oak Ridg, Tenessee, 1985.

[167] S. Y. Lai et al. “The relationship between electron and ion induced secondary electron imaging: A review with new experimental observations”. In: *Surf. Interface Anal.* 8.93-111 (1986).

[168] P. D. Desai et al. “Electrical Resistivity of Selected Elements”. In: *J. Phys. Chem. Ref. Data* 13.4 (1984), p. 1069.

[169] W. B. Nottingham. “Remarks on energy losses attending thermionic emission of electrons from metals”. In: *Phys. Rev.* 59.11 (1941), pp. 906–907.

[170] E. Morse. *Nuclear Fusion*. Graduate Texts in Physics. Cham, Switzerland: Springer International Publishing, 2018.

[171] M. J. de Loos and S. B. van der Geer. “General Particle Tracer”. In: *EPAC*. Vol. 96. 1996, p. 1241.

[172] *GPT*. URL: `http://www.pulsar.nl/gpt/` (visited on Jan. 13, 2019).

[173] L. Obst et al. “Efficient laser-driven proton acceleration from cylindrical and planar cryogenic hydrogen jets”. In: *Sci. Rep.* 7.1 (2017), p. 10248.

[174] G. Miley et al. “Discharge characteristics of the spherical inertial electrostatic confinement (IEC) device”. In: *IEEE Trans. Plasma Sci.* 25.4 (1997), pp. 733–739.

[175] A. Kamal. *Passage of Charged Particles Through Matter. In: Nuclear Physics*. Berlin, Heidelberg: Springer.

[176] D. H. E. Dubin and T. M. O'Neil. "Trapped nonneutral plasmas, liquids, and crystals (the thermal equilibrium states)". In: *Rev. Mod. Phys.* 71.1 (1999), pp. 87–172.

[177] G. Miley, H. Towner, and N. Ivich. *Fusion cross sections and reactivities*. Tech. rep. Urbana: University of Illinois, C-U Campus, 1974, Report C00–2218–17.

[178] *LHC report: full house for the LHC*. URL: https://home.cern/news/news/accelerators/lhc-report-full-house-lhc (visited on Mar. 10, 2019).

[179] *CERN: Quick Facts*. URL: http://united-states.cern/resources-journalists/quick-facts (visited on Mar. 10, 2019).

[180] *CERN Control Centre Animations 09 "LHC accelerating cavities"*. URL: https://videos.cern.ch/record/1750705%7B%5C%%7D0A (visited on Mar. 10, 2019).

[181] *The Large Hadron Collider*. URL: https://home.cern/science/accelerators/large-hadron-collider (visited on Mar. 10, 2019).

[182] S. Krupaker Murali, G. L. Kulcinski, and J. F. Santarius. "Study of ion flow dynamics in an inertial electrostatic confinement device through sequential grid construction". In: *Phys. Plas]* 15 (2008), p. 122702.

[183] M. K. Sundaresan. *Handbook of Particle Physics*. Pure and Applied Physics. CRC Press, 2001, p. 67.

[184] W. R. Leo. *Techniques for Nuclear and Particle Physics Experiments: A How-to Approach*. Springer Berlin Heidelberg, 2012, p. 24.

List of publications

This thesis is based on the following publications

- **Evolution of the central safety factor during stabilized sawtooth instabilities at KSTAR**
  Messmer M.C.C., Ko J. Chung J. Woo M. H., Lee K.-D. and Jaspers R.J.E
  Nuclear Fusion, Volume 58, Number 1, 2017

- **Optimal MSE polarisation angle and q-profile estimation using Kalman Filters and the plasma simulator RAPTOR**
  Messmer M.C.C., Felici F., Sauter, O., Teplukhina, A.A., Loenen J.P.G., Reich M., Fischer R., Rittich D., Jaspers R.J.E., the ASDEX Upgrade Team and the EUROfusion MST1 team
  Plasma Physics and Controlled Fusion, Volume 61, Number 3, 2019

- **A model-based approach for filtering magnetic pitch angles obtained by the Motional Stark Effect diagnostic**
  M.C.C Messmer, F. Felici, J. Loenen, R.J.E. Jaspers, M. Reich, the ASDEX-Upgrade Team and the EUROfusion MST1 Team
  44th EPS Conference on Plasma Physics, 2017

The author of this thesis was also co-author of the following publications

- **Stark and Zeeman effects as tools for magnetic diagnostics in toroidal plasmas**
  J. Ko, J. Chung and M.C.C. Messmer
  2015 11th Conference on Lasers and Electro-Optics Pacific Rim, 2015

- **Initial operation of a newly developed multichord motional Stark effect diagnostic in KSTAR**
  J. Chung, J. Ko, H. Wi, M. Messmer, S. Schenkelaars, M. Scheffer, and R. J. E. Jaspers
  Review of Scientific Instrument, Volume 87, Number 11, 2016

- **Diagnostic development for current density profile control at KSTAR**
  J.Ko, J.Chung and M.C.C.Messmer *Fusion Engineering and Design*, Volumes 109?111, Pages 742-746, 2016

Curriculum Vitae

Maximilian Claus Constantin Messmer was born on June 12th, 1986 in Würzburg, Germany. He grew up in the village Kirchheim and completed middle school at in 2002. From 2002 to 2004 he visited the Atlantic Technical College in Fort Lauderdale, Florida where he studied computer and network support services. After completion, Maximilian started a 3-year apprenticeship at SSI Schaefer-Noell to become a certified IT specialist, after which he returned to an upper vocational school, the Franz-Oberthür-Schule in Würzburg, and obtained his A-levels in 2009. Following this, Maximilian studied applied physics at the Dresden University of Technology where he obtained his bachelor?s degree in 2012 and his master?s degree in 2014. He specialised in laser and semiconductor physics and conducted his graduation project researching the phenomena of laser wakefield acceleration at the Helmholtz-Zentrum Dresden-Rossendorf. Maximilian continued his academic career by starting a Ph.D. in the group science and technology of nuclear fusion at the Eindhoven University of Technology in February 2015. The research was in part carried out at the KSTAR tokamak in South Korea and the ASDEX Upgrade tokamak in Germany where Maximilian collaborated with the resident scientists to determine the current density profile of the tokamak plasma using the motional Stark effect diagnostic. Furthermore, Maximilian conducted research on electrostatic confinement devices at the Eindhoven University of Technology where he designed a novel low-loss ion accelerator. The research of his Ph.D. work are described in this dissertation.

Acknowledgement

This thesis marks not only the end of my time as a Ph.D. student, but also the end of one of the most important and difficult chapters of my live. A four year journey of immense joy, fantastic experiences, connections with amazing friends, and never-ending challenges, but also sacrifices, doubts and countless hurdles along the way. All of which would not have been possible without my family, my friends and my colleagues - I could not have asked for better companions during this adventure.

First and foremost my wife, mother and sister. Thanks mum for letting me find my own way and trusting that things will turn out all right. I think I made it! You took a big risk to give me the freedom I needed when I needed it and gave me the chance to learn from my own choices. Thank you for all your love, all your help, and all you've taught me. And sorry for asking so many questions (don't get your hopes up that I'll stop with that anytime soon).
Theresa, although you didn't fulfil the very specific gender requirements I gave to our mum, you are everything I ever wished for in a sibling. It's been a pleasure seeing you grow from the little ballet-dancing girl into a woman, and the adventures we had together are some of my best memories. Don't change and *mach dein ding*, you can achieve anything you set your mind to!
Besides the doctorate, these four years led to an even more important result: a family of my own. Ivana, my love, thank you for everything, thank you for making Eindhoven a home, thank you for supporting me in all my choices and thank you for the greatest gift of all: our daughter Emma. After being together for just a few months, then being separated for almost half a year, you were bold enough to take a big chance to move in together straight away and our fantastic relationship took off. I am still having the best time with you, and going through my pictures, it is amazing how much we have already experienced together, climaxing in 2018. Sadly life is not all sunshine and we have had our share of rain together. We have managed the uncertainties and hardship and I know we will manage in the future together, especially with our little bunny at our side. Emma, you do not know it yet, but you were the bright shining star during my days of writing and kept me focussed to finish this thesis on time! I cannot wait to see you growing up!
A huge thank you to Miki, Zoki, Ana and Ronald for all your support during the crunch mode and for taking me in in your family! Thanks for giving Ivana company and helping out with Emma when I was stuck with writing. Without you this thesis would have not been ready yet. I am happy that this period is over and that there is more time for canasta and hanging out together again!

This story would have never started without Niek and Roger - thank you for making all of this possible. Thanks for all the guidance and counselling, for all the fruitful discussions, for pointing me in the right direction when I was looking the other way, and for making sure I stuck around and was able to finish when the famous Ph.D. dip hit! Roger, your easy-going attitude makes working with you a true pleasure and lots of fun. The possibility to walk into your office at any time to pick your brain and (almost) never being rejected is more helpful than you might realise. Your overview of the field was invaluable for me when I got stuck and did not know how to continue and you were always happy to discuss wild ideas.
Niek, we have started really working together in the second half of my Ph.D. and I appreciate all you have taught me. Your rigorousness and precision, your ability to bring order into chaos and to find the essence of the problem are truly inspiring. Thank you for not only taking me in, but also for convincing me to finish the Ph.D. by pursuing the research on the fusor. Without you this project might have ended halfway.
I also want to express my gratitude to Federico who supervised me for over a year and gave me a peek into the world of control engineering. I am sorry it did not work out as originally planned, but the lessons learned were nonetheless important. You helped me make big improvements on my physics-style coding and your drive and passion are truly inspiring. I am excited to see where your journey with RAPTOR will lead you.

Besides my supervisors, such a project can not succeed without collaborators and support, even more when conducting research at big experiments abroad. From Eindhoven, I want to thank Mark for his support on the MSE system and the coding advices, Guido for introducing me the the MSE diagnostic and nuclear fusion and Herman for all he has done for the fusor. From the NFRI in South Korea, I want to thank Jinil, Jinseok, Hyun-Seok and Sang-Hee who took care of me during my many visits, introduced me to everyone and made sure the organisation ran smoothly. You showed me the ins and outs of the local infrastructure, introduced me to the MSE system and equilibrium reconstruction and were an invaluable source of knowledge to commission the diagnostic and get our first q-profiles. I am really excited how well the MSE system is working and wish you many more high-class publications with exciting results. From Germany at the IPP Garching I want to thank Alexander, David, Ondrej and Rainer for getting me started at ASDEX Upgrade, showing me around, and for all the explanations and the fruitful discussions. Without your support the work on the MSE observer would not have been possible.

Being able to concentrate on the research and not having to worry about administrative overhead sure makes life a lot easier, not to mention all the cake treats and coffee breaks to clear the mind. Clazien and Hélène, thank you for all you have done for me and the group, you are two of the key players who keep the fusion group going. Most important for the daily survival, staying sane and enjoying coming to work: Carlos, Daan, Ivana, Josefine and Peter - Thanks for being

there, you are the best colleagues turned friends I could have asked for and made Eindhoven inside and outside of the office a tons of fun! I will miss seeing you every day, our discussions, (frequent) trips to the bar, and the projects we started. When I joined the group I was the only Ph.D. student and worried about my office life to come, but things turned out more than fine!
Getting to this point was not easy, and an important step along the way was my study time in Dresden. There I was lucky to find the right crowd - lots of love to my friends Alex, Basti, Const, Lukas and Stefan. God knows how I would have finished my studies without you, certainly not with excellence. In retrospect, the countless hours spent studying in the library do not seem so bad anymore, probably because of all the fun and silliness. Not to mention the endless parties, Vorglühen, Eier braten, lan parties and lake visits. Thanks for giving me five of the best years of my life – it was a blast!

Lastly, Tobi, thanks for always being there. Even though we might never be able to hang out again as we used to when we were stupid teenagers, every time we meet it feels like nothing has changed.